

UNIMORE
UNIVERSITÀ DEGLI STUDI DI
MODENA E REGGIO EMILIA

Università degli Studi di Modena e Reggio Emilia

Dipartimento di Ingegneria “Enzo Ferrari”

Corso di Laurea Magistrale in

Electronics Engineering

Design and Simulation of a Cryogenic BiCMOS Readout Chain for Superconducting Transmon Qubits via Dispersive Reflectometry

---

Relatore:
Prof. Mattia Borgarino

Candidato:
Ing. Gregory Cordisco

Anno Accademico 2025/2026

"If you can dream it, you can do it."

— Walt Disney

Contents

Contents **5**

1 Introduction **9**
1.1 A New Machine for a New Kind of Problem 9
1.2 The Qubit: Between Abstraction and Fragility 10
1.3 The Coldest Corner of the Machine: Dilution Refrigerators 11
1.3.1 From Room Temperature to 4 K: Taming the Wiring Bottleneck 12
1.4 Reading Out a Superconducting Qubit 13
1.5 Thesis Objectives and Outline 13

2 Device Operation at 4K **15**
2.1 Introduction to Cryogenic Electronics 15
2.2 Operating Principles at 4 Kelvin 16
2.3 Device Characteristics at Cryogenic Temperatures 17
2.3.1 SiGe HBT Behaviour at 4 K 17
2.3.2 CMOS Behaviour at 4 K 22

3 Reflectometry for qubit readout **25**
3.1 Basic Reflectometry Configuration 26
3.1.1 Wave Propagation and Transmission Lines 26
3.1.2 Scattering at Impedance Discontinuities 27
3.2 Resonant Loading and Dispersive Coupling 28
3.2.1 The Resonator as Load Impedance 29
3.2.2 External Coupling and Quality Factors 30
3.2.3 Reflection Coefficient of the Coupled Resonator 31
3.2.4 The Qubit as Reactive Load 33
3.2.5 Dispersive Frequency Shift and State Discrimination 36
3.3 Quadrature Measurement and Signal Representation 37
3.3.1 From RF Reflection to Baseband Detection 37
3.3.2 The IQ Demodulator: Hardware Implementation 38
3.3.3 Complex Signal Representation 39

3.3.4 Threshold Discrimination . . . 40
3.4 Noise and Amplification in Dispersive Readout . . . 41
3.4.1 Noise Sources in Dispersive Readout . . . 41
3.4.2 Gaussian Noise on the IQ Plane . . . 44
3.4.3 Signal-to-Noise Ratio (SNR) Definition . . . 45
3.4.4 Measurement Fidelity and Effective SNR . . . 46
3.5 LNA Noise Requirements for High-Fidelity Readout . . . 47
3.5.1 Signal-to-Noise Requirements from Target Fidelity . . . 48
3.5.2 System Noise Temperature and LNA Contribution . . . 48
3.5.3 Derivation of Required LNA Noise Temperature . . . 49
3.6 Probing signal . . . 52
3.7 Complete Readout Architecture . . . 52

4 Superconducting Transmon Qubit 55
4.1 Harmonic Oscillator and Anharmonic Qubit . . . 55
4.2 Josephson Junction Physics . . . 58
4.2.1 Current Components and the RCSJ Model . . . 59
4.2.2 DC Josephson Effect . . . 64
4.2.3 AC Josephson effect . . . 67
4.2.4 I-V . . . 67
4.3 From Classical Junction Dynamics to the Transmon Qubit . . . 69
4.3.1 Classical Hamiltonian and Canonical Quantization . . . 70
4.3.2 Representation in the Charge Basis . . . 71
4.3.3 Energy Spectrum and Anharmonicity . . . 72
4.3.4 Wavefunctions in the Phase Representation . . . 75
4.4 Effective Circuit Model for Dispersive Readout . . . 77
4.4.1 State-Dependent Junction Properties . . . 78
4.4.2 Implementation via Effective Critical Current . . . 78
4.4.3 Limitations of the Effective Model . . . 79
4.5 Validation and Application of the Effective Junction Model . . . 80
4.5.1 Design Rationale and Parameter Selection . . . 80
4.5.2 DC Current-Phase Relation . . . 82
4.5.3 Voltage-Driven Josephson Oscillations . . . 83
4.5.4 Shapiro Step Formation . . . 84
4.5.5 State-Dependent Frequency Response . . . 85

5 Low Noise Amplifier 87
5.1 LNA Requirements . . . 88
5.2 Cascoded based LNA . . . 89

5.2.1 Circuit Topology and Design Methodology . . . 89
5.2.2 DC Biasing and Operating Point . . . 90
5.2.3 Small-Signal Analysis . . . 91
5.2.4 Noise Analysis . . . 93
5.2.5 Component Selection and Input Matching Design . . . 99
5.2.6 Simulation and Performance Evaluation . . . 100
5.3 Common emitter based LNA . . . 103
5.3.1 Circuit Topology and Design Methodology . . . 103
5.3.2 DC Biasing and Operating Point . . . 103
5.3.3 Small-Signal Analysis . . . 105
5.3.4 Noise Analysis . . . 106
5.3.5 Component Selection and Input Matching Design . . . 108
5.3.6 Simulation and Performance Evaluation . . . 111
5.4 LNA State of the Art . . . 114

6 CMOS Circulator 119
6.1 The Ideal Three-Port Circulator . . . 119
6.1.1 Phase-Interference Interpretation . . . 119
6.1.2 Staggered-Commutation Architecture . . . 120
6.1.3 Target Specifications . . . 121
6.2 Non-Reciprocal Branch: From Gyrators to All-Pass Filters . . . 122
6.2.1 Gyrator Principle via Staggered Mixing . . . 122
6.2.2 Signal-Flow Analysis in the Phase–Frequency Domain . . . 124
6.2.3 Design Equations and Clock-Phase Selection . . . 126
6.3 All-Pass Filter Design . . . 127
6.3.1 Clock Frequency and Modulation Index . . . 127
6.3.2 Limitations of Artificial Transmission Lines . . . 127
6.3.3 Second-Order Bridged-T All-Pass Filter . . . 128
6.3.4 Determination of the Quality Factor . . . 131
6.3.5 Dimensioning of the All-Pass Filter Components . . . 132
6.3.6 First-Order Lattice All-Pass Filter (Reciprocal Branches) . . . 132
6.4 Bandwidth Analysis . . . 134
6.5 CMOS Circulator Implementation . . . 135
6.5.1 Mixer Design . . . 136
6.6 Clock Generation Circuit . . . 137
6.6.1 Architecture . . . 137
6.6.2 Active Balun . . . 137
6.6.3 Squaring Stage . . . 140
6.6.4 Frequency Divider . . . 142

6.6.5 Phase Alignment and Output Buffers . . . 146
6.7 Results . . . 148
6.7.1 Circulator . . . 148
6.7.2 LO Generation Chain . . . 152
6.7.3 Summary . . . 158

7 System-Level Simulations and Performance 159
7.1 Complete Readout Chain Integration . . . 159
7.2 Readout Resonator Design . . . 160
7.2.1 Specifications and Design Constraints . . . 160
7.2.2 Analytical Sizing . . . 160
7.2.3 Circuit Implementation and Simulation . . . 162
7.2.4 Simulation Results . . . 163
7.3 Simulation Results . . . 165
7.3.1 Noise Analysis . . . 167

8 Conclusions and Future Work 169
8.1 Summary of the Work . . . 169
8.2 Main Results . . . 170
8.3 Limitations and Expected Discrepancies with Measurements . . . 172
8.4 Future Directions . . . 172
8.5 Closing Remarks . . . 174

A Verilog-A Code for Josephson Junction 175
A.0.1 Module Structure and Interface . . . 175
A.0.2 Internal Variables . . . 176
A.0.3 Verilog-A Source Code . . . 176
A.0.4 Analog Block: Operational Logic . . . 178

AI Disclaimer: Artificial intelligence tools were used solely to improve the English grammar, vocabulary, and formal style of this thesis. All concepts, mathematical derivations, code, simulations, analyses, and results were developed independently by the author.

Chapter 1 Introduction

1.1 A New Machine for a New Kind of Problem

The modern digital computer is a universal machine capable of executing any algorithm that can be expressed in a finite number of steps. Its power stems out from the ability to manipulate information encoded in binary digits, or bits: in practice, nothing more exotic than an electrical signal switched between a low and a high voltage, conventionally denoted 0 and 1. A classical register of n bits can therefore encode one of 2^n possible configurations at a time, and a classical processor can only operate on one configuration at a time.

And yet, for all its versatility, this paradigm meets a wall. Some problems, such as factoring large integer numbers, certain cryptographic tasks, molecular simulations, and combinatorial optimization requires an exponential number of steps in the size of the input, placing them permanently beyond the reach of even the most powerful classical supercomputers. Quantum computing does not attempt to push past this wall by brute force, but it proposes a different machine altogether; one that exploits the principles of quantum mechanics to process information in ways that have no classical counterpart, promising exponential speed-ups for precisely the problems that classical computing cannot solve efficiently.

The source of this advantage lies in two genuinely non-classical resources: superposition, which allows a quantum register to encode a linear combination of all its classical configurations at once, and entanglement, which correlates the state of different qubits in a way that has no classical analogue. Superposition alone does not yield a computational speed-up, since a superposed state cannot be read out deterministically; it is the combination of superposition and entanglement, exploited by a dedicated family of algorithms, that enables a quantum processor to outperform its classical counterpart on specific tasks [1].

The simplest useful algorithms that could beat a supercomputer require only hundreds to thousands of ideal qubits, a number apparently within reach of today's quantum processors, which already showcase more than one thousand physical qubits. The difficulty is that physical qubits are far from ideal. Unwanted coupling with the environment limits their fidelity, i.e. the probability that an operation or a measurement produces the intended result, well below the 100 % needed for a faithful algorithm execution. Quantum error correction (QEC) compensates for this with redundancy, encoding a single logical qubit into up to thousands of physical ones [2], [3]. The consequence is a formidable one: a practical fault-tolerant quantum computer is expected to require millions of physical qubits, each of which must be individually controlled and read out, a demand that turns quantum computing from a physics problem into an engineering problem of the first order.

Several hardware platforms are racing toward this goal: superconducting qubits, spin qubits in semi-

conductors, colour centres in diamond, trapped ions, and others. Among them, superconducting qubits are today the most mature in terms of processor size and are the platform considered in this thesis. They are microwave quantum objects operating in the 4–8 GHz band, controlled and measured through 50 Ω matched interfaces, which makes them a natural, if unforgiving, application field for RF and microwave circuit design [2], [4].

1.2 The Qubit: Between Abstraction and Fragility

Before addressing any physical implementation, it is worth stressing that the qubit is first of all an abstract mathematical entity, indifferent to the substrate that carries it. A qubit is a two-level quantum system whose state is a unit vector in a two-dimensional complex Hilbert space,

$$|\psi\rangle = \alpha|0\rangle + \beta|1\rangle, \qquad \alpha, \beta \in \mathbb{C}, \quad |\alpha|^2 + |\beta|^2 = 1, \tag{1.1}$$

where $|0\rangle$ and $|1\rangle$ form the computational basis. Up to an irrelevant global phase, the state can be represented as a point on a sphere, known as the Bloch sphere, with $|0\rangle$ and $|1\rangle$ at the north and south poles and any other point corresponding to a superposition. Single-qubit operations are azimuthal or polar rotations on this sphere, allowing the qubit state to be steered with continuous control. A measurement in the computational basis projects the state onto one of the two poles, returning $|0\rangle$ with probability $|\alpha|^2$ and $|1\rangle$ with probability $|\beta|^2$. This probabilistic nature of the readout has a direct engineering consequence: the state of a qubit cannot be inferred from a single ideal measurement unless it lies exactly on a pole, and the quality of a readout chain is therefore judged by its ability to discriminate the two basis states reliably in a single shot and within a time short compared to the qubit coherence time.

This formal description is elegant precisely because it is independent of the physical carrier of the information. Any two-level system with a sufficiently isolated pair of energy eigenstates, separated by $\Delta E = \hbar\omega_{01}$, can in principle encode a qubit. What differentiates the various platforms, and what ultimately decides which of them will prevail, is the physical nature of the two-level system: it determines the frequency ω_{01}, the control and readout mechanisms, and, most importantly, the coherence properties.

By the term coherence, we refer to the ability of a quantum system to preserve its state over time; it is the currency in which every quantum computation is paid. Unlike its mathematical description, a qubit implementation, whatever its physical form, is a real physical system, and no real system is ever truly isolated. The instant a qubit is carved out of a physical substrate, it begins to leak information into its surroundings, a slow haemorrhage of quantumness known as decoherence, characterized by two timescales T_1 and T_2. A qubit with long coherence times can undergo more operations before this haemorrhage becomes fatal to the computation, which is why the race for longer T_1 and T_2 underlies nearly every advance in the field. It is also the reason why quantum computers are operated

at cryogenic temperatures, where thermal noise and other sources of interaction are suppressed and coherence times can be stretched to hundreds of microseconds.

At the same time, different physical qubit implementations require cryogenic environments for reasons that go beyond preserving coherence: some qubits need the cold to exist as quantum objects in the first place. Superconducting qubits, for instance, are built around Josephson junctions, superconducting devices that exhibit a non-linear inductance and can be used to create anharmonic oscillators, whose very operation presupposes the absence of thermal excitation and electrical resistance that only cryogenic temperatures can guarantee.

1.3 The Coldest Corner of the Machine: Dilution Refrigerators

Solid-state qubits reveal their quantum behaviour only when the thermal energy $k_B T$ is negligible with respect to the level separation $\hbar\omega_{01}$. For a transmon at 6 GHz this corresponds to a temperature of roughly 300 mK, and in practice superconducting processors are operated at 10–20 mK. Reaching and sustaining such temperatures continuously is the task of the dilution refrigerator (DR), which has become the workhorse of sub-kelvin refrigeration for condensed-matter physics and, more recently, for quantum computing [5].

The operating principle exploits the peculiar thermodynamics of ^{3}He–^{4}He mixtures. Below about 0.87 K the mixture separates into a ^{3}He-rich concentrated phase, which floats on top of a dilute phase; even at $T \to 0$ the dilute phase retains a finite ^{3}He solubility of 6.6 %. Forcing ^{3}He atoms across the phase boundary in the mixing chamber, from the concentrated into the dilute phase, is analogous to an evaporation process and produces cooling. The ^{3}He is then extracted from the dilute phase in the still, held at about 0.7 K, where its apour pressure is much higher than that of ^{4}He, and recirculated by pumps through a chain of heat exchangers [5]. The concept was proposed by H. London in 1951 and the first working refrigerator was built in Leiden in 1965, reaching 220 mK. Progressive improvements in heat-exchanger technology brought the minimum temperature down to the current record of 1.75 mK [5]. A decisive step for their diffusion was the transition from ”wet” systems, precooled by liquid-helium baths, to cryogen-free (”dry”) systems precooled by pulse-tube cryocoolers, which now dominate the market.

From the point of view of the electronics designer, the most relevant characteristic of a DR is its stratified, and severely rationed, cooling budget. Commercial systems offer a cooling budget of the order of tens of microwatts at 20 mK and of the order of one milliwatt at 100 mK, with the largest platforms reaching 2 mW at 100 mK [5]; conversely, the 4 K stage provided by the pulse-tube cooler offers watts of cooling power [2]. Any active circuit placed inside the cryostat must therefore be located at a stage whose cooling power can absorb its dissipation, and every additional wire or coaxial line running between stages constitutes a heat load that quietly consumes this precious budget.

1.3.1 From Room Temperature to 4 K: Taming the Wiring Bottleneck

Today, the signals that control and read out the qubits are generated and acquired almost entirely by room-temperature instrumentation and routed into the cryostat through meter-long coaxial cables, typically one or two per qubit. Early demonstrators, built around a handful of qubits, could afford this architecture without penalty. As processors have grown to the few hundred qubits now available, however, this same wiring scheme is already stretched to its practical limits, and it does not extend any further: a processor with millions of qubits would require millions of cables threaded through the refrigerator, with prohibitive size, cost, heat leak and reliability [2]. This wiring bottleneck is recognized as one of the main obstacles between current demonstrators and practical large-scale machines, and it is one of the key drivers, alongside the need for higher channel density, low noise and high fidelity, behind the effort to move part of the classical electronics into the cryostat itself, anchored at the 4 K stage.

The proposed way around it is to move part of the classical interface, signal generation, amplification, down-conversion, multiplexing and digital processing, close to the qubits, inside the cryostat. This imposes three requirements on the electronics. First, it must be integrated, so that a large number of channels can fit in the limited volume of the cryostat. Second, its performance must not limit the qubit fidelity, which calls for co-simulation of the quantum and classical parts of the system. Third, its power dissipation must be compatible with the available cooling power, which in practice confines the bulk of the electronics to the $1 - 4$ K stages and leaves only very-low-power functions, such as amplification of the readout signal, closer to the qubits [2].

Commercial silicon technologies operated at cryogenic temperature, collectively referred to as cryo-CMOS or, when bipolar devices are included, cryogenic BiCMOS, have emerged as the preferred solution owing to their ability to integrate the complex systems-on-chip needed to drive millions of qubits. Transistors fabricated in standard processes remain functional at 4 K and even improve in some respects: carrier mobility increases, passive components retain their nominal values while gaining in quality factor, and thermal noise decreases. However, the designer must also face a threshold-voltage shift of $100 - 200$ mV that reduces the available headroom, a degraded device matching, a saturation of the noise improvement at low temperature attributed to shot noise, significant self-heating and thermal crosstalk [2]. The most limiting issue in practice is the lack of validated cryogenic compact models: designers are usually forced to simulate at the lowest temperature offered by the process design kit, typically -40 or -55 °C, and extrapolate the behaviour at 4 K, leaving wide margins and relying on calibration knobs. Technologies for which cryogenic models are available therefore offer a substantial advantage, and this is one of the motivations for the choice of the IHP SG13G2 SiGe BiCMOS process adopted in this work, whose design kit includes device models valid at 4 K.

1.4 Reading Out a Superconducting Qubit

Among the functions that a cryogenic interface must provide, qubit readout is arguably the most demanding from the analogue point of view, and the one on which the credibility of an entire computation ultimately rests. In superconducting processors the qubit is dispersively coupled to a linear resonator, whose resonant frequency shifts by a small amount depending on whether the qubit is in $|0\rangle$ or $|1\rangle$. Probing the reflection coefficient of the resonator with a weak microwave tone and demodulating the reflected signal with an I/Q receiver thus converts the qubit state into a shift of amplitude and phase of a classical signal [2], [4]. Because the probing power must be kept below roughly -125 dBm to avoid perturbing the very state it seeks to measure, the reflected signal is exceedingly weak, little more than a whisper, and the sensitivity of the whole chain is set by its first amplification stages. State-of-the-art systems employ a superconducting Josephson parametric amplifier operating near the quantum noise limit, followed by a cryogenic low-noise amplifier, traditionally a discrete InP HEMT; SiGe and CMOS LNAs are being actively investigated as integrated alternatives [6], [7]. In addition, the reflectometry architecture needs a circulator to separate the incident and reflected waves and to protect the qubit from amplifier noise. Ferrite circulators are bulky, incompatible with integration and a major obstacle to scaling; an active, integrated replacement is therefore highly desirable, provided that its noise and its own power dissipation remain acceptable.

Designing such a readout chain requires a quantitative link between the qubit physics and the circuit specifications: the dispersive shift and the resonator linewidth determine the achievable signal contrast, the integration time determines the bandwidth, and together with the noise temperature of the chain they set the signal-to-noise ratio and hence the single-shot readout fidelity. Establishing this link, and verifying it through a complete circuit-level simulation in which the qubit itself is represented by a compact model, is the central aim of this thesis.

1.5 Thesis Objectives and Outline

The objective of this work is the design and simulation, in the SiGe BiCMOS IHP technology, offering available cryogenic device models, of a complete reflectometry-based readout chain for a superconducting transmon qubit, including the qubit model itself, and the assessment of its state-discrimination performance. The thesis is organised as follows.

Chapter 2 addresses by simulation the devices of the IHP SG13G2 technology using the 4 K models provided in the process design kit for Cadence Virtuoso. The relevant figures of merit of the active devices are extracted and compared with their room-temperature counterparts, providing the design basis for the circuits developed in the following chapters.

Chapter 3 introduces the fundamental concepts of qubit measurement through microwave reflectometry. Starting from the mathematical description of a reflectometer measurement system, the

dispersive interaction qubit-resonator is described and translated into a set of performance requirements for the readout electronics, in particular in terms of noise, signal contrast and integration time.

Chapter 4 addresses the physical implementation of the qubit as a superconducting transmon. The Josephson junction is treated and modelled; a Verilog-A implementation based on the resistively and capacitively shunted junction (RCSJ) model is developed and verified. A modified version of the model, derived from a quantum-mechanical treatment of the junction, is then introduced to simulate a transmon composed of a single junction and a shunt capacitor in a static regime: no decay or transition between levels is included, and the quantum state of the qubit imposes the operating parameters of the circuit element seen by the resonator.

Chapter 5 presents the design of two cryogenic low-noise amplifiers in BiCMOS technology, one based on a cascode topology and one on a common-emitter topology; a small-signal and noise analysis are carried out and compared with simulations.

Chapter 6 describes an active CMOS circulator intended to replace the ferrite component in the reflectometry path, together with the auxiliary circuits that generate the required carriers from a single reference signal delivered from room temperature. This approach reduces the number of lines entering the cryostat, and hence the heat load, and facilitates scaling. The operation of the circulator is analysed in the frequency domain.

Chapter 7 combines all the blocks into the complete reflectometry system and reports the simulation of the readout of the superconducting qubit model in the $|0\rangle$ and $|1\rangle$ states, including the I/Q demodulator outputs, the state separation on the I/Q plane for a 40 ns capture time, and the noise analysis of the chain for the two LNA options.

Chapter 8 summarises the results and discusses possible future developments.

Chapter 2 Device Operation at 4K

2.1 Introduction to Cryogenic Electronics

The rapid growth of quantum computing, radio astronomy, and deep-space instrumentation has generated an intense demand for electronic circuits capable of operating reliably at temperatures far below the commercial and military specification ranges. Whereas conventional semiconductor electronics are qualified between approximately $-55\,^{\circ}\mathrm{C}$ and $+125\,^{\circ}\mathrm{C}$, the read-out and control of superconducting qubits requires active circuitry that functions at, or in close thermal proximity to, the millikelvin quantum plane, typically at the $4\,K$ stage of a dilution refrigerator [8].

Placing classical electronics at cryogenic temperatures offers two compelling advantages. First, thermal noise drops in direct proportion to the absolute temperature: for instance, the voltage noise spectral density of a resistor ($S_v = 4kTR$) decreases by a factor of 75 when cooling from $300\,\mathrm{K}$ to $4\,\mathrm{K}$, from roughly $1.29\ \mathrm{nV}/\sqrt{\mathrm{Hz}}$ to $0.15\ \mathrm{nV}/\sqrt{\mathrm{Hz}}$ (for $R = 50\ \Omega$). Second, co-locating amplifiers with the quantum processor dramatically reduces the number of coaxial cables that must traverse the cryostat, relieving both the thermal budget and the wiring complexity that currently limit qubit scaling [9].

Among the available semiconductor technologies, Silicon-Germanium (SiGe) Heterojunction Bipolar Transistor (HBT) platforms occupy a privileged position for cryogenic applications. As Cressler notes, "virtually all of the parameters one cares about harnessing in the SiGe HBT from an analog and RF circuit design perspective naturally improve with cooling'"[10]. This improvement arises from the thermally activated nature of carrier transport in bandgap-engineered devices: as temperature decreases, the exponentials governing injection efficiency, current gain, and transconductance grow enormously, often yielding a doubling or more of performance [10].

At the same time, CMOS technologies are being actively developed for cryogenic operation, motivated by their unparalleled integration density and digital processing capability [11], [12]. While CMOS devices benefit from enhanced mobility and steeper subthreshold swing at low temperatures, they also face challenges including threshold voltage shifts due to incomplete ionization, increased parameter variability, and the *kink effect* in the output characteristics and increased parameter dispersion (low matching) [13].

This chapter provides a systematic overview of semiconductor device behaviour at cryogenic temperatures, with emphasis on the IHP SG13G2 130 nm SiGe BiCMOS platform that is employed in the LNA designs presented in the subsequent chapters. Section 2.2 reviews the fundamental physical mechanisms that govern device operation at 4 K. Section 2.3 presents the characterisation of both SiGe HBTs and NMOS transistors from the SG13G2 process design kit (PDK), supplemented by a comparative literature survey.

2.2 Operating Principles at 4 Kelvin

The electrical behaviour of semiconductor devices at cryogenic temperatures departs markedly from room-temperature predictions because several fundamental physical quantities exhibit strong temperature dependencies. This section summarises the key mechanisms that dominate at 4 K.

At room temperature, the thermal energy $kT \approx 26$ meV is sufficient to ionize virtually all shallow dopants in silicon (donor ionization energy $E_D \approx 45$ meV for phosphorus). At $4\,K$, the thermal energy drops to $kT \approx 0.34$ meV, and carrier freeze-out would, in principle, render lightly doped regions insulating. In practice, heavily doped regions such as the emitter and base of modern SiGe HBTs, which are degenerately doped above 10^{19} cm^{-3}, remain essentially fully ionized even at millikelvin temperatures, because the impurity band merges with the conduction (or valence) band [10], [14]. This is a crucial enabler for bipolar transistor operation at deep cryogenic temperatures. In MOSFET devices, freeze-out predominantly affects the lightly doped substrate and well regions, leading to increased threshold voltage and modified body effect [11], [13].

The silicon bandgap increases from approximately 1.12 eV at $300\,K$ to 1.17 eV at $4\,K$, following the Varshni relation [15]. This widening shifts the intrinsic carrier concentration n_i to negligibly small values, which reduces leakage currents but also modifies the threshold voltage in MOSFETs and the turn-on voltage in bipolar devices. In SiGe HBTs, the bandgap difference $\Delta E_{g,\mathrm{Ge}}$ between the Si emitter and the SiGe base is preserved and, importantly, appears as an exponential factor $\exp(\Delta E_{g,\mathrm{Ge}}/kT)$ that increases dramatically as temperature decreases, directly enhancing emitter injection efficiency [10].

Lattice (phonon) scattering decreases dramatically at cryogenic temperatures because the phonon population scales as $1/(e^{\hbar\omega/kT}-1)$. Consequently, carrier mobility rises substantially upon cooling. Benserhir et al. report a 70 % improvement in minority carrier mobility in the base of IHP SG13G2 SiGe HBTs when cooled from 293 K to 4 K [16]. In MOSFETs, enhanced mobility translates directly into higher drive current and transconductance for a given bias point [13].

Below approximately 50 K, the conventional drift-diffusion model fails to account for the observed collector currents in SiGe HBTs [10], [14]. Rücker, Korn, and Schmidt demonstrated that at cryogenic temperatures the collector current is dominated by quantum-mechanical tunnelling of electrons from the emitter to the collector through the potential barrier defined by the conduction band edge in the base [14]. This tunnelling current is essentially temperature-independent, which explains the experimentally observed "quenching" of the Gummel characteristics below approximately 20 K: the I_C–V_BE curves for 10 K and 17 K overlap almost exactly [10], [14]. The tunnelling probability depends exponentially on the base width and the height of the potential barrier, both of which are set by the doping and germanium profiles. This provides a pathway for device-level optimisation specifically targeting cryogenic performance.

The subthreshold slope $SS = \ln(10)\, n\, kT/q$ decreases linearly with temperature for an ideal MOSFET, reaching approximately 0.8 mV/dec at 4 K (with ideality factor $n = 1$). In practice, interface traps limit the achievable improvement; nevertheless, measured values of $SS \approx 14$ mV/dec at 4 K have been reported for bulk CMOS [13], and analogous improvements in the Gummel slope of SiGe HBTs have been observed, with the slope improving from 40 mV/dec at 293 K to 14 mV/dec at 4 K [16].

2.3 Device Characteristics at Cryogenic Temperatures

This section presents the simulated characteristics of the SiGe HBT (`npn13G2`) and NOMS (`sg13_lv_nmos`) devices available in the IHP SG13G2 PDK.All simulations were performed in the Cadence Virtuoso environment using the cryogenic model cards provided by IHP, maintaining identical testbench configurations at 300 K and 4 K.

2.3.1 SiGe HBT Behaviour at 4 K

Current gain

Figure 2.3.1 presents the DC current gain β as a function of the collector current density J_C at both 300 K and 4 K. At room temperature, β exhibits a broad plateau of approximately 820, with a gentle roll-off at high current densities due to the Kirk effect and base push-out. At 4 K, the peak current gain rises to approximately 2700, representing an enhancement factor of roughly $3.3\times$. The current-density dependence at 4 K is notably more pronounced: β displays a sharper peak and a narrower "bell-shaped" curve, indicating that the optimal bias window for achieving maximum gain is considerably reduced.

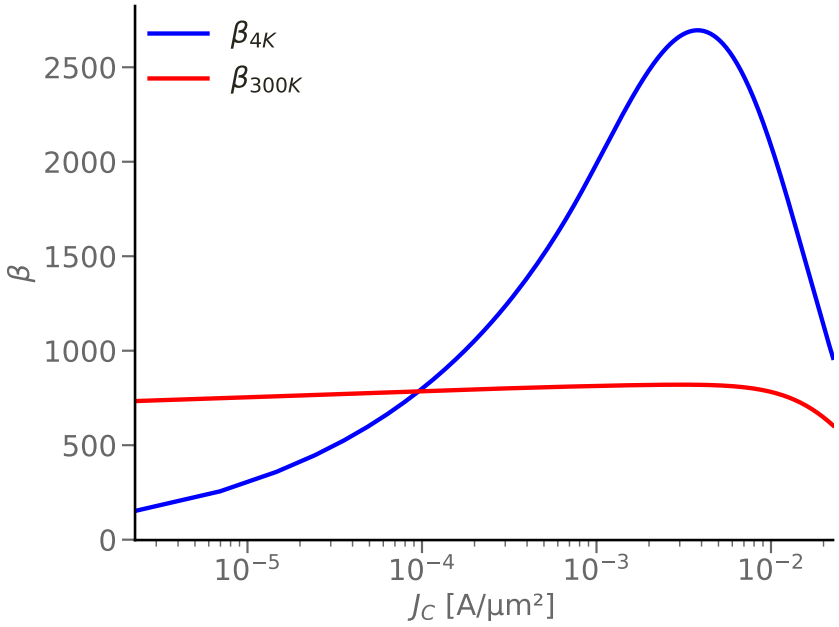


Figure 2.3.1: Simulated DC current gain β as a function of collector current density J_C at 300 K and 4 K for the IHP SG13G2 npn13G2 HBT.

This enhancement is a direct consequence of the bandgap engineering inherent to SiGe HBTs. The graded germanium profile in the base creates a built-in electric field that aids minority carrier transport, while the bandgap offset $\Delta E_{g,\mathrm{Ge}}$ at the emitter-base junction exponentially suppresses hole back-injection into the emitter. Since these effects enter through Boltzmann-type exponentials $\exp(\Delta E_g/kT)$, cooling from 300 K to 4 K amplifies them enormously [10], [17]. The enhanced current gain at low temperatures is particularly important for LNA design, as it directly influences the minimum noise figure achievable and the input matching conditions.

Gummel plot

Figure 2.3.2 shows the Gummel characteristics, collector and base currents versus base-emitter voltage V_{BE}, at both operating temperatures. Two salient features are immediately evident. First, the slope of the $I_{\mathrm{C}} - V_{\mathrm{BE}}$ curve increases dramatically upon cooling, reflecting the enhanced transconductance $g_m \approx qI_{\mathrm{C}}/(nkT)$. The ideality factor η at room temperature is close to unity (consistent with diffusion-dominated transport), whereas at 4 K the effective ideality factor increases to approximately 20, reflecting the transition from thermally activated transport to tunnelling-dominated transport [14], [16]. Second, the turn-on voltage increases from approximately 0.80 V at 300 K to roughly 0.87 V at 4 K, consistent with the well-known negative temperature coefficient of V_{BE} (approximately -2 mV/°C) and the freezing of majority carriers in the emitter [18].

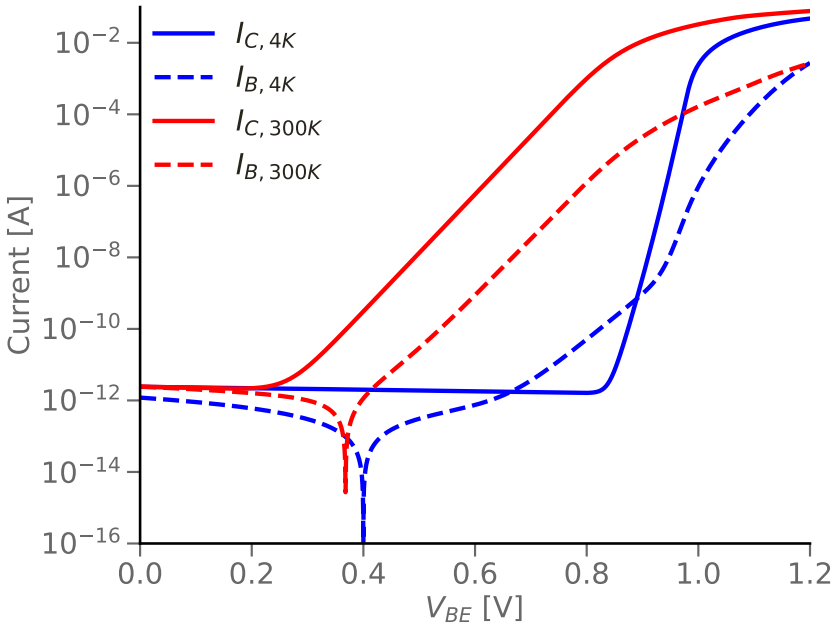


Figure 2.3.2: Simulated Gummel characteristics at 300 K and 4 K for the IHP SG13G2 npn13G2 HBT.

Output characteristics and Early effect

The output characteristics (I_C versus V_{CE} at fixed I_B) reveal significant differences between room-temperature and cryogenic operation. At 300 K, the curves display a discernible negative slope at high power dissipation levels, attributable to self-heating: as the junction temperature rises, the current gain decreases, leading to a reduction in I_C with increasing V_{CE} [18]. At 4 K, this self-heating effect is strongly suppressed because the vastly increased thermal gradient between the device and the ambient facilitates efficient heat removal, resulting in nearly ideal flat output characteristics over the entire V_{CE} range.

A second notable observation is the quasi-absence of the Early effect at cryogenic temperatures. The Early voltage V_A, which quantifies the output resistance of the transistor in the forward-active region, is related to the modulation of the neutral base width by the collector-base depletion layer. In SiGe HBTs with a graded germanium profile, the early voltage V_A is inherently higher than in Si BJTs because the Ge grading introduces a position-dependent bandgap that exponentially weights the base charge distribution [19]. At cryogenic temperatures, Rücker et al. [14] and Cherepanov et al. [18] report a reduction in V_A, attributed to enhanced neutral base recombination (NBR). The NBR manifests as a dependence of the base current on V_{CB}: at fixed base current forcing, V_{BE} must increase with V_{CE} to compensate for the additional recombination, producing an apparent positive slope in the output curves [18], [19]. In our simulations, however, the output characteristics at 4 K appear nearly flat within the safe operating area, this permitting the use of a simplified small-signal model without early voltage compensation for LNA design.

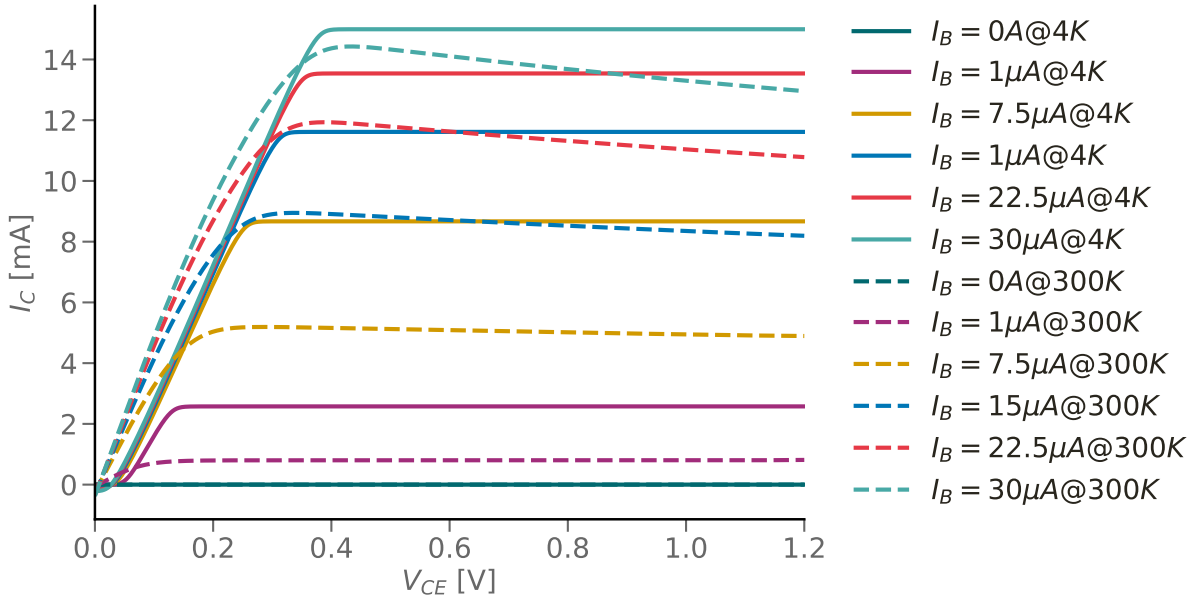


Figure 2.3.3: Simulated output characteristics at 300 K and 4 K for the IHP SG13G2 npn13G2 HBT.

Ideality factor

The ideality factor η can be extracted from the Gummel characteristics in Figure 2.3.2 as follow:

$$I_{\mathrm{C}} = I_{\mathrm{S}} \exp\left(\frac{V_{\mathrm{BE}}}{\eta V_{\mathrm{T}}}\right) \tag{2.1}$$

$$\ln(I_{\mathrm{C}}) = \ln(I_{\mathrm{S}}) + \frac{V_{\mathrm{BE}}}{\eta V_{\mathrm{T}}} \Rrightarrow \eta = \frac{1}{V_{\mathrm{T}}} \left(\frac{d \ln I_{\mathrm{C}}}{d V_{\mathrm{BE}}}\right)^{-1} \tag{2.2}$$

As shown in figure 2.3.4, the ideality factor increases from approximately 1 at 300 K to roughly 20 at 4 K (at $V_{\mathrm{BE}} = 0.98$ V or $I_{\mathrm{C}} \approx 0.36$ mA), consistent with the transition from diffusion-dominated transport to tunnelling-dominated transport [14], [16]. The subthreshold slope correspondingly decreases from approximately 40 mV/dec at 300 K to roughly 9.6 mV/dec at 4 K, reflecting the enhanced injection efficiency and reduced thermal voltage.

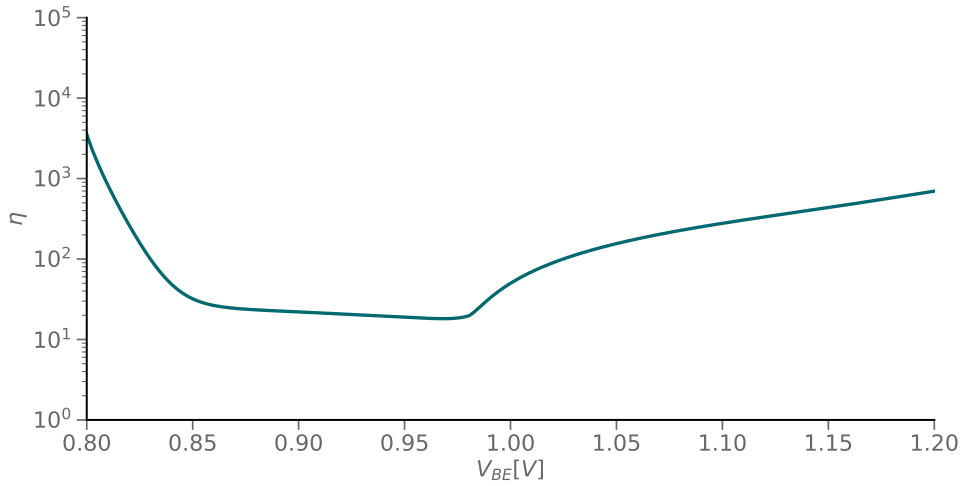


Figure 2.3.4: Ideality factor as a function of base-emitter voltage at different temperatures.

Parasitic capacitances

The junction capacitances C_{BE} and C_{BC} are critical parameters for high-frequency performance, as they directly influence the transit frequency f_{T} and the maximum oscillation frequency f_{max}. Benserhir et al. report that C_{BE} and C_{BC} exhibit relatively modest changes upon cooling to $4\,K$ [16]: the base-collector capacitance decreases slightly due to the widening of the depletion region associated with the increased built-in potential, while the base-emitter capacitance may increase marginally because of the higher transconductance (the diffusion capacitance scales as $C_{\mathrm{diff}} = \tau_F g_m$, where τ_F is the forward transit time). The net effect is a modest increase in f_{T} at cryogenic temperatures. Benserhir et al. measured a peak f_{T} of 510 GHz at 4 K compared to 350 GHz at 293 K [16], consistent with the combined effects of enhanced g_m and reduced base transit time.

Literature survey of SiGe HBT cryogenic performance

To contextualise the performance of the SG13G2 device within the broader landscape of cryogenic SiGe HBT research, Table 2.1 compiles key DC and AC parameters reported in the literature for various SiGe HBT technologies operated at cryogenic temperatures. The table includes the operating temperature, turn-on voltage at a fixed current density, current gain at cryogenic and room temperatures, ideality factor, subthreshold slope, and the presence of anomalous effects such as the collector-current kink and Early voltage degradation.

Reference	Technology	A_E [μm^2]	T [K]	$V_{BE,on}$ [V]	β_{CT}	β_{RT}	η	SS	Kink	Early
Chakraborty [20]	130 nm BiCMOS	NA	4.3	NA	3369	1000	NA	7	N	N
Schröter [21]	130 nm BiCMOS	NA	4	0.89	NA	NA	1.85	NA	N	N
Yuan [22]	500 nm BiCMOS	0.5×2.5	43	NA	NA	NA	2	NA	Y	Y
Bardin [17]	130 nm BiCMOS	NA	18	0.91	NA	NA	1.75	NA	NA	NA
Benserhir [16]	130 nm BiCMOS	NA	4	0.91	2750	1000	30	24	N	Y
Song [23]	160 nm BiCMOS	5×5	7	NA	0.1	60	100	NA	NA	NA
Ying [24]	130 nm BiCMOS	0.12×8	12	NA	1250	NA	96	NA	N	N
Liu [25]	500 nm BiCMOS	0.46×0.46	77	1.02	0.2	3	NA	NA	N	Y
Bonen [26]	55 nm BiCMOS	0.1×4.5	2	0.95	10000	NA	NA	NA	Y	N
Rücker [14]	130 nm BiCMOS	0.12×0.96	10	0.91	50000	8000	10	NA	N	Y
Prêle [27]	350 nm BiCMOS	2.8	4	NA	1000	200	NA	NA	NA	NA
Najafizadeh [28]	500 nm BiCMOS	0.5×2.5	1.4	NA	NA	NA	NA	NA	N	N
Cherepanov [18]	600 nm BiCMOS	0.6×10.16	77	NA	250	200	NA	NA	N	Y
Weinreb [29]	130 nm BiCMOS	18×0.12	15	NA	8000	500	NA	NA	N	Y
Crabbé [30]	NA	1.0×4.6	84	0.8	120	95	NA	NA	N	Y
Cressler [31]	55 nm BiCMOS	0.5×2.5	4.5	NA	7693	827	NA	NA	N	N
This work	130 nm BiCMOS	0.07×0.9	4	0.87	2696	820	20.5	9.6	N	N

Table 2.1: Comparative survey of SiGe HBT performance at cryogenic temperatures. “CT” and “RT” denote cryogenic and room temperature, respectively. “NA” indicates that the parameter was not reported; “N” and “Y” indicate the absence or presence of the effect, respectively.

Several trends emerge from this survey. First, the current gain enhancement upon cooling is a universal feature of SiGe HBTs, though its magnitude varies considerably depending on the germanium profile, base width, and doping concentrations. The highest reported β at cryogenic temperatures ($\sim$50 000 at 10 K) was achieved by Rücker et al. [14] using a modified SG13G2 process with increased germanium content and reduced base doping, a configuration specifically optimised for cryogenic operation. Second, the ideality factor n generally increases at cryogenic temperatures, reflecting the transition from diffusion to tunnelling transport. Third, the collector-current kink effect, which manifests as a region of negative differential resistance in the output characteristics, is absent in most modern devices but has been observed in certain early-generation SiGe HBTs at deep cryogenic temperatures.

2.3.2 CMOS Behaviour at 4 K

Although the LNA designs presented in the subsequent chapters primarily employ SiGe HBTs, the IHP SG13G2 platform also provides NMOS and PMOS transistors that are used for circulator and other anolog-mixed-signal applications.

The most prominent effect of cooling on MOSFET behaviour is the increase in threshold voltage V_{th}. This shift arises from the increase in the substrate Fermi potential $\phi_{\text{F}} = (kT/q)\ln(N_A/n_i)$, which grows as n_i decreases exponentially with temperature, combined with incomplete ionization of the substrate dopants [11]. For the SG13G2 low-voltage NMOS device ($L_{\text{min}} = 130$ nm, $V_{\text{th}} \approx 0.5$ V at 300 K), the cryogenic model predicts a threshold voltage increase of approximately 100-200 mV at 4 K, consistent with the trends reported in the literature [11], [13].

The transfer characteristic (I_{D}-V_{GS}) at 4 K exhibits a markedly steeper subthreshold slope, approaching 10 mV/dec compared to room temperature 80 mV/dec, enabling sharper on/off transitions [13]. Above threshold, the enhanced carrier mobility yields higher drive currents for a given overdrivevoltage.

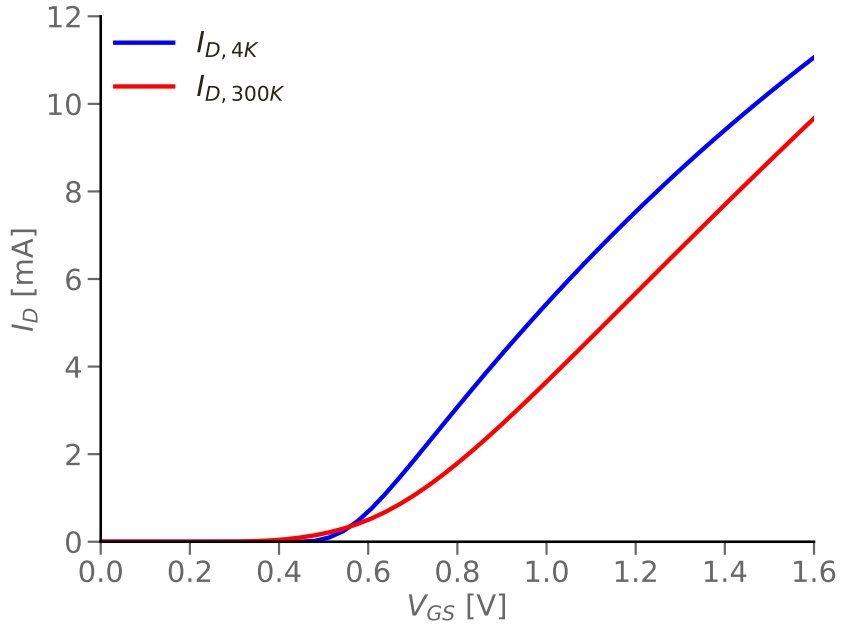


Figure 2.3.5: Simulated transfer characteristics of the IHP SG13G2 low-voltage NMOS device at 300 K and 4 K.

However, the output characteristics (I_{D}-V_{DS}) may display the so-called “kink effect” at cryogenic temperatures: an abrupt increase in drain current at moderate V_{DS}, attributed to impact-ionisation-genera holes that accumulate in the substrate due to the freeze-out of the body contact [13].

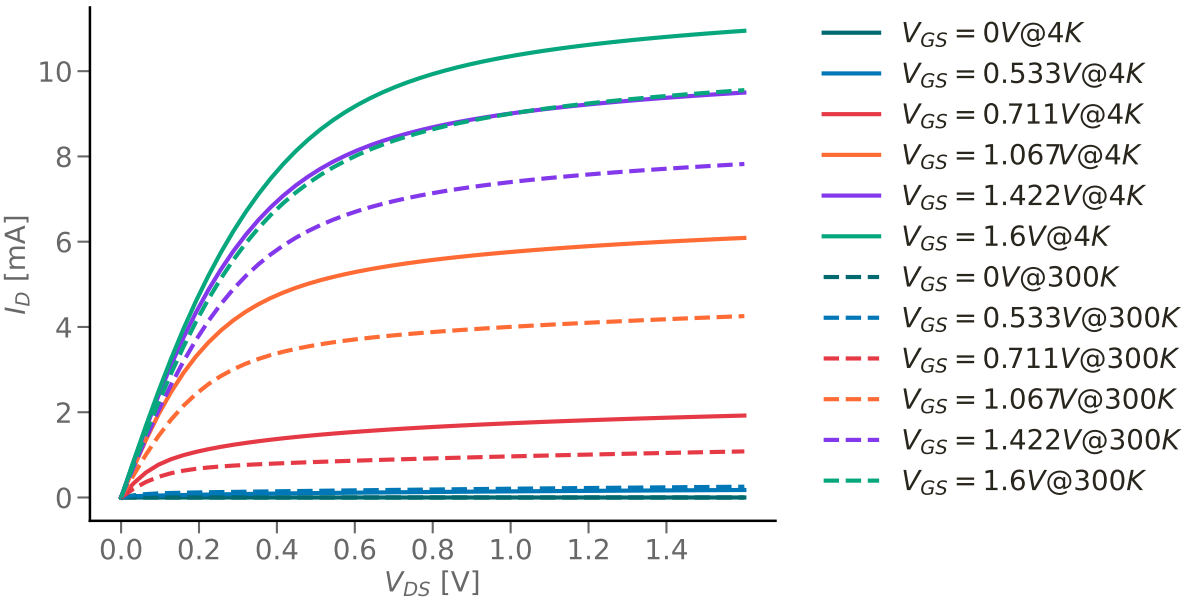


Figure 2.3.6: Simulated output characteristics at 300 K and 4 K for the IHP SG13G2 low-voltage NMOS.

Transconductance and figures of merit

The transconductance g_m of MOSFET devices increases upon cooling due to the combined effects of steeper I_D–V_{GS} slope and higher mobility. However, the figure of merit g_m/I_D, the transistor efficiency-saturates at $q/(nkT_{\text{eff}})$, where T_{eff} represents an effective temperature that accounts for non-equilibrium transport. At 4 K, the measured g_m/I_D in weak inversion can exceed 100 V^{-1}, compared to approximately 25 V^{-1} at room temperature. This improvement is advantageous for ultra-low-power bias circuit design.

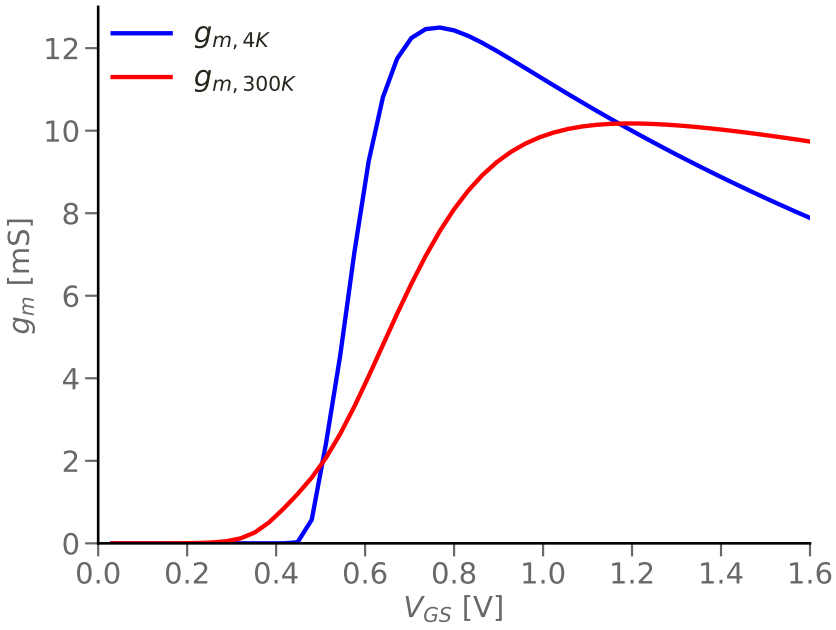


Figure 2.3.7: Simulated transfer characteristics of the IHP SG13G2 low-voltage NMOS at 300 K and 4 K.

Chapter 3 Reflectometry for qubit readout

Reflectometry is a fundamental measurement technique in microwave engineering wherein an electromagnetic signal directed toward a device under test yields information about the device's electrical properties through analysis of the reflected wave. The physical principle underlying reflectometry rests on wave scattering at boundaries where electromagnetic impedance changes. When a traveling wave encounters a medium or termination whose impedance differs from that of the propagation channel, partial reflection occurs, with the ratio of reflected to incident wave amplitude determined by the impedance mismatch magnitude and character. This reflection coefficient, is a complex quantity incorporating both amplitude and phase information, serves as the primary observable in reflectometry measurements and encodes detailed information about the device's electrical properties.

In quantum circuit characterization, reflectometry proves powerful for non-invasive state discrimination. The essence of the reflectometry paradigm lies in viewing the system of interest as a state-dependent impedance accessible through microwave scattering measurements. A microwave signal transmitted toward a quantum device is reflected with amplitude and phase changes that depend on the quantum device's state. By measuring this reflected signal with sufficient sensitivity and temporal resolution, one can infer the quantum state without the invasive measurements that would induce unwanted decoherence.

The effectiveness of reflectometry for quantum measurements is dramatically enhanced when the quantum device under test exhibits resonant behavior. A resonant element, whether realized as a lumped LC circuit or a distributed transmission line cavity, concentrates electromagnetic energy within a narrow frequency band and transforms modest state-dependent impedance shifts into pronounced modifications of the reflected signal. This resonant enhancement forms the cornerstone of sensitive dispersive readout schemes employed in circuit quantum electrodynamics, where a microwave resonator coupled to a superconducting qubit converts quantum state information into measurable changes in the reflection coefficient.[32]

This chapter establishes the conceptual foundation for understanding dispersive qubit readout through progressive examination of the underlying principles. We begin with the minimal reflectometry configuration and the formalism of scattering parameters, then we examine how electromagnetic wave propagation on transmission lines influences measurements. The introduction of resonant loading demonstrates how quality-factor enhancement enables sensitive detection of small impedance variations. Signal representation in terms of in-phase and quadrature components leads naturally to IQ demodulation techniques. Finally, we present the complete readout architecture employed, identifying each component's function and the performance trade-offs that govern the system design.

3.1 Basic Reflectometry Configuration

The baseline measurement architecture comprises four functional blocks arranged in series. A microwave source generates a coherent tone at frequency ω_{probe}, which is coupled by a directional coupler (DC) and propagates toward the device under test (DUT) representing the load impedance to be characterized. The reflected signal, modified in amplitude and phase by the DUT's impedance, enters a Low-Noise Amplifier (LNA) that boosts the signal power above the noise floor of subsequent detection stages. Finally, an IQ demodulator extracts the signal's magnitude and phase, yielding a pair of output signals $(v_{\text{I}}, v_{\text{Q}})$ that encode the complex-valued reflection coefficient.

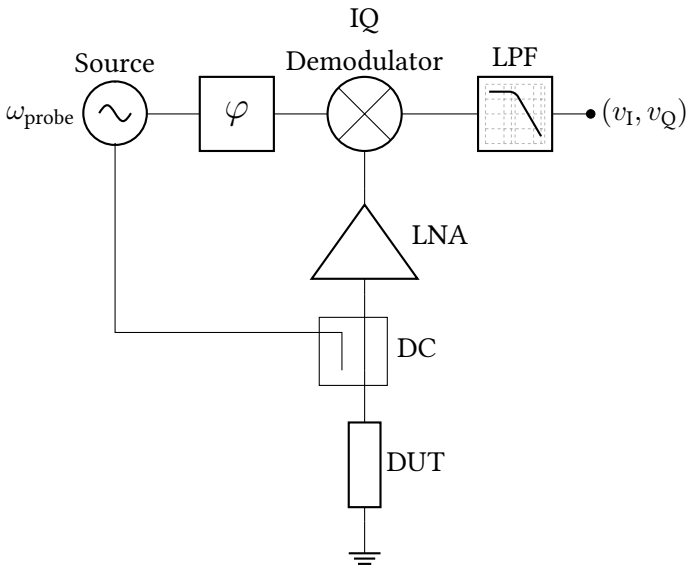


Figure 3.1.1: Basic reflectometry configuration. A microwave source generates a probe tone at frequency ω_{probe} that propagates toward the device under test (DUT). The reflected signal, modified in amplitude and phase by the DUT's impedance, is amplified by a low-noise amplifier (LNA) and demodulated by an IQ mixer to extract in-phase (v_I) and quadrature (v_Q) components.

This simplified configuration, already contains the essential ingredients for quantum state discrimination. If the DUT's impedance depends on the quantum state of a coupled qubit, then monitoring the reflected signal provides information about qubit state.

3.1.1 Wave Propagation and Transmission Lines

A uniform transmission line supporting transverse electromagnetic (TEM) mode propagation admits solutions to Maxwell's equations in the form of voltage and current waves traveling at phase velocity $v_p = c/\sqrt{\varepsilon_r}$, where ε_r denotes the effective relative permittivity of the surrounding dielectric. At a given position z along the line and time t, the total voltage and current decompose into forward-traveling (incident) and backward-traveling (reflected) components.

In phasor representation we can write: [33]

$$V(z,t) = V^+ e^{i(\omega t - \beta z)} + V^- e^{i(\omega t + \beta z)} \tag{3.1}$$

$$I(z,t) = \frac{V^+}{Z_0} e^{i(\omega t - \beta z)} - \frac{V^-}{Z_0} e^{i(\omega t + \beta z)} \tag{3.2}$$

where for a loss-free line $\beta = \omega\sqrt{L'C'} = \omega/v_p$ is the propagation constant and $Z_0 = \sqrt{L'/C'}$ is the characteristic impedance determined by the line's per-unit-length inductance L' and capacitance C'. For coaxial cables commonly used in cryogenic microwave systems, Z_0 typically equals 50Ω, a value chosen historically to balance power handling capability and signal attenuation.

The physical interpretation becomes clear when considering energy flow. The time-averaged power carried by each wave equals $P^{\pm} = |V^{\pm}|^2/(2Z_0)$, with the positive sign indicating power flow in the $+z$ direction (toward the load) and the negative sign indicating reverse flow (toward the source). Conservation of energy requires that power entering the DUT either dissipates as heat, stores in reactive elements, or reflects back toward the source.

3.1.2 Scattering at Impedance Discontinuities

When a forward-propagating wave encounters a load impedance Z_L terminating the transmission line, boundary conditions enforcing voltage and current continuity determine the amplitude of the reflected wave. At the load position $z = 0$, the total voltage must equal the product of total current and load impedance: $V^+ + V^- = Z_L(V^+ - V^-)/Z_0$. Solving for the ratio of reflected to incident voltage amplitudes yields the voltage reflection coefficient:

$$\Gamma = \frac{V^-}{V^+} = \frac{Z_L - Z_0}{Z_L + Z_0} \tag{3.3}$$

The reflection coefficient is a complex number whose magnitude $|\Gamma|$ ranges from zero (perfect match, $Z_L = Z_0$) to unity (total reflection, achieved for open or short circuits), while its phase $\arg(\Gamma)$ encodes the reactive character of the mismatch. A purely resistive load with $Z_L > Z_0$ produces a real positive Γ, indicating in-phase reflection, whereas capacitive or inductive loads introduce phase shifts of $-90°$ or $+90°$ respectively in the limit of pure reactance.

The reflected power fraction $|\Gamma|^2$ directly determines measurement sensitivity. For weak impedance perturbations $\delta Z_L \ll Z_0$ about a matched baseline, the reflection coefficient varies linearly as $\delta\Gamma \approx (2\delta Z_L)/(Z_0)$, establishing the minimum detectable impedance change in terms of the measurement noise floor. This linear response regime proves essential for qubit readout, where state-dependent impedance shifts typically amount to fractions of an Ohm against a nominal 50Ω.

The frequency dependence of Z_L translates directly into spectral features in the reflection coefficient. A simple parallel RLC circuit exhibits a Lorentzian resonance in its impedance magnitude, peaking at the resonant frequency $\omega_0 = 1/\sqrt{LC}$ with maximum value R.

3.2 Resonant Loading and Dispersive Coupling

The linear response regime identified above, where small impedance perturbations δZ_L produce proportionally small reflection changes $\delta\Gamma \approx 2\delta Z_L/(Z_0)$, reveals a fundamental challenge for quantum state readout. Quantum systems typically present extremely weakly state-dependent impedance variations. Consider a charge qubit capacitively coupled to a transmission line: the difference in capacitance between quantum states $|0\rangle$ and $|1\rangle$ might be of order $\delta C \sim 100\ aF$ [34], corresponding at microwave frequencies to a reactance change $\delta X = 1/(\omega\delta C) \sim 100\ m\Omega$. Against the standard 50Ω transmission line impedance, this produces a reflection coefficient change:

$$|\delta\Gamma| \sim \frac{\delta X}{2Z_0} \sim 10^{-4} - 10^{-3} \tag{3.4}$$

Detecting such minute reflection changes requires that the measurement apparatus resolves voltage variations $\delta V/V \sim 10^{-4}$, or equivalently, detect signals at power levels more than 80dB below the incident probe power.[35] While achievable in principle, direct broadband reflectometry at these sensitivity levels faces severe practical limitations:

- **Noise floor limitations**: Thermal noise, amplifier noise, and various technical noise sources establish a measurement noise floor. To resolve signals 80dB below the incident power requires integration times that may exceed the quantum coherence time, rendering the measurement impractical.
- **Bandwidth-sensitivity trade-off**: Broadband measurements inherently integrate noise over wide frequency ranges. Reducing the measurement bandwidth improves signal-to-noise ratio but demands longer integration times, again conflicting with finite coherence times.
- **Dynamic range**: The coexistence of strong incident signals and weak reflected signals within the same measurement channel places extreme demands on amplifier linearity and dynamic range, particularly when operating near saturation to maximize signal levels.

Rather than attempting to measure minute impedance variations directly across a broad frequency range, one can instead employ a **resonant impedance transformer** that converts small, state-dependent perturbations into large, frequency-selective reflection changes within a narrow band. This is the role of the readout resonator in dispersive quantum measurements.

The resonator serves three essential functions [36], [37]:

1. **Impedance amplification**: By concentrating electromagnetic energy within a narrow linewidth κ, the resonator transforms small impedance perturbations into large variations in the complex reflection coefficient. The quality factor $Q = \omega_0/\kappa$ directly quantifies this enhancement: perturbations that would produce $\delta\Gamma \sim 10^{-4}$ in direct measurement can generate $|\delta\Gamma| \sim 0.1$–0.5 when transduced through a high-Q resonator.
2. **Frequency selectivity**: The resonance confines the measurement to a narrow spectral window, dramatically reducing the integrated noise power. Rather than measuring across gigahertz bandwidths, one probes only within the resonator linewidth (typically megahertz range), improving the signal-to-noise ratio by a factor of order Q.
3. **Energy localization**: The resonator stores electromagnetic energy in its reactive elements, establishing enhanced field amplitudes in the vicinity of the quantum device. This localization strengthens the interaction between probe photons and the quantum device, increasing the state-dependent frequency shift that encodes quantum information.

The transition from direct impedance measurement to resonator-enhanced dispersive readout thus represents not a technical improvement but a qualitative shift in measurement strategy.
The resonator must fulfill two essential requirements: it must exhibit a sharp, high-quality-factor resonance to provide impedance amplification, and it must couple to both the external measurement circuitry (to extract signal) and the quantum device (to sense its state).

3.2.1 The Resonator as Load Impedance

Consider the idealized parallel RLC circuit shown in Fig. 3.2.1, connected as the load terminating a transmission line. The circuit comprises three elements: an inductance L storing magnetic energy, a capacitance C storing electric energy, and a resistance R representing internal dissipation mechanisms (dielectric loss, conductor surface resistance, radiation).

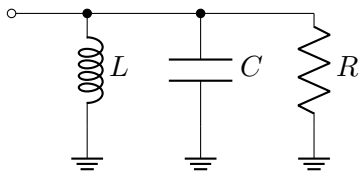


Figure 3.2.1: Parallel RLC resonator circuit. The impedance exhibits a resonance at $\omega_0 = 1/\sqrt{LC}$ where inductive and capacitive reactances cancel, leaving only the resistance R.

The total impedance of this parallel combination is:

$$Z(\omega) = \left(\frac{1}{R} + i\omega C + \frac{1}{i\omega L}\right)^{-1} = \frac{R}{1 + iR\left(\omega C - \frac{1}{\omega L}\right)} \tag{3.5}$$

At the resonance frequency $\omega_0 = 1/\sqrt{LC}$, the imaginary terms cancel and the impedance becomes purely real: $Z(\omega_0) = R$. Near resonance, we can linearize the frequency-dependent term by defining the detuning $\delta\omega = \omega - \omega_0$ and using $\omega C - 1/(\omega L) \approx 2C\delta\omega$ for $|\delta\omega| \ll \omega_0$. This yields:

$$Z(\omega) \approx \frac{R}{1 + i(2RC\delta\omega)} = \frac{R}{1 + i(\omega_0/\kappa_{\text{int}})(2\delta\omega/\omega_0)} = \frac{R}{1 + iQ_{\text{int}}(2\delta\omega/\omega_0)}, \tag{3.6}$$

where we have introduced the internal energy decay rate:

$$\kappa_{\text{int}} = \frac{1}{RC} = \frac{\omega_0}{Q_{\text{int}}} \tag{3.7}$$

and the internal quality factor for an RLC parallel [33]:

$$Q_{\text{int}} = \omega_0 RC = R\sqrt{\frac{C}{L}} \tag{3.8}$$

The quality factor Q_{int} quantifies the sharpness of the resonance and represents the ratio of energy stored in reactive elements to energy dissipated per cycle:

$$Q_{\text{int}} = \omega_0 \times (\text{stored energy})/(\text{power dissipated}) \tag{3.9}$$

High-Q resonators ($Q_{\text{int}} \gtrsim 10^4$) store energy for many oscillation cycles before dissipation, producing narrow resonance linewidths κ_{int} and strong frequency selectivity[38].

This idealized resonator, however, remains isolated from the external measurement apparatus. To extract signal, we must couple it to a transmission line, a process that introduces additional energy decay mechanisms and modifies the resonance behavior.

3.2.2 External Coupling and Quality Factors

Practical implementation requires coupling the resonator to a 50Ω transmission line through which probe signals enter and reflected signals exit. This coupling is typically realized via a capacitive coupling element C_c placed in series between the feedline and the resonator, as shown in Fig. 3.2.2.

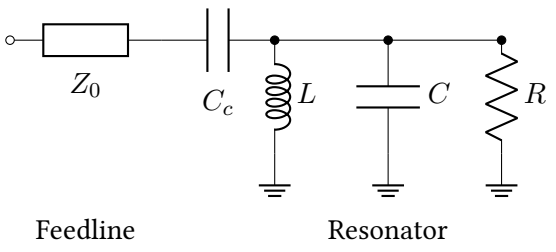


Figure 3.2.2: Capacitively-coupled parallel RLC resonator. The coupling capacitor C_c controls the external quality factor Q_{ext}, which determines power transfer efficiency between feedline and resonator.

The coupling capacitor provides AC coupling while blocking DC currents, and it controls the strength of interaction between the feedline and resonator. A small coupling capacitance (large reactance $1/(\omega_0 C_c)$) yields weak coupling and slow energy transfer, while large C_c produces strong coupling and rapid energy exchange.

To quantify this coupling strength, we analyze the power flow. When the resonator is excited on resonance, energy decays through two parallel mechanisms: internal dissipation in R at rate κ_{int}, and leakage back into the feedline at rate κ_{ext}. The external decay rate can be derived by treating the transmission line impedance Z_0 as an effective load resistance seen by the resonator through the coupling capacitor. For $C_c \ll C$ (weak coupling regime), the external quality factor is[39]:

$$Q_{\text{ext}} = \frac{C}{Z_0 \omega_0 C_c^2} = \frac{C\sqrt{LC}}{Z_0 C_c^2} \tag{3.10}$$

and the corresponding decay rate:

$$\kappa_{\text{ext}} = \frac{\omega_0}{Q_{\text{ext}}} = \frac{\omega_0^2 C_c^2 Z_0}{C\sqrt{LC}} \tag{3.11}$$

The total quality factor and the corresponding total decay rate are given by combining internal and external contributions:

$$\frac{1}{Q_{\text{tot}}} = \frac{1}{Q_{\text{int}}} + \frac{1}{Q_{\text{ext}}} \tag{3.12}$$

$$\kappa_{\text{tot}} = \kappa_{\text{int}} + \kappa_{\text{ext}} = \frac{\omega_0}{Q_{\text{tot}}} \tag{3.13}$$

The ratio of external to total decay rate determines the coupling regime:

- **Undercoupled** ($\kappa_{\text{ext}} \ll \kappa_{\text{int}}$): Energy primarily dissipates internally. Weak signal extraction, but minimal perturbation to resonator.
- **Critically coupled** ($\kappa_{\text{ext}} = \kappa_{\text{int}}$): Balanced decay mechanisms. Maximum power transfer from feedline to resonator at resonance.
- **Overcoupled** ($\kappa_{\text{ext}} \gg \kappa_{\text{int}}$): Energy predominantly leaks to feedline. Strong signal extraction but reduced resonator quality factor.

3.2.3 Reflection Coefficient of the Coupled Resonator

To derive the reflection coefficient of the coupled resonator measured from the feedline, which relates the intracavity field to the incident and reflected fields in the transmission line. The resonator dynamics are governed by the equation of motion for the intracavity field amplitude a:

$$\frac{da}{dt} = -\left(\frac{\kappa_{\text{tot}}}{2} + i\omega_0\right) a + \sqrt{\kappa_{\text{ext}}}\, a_{\text{in}} \tag{3.14}$$

where a_{in} is the amplitude of the field incident from the transmission line, and $\sqrt{\kappa_{\text{ext}}}$ is the coupling strength. The total decay rate $\kappa_{\text{tot}} = \kappa_{\text{int}} + \kappa_{\text{ext}}$ accounts for both internal losses and leakage through the coupling port. The input-output relation connects the outgoing field to the intracavity field:

$$a_{\text{out}} = a_{\text{in}} - \sqrt{\kappa_{\text{ext}}}\, a \tag{3.15}$$

For a continuous-wave drive at frequency ω, we seek steady-state solutions of the form $a(t) = \alpha e^{-i\omega t}$ and $a_{\text{in}}(t) = \alpha_{\text{in}} e^{-i\omega t}$. Substituting into Eq. (3.14):

$$-i\omega\alpha e^{-i\omega t} = -\left(\frac{\kappa_{\text{tot}}}{2} + i\omega_0\right)\alpha e^{-i\omega t} + \sqrt{\kappa_{\text{ext}}}\,\alpha_{\text{in}} e^{-i\omega t} \tag{3.16}$$

Canceling the time dependence and rearranging:

$$\left[\frac{\kappa_{\text{tot}}}{2} + i(\omega_0 - \omega)\right]\alpha = \sqrt{\kappa_{\text{ext}}}\,\alpha_{\text{in}} \tag{3.17}$$

Solving for the steady-state intracavity amplitude:

$$\alpha = \frac{\sqrt{\kappa_{\text{ext}}}\,\alpha_{\text{in}}}{\kappa_{\text{tot}}/2 - i(\omega - \omega_0)} \tag{3.18}$$

Substituting this into the input-output relation Eq. (3.15):

$$\alpha_{\text{out}} = \alpha_{\text{in}} - \sqrt{\kappa_{\text{ext}}} \cdot \frac{\sqrt{\kappa_{\text{ext}}}\,\alpha_{\text{in}}}{\kappa_{\text{tot}}/2 - i(\omega - \omega_0)} = \alpha_{\text{in}}\left[1 - \frac{\kappa_{\text{ext}}}{\kappa_{\text{tot}}/2 - i(\omega - \omega_0)}\right] \tag{3.19}$$

The reflection coefficient is the ratio of output to input amplitudes:

$$\Gamma(\omega) = \frac{\alpha_{\text{out}}}{\alpha_{\text{in}}} = 1 - \frac{\kappa_{\text{ext}}}{\kappa_{\text{tot}}/2 - i(\omega - \omega_0)} \tag{3.20}$$

This expression reveals the Lorentzian lineshape of the resonator response. At resonance ($\omega = \omega_0$), the denominator becomes purely real:

$$\Gamma(\omega_0) = 1 - \frac{\kappa_{\text{ext}}}{\kappa_{\text{tot}}/2} = 1 - \frac{2\kappa_{\text{ext}}}{\kappa_{\text{tot}}} = \frac{\kappa_{\text{tot}} - 2\kappa_{\text{ext}}}{\kappa_{\text{tot}}} = \frac{\kappa_{\text{int}} - \kappa_{\text{ext}}}{\kappa_{\text{int}} + \kappa_{\text{ext}}} \tag{3.21}$$

For critical coupling ($\kappa_{\text{ext}} = \kappa_{\text{int}}$), we obtain $\Gamma(\omega_0) = 0$, indicating perfect impedance matching and complete absorption of incident power. This represents the optimal configuration for broadband matching, but quantum readout often operates in the undercoupled regime ($\kappa_{\text{ext}} < \kappa_{\text{int}}$) to minimize measurement-induced decoherence through Purcell decay. The complex nature of $\Gamma(\omega)$ encodes both amplitude and phase information. Far from resonance ($|\omega - \omega_0| \gg \kappa_{\text{tot}}$), the reflection coefficient approaches unity: $\Gamma(\omega) \to 1$, corresponding to total reflection as the resonator becomes transparent. Near resonance, the imaginary part of the denominator produces a phase rotation in the complex plane, which forms the basis for dispersive qubit readout.

3.2.4 The Qubit as Reactive Load

Up to this point, the resonator has been treated as an isolated RLC circuit coupled only to the external feedline. To perform quantum state readout, we must now introduce the quantum device, which refers to generically as a "qubit" or "device under test" (DUT). The key insight is that a qubit can be modeled, to first approximation, as state-dependent reactive elements: capacitances or inductances whose values depend on the quantum state.
Consider a qubit (e.g., a transmon or charge qubit) capacitively coupled to the readout resonator, as shown in Fig. 3.2.3.

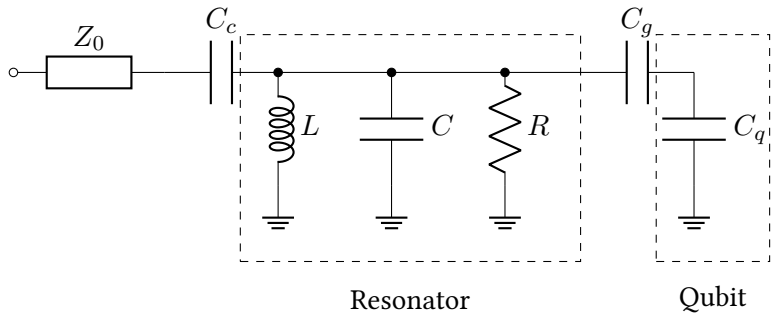


Figure 3.2.3: Resonator coupled to a qubit (DUT) via capacitance C_g. The qubit's quantum state modulates its effective capacitance C_q, which in turn shifts the resonator frequency.

The qubit couples to the resonator through a gate capacitance C_g and presents an effective capacitance C_q to ground. Crucially, this effective capacitance depends on the qubit's quantum state. For a qubit with ground state $|g\rangle$ and excited state $|e\rangle$, the capacitance takes different values:

$$C_q = \begin{cases} C_q^{(g)} & \text{when qubit in state } |g\rangle \\ C_q^{(e)} & \text{when qubit in state } |e\rangle \end{cases} \tag{3.22}$$

This state-dependent capacitance arises from the different charge distributions associated with each quantum state. In a transmon qubit, for example, the ground and excited states correspond to different Cooper pair number distributions on the qubit island, producing measurably different capacitances to the surrounding electrode [40].
The total capacitance of the resonator now includes the qubit contribution. For weak coupling ($C_g \ll C$), the capacitance added by the qubit is::

$$C_{\text{qubit}} = \frac{C_g C_q}{C_g + C_q} \approx C_g \frac{C_q}{C_q} = C_g \quad (\text{if } C_g \ll C_q) \tag{3.23}$$

and so the total capacitance seen by the resonator is:

$$C_{\text{tot}} = C + C_{\text{qubit}} \approx C + C_g \tag{3.24}$$

The resonator frequency, initially $\omega_r^{\text{bare}} = 1/\sqrt{LC}$, becomes for $C_{\text{qubit}} \ll C$:

$$\omega_r = \frac{1}{\sqrt{L(C + C_{\text{qubit}})}} \approx \omega_r^{\text{bare}} \left(1 - \frac{C_{\text{qubit}}}{2C}\right) \tag{3.25}$$

Since C_{qubit} depends on the qubit state, the resonator frequency shifts between two values:

$$\omega_r^{(g)} = \omega_r^{\text{bare}} \left(1 - \frac{C_{\text{qubit}}^{(g)}}{2C}\right) \qquad \omega_r^{(e)} = \omega_r^{\text{bare}} \left(1 - \frac{C_{\text{qubit}}^{(e)}}{2C}\right) \tag{3.26}$$

The dispersive regime is characterized by a large detuning between the qubit and resonator frequencies. The system is defined by three fundamental frequencies. The bare transition frequency of the transmon qubit ω_q typically lies in the range 4-6 GHz, while the bare frequency of the readout resonator ω_r is usually designed to be 6-8 GHz for dispersive readout. The third crucial parameter is the vacuum Rabi coupling strength g, which quantifies the interaction between a single photon in the resonator and the qubit transition. According [41], the coupling strength can be expressed in terms of the circuit parameters as:

$$g = \frac{C_g}{2C_q} \omega_q \sqrt{\frac{C_q}{C_r}} \tag{3.27}$$

with C_q being the transmon capacitance. In the limit where the resonator capacitance dominates ($C_r \gg C_g$), this reduces to the commonly used simplified form $g \approx (C_g/2C_q)\omega_q$. Typical values of g range from 50 to 200 MHz for standard dispersive readout architectures.

The dispersive approximation is valid when the detuning $\Delta = \omega_r - \omega_q$ satisfies $|\Delta| \gg g$. In this regime, the qubit and resonator remain approximately in their respective eigenstates, but virtual photon exchange between them leads to state-dependent frequency shifts. This effect is the foundation of quantum non-demolition readout.

The key observable is the dispersive shift χ, which quantifies how much the resonator frequency changes depending on the qubit state. When the qubit is in the ground state $|g\rangle$, the dressed resonator frequency is $\omega_r^{(g)}$, while in the excited state $|e\rangle$, it becomes $\omega_r^{(e)}$. The dispersive shift is defined as their difference:

$$\chi = \omega_r^{(e)} - \omega_r^{(g)} \approx \frac{g^2}{\Delta} \tag{3.28}$$

The dispersive interaction shifts both the qubit and resonator frequencies symmetrically around their bare values. Figure 3.2.4 illustrates this effect on a frequency axis. The bare qubit frequency ω_q and resonator frequency ω_r are separated by the detuning Δ. The weak coupling induces a symmetric splitting of the resonator frequency: $\omega_r^{(g)} = \omega_r + \chi/2$ when the qubit is in the ground state, and $\omega_r^{(e)} = \omega_r - \chi/2$ when the qubit is excited. The total separation between the two dressed resonator frequencies is χ, which is the operationally relevant quantity for dispersive readout.

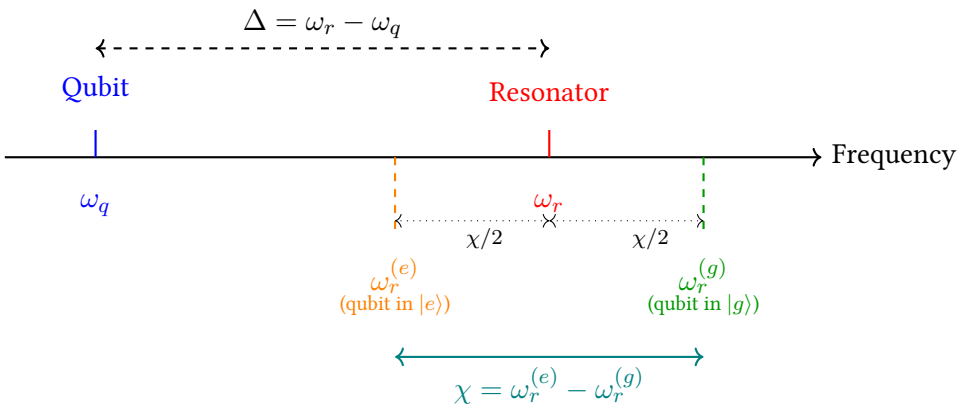


Figure 3.2.4: Frequency diagram illustrating the dispersive regime of circuit QED. The bare qubit frequency ω_q and resonator frequency ω_r are separated by a large detuning $\Delta \gg g$. The coupling g induces virtual photon exchange, causing the resonator frequency to split symmetrically i nto two dressed values: $\omega_r^{(g)}$ when the qubit is in $|g\rangle$ and $\omega_r^{(e)}$ when in $|e\rangle$. Each dressed frequency is shifted by $\pm\chi/2$ from the bare resonator frequency, resulting in a total dispersive shift χ between the two readout frequencies.

Purcell Decay Rate

While the dispersive interaction enables quantum non-demolition readout, the coupling to the resonator also provides an unwanted decay channel for the qubit through the lossy transmission line. This phenomenon, known as the Purcell effect in circuit QED, fundamentally limits the qubit coherence time T_1 and represents one of the most important design constraints in dispersive readout architectures [42], [43]. The Purcell decay rate κ_{Purcell} quantifies the rate at which the qubit loses energy by emitting photons into the resonator, which subsequently decay through the external coupling to the transmission line. In the dispersive regime, this rate is given by [40]:

$$\kappa_{\text{Purcell}} = \frac{\kappa_{\text{ext}} g^2}{\Delta^2} \tag{3.29}$$

where κ_{ext} is the external decay rate of the resonator (the rate of photon loss to the transmission line), and Δ is the qubit-resonator detuning. This expression reveals the key scaling: the Purcell decay is suppressed quadratically with detuning, which is why large detunings are generally favorable for preserving qubit coherence.

The Purcell decay rate can be rewritten as $\kappa_{\text{Purcell}} = \kappa_{\text{ext}}(\chi/g)(g/\Delta) = \kappa_{\text{ext}}\chi/\Delta$, which provides physical insight into the decay mechanism. The dispersive shift $\chi \propto g^2/\Delta$ represents the effective strength of the qubit-resonator interaction in the off-resonant regime, while the additional suppression factor g/Δ accounts for the reduced coupling due to the frequency mismatch. The external decay rate κ_{ext} sets the overall timescale for photon leakage from the resonator into the measurement chain.

This formulation immediately reveals a fundamental trade-off in dispersive readout design. Increasing the detuning Δ suppresses Purcell decay, which is beneficial for qubit coherence, but simultaneously reduces the dispersive shift χ, which degrades readout contrast and increases measurement time. For a cavity with lifetime $1/\kappa_{\text{ext}} = 160\,\text{ns}$ and $g/\Delta = 0.1$, the Purcell effect leads to a contribution of $16\,\mu$s.

Modern circuit experiments address this trade-off using Purcell filters, additional circuit elements strategically placed between the qubit-resonator system and the transmission line [44]. These filters provide frequency-selective suppression of qubit decay without significantly attenuating the readout signal at the resonator frequency, thereby decoupling the constraints on coherence and readout fidelity.

3.2.5 Dispersive Frequency Shift and State Discrimination

The measurement strategy is to apply a continuous probe tone at frequency ω_p and monitor the reflected signal's amplitude and phase, which encode information about the instantaneous resonator frequency—and thus the qubit state. The reflection coefficient from Eq. (3.20) becomes state-dependent:

$$\Gamma_{g/e}(\omega_p) = 1 - \frac{\kappa_{\text{ext}}}{\kappa_{\text{tot}}/2 - i(\omega_p - \omega_r^{(g/e)})} \tag{3.30}$$

To maximize state discrimination, we must choose the probe frequency ω_p to produce the largest separation between Γ_g and Γ_e in the complex plane. Two common strategies exist [45]:

On-resonance probing. Set $\omega_p = \omega_r^0$, midway between the two state-dependent resonances. This yields symmetric detuning:

$$\omega_p - \omega_r^{(g)} = \omega_r^0 - \omega_r^0 - \chi/2 = -\chi/2 \tag{3.31}$$

$$\omega_p - \omega_r^{(e)} = -\omega_r^0 + \omega_r^0 + \chi/2 = +\chi/2 \tag{3.32}$$

Thus, the reflection coefficients for the two qubit states are:

$$\Gamma_g = 1 - \frac{2\kappa_{\text{ext}}}{\kappa_{\text{tot}} - i\chi} = 1 - \frac{2\kappa_{\text{ext}}\left(\kappa_{\text{tot}} + i\chi\right)}{\kappa_{\text{tot}}^2 + \chi^2} \tag{3.33}$$

$$\Gamma_e = 1 - \frac{2\kappa_{\text{ext}}}{\kappa_{\text{tot}} + i\chi} = 1 - \frac{2\kappa_{\text{ext}}\left(\kappa_{\text{tot}} - i\chi\right)}{\kappa_{\text{tot}}^2 + \chi^2} \tag{3.34}$$

The two reflection coefficients lie symmetrically displaced around the real axis in the complex plane. Their separation is thus the difference of the two imaginary components:

$$|\Gamma_g - \Gamma_e| = \frac{2\kappa_{\text{ext}}\chi}{|\kappa_{\text{tot}}^2 + \chi^2|} \tag{3.35}$$

This separation maximizes when $\chi \approx \kappa_{\text{tot}}/2$, i.e., when the dispersive shift is comparable to the total linewidth. For $\chi \ll \kappa_{\text{tot}}$, the separation scales linearly with χ; for $\chi \gg \kappa_{\text{tot}}$, the resonances are well-resolved but the separation saturates.

Slope-sensitive probing. Alternatively, one can probe on the flank of one resonance, where $d|\Gamma|/d\omega$ is maximal. This sacrifices some signal amplitude but can improve sensitivity to small frequency shifts in the regime $\chi \ll \kappa_{\text{tot}}$.

In practice, most experiments employ on-resonance probing with $\omega_p = \omega_r^0$, as this provides robust operation and simplifies calibration. The achievable signal contrast and thus readout fidelity depends critically on the ratio χ/κ_{tot} and the measurement signal-to-noise ratio.

3.3 Quadrature Measurement and Signal Representation

The previous section established that qubit state information is encoded in the amplitude and phase of a microwave reflection coefficient $\Gamma_{g/e}(\omega_p)$. The quantum information resides not in the absolute carrier frequency but in the slowly-varying amplitude and phase modulations induced by the qubit state.

To extract this information, quadrature demodulation (or homodyne detection) down-converts the microwave signal to baseband by mixing with a phase-coherent local oscillator (LO). The result is a pair of real-valued signals, termed in-phase (I) and quadrature (Q) components (see Figure 3.1.1), which together encode the complex reflection coefficient. This IQ representation forms the foundation for all subsequent signal processing.

3.3.1 From RF Reflection to Baseband Detection

Consider the reflected signal from the readout resonator:

$$V_{\text{refl}}(t) = A(t)\cos\left[\omega_p t + \phi(t)\right] \tag{3.36}$$

where ω_p is the probe frequency, $A(t)$ is the slowly-varying amplitude, and $\phi(t)$ is the slowly-varying phase. Both $A(t)$ and $\phi(t)$ encode the qubit state: when the qubit is in $|g\rangle$, the reflection coefficient is $\Gamma_g = |\Gamma_g|e^{i\phi_g}$, producing $A = |\Gamma_g|$ and $\phi = \phi_g$; when in $|e\rangle$, we have $A = |\Gamma_e|$ and $\phi = \phi_e$.
The reflection coefficient is a complex number:

$$\Gamma_{g/e} = |\Gamma_{g/e}|e^{i\phi_{g/e}} = \underbrace{|\Gamma_{g/e}|\cos\phi_{g/e}}_{I_{g/e}} + i\,\underbrace{|\Gamma_{g/e}|\sin\phi_{g/e}}_{Q_{g/e}} \tag{3.37}$$

To extract these slowly-varying I and Q components from the high-frequency carrier, the signal is split and mixed with two copies of the local oscillator (LO) in phase quadrature (90° apart), followed by low-pass filtering to remove the sum-frequency component.

3.3.2 The IQ Demodulator: Hardware Implementation

Figure 3.3.1 shows the schematic of a quadrature demodulator.

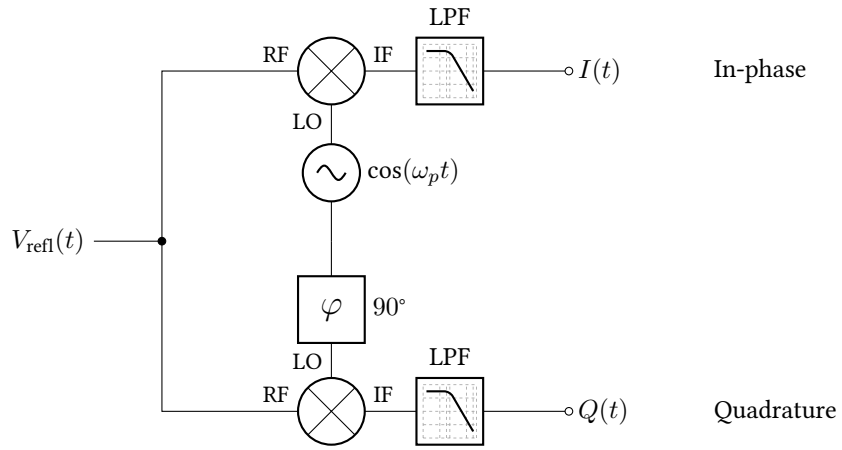


Figure 3.3.1: Quadrature (IQ) demodulator schematic. The reflected signal is mixed with both the in-phase LO ($\cos\omega_p t$) and the quadrature LO ($\sin\omega_p t$), producing sum and difference frequency components. Low-pass filters (LPF) remove the sum-frequency ($2\omega_p$) terms, leaving baseband signals $I(t)$ and $Q(t)$ that represent the real and imaginary parts of the complex reflection coefficient.

The mathematical operation performed by each mixer can be approximated as a multiplication, recalling the trigonometric identities: $\cos\alpha\cos\beta = \frac{\cos(\alpha-\beta)+\cos(\alpha+\beta)}{2}$ we get:

$$V_I^{(\text{mixer})}(t) = V_{\text{refl}}(t)\cdot\cos(\omega_p t) \tag{3.38}$$

$$= A(t)\cos[\omega_p t + \phi(t)]\cdot\cos(\omega_p t) \tag{3.39}$$

$$= \frac{A(t)}{2}\left\{\cos[\phi(t)] + \cos[2\omega_p t + \phi(t)]\right\} \tag{3.40}$$

while using the trigonometric identity $\sin\alpha\sin\beta = \frac{\cos(\alpha-\beta)-\cos(\alpha+\beta)}{2}$ we get:

$$V_Q^{(\text{mixer})}(t) = V_{\text{refl}}(t)\cdot\sin(\omega_p t) \tag{3.41}$$

$$= A(t)\cos[\omega_p t + \phi(t)]\cdot\sin(\omega_p t) \tag{3.42}$$

$$= \frac{A(t)}{2}\left\{\sin[\phi(t)] + \sin[2\omega_p t + \phi(t)]\right\} \tag{3.43}$$

Each mixer output contains a baseband component (DC to ∼MHz, determined by the bandwidth of $A(t)$ and $\phi(t)$) and a sum-frequency component at $2\omega_p$ (∼10–20 GHz). The low-pass filters (LPF), typically with cutoff frequencies of 10–100 MHz, remove the high-frequency terms, leaving:

$$I(t) = \frac{A(t)}{2}\cos[\phi(t)] = \frac{1}{2}\mathrm{Re}[\Gamma(t)] \tag{3.44}$$

$$Q(t) = \frac{A(t)}{2}\sin[\phi(t)] = \frac{1}{2}\mathrm{Im}[\Gamma(t)] \tag{3.45}$$

The factor of $1/2$ is often absorbed into calibration gains.

3.3.3 Complex Signal Representation

It is convenient to combine the two real signals into a single complex quantity:

$$S(t) = I(t) + iQ(t) \propto \Gamma(t) = |\Gamma(t)|e^{i\phi(t)} \tag{3.46}$$

In this representation, the qubit state is encoded as a point on the complex plane (IQ plane):

$$S_g = I_g + iQ_g \propto \Gamma_g \tag{3.47}$$

$$S_e = I_e + iQ_e \propto \Gamma_e \tag{3.48}$$

The state discrimination problem reduces to distinguishing between two points or, accounting for noise, two clouds on the IQ plane, as illustrated in Figure 3.3.2.

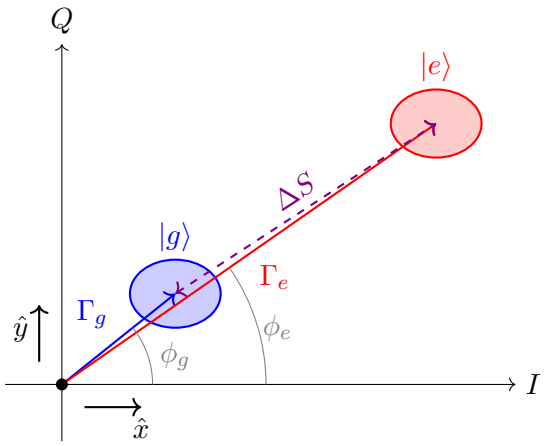


Figure 3.3.2: State discrimination on the IQ plane. Ground state $|g\rangle$ and excited state $|e\rangle$ produce distinct reflection coefficients Γ_g and Γ_e, represented as points (or noise-broadened distributions) in the complex plane. Measurement noise (not shown) creates Gaussian clouds around each point.

Unlike power detection ($|V|^2$), IQ detection preserves phase information, crucial when Γ_g and Γ_e differ primarily in phase rather than amplitude. Baseband I and Q signals can be digitized at moderate rates (10-100 MS/s) and processed with standard techniques (filtering, averaging, thresholding). Thermal and amplifier noise appears as Gaussian fluctuations on the IQ plane, simplifying statistical analysis.

3.3.4 Threshold Discrimination

While the heterodyne measurement provides a two-dimensional IQ representation of the reflected signal, single-shot qubit state discrimination requires extracting a single real-valued observable that maximizes the separation between $|g\rangle$ and $|e\rangle$. The optimal strategy is to project the measured signal onto the axis connecting the two state centroids in the IQ plane.

Given the mean signals $S_g = I_g + iQ_g$ and $S_e = I_e + iQ_e$ for the ground and excited states, the separation vector is:

$$\Delta S = S_e - S_g = (I_e - I_g) + i(Q_e - Q_g) \tag{3.49}$$

The optimal measurement observable is obtained by projecting any measured signal $S(t) = I(t)+iQ(t)$ onto the normalized separation direction $\hat{u} = \Delta S/|\Delta S|$:

$$M(t) = \mathrm{Re}\left[\hat{u} \cdot S(t)\right] = \frac{1}{|\Delta S|}\left[(I_e - I_g)I(t) + (Q_e - Q_g)Q(t)\right] \tag{3.50}$$

This weighted combination of the two quadratures yields a one-dimensional signal with mean values M_g and M_e for the two states, separated by the maximum possible distance $|M_e - M_g| = |\Delta S|$. The qubit state is then determined by comparing $M(t)$ to a threshold value:

This weighted combination of the two quadratures yields a one-dimensional signal with mean values M_g and M_e for the two states, separated by the maximum possible distance $|M_e - M_g| = |\Delta S|$. The qubit state is then determined by comparing $M(t)$ to a threshold value:

$$\text{Qubit state} = \begin{cases} |g\rangle & \text{if } M(t) < M_{\text{th}} \\ |e\rangle & \text{if } M(t) \geq M_{\text{th}} \end{cases} \tag{3.51}$$

For symmetric noise distributions with equal variance in both states, the optimal threshold is the midpoint, as illustrated in Figure 3.3.3.:

$$M_{\text{th}} = \frac{M_g + M_e}{2} \tag{3.52}$$

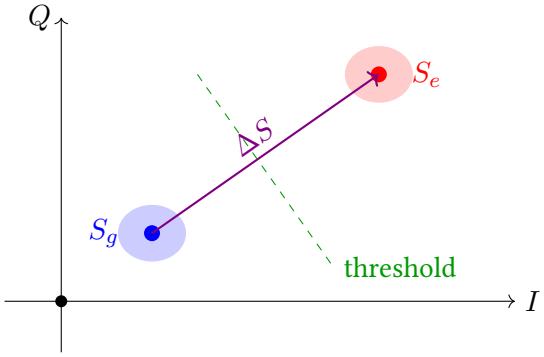


Figure 3.3.3: The two quantum states form distributions centered at S_g and S_e in the IQ plane. A threshold (green) perpendicular divides the plane into two decision regions.

3.4 Noise and Amplification in Dispersive Readout

In an ideal, noise-free measurement, the two states would appear as distinct points in the IQ plane, separated by $\Delta S = S_e - S_g$. In reality, noise from multiple sources, thermal fluctuations, amplifier noise, and quantum shot noise, broadens these points into overlapping Gaussian distributions, limiting the ability to distinguish $|g\rangle$ from $|e\rangle$ with certainty.

A critical complication arises from qubit relaxation: during the finite measurement interval τ_{meas}, an initially excited qubit may decay to the ground state with rate $\Gamma_1 = 1/T_1$, reducing the effective signal. This introduces an optimal measurement time τ_{opt} that balances noise reduction (favoring longer integration) against signal loss from relaxation (favoring shorter integration)[46].

3.4.1 Noise Sources in Dispersive Readout

The baseband signal suffuses from noise generated by several physical mechanisms. Each contributes a characteristic power spectral density (PSD) $S_n(f)$.

Quantum shot noise: The discrete nature of photons introduces fundamental fluctuations. For a coherent state [47], the single-sided power spectral density is frequency-independent (white noise):

$$S_n^{(\text{shot})}(f) = \frac{\hbar\omega_r}{2} \quad [\text{J/Hz}] \tag{3.53}$$

where $\hbar$ is the reduced Planck constant and ω_r is the resonator frequency. This is the quantum limit for phase-preserving amplification. The equivalent noise temperature of the quantum shot noise is:

$$T_n^{(\text{shot})} = \frac{\hbar\omega_r}{2k_B} \approx 240\,\text{mK} \times \left(\frac{\omega_r}{2\pi \cdot 7\,\text{GHz}}\right) \tag{3.54}$$

where k_B is the Boltzmann constant. For a typical superconducting qubit readout at $\omega_r/2\pi \sim 7$ GHz, this corresponds to a noise temperature of approximately 240 mK, which sets the fundamental limit for low-noise amplification.

Thermal noise: Dissipative elements at temperature T generate voltage fluctuations:

$$S_V^{(\text{thermal})}(f) = 4k_BTR \quad [\text{V}^2/\text{Hz}] \tag{3.55}$$

where R is the resistance of the element. In cryogenic systems, thermal noise is typically negligible compared to quantum shot noise, but becomes significant in higher-temperature stages or lossy components.

Flicker noise (1/f): Flicker noise, also known as 1/f noise, is a ubiquitous low-frequency phenomenon observed in a wide range of electronic devices, with a power spectral density that diverges at low frequencies [48]:

$$S_n^{(1/f)}(f) = \frac{A}{f^\alpha}, \quad 0.8 \lesssim \alpha \lesssim 1.2 \tag{3.56}$$

where A is a material- and device-dependent constant. In semiconductor devices such as MOSFETs, JFETs, and BJTs, flicker noise arises primarily from charge trapping and detrapping at oxide interfaces and defects in the channel region. In superconducting circuits, additional contributions come from critical current fluctuations in Josephson junctions due to two-level systems in tunnel barriers [48].
A key parameter characterizing flicker noise in amplifiers and transistors is the **corner frequency** f_c, defined as the frequency where the 1/f power spectral density equals the white noise floor:

$$S_n^{(1/f)}(f_c) = S_n^{\text{white}} \tag{3.57}$$

The corner frequency depends strongly on device technology: MOSFETs typically exhibit $f_c \sim 0.1$–10 MHz, while JFETs and BJTs have significantly lower values, $f_c \sim 100$ Hz–10 kHz.
For dispersive readout of superconducting qubits, the measurement operates at microwave frequencies ($\sim$ GHz) with integration bandwidths $B \sim 1$–100 MHz, well above typical corner frequencies. The integrated contribution of flicker noise to the readout signal is therefore negligible:

$$\sigma_{1/f}^2 \sim \int_{f_0}^{f_0+B} \frac{A}{f} df \approx A \ln\left(1 + \frac{B}{f_0}\right) \ll \sigma_{\text{white}}^2 \approx S_n^{\text{white}} \cdot B \tag{3.58}$$

where $f_0 \gg f_c$ is the carrier frequency.

However, flicker noise dominates at long timescales (seconds to minutes) and remains the primary source of low-frequency qubit dephasing, frequency drift, and amplifier gain fluctuations in extended measurement sequences.

Quasiparticle shot noise: In superconducting circuits at $T \ll T_c$, thermally excited quasiparticles introduce shot noise:

$$S_I^{(\text{qp})}(f) = 2eI_{\text{qp}} \quad [\text{A}^2/\text{Hz}] \tag{3.59}$$

where I_{qp} is the quasiparticle tunneling current.

Noise power spectral density and variance: Consider a stationary random noise process $n_{\text{in}}(t)$ at the input of a linear time-invariant (LTI) system with frequency response $H(f)$. The output noise process $n_{\text{out}}(t)$ is related to the input by convolution with the impulse response $h(t)$:

$$n_{\text{out}}(t) = \int_{-\infty}^{\infty} h(\tau) n_{\text{in}}(t-\tau) d\tau \tag{3.60}$$

The power spectral density (PSD) transforms through the system according to:

$$S_{n,\text{out}}(f) = |H(f)|^2 \cdot S_{n,\text{in}}(f) \tag{3.61}$$

where $|H(f)|^2$ is the power transfer function. The output noise variance σ^2_{out} is obtained from the autocorrelation function $R_{n,\text{out}}(\tau)$ evaluated at zero lag:

$$\sigma^2_{\text{out}} = \langle n^2_{\text{out}}(t) \rangle = R_{n,\text{out}}(0) \tag{3.62}$$

By the Wiener-Khinchin theorem, the autocorrelation is the inverse Fourier transform of the PSD:

$$R_{n,\text{out}}(\tau) = \int_{-\infty}^{\infty} S_{n,\text{out}}(f) e^{i2\pi f\tau} df \tag{3.63}$$

Evaluating at $\tau = 0$ and substituting Eq. (3.61):

$$\sigma^2_{\text{out}} = \int_{-\infty}^{\infty} S_{n,\text{out}}(f) df = \int_{-\infty}^{\infty} |H(f)|^2 S_{n,\text{in}}(f) df \tag{3.64}$$

This is the fundamental result for noise propagation: the output variance is the integral of the input PSD weighted by the power transfer function of the system.

For white noise with PSD S_n and integrating time window τ_{int}:

$$\sigma^2 = \frac{S_n}{\tau_{\text{int}}} \tag{3.65}$$

Each IQ quadrature has variance σ^2; total noise power is $2\sigma^2$.

In dispersive qubit readout, the reflected microwave signal is demodulated to baseband and acquired after a time window τ_{int}. The integrator acts as a low-pass filter with frequency response:

$$H_{\text{int}}(f) = \frac{\sin(\pi f \tau_{\text{int}})}{\pi f \tau_{\text{int}}} e^{-i\pi f \tau_{\text{int}}} \tag{3.66}$$

with power transfer function:

$$|H_{\text{int}}(f)|^2 = \text{sinc}^2(\pi f \tau_{\text{int}}) = \left[\frac{\sin(\pi f \tau_{\text{int}})}{\pi f \tau_{\text{int}}} \right]^2 \tag{3.67}$$

For white noise with constant two-sided PSD S_n (independent of frequency), the output variance becomes:

$$\sigma^2_{\text{out}} = S_n \int_{-\infty}^{\infty} \text{sinc}^2(\pi f \tau_{\text{int}}) df \tag{3.68}$$

Using the standard integral identity:

$$\int_{-\infty}^{\infty} \text{sinc}^2(x)dx = 1 \quad \Rightarrow \quad \int_{-\infty}^{\infty} \text{sinc}^2(\pi f \tau_{\text{int}})df = \frac{1}{\tau_{\text{int}}} \tag{3.69}$$

we obtain:

$$\sigma^2_{\text{out}} = \frac{S_n}{\tau_{\text{int}}} \tag{3.70}$$

3.4.2 Gaussian Noise on the IQ Plane

Under the assumption that noise sources are Gaussian, stationary, and additive, the measured noisy IQ signal for a qubit in state $|j\rangle$ ($j = g, e$) can be modeled as:

$$S_j^{(\text{meas})} = S_j + n_I + in_Q \tag{3.71}$$

where $S_j = I_j + iQ_j$ is the noiseless signal point and n_I, n_Q are independent Gaussian random variables with zero mean and variance σ^2:

$$\langle n_I \rangle = \langle n_Q \rangle = 0, \quad \langle n_I^2 \rangle = \langle n_Q^2 \rangle = \sigma^2 \tag{3.72}$$

The noise power spectral density S_n single-sided $[V^2/Hz]$ after detection is related to σ^2 by:

$$\sigma^2 = S_n \cdot B, \tag{3.73}$$

where B is the measurement bandwidth, typically set by low-pass filters after the mixers ($B \sim 10$–100 MHz in typical setups).

In this framework I and Q are random variables whose probability distributions are:

$$P(I, Q \,|\, |g\rangle) = \frac{1}{2\pi\sigma^2} \exp\left[-\frac{(I - I_g)^2 + (Q - Q_g)^2}{2\sigma^2}\right] \tag{3.74}$$

$$P(I, Q \,|\, |e\rangle) = \frac{1}{2\pi\sigma^2} \exp\left[-\frac{(I - I_e)^2 + (Q - Q_e)^2}{2\sigma^2}\right] \tag{3.75}$$

On the IQ plane, the variance σ^2 describes circularly Gaussian blobs centered at (I_g, Q_g) and (I_e, Q_e), as illustrated in Figure 3.4.1.

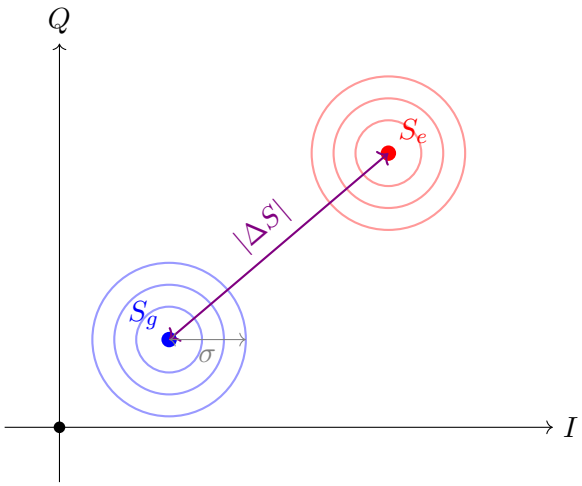


Figure 3.4.1: Gaussian noise distributions in the IQ plane. The qubit states $|g\rangle$ (blue) and $|e\rangle$ (red) produce Gaussian clouds with standard deviation σ.

3.4.3 Signal-to-Noise Ratio (SNR) Definition

The signal-to-noise ratio quantifies the ratio between signal power and noise power in the measurement chain. In terms of power, the SNR is defined as:

$$\text{SNR}_{\text{power}} = \frac{P_{\text{signal}}}{P_{\text{noise}}} \tag{3.76}$$

or in terms of voltage, the SNR is defined as:

$$\text{SNR}_{\text{voltage}} = \sqrt{\text{SNR}_{\text{power}}} = \frac{V_{\text{signal}}}{\sigma_V} \tag{3.77}$$

where P_{signal} is the signal power, V_{signal} is the signal voltage amplitude, and σ_V is the RMS noise voltage.

For a measurement sampling the instantaneous voltage after a low-pass filter with bandwidth B_{filter}, the noise variance is determined by integrating the noise power spectral density (PSD) S_n over the measurement bandwidth:

$$\sigma_V^2 = S_n \cdot B_{\text{filter}} \tag{3.78}$$

3.4.4 Measurement Fidelity and Effective SNR

The measurement fidelity F quantifies the probability of correctly assigning the qubit state in a single-shot readout. Assuming equal prior probabilities $P(|g\rangle) = P(|e\rangle) = 1/2$ and Gaussian noise distributions with equal variance in both states, the assignment error is determined by the overlap of the two distributions along the optimal discrimination axis.

As discussed in Section 3.3.4, the optimal strategy is to use the measurement observable $M(t)$ defined in Eq. (3.50), which projects the measured IQ signal onto the axis connecting the two state centroids. For a measured signal $S(t) = I(t) + iQ(t)$, this projection yields:

$$M(t) = \frac{1}{|\Delta S|}\left[(I_e - I_g)I(t) + (Q_e - Q_g)Q(t)\right] \tag{3.79}$$

where $\Delta S = S_e - S_g = (I_e - I_g) + i(Q_e - Q_g)$ is the complex separation vector, and $|\Delta S| = \sqrt{(I_e - I_g)^2 + (Q_e - Q_g)^2}$ is the Euclidean distance between the two state centroids.
The mean values of the observable for the two states are:

$$M_g = \frac{1}{|\Delta S|}\left[(I_e - I_g)I_g + (Q_e - Q_g)Q_g\right] \tag{3.80}$$

$$M_e = \frac{1}{|\Delta S|}\left[(I_e - I_g)I_e + (Q_e - Q_g)Q_e\right] \tag{3.81}$$

with separation:

$$\Delta M = M_e - M_g = \frac{(I_e - I_g)^2 + (Q_e - Q_g)^2}{|\Delta S|} = |\Delta S| \tag{3.82}$$

The single-quadrature noise variance given by Eq. (3.78) determines how well the two states can be discriminated. With the threshold placed at the midpoint $M_{\text{th}} = |\Delta S|/2$, the probability of misclassifying state $|g\rangle$ as $|e\rangle$ is:

$$P(e|g) = \frac{1}{2}\text{erfc}\left(\frac{|\Delta S|}{2\sqrt{2}\sigma}\right) \tag{3.83}$$

and by symmetry, $P(g|e) = P(e|g)$. The average error probability is:

$$P_{\text{error}} = \frac{1}{2}\left[P(e|g) + P(g|e)\right] = \frac{1}{2}\text{erfc}\left(\frac{|\Delta S|}{2\sqrt{2}\sigma}\right) \tag{3.84}$$

where $\text{erfc}(x) = \frac{2}{\sqrt{\pi}}\int_x^\infty e^{-t^2}dt$ is the complementary error function. The measurement fidelity is:

$$F = 1 - P_{\text{error}} = 1 - \frac{1}{2}\text{erfc}\left(\frac{|\Delta S|}{2\sqrt{2}\sigma}\right) \tag{3.85}$$

To express this in terms of a signal-to-noise metric, we define the discrimination SNR (or readout SNR) as:

$$\mathrm{SNR}_{\mathrm{readout}} = \frac{|S_{\mathrm{e}} - S_{\mathrm{g}}|^2}{\sigma_{\mathrm{e}}^2 + \sigma_{\mathrm{g}}^2} = \frac{|\Delta S|^2}{2\sigma^2} \tag{3.86}$$

where $|\Delta S| = |S_e - S_g|$ is the separation between state centroids and assumes equal noise variances $\sigma_{\mathrm{e}}^2 = \sigma_{\mathrm{g}}^2$. Substituting into Eq. 3.85, we obtain:

$$F = 1 - \frac{1}{2}\mathrm{erfc}\left(\frac{\sqrt{\mathrm{SNR}_{\mathrm{readout}}}}{2}\right) \tag{3.87}$$

The discrimination SNR (Eq. 3.86) differs from the conventional signal-to-noise ratio in that it is based on the state separation $|\Delta S|$ rather than just the signal power itself. This metric directly quantifies the distinguishability of the two qubit states and governs the measurement fidelity.

It is crucial to distinguish between the **readout SNR** defined in Eq. (3.86) and the conventional **engineering SNR** used in signal processing. The engineering SNR is typically defined as the ratio of signal power to noise power:

$$\mathrm{SNR}_{\mathrm{eng}} = \frac{\langle |S|^2 \rangle}{\sigma^2} = \frac{P_{\mathrm{signal}}}{P_{\mathrm{noise}}} \tag{3.88}$$

where $\langle |S|^2 \rangle$ is the mean signal power (e.g., reflected microwave power from the resonator).

In contrast, the readout SNR has a fundamentally **physical interpretation**: it quantifies the *distinguishability* of two quantum states rather than the quality of signal transmission.
Maximizing engineering SNR (e.g., by increasing drive power) does not necessarily improve measurement fidelity if the state separation $|\Delta S|$ does not increase proportionally.
Typical high-fidelity readout requires $\mathrm{SNR}_{\mathrm{readout}} \gtrsim 10$ (corresponding to $F \gtrsim 99\%$), which translates to a state separation of at least $|\Delta S| \gtrsim 4.5\sigma$ in the IQ plane.

3.5 LNA Noise Requirements for High-Fidelity Readout

In dispersive readout of superconducting qubits, the low-noise amplifier (LNA) receives a weak microwave signal reflected from a resonator coupled to the qubit. The reflected signal power is constrained by the need to avoid driving the qubit out of the dispersive regime [32], [41]. Typically, the signal arrives at the LNA input at power levels between -100 and $-120\,\mathrm{dBm}$, necessitating careful noise management to achieve high measurement fidelity.

3.5.1 Signal-to-Noise Requirements from Target Fidelity

We begin by establishing the relationship between target measurement fidelity and the required signal-to-noise ratio. For a Gaussian noise model, the single-shot readout fidelity F is determined by the separation between qubit state distributions relative to their noise width [46]:

$$F = \frac{1}{2}\left[1 + \text{erf}\left(\frac{|\Delta S|}{2\sqrt{2}\sigma}\right)\right] \tag{3.89}$$

where $|\Delta S|$ is the voltage separation between the two qubit states in the IQ plane and σ is the noise standard deviation in each quadrature (see figure 3.3.2).
For a target fidelity of $F = 99\%$, the error probability is $1 - F = 0.01$, which gives:

$$\frac{1}{2}\text{erfc}\left(\frac{|\Delta S|}{2\sqrt{2}\sigma}\right) = 0.01 \tag{3.90}$$

Taking the inverse complementary error function yields:

$$\frac{|\Delta S|}{2\sqrt{2}\sigma} = \text{erfc}^{-1}(0.02) \approx 2.326 \tag{3.91}$$

and thus:

$$\frac{|\Delta S|}{\sigma} = 2\sqrt{2} \times 2.326 \approx 6.58 \tag{3.92}$$

The noise standard deviation σ in each quadrature is related to the system noise temperature by:

$$\sigma = \sqrt{G_{\text{total}} \cdot k_B T_{\text{sys}} \cdot B_{\text{filter}} \cdot Z_0} \tag{3.93}$$

where G_{total} is the total system available power gain, k_B is Boltzmann's constant, T_{sys} is the system noise temperature referred to the input, B_{filter} is the measurement bandwidth (typically 1–$10\,\text{MHz}$), and $Z_0 = 50\,\Omega$ is the load impedance.

3.5.2 System Noise Temperature and LNA Contribution

The system noise temperature at the LNA input comprises several contributions. In a well-designed cryogenic readout chain, the Friis formula shows that the system noise temperature is dominated by the source noise and the LNA noise temperature [38]:

$$T_{\text{sys}} = T_{\text{source}} + T_N^{\text{LNA}} + \frac{T_{\text{subsequent}}}{G_{\text{LNA}}} \tag{3.94}$$

where T_{source} is the equivalent noise temperature at the input of the LNA, T_N^{LNA} is the LNA noise temperature, and $T_{\text{subsequent}}$ accounts for noise from downstream stages. With high enough LNA gain ($G_{\text{LNA}} \gg 1$), the contribution from subsequent stages becomes negligible.

For a resonator cooled at the mixing chamber temperature ($T_{\text{source}} \sim 20\,\text{mK}$), the source contribution is negligible compared to typical LNA noise temperatures. At microwave frequencies ($\sim 6\,\text{GHz}$), the quantum noise temperature $\hbar\omega/k_B \approx 0.3\,\text{K}$ exceeds the physical temperature, but remains small compared to practical LNA noise. Because in this works we are using an active circulator, the source noise temperature include the contribution of the circulator's noise in addition to the thermal noise of the resonator. Therefore, the system noise temperature at the output:

$$T_{\text{sys}} \approx T_N^{\text{Circ}} G_{\text{total}} + T_N^{\text{LNA}} \tag{3.95}$$

3.5.3 Derivation of Required LNA Noise Temperature

Form equation (3.33) and (3.34) we can see that the reflection coefficients for the ground and excited states are:

$$\Gamma_g = 1 - \frac{\kappa_{\text{ext}}\left(\kappa_{\text{tot}}/2 + i\chi\right)}{(\kappa_{\text{tot}}/2)^2 + \chi^2} = I_g + jQ_g \tag{3.96}$$

$$\Gamma_e = 1 - \frac{\kappa_{\text{ext}}\left(\kappa_{\text{tot}}/2 - i\chi\right)}{(\kappa_{\text{tot}}/2)^2 + \chi^2} = I_e + jQ_e \tag{3.97}$$

with

$$I_g = I_e = 1 - \frac{\kappa_{\text{ext}}\kappa_{\text{tot}}/2}{(\kappa_{\text{tot}}/2)^2 + \chi^2}, \quad Q_g = -Q_e = -\frac{\kappa_{\text{ext}}\chi}{(\kappa_{\text{tot}}/2)^2 + \chi^2} \tag{3.98}$$

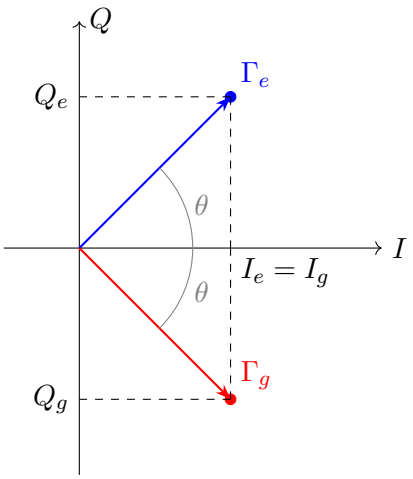


Figure 3.5.1: Representation of the reflection coefficients Γ_g and Γ_e on the IQ plane. The in-phase components I_g and I_e are equal, while the quadrature components Q_g and Q_e are equal in magnitude but opposite in sign. The angle θ represents the phase difference between the two states.

Then from equation (3.48), (3.47), (3.49)

$$\Delta S = (I_e - I_g) + j(Q_e - Q_g) = j2Q_e \Rightarrow Q_e = \frac{\Delta S}{2j} \tag{3.99}$$

with this result we can define the contrast factor C as:

$$C = \frac{|\Gamma_e - \Gamma_g|}{|\Gamma_e + \Gamma_g|} = \left|\frac{I_e + jQ_e - I_g - jQ_g}{I_e + jQ_e + I_g + jQ_g}\right| = \left|\frac{j2Q_e}{2I_e}\right| = \left|\frac{Q_e}{I_e}\right| = \frac{|\Delta S|}{2|I_e|} \tag{3.100}$$

with this definition the contrast factor can be interpreted, using the figure 3.5.1, as $C = \tan(\theta)$.
From the definition of the contrast factor we can express the signal separation in terms of the contrast factor and the in-phase component:

$$|\Delta S| = 2C|I_e| \tag{3.101}$$

The in-phase component is related to the input signal power P_{signal} and the system impedance Z_0 as:

$$P_{\text{signal}} = \frac{|I_e|^2}{Z_0} \Rightarrow |I_e| = \sqrt{P_{\text{signal}} Z_0} \tag{3.102}$$

and therefore the signal separation can be expressed in terms of the input signal power and the contrast factor:

$$|\Delta S| = 2C\sqrt{P_{\text{signal}} Z_0} = 2\sqrt{C^2 Z_0 P_{\text{signal}}} \tag{3.103}$$

At the output of the LNA of available power gain G_{LNA} the signal power is amplified to $P^{\text{out}}_{\text{signal}} = G_{\text{LNA}} P_{\text{signal}}$, so the signal separation at the output of the LNA is:

$$|\Delta S|_{\text{out}} = 2\sqrt{C^2 Z_0 G_{\text{LNA}} P_{\text{signal}}} \tag{3.104}$$

The noise variance at the output of the LNA σ^2_{out} is the sum of the amplified input noise which includes the circulator's noise contribution:

$$\sigma^2_{\text{CIRC}} = G_{\text{CIRC}} k_B T_{\text{CIRC}} B Z_0 G_{\text{LNA}} \tag{3.105}$$

where G_{CIRC} is the circulator's insertion loss, T_{CIRC} is the circulator's input referred noise temperature; and the LNA's own noise contribution:

$$\sigma^2_{\text{LNA}} = k_B T_{\text{LNA}} B Z_0 G_{\text{LNA}} \tag{3.106}$$

So we can express the signal-to-noise ratio at the output of the LNA as:

$$\frac{|\Delta S|_{\text{out}}}{\sigma_{\text{out}}} = \frac{2\sqrt{C^2 Z_0 G_{\text{LNA}} P_{\text{signal}}}}{\sqrt{k_B B Z_0 G_{\text{LNA}} \left(G_{\text{CIRC}} T_{\text{CIRC}} + T_{\text{LNA}}\right)}} = \frac{2\sqrt{C^2 P_{\text{signal}}}}{\sqrt{k_B B \left(G_{\text{CIRC}} T_{\text{CIRC}} + T_{\text{LNA}}\right)}} \tag{3.107}$$

By assuming for sake of simplicity the circulator gain $G_{\text{CIRC}} = 1$ (or equivalently, the circulator's insertion loss is negligible), we can simplify the expression to:

$$\frac{|\Delta S|_{\text{out}}}{\sigma_{\text{out}}} = \frac{2\sqrt{C^2 P_{\text{signal}}}}{\sqrt{k_B B \left(T_{\text{CIRC}} + T_{\text{LNA}}\right)}} \tag{3.108}$$

Combining with equations (3.92) and (3.93), you get:

$$\frac{|\Delta S|}{\sigma_{\text{out}}} = \frac{2\sqrt{C^2 P_{\text{signal}}}}{\sqrt{k_B B \left(T_{\text{CIRC}} + T_{\text{LNA}}\right)}} = 6.58 \tag{3.109}$$

Solving for the total system noise temperature $T_{\text{sys}} = T_{\text{CIRC}} + T_{\text{LNA}}$:

$$T_{\text{sys}} = \frac{4C^2 P_{\text{signal}}}{43.3 \cdot k_B \cdot B} \tag{3.110}$$

Using representative parameters from the literature [49]: input signal power $P_{\text{signal}} = -100\,\text{dBm} = 10^{-13}\,\text{W}$, contrast factor $C = 0.2$, and filter bandwidth $B_{\text{filter}} = 1\,\text{MHz}$:

$$T_{\text{sys}} = \frac{10^{-13} \times (0.2)^2}{43.3 \times 1.38 \times 10^{-23} \times 10^{6}} \approx 26.8\,\text{K} \tag{3.111}$$

If an active circulator (or isolator) with insertion loss $L_{\text{CIRC}} = 0.5\,\text{dB}$ (corresponding to $G_{\text{CIRC}} = 10^{-0.05} \approx 0.89$) and physical temperature $T_{\text{phys}} = 4\,\text{K}$ is placed before the LNA, its noise contribution referred to the LNA input is:

$$G_{\text{CIRC}} T_{\text{CIRC}} \tag{3.112}$$

Therefore, the required LNA noise temperature is:

$$T_{\text{LNA}} = T_{\text{sys}} - G_{\text{CIRC}} T_{\text{CIRC}} \approx 26.8 - 0.5 = 26.3\,\text{K} \tag{3.113}$$

The corresponding noise figure, referenced to room temperature ($T_0 = 290\,\text{K}$), is:

$$\text{NF}_{\text{LNA}} = 10\log_{10}\left(1 + \frac{T_{\text{LNA}}}{T_0}\right) = 10\log_{10}\left(1 + \frac{26.3}{290}\right) \approx 0.38\,\text{dB} \tag{3.114}$$

This noise figure of $\sim 0.4\,\text{dB}$ is **below the quantum limit** for a phase-preserving linear amplifier at 6 GHz, which is approximately:

$$\text{NF}_{\text{quantum}} = 10\log_{10}\left(1 + \frac{\hbar\omega}{k_B T_0}\right) \approx 10\log_{10}\left(1 + \frac{0.29\,\text{K}}{290\,\text{K}}\right) \approx 0.004\,\text{dB} \tag{3.115}$$

Wait—this suggests the required noise figure is actually *above* the quantum limit, which is physically reasonable. However, achieving NF $< 0.5\,\text{dB}$ with conventional HEMT amplifiers is challenging.

3.6 Probing signal

Until now we have considered reflectometry measurements performed with a simple continuous-wave tone at frequency ω_{probe}. In an ideal case, this is the optimal choice because the tone's energy spectrum is a Dirac delta function with maximum energy concentration at a single frequency. However, in practice, the tone is generated by a microwave source with finite rise/fall times, leading to spectral broadening. This means the tone's spectrum has energy at frequencies other than ω_{probe}, which can cause unwanted effects such as excitation of parasitic modes or increased noise coupling.

To mitigate this, in real experiments the probing signal is generated via IQ modulation with a raised-cosine envelope on the in-phase component and its derivative on the quadrature component. The spectrum of the modulated signal is asymmetric, with a maximum at the probe frequency and small sidebands both above and below ω_{probe}. The raised-cosine envelope suppresses sidebands more effectively than a rectangular pulse, reducing spectral leakage into adjacent frequency bands where other resonators or qubit transitions may reside. This shaped pulse minimizes crosstalk while preserving measurement fidelity.

3.7 Complete Readout Architecture

Having established the physical principles underlying reflectometry, resonant loading, and quadrature detection, we now assemble these elements into the complete measurement chain employed for dispersive qubit readout. The architecture integrates five primary functional blocks: the readout resonator, a directional coupler (circulator), the qubit, a low-noise amplifier, and an IQ demodulator.

The readout resonator provides the impedance transformation that converts qubit-state-dependent frequency shifts into measurable reflection coefficient changes. Its coupling to the feedline is tuned to achieve critical or slight under-coupling, balancing the need for efficient power extraction against Purcell decay, the enhanced spontaneous emission rate that occurs when a qubit couples to a low-Q electromagnetic environment through the resonator. The resonator's internal quality factor, limited by dielectric loss in the substrate and conductor surface resistance, must exceed 10^4 to resolve typical dispersive shifts of a few megahertz while maintaining integration times compatible with qubit coherence times. In cryogenic environments, superconducting inductors exhibit quality factors two to three orders of magnitude higher than at room temperature [50], enabling low-loss readout.

The circulator routes signals directionally around the measurement loop. Port 1 connects to the probe source, port 2 to the resonator (and qubit), and port 3 to the amplifier chain. Forward propagation from port 1 to port 2 experiences minimal loss (typically < 0.5 dB), while port-2-to-port-1 transmission is suppressed by > 20 dB isolation, forcing the reflected signal to exit through port 3 toward the amplifier. This directional routing separates the weak reflected signal from the strong incident drive, preventing source-pulling effects and enabling sensitive detection without saturating the amplifier with the

outgoing probe power. Traditional ferrite-based circulators are bulky (typically 1-2 cm diameter) and non-integrable with standard CMOS processes. Recent CMOS circulators based on staggered commutation exhibit insertion loss below 2 dB and strong non-reciprocity in compact, reconfigurable designs [50]. Typical CMOS circulators occupy chip areas of 0.1-0.9 mm^2[51], enabling monolithic integration. In this work we implement a quasi-circulator in CMOS technology to reduce footprint and cost.

The superconducting qubit couples capacitively to the readout resonator with strength chosen to place the system firmly in the dispersive regime. For transmon qubits, typical coupling strengths $g/(2\pi)$ range from 50 MHz to 150 MHz, while the qubit-resonator detuning $\Delta/(2\pi)$ exceeds 1 GHz, yielding dispersive shifts $\chi/(2\pi) \sim g^2/\Delta$ of 1 MHz to 10 MHz. The qubit's quantum state modulates the resonator's complex admittance, which in turn modulates the reflected signal's amplitude and phase according to the impedance matching relations derived earlier. Crucially, the qubit does not simply act as a passive load but as a quantum degree of freedom subject to decoherence mechanisms—energy relaxation (T_1), dephasing (T_2), and measurement-induced dephasing—that limit the available integration time and thus the achievable signal-to-noise ratio.

The cryogenic low-noise amplifier (LNA), positioned at the 4 K stage of the dilution refrigerator, provides the first stage of signal amplification above the ambient thermal noise floor. Based on high-electron-mobility transistor (HEMT) technology, these amplifiers achieve noise temperatures of 2 K to 5 K while delivering 30 to 40 dB of gain across multi-gigahertz bandwidths. The amplifier's noise, referred back to its input, must remain below the signal level to avoid dominating the measurement uncertainty. Cascading additional amplification stages at higher temperature stages (40 K, room temperature) boosts the signal further without adding significant referred noise, as each stage's noise contribution scales inversely with the preceding gain.

Modern Josephson parametric amplifiers (JPAs) provide gains exceeding 20 dB across bandwidths of 3 MHz to 500 MHz [52], with added noise approaching two photons (near the quantum limit of 0.5 photons). However, JPAs require a superconducting Josephson junction, a circulator for pump isolation, and a high-power pump signal, increasing circuit complexity and on-chip real estate. The superconducting junction itself demands careful fabrication and flux biasing. Despite the noise advantage, we omit the JPA stage in this work to reduce system complexity and demonstrate that competitive readout performance can be achieved with a single-stage SiGe BJT LNA, maintaining CMOS compatibility and simpler circuit design.

The amplified signal, now at power levels of -80 dBm or higher, enters the IQ demodulator at 4K. The output signals $I(t)$ and $Q(t)$ are Analog-to-digital converted at rates of tens to hundreds of megahertz, providing time-resolved trajectories of the IQ point as the qubit state evolves.

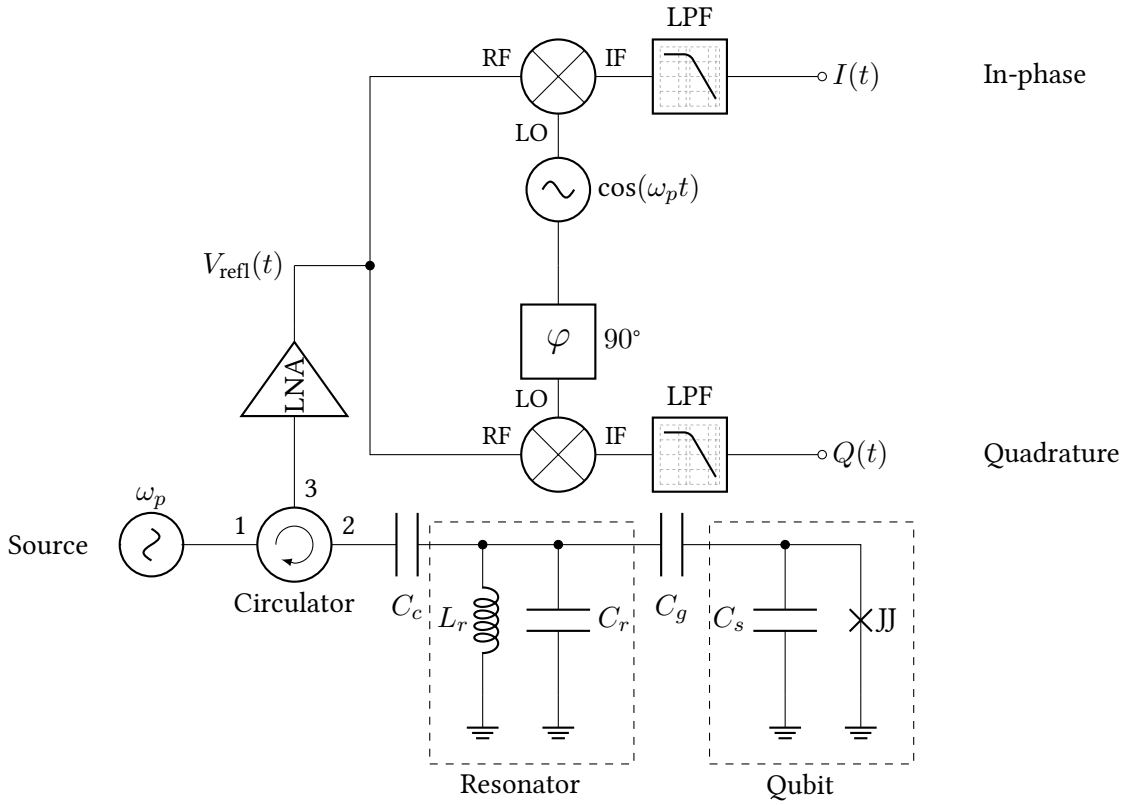


Figure 3.7.1: Readout architecture for quantum state measurement. The probe signal at frequency ω_p is injected into the readout resonator through a circulator, which routes the reflected signal to a low-noise amplifier (LNA). The amplified signal is then down-converted using an IQ demodulator, producing baseband in-phase $I(t)$ and quadrature $Q(t)$ signals for further processing.

Chapter 4 Superconducting Transmon Qubit

A physical implementation of a qubit requires a quantum two-level system that satisfies the DiVincenzo criteria: it must be initializable to a known state, controllable via external fields, measurable through a projective readout mechanism, and possess sufficiently long coherence times to enable multi-gate sequences [53]. Among the several physical realizations (trapped ions, neutral atoms, quantum dots, and superconducting circuits) the latter have emerged as a leading platform for fault-tolerant quantum computation, owing to their lithographic scalability, integration with microwave control infrastructure, and rapid improvement in coherence times [54], [55].

The fundamental nonlinear element underlying superconducting qubits is the Josephson junction, a nanoscale tunnel barrier between two superconductors that exhibits macroscopic quantum coherence and provides the anharmonicity necessary to isolate computational states. This chapter develops a circuit-level model of the transmon qubit [56], starting from the quantum harmonic oscillator formed by a linear LC resonator, progressing through the introduction of Josephson nonlinearity, and culminating in a Verilog-A implementation suitable for large-scale circuit simulation of readout architectures.

4.1 Harmonic Oscillator and Anharmonic Qubit

The simplest electromagnetic oscillator consists of an inductor L and capacitor C in parallel, storing energy alternately in magnetic and electric fields. At cryogenic temperatures ($T \ll \hbar\omega_0/k_B$, where $\omega_0 = 1/\sqrt{LC}$ is the classical resonance frequency), thermal fluctuations are frozen out and the circuit's behavior is governed by quantum mechanics.

The voltage V across the LC tank is related to the magnetic flux Φ through the inductor by the Faraday's law, $V = \mathrm{d}\Phi/\mathrm{d}t$, and to the charge Q on the capacitor by $V = Q/C$. The current through the inductor is $I_L = \Phi/L$ (integrated form of $V = L\,\mathrm{d}I/\mathrm{d}t$), and through the capacitor is $I_C = \mathrm{d}Q/\mathrm{d}t$. Since the elements are in parallel, $I_L + I_C = 0$, yielding:

$$\frac{\Phi}{L} + C\frac{\mathrm{d}^2\Phi}{\mathrm{d}t^2} = 0 \tag{4.1}$$

which is the equation of a classical harmonic oscillator with "mass" C and "spring constant" $1/L$. The energy stored in the circuit is:

$$H_{\mathrm{LC}} = \frac{Q^2}{2C} + \frac{\Phi^2}{2L} \tag{4.2}$$

To construct the quantum Hamiltonian, we identify the flux Φ as the generalized coordinate and the charge Q as the canonical momentum. Canonical quantization proceeds by promoting Φ and Q to operators $\hat{\Phi}$ and $\hat{Q}$ satisfying the commutation relation:

$$[\hat{\Phi}, \hat{Q}] = i\hbar \tag{4.3}$$

analogous to $[\hat{x}, \hat{p}] = i\hbar$ for position and momentum; the quantum form of the classical Poisson's bracket, according to the formalism $[\hat{\Phi}, \hat{Q}] \Leftrightarrow i\hbar\{\Phi, Q\}$ with $\{\Phi, Q\} = 1$. Substituting the operators into Eq. (4.2) yields the quantum Hamiltonian:

$$\hat{H}_{\text{LC}} = \frac{\hat{Q}^2}{2C} + \frac{\hat{\Phi}^2}{2L} \tag{4.4}$$

To solve for the energy eigenstates, we define dimensionless ladder operators $\hat{a}$ and $\hat{a}^\dagger$ dubbed creation and destruction:

$$\hat{\Phi} = \sqrt{\frac{\hbar}{2\omega_0 C}} \left(\hat{a} + \hat{a}^\dagger\right) = \Phi_{\text{zpf}} \left(\hat{a} + \hat{a}^\dagger\right), \tag{4.5}$$

$$\hat{Q} = i\sqrt{\frac{\hbar\omega_0 C}{2}} \left(\hat{a}^\dagger - \hat{a}\right) = iQ_{\text{zpf}} \left(\hat{a}^\dagger - \hat{a}\right), \tag{4.6}$$

where $\Phi_{\text{zpf}} = \sqrt{\hbar/(2\omega_0 C)} = \sqrt{\hbar L/2}$ and $Q_{\text{zpf}} = \sqrt{\hbar\omega_0 C/2} = \sqrt{\hbar C/(2L)}$ are the zero-point fluctuations of flux and charge. These operators satisfy the bosonic commutation relation $[\hat{a}, \hat{a}^\dagger] = 1$, and substituting into Eq. (4.4) gives:

$$\hat{H}_{\text{LC}} = \hbar\omega_0 \left(\hat{a}^\dagger\hat{a} + \tfrac{1}{2}\right) \tag{4.7}$$

The energy eigenstates $|n\rangle$ satisfy $\hat{a}^\dagger\hat{a}\,|n\rangle = n\,|n\rangle$, with eigenvalues:

$$E_n^{\text{LC}} = \hbar\omega_0 \left(n + \tfrac{1}{2}\right) \qquad n = 0, 1, 2 \ldots \tag{4.8}$$

This is the celebrated Fock state ladder: equally spaced energy levels separated by $\hbar\omega_0$, representing discrete excitations (photons) of the electromagnetic field confined in the LC circuit.

While the LC oscillator exhibits quantum behavior at low temperatures, its equally spaced spectrum is unsuitable for qubit implementation. Consider a microwave drive at frequency ω_0 intended to excite the $|0\rangle \to |1\rangle$ transition. Since the $|1\rangle \to |2\rangle$ transition has the same frequency, the drive inevitably populates higher levels $|2\rangle, |3\rangle, \ldots$, causing leakage out of the computational subspace $\{|0\rangle, |1\rangle\}$. This violates the qubit paradigm: we cannot address the two-level system in isolation. Mathematically, the transition matrix elements $\langle n+1|\hat{a}|n\rangle = \sqrt{n+1}$ increase with n, so higher transitions are stronger, not weaker—the opposite of what is needed.

To construct a controllable qubit, is required **anharmonicity**: a nonuniform energy spectrum in which $E_2 - E_1 \neq E_1 - E_0$. This allows selective addressing of the $|0\rangle \leftrightarrow |1\rangle$ transition with negligible leakage to $|2\rangle$. The nonlinearity must be strong enough to resolve transitions spectrally (typical control pulses have $\sim$ 10-100 MHz bandwidth), yet weak enough to avoid complicating higher-order processes. To introduce the necessary nonlinearity, we must replace the linear inductor L with a nonlinear reactive element. The Josephson junction, which exhibits a sinusoidal current-phase relation (detailed in Section 4.2), behaves as a nonlinear inductor with potential energy:

$$U_J(\phi) = -E_J \cos\phi, \qquad E_J = \frac{\Phi_0 I_c}{2\pi}, \tag{4.9}$$

where $\phi = 2\pi\Phi/\Phi_0$ is the gauge-invariant phase difference across the junction, $\Phi_0 = h/(2e)$ is the magnetic flux quantum, and I_c is the critical current. Unlike the parabolic potential $\Phi^2/(2L)$, the cosine potential $-E_J \cos\phi$ contains higher-order terms $\sim \phi^4, \phi^6, \ldots$ that break the harmonic spectrum and introduce anharmonicity.

By replacing the inductor in an LC circuit with a Josephson junction (and including a large shunt capacitance C_Σ to suppress charge noise), we obtain the transmon qubit [56], whose low-energy spectrum (derived in Section 4.3.3) exhibits the desired anharmonicity:

$$\alpha = \omega_{12} - \omega_{01} \simeq -\frac{E_C}{\hbar}, \qquad E_C = \frac{e^2}{2C_\Sigma}, \tag{4.10}$$

where E_C is the charging energy of the capacitor. For typical transmons with $C_\Sigma \sim 100 - 200$ fF, this yields $\alpha/(2\pi) \sim -200$ to -300 MHz, sufficient to isolate the computational subspace while maintaining strong dispersive coupling to readout resonators.

4.2 Josephson Junction Physics

The quantum description of superconducting circuits relies on the macroscopic nature of the superconducting condensate. In quantum mechanics, the state of a system evolves according to the time-dependent Schrödinger equation

$$i\hbar\frac{\partial\psi}{\partial t} = \hat{H}\psi \tag{4.11}$$

where $\hat{H}$ is the Hamiltonian operator, ψ is the wavefunction, and $\hbar = h/(2\pi)$ is the reduced Planck constant. The square modulus $|\psi|^2$ represents the probability density of finding the system in a given state.

In a superconductor, electrons pair into Cooper pairs—bound states of two electrons with opposite spin and momentum, mediated by the electron-phonon interaction [57]. Below the critical temperature, these pairs condense into a single macroscopic quantum state described by a collective wavefunction

$$\Psi(\mathbf{r}) = \sqrt{n_s(\mathbf{r})}\, e^{i\chi(\mathbf{r})} \tag{4.12}$$

where n_s is the local density of Cooper pairs and χ is the phase. Unlike the microscopic wavefunction of individual particles, both the amplitude and the phase of Ψ are macroscopic variables that can be manipulated and measured, forming the basis of superconducting quantum circuits [58].
Two fundamental consequences follow from Eq. (4.12). First, the requirement that Ψ be single-valued imposes the quantisation of magnetic flux through any closed loop within a superconductor:

$$\Phi = n\,\Phi_0, \qquad \Phi_0 = \frac{h}{2e} \simeq 2.07 \times 10^{-15}\,\mathrm{Wb} \tag{4.13}$$

where n is an integer and Φ_0 is the magnetic flux quantum [59], [60]. Second, when two superconductors are separated by a thin insulating barrier, forming a Josephson junction,a supercurrent can flow across the junction even in the absence of a voltage drop, provided the barrier thickness d is small enough that Cooper pairs can tunnel through it. The current is then governed not by the local voltage, but by the phase difference $\phi = \chi_2 - \chi_1$ between the two superconductors [61]. This is the Josephson effect, expressed by the current-phase relation

$$I = I_c \sin\phi \tag{4.14}$$

and the voltage-phase relation or second Josephson relation

$$V = \frac{\Phi_0}{2\pi}\frac{\mathrm{d}\phi}{\mathrm{d}t} \tag{4.15}$$

where I_c is the critical current of the junction, which is the maximum supercurrent that can flow through the junction without any voltage drop, Acording to the Josephson relations, if the current across the junction is less than the critical current, $|I| < I_c$, the junction behaves as a superconducting

resistor with zero resistance, this involve a constant Josesphon phase difference ϕ

$$\dot{\phi}_n = \arcsin\left(\frac{I}{I_c}\right) + 2n\pi \tag{4.16}$$

consequently a zero voltage drop across the junction. This state is called *S state* (superconducting state). In this state no energy is dissipated in the junction but the junction can store energy in the form of magnetic field.

4.2.1 Current Components and the RCSJ Model

Consider an external system responsible for the current flowing through the junction, or in other words, of the phase change form ϕ_1 to ϕ_2. The energy stored in the junction is given by the work done by the external system to change the phase difference:

$$E = \int_{\phi_1}^{\phi_2} VIdt = \frac{\hbar}{2e}\int_{\phi_1}^{\phi_2} Id\phi = \frac{\hbar I_c}{2e}\int_{\phi_1}^{\phi_2} \sin(\phi)d\phi = E_J\left[\cos(\phi_1) - \cos(\phi_2)\right] \tag{4.17}$$

where $E_J = \frac{\hbar I_c}{2e}$ is the Josephson energy, which is the maximum energy that can be stored in the junction. In other words, the previous equation notes that the energy stored in the junction is not dependent on the path taken to change the phase difference, but only on the initial and final values of the phase difference. The potential energy associated to the junction describes thus a field of conservative force, where the potential energy is give by:

$$U(\phi) = E_J\left[1 - \cos(\phi)\right] + const \tag{4.18}$$

so that the energy stored in the junction is given by the difference of the potential energy at the two phase values:

$$E = U(\phi_2) - U(\phi_1) \tag{4.19}$$

Under a didactical point of view, the Josephson junction can be modeled as a non-linear reactance. Consider an arbitrary small perturbation of the phase difference $\tilde{\phi} \ll 1$ around a bias point ϕ_0:

$$\phi = \phi_0 + \tilde{\phi} \tag{4.20}$$

substituting into the first Josephson relation and expanding to first order in $\tilde{\phi}$, we obtain:

$$\begin{aligned} I_S + \tilde{I}_S &= I_c \sin(\phi_0 + \tilde{\phi}) \\ &= I_c\big(\sin\phi_0 \cos\tilde{\phi} + \cos\phi_0 \sin\tilde{\phi}\big) \\ &\approx I_c \sin\phi_0 + I_c \cos\phi_0\ \tilde{\phi} \end{aligned} \tag{4.21}$$

in virtu of $\cos\tilde{\phi} \approx 1$ and $\sin\tilde{\phi} \approx \tilde{\phi}$. So the perturbation of the supercurrent is:

$$\tilde{I_S} = I_c \cos\phi_0 \; \tilde{\phi} \qquad \dot{\tilde{I}}_S = I_c \cos\phi_0 \; \dot{\tilde{\phi}} \tag{4.22}$$

Substituting in the second Josephson relation we obtain:

$$\tilde{V} = \frac{\Phi_0}{2\pi}\dot{\tilde{\phi}} = \frac{\Phi_0}{2\pi}\frac{1}{I_c \cos\phi_0}\dot{\tilde{I}}_S = L_J \dot{\tilde{I}}_S \tag{4.23}$$

This voltage-current relation is the same as that of an inductor with inductance:

$$L_J = \frac{\Phi_0}{2\pi I_c \cos\phi_0} = \frac{L_{J0}}{\cos\phi_0} \quad L_{J0} = \frac{\Phi_0}{2\pi I_c} \tag{4.24}$$

where L_{J0} is the Josephson inductance at zero phase difference. This result shows that the Josephson junction can be modeled as a non-linear inductor, whose inductance depends on the phase difference across the junctio and so on the current flowing through the junction. One particular property of this non-liner inductor is that its ability to take negative values at intervals of $\pi/2+2\pi n < \phi < 3\pi/2+2\pi n$. This property is the basis of the operation of the Josephson parametric amplifier, which is a non-linear amplifier that can achieve quantum-limited noise performance.

In reality, the net current flowing through the junction is not only the supercurrent but also includes a normal (quasiparticle) current and a displacement current. At finite temperature, thermal fluctuations break a small fraction of Cooper pairs, creating quasiparticles that can tunnel through the barrier as normal electrons. This normal current I_N obeys Ohm's law:

$$I_N = \frac{V}{R_N} \tag{4.25}$$

where R_N is the normal-state resistance of the junction (i.e., the resistance measured above the critical temperature). For tunnel junctions, the critical current I_c and the normal resistance R_N are not independent but related by the *Ambegaokar-Baratoff relation* [62]

$$I_c R_N = \frac{\pi\Delta(T)}{2e}\tanh\left(\frac{\Delta(T)}{2k_B T}\right) \tag{4.26}$$

where $\Delta(T)$ is the temperature-dependent superconducting gap. At $T \ll T_c$, this simplifies to $I_c R_N \simeq \pi\Delta(0)/(2e)$, providing a natural energy scale for the junction.

When the total current through the junction satisfies $|I| < I_c$, the phase ϕ_0 remains constant in time and the junction acts as a dissipationless superconducting short. Conversely, when $|I| \geq I_c$ or when external noise induces phase slips, ϕ_0 evolves in time and a finite voltage $V = (\Phi_0/2\pi)\,\mathrm{d}\phi/\mathrm{d}t$ appears across the junction (Eq. 4.15). In this *resistive state* (or *R state*), energy is dissipated as Joule heating through the normal resistance R_N.

It is useful to define two characteristic scales for the junction. The characteristic voltage

$$V_c = I_c R_N \tag{4.27}$$

sets the typical voltage drop in the resistive state, and the associated characteristic frequency (from the second Josephson relation) is

$$\omega_c = \frac{2\pi}{\Phi_0} V_c = \frac{2e}{\hbar} V_c, \qquad f_c = \frac{V_c}{\Phi_0} \tag{4.28}$$

Using the Josephson inductance $L_J = \Phi_0/(2\pi I_c \cos\phi)$ (Eq. 4.24), evaluated at $\phi_0 = 0$, we obtain the useful relation

$$\omega_c L_J(0) = R_N \tag{4.29}$$

The third current contribution arises from the physical capacitance C_J formed by the two superconducting electrodes separated by the thin insulator. The displacement current is

$$I_D = C_J \frac{\mathrm{d}V}{\mathrm{d}t} \tag{4.30}$$

The relative importance of these three currents depends on the operating frequency. In the small-signal regime around a bias point, we can compare their magnitudes. For a sinusoidal voltage $V \sim V_0 e^{i\omega t}$, the supercurrent (linearised) gives $I_s \lesssim I_c = V/(\omega_c L_J)$, the normal current is $I_N = V/R_N$, and the displacement current is $I_D = i\omega C_J V$. The ratio of supercurrent to displacement current is

$$\frac{I_c}{I_D} \sim \frac{1}{\omega^2 L_J C_J} = \left(\frac{\omega_p}{\omega}\right)^2 \tag{4.31}$$

where the plasma frequency of the junction is

$$\omega_p = \frac{1}{\sqrt{L_J C_J}} = \sqrt{\frac{2eI_c}{\hbar C_J}} \tag{4.32}$$

At frequencies $\omega \ll \omega_p$, the displacement current is negligible and the junction dynamics are dominated by the supercurrent and the resistive damping. Conversely, at $\omega \gg \omega_p$ the junction behaves essentially as a linear capacitor and resistor in parallel, with the supercurrent playing a minor role.

Finally, we note that the dissipative normal current in a realistic Josephson junction gives rise to thermal and shot noise, which can be modelled by a stochastic current source $I_F(t)$.

Combining all four contributions, the current through a Josephson junction is modeled as the sum of the supercurrent I_S, normal current I_N, displacement current I_D, and noise current I_F:

$$I = I_S(\phi) + I_N(V) + I_D(\dot{V}) + I_F(t) \tag{4.33}$$

$$= I_c \sin\phi + \frac{V}{R_N} + C_J \frac{\mathrm{d}V}{\mathrm{d}t} + I_F(t) \tag{4.34}$$

This current equation describes the equivalent circuit of a Josephson junction, that can be represented as a parallel combination of a non-linear inductor L_J, a resistor R_N, a capacitor C_J and a noise source I_F, as shown in Figure 4.2.1. This model is called the resistively and capacitively shunted junction (RCSJ) model, and it is widely used to describe the dynamics of Josephson junctions.

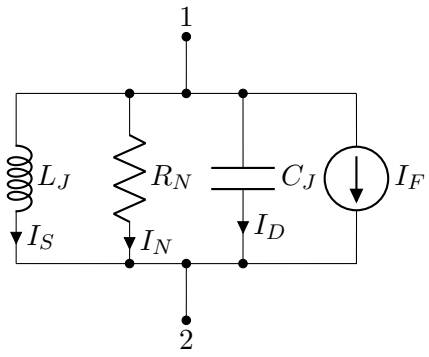


Figure 4.2.1: Equivalent circuit of a Josephson junction, modeled as a parallel combination of a non-linear inductor L_J, a resistor R_N and a capacitor C_J.

The RCSJ model (Eq. 4.33) rests on a few simplifying assumptions that are well satisfied in typical transmon operating conditions. First, we neglect the stochastic noise current $I_F(t)$ mentioned above: in the present work we focus on the coherent dynamics of the qubit, and moreover, at dilution refrigerator temperatures ($T \sim$ 10–20 mK) where $k_B T \ll \hbar\omega_q$, thermal and shot noise are exponentially suppressed and have negligible impact on the phenomena of interest. Second, the model assumes that the quasiparticle relaxation time [1] is much faster than the junction dynamics ($\tau_{qp} \ll 1/\omega_p$), so that the normal resistance R_N provides instantaneous dissipation. Third, the junction operates far below the superconducting gap frequency ($f_q \sim 5$ GHz $\ll f_\Delta = 2\Delta/h \sim 100$ GHz for aluminum), ensuring that the simple sinusoidal current-phase relation (4.14) remains valid. Finally, we assume that the geometric self-inductance of the junction and leads is negligible compared to the Josephson inductance L_J, so that the phase dynamics are dominated by the junction itself. Under these conditions, the RCSJ model provides an accurate classical description of the junction, which we now quantize to obtain the transmon Hamiltonian.

[1] The quasiparticle relaxation time is the average time it takes for a quasiparticle to lose its energy through interactions with the lattice and other quasiparticles.

It is often convenient to rewrite the RCSJ equation (4.34) in normalized form. Dividing by the critical current I_c and expressing all currents in terms of the phase ϕ via the Josephson relations, we obtain

$$i(\tau) = \sin\phi + \frac{\Phi_0}{2\pi I_c R_N}\frac{\mathrm{d}\phi}{\mathrm{d}t} + \frac{C_J\Phi_0}{2\pi I_c}\frac{\mathrm{d}^2\phi}{\mathrm{d}t^2} \tag{4.35}$$

where $i = I/I_c$ is the normalized drive current. Before proceeding to full normalization, it is instructive identifying the dimensionless parameter that governs the junction's dynamical regime. The competition between capacitive energy storage and resistive dissipation in a Josephson junction is captured by the *Stewart-McCumber parameter* [63], [64]:

$$\beta_c = \frac{2\pi I_c R_N^2 C_J}{\Phi_0} \tag{4.36}$$

which compares the energy stored in the junction capacitance during one Josephson oscillation period to the energy dissipated through the normal resistance over the same interval. Physically, β_c determines whether the junction behaves as an overdamped or underdamped nonlinear oscillator:

- **Overdamped regime ($\beta_c < 1$):** Dissipation dominates over inertia. The phase ϕ relaxes monotonically to equilibrium without oscillations, and the current–voltage (I-V) characteristic is single-valued with no hysteresis. The capacitive term in Eq. (4.35) becomes negligible, reducing the dynamics to a first-order equation
$$\frac{\Phi_0}{2\pi I_c R_N}\frac{\mathrm{d}\phi}{\mathrm{d}t} \approx i(t) - \sin\phi \tag{4.37}$$
characteristic of resistive junctions used in some classical SQUID applications.
- **Underdamped regime ($\beta_c > 1$):** Inertial effects dominate, and the phase can execute sustained oscillations about the potential minima. The I-V characteristic exhibits pronounced **hysteresis**: the forward switching current I_c^+ (from zero-voltage to resistive state) exceeds the retrapping current $I_c^- < I_c^+$ (return to zero-voltage state). This regime supports rich nonlinear phenomena including phase slips, metastable states, and, under strong AC drive, deterministic chaos. Transmon qubits are designed to operate deeply in the underdamped regime, with typical values $\beta_c \sim$ 10-100, to minimize dissipation during quantum coherent evolution while maintaining sufficient anharmonicity for selective qubit control [56].

To make the universal scaling manifest, we introduce the natural frequency scale of small oscillations about $\phi = 0$. Linearizing the Josephson inductance as $L_J = \Phi_0/(2\pi I_c)$ and forming an LC oscillator with C_J, we obtain the **plasma frequency** ω_p:

$$\omega_p = \frac{1}{\sqrt{L_J C_J}} = \sqrt{\frac{2\pi I_c}{\Phi_0 C_J}} \tag{4.38}$$

Defining dimensionless time $\tau = \omega_p t$ and substituting into Eq. (4.35), we arrive at the canonical form

$$\frac{\mathrm{d}^2\phi}{\mathrm{d}\tau^2} + \alpha\frac{\mathrm{d}\phi}{\mathrm{d}\tau} + \sin\phi = i(\tau), \tag{4.39}$$

where the dimensionless *dumping coefficient* is

$$\alpha = \frac{1}{\omega_p R_N C_J} = \frac{1}{\sqrt{\beta_c}} \tag{4.40}$$

This normalized pendulum equation reveals the universal character of Josephson dynamics: all junctions with identical α (or equivalently β_c) and normalized drive $i(\tau)$ follow the same phase trajectory $\phi(\tau)$, independent of their absolute parameter values (I_c, R_N, C_J). The damping coefficient α is the inverse square root of the Stewart-McCumber parameter, providing an alternative parametrization.

4.2.2 DC Josephson Effect

Let address a Josephson junction biased with a constant current $I < I_c$. In this regime the junction remains in the superconducting state, and the solution of the normalized RCSJ equation 4.39 define two set of equilibrium points for the phase ϕ:

$$\begin{aligned} \phi_n^+ &= \arcsin(i) + 2n\pi \quad \text{(stable)} \\ \phi_n^- &= \pi - \arcsin(i) + 2n\pi \quad \text{(unstable)} \end{aligned} \tag{4.41}$$

In order to analyze the stability of these equilibrium points, we can recall the concept of thermodynamic potentials. In classical mechanics, a system in equilibrium minimizes its potential energy. Analogously, in thermodynamics, a system at fixed temperature and pressure minimizes its Gibbs free energy. For the Josephson junction, we recognize that the DC bias current plays a role analogous to an applied force in mechanical systems or an applied field in magnetic systems. The total potential energy that captures the energy landscape experienced by the phase variable ϕ under the influence of an external bias current, can be expressed as a Gibbs-like potential:

$$G = E - Fx \tag{4.42}$$

where E is the internal energy of the system, F is the external force and x is the displacement along the direction of the force. In our case, the internal energy is given by the Josephson potential $U_J(\phi)$, the external force is represented by the bias current I. The conjugate variable should be chosen such that the product $I \cdot \dot{x}$ has units of power, that for a Josephson junction is given by the product of current and voltage. Using the second Josephson relation (Eq. 4.15), we can identify the conjugate variable x as the phase ϕ. Therefore, we can write:

$$x = \int V dt = \frac{\hbar\phi}{2e} + const \tag{4.43}$$

Therefore, the Gibbs-like potential for a current-biased Josephson junction can be expressed as:

$$G(\phi, I) = U_J(\phi) - I\frac{\hbar\phi}{2e} = E_J\left(1 - \cos(\phi) - i\,\phi\right) = U(\phi) \tag{4.44}$$

With this expression, the potential energy landscape for the phase variable ϕ can be visualized as a washbord potential that is tilted by the applied bias current I, as shown in Fig. 4.2.2.

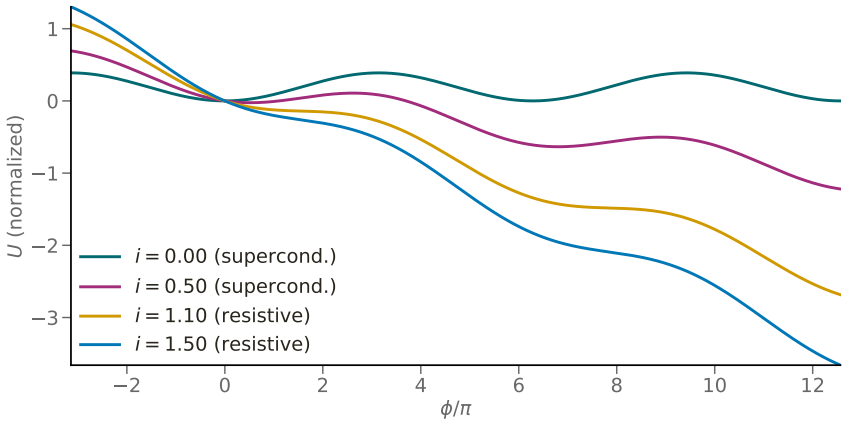


Figure 4.2.2: Tilted washboard potential for various bias currents. $i = 0$: symmetric cosine potential with degenerate minima at $\phi = 2\pi n$. $i = 0.5 < 1$: metastable minima exist; phase particle trapped in local well corresponds to zero-voltage state. $i = 1.0$: critical bias; barrier height vanishes. $i = 1.5 > 1$: no stable minima; phase particle rolls down continuously (running state, $V > 0$).

With this Gibbs-like potential, the equilibrium points correspond to local minima of G, the points that satisfy the condition:

$$\frac{\partial G}{\partial \phi} = 0 \qquad \frac{\partial^2 G}{\partial \phi^2} > 0 \tag{4.45}$$

For subcritical bias ($|I| < I_c$), the potential $U(\phi)$ has local minima at ϕ_n^+ corresponding to stable equilibrium points and local maxima at ϕ_n^- corresponding to unstable equilibrium points. As the bias current approaches the critical current ($|I| \to I_c$), the local minima and maxima merge, and the potential becomes monotonic, leading to a loss of stability and transition to the voltage state.
In particular from the first equilibrium condition it is possible to obtain the DC Josephson relation:

$$\frac{\partial G}{\partial \phi} = E_J(\sin(\phi) - i) = 0 \to I = I_c \sin(\phi_{\text{eq}}) \tag{4.46}$$

At critical bias ($|I| = I_c$), we have $\phi_{\text{eq}} = \pi/2$ and:

$$\cos(\phi_{\text{eq}}) = 0 \quad \Rightarrow \quad \frac{\partial^2 G}{\partial \phi^2} = 0 \tag{4.47}$$

This is a critical point where the potential barrier vanishes, and the system undergoes a transition from the superconducting state to the resistive state.

Let address a small perturbation around a stable equilibrium point ϕ_0:

$$\phi(t) = \phi_0 + \tilde{\phi}(t) \tag{4.48}$$

If the junction capacitance is large enough, in terms of the Stewart-McCumber parameter $\beta_c \gg 1$, phase oscillations, with frequency ω_0 can be observed. To find the oscillation frequency, it is useful to express the Gibbs energy, as sum of kinetic and potential energy:

$$G = K + U = E_J(\frac{1}{2\omega_p^2}\dot{\phi}^2 + 1 - \cos(\phi) - i\phi) \tag{4.49}$$

A small perturbation $\tilde{\phi}$ generates a variation of the Gibbs energy around the equilibrium $G_0 = G(\phi_0)$:

$$\Delta G = G - G_0 = E_J(\frac{1}{2\omega_p^2}\dot{\tilde{\phi}}^2 + \frac{1}{2}\cos(\phi_0)\tilde{\phi}^2) = -\frac{\mu}{2}\dot{\tilde{\phi}}^2 - \frac{k}{2}\tilde{\phi}^2 \tag{4.50}$$

This last expression is very interessing because it is the same of an harmonic oscillator mass-spring system. This means that we can interpret this system as a particle with an effective mass $\mu = E_c/\omega_p^2$ placed in a one-dimensional field with the potential U, or in other words, the mass connected to a spring with an effective spring constant $k = E_c\cos(\phi_0)$, which corresponds to the second derivative of the potential energy at the equilibrium point. So the oscillation frequency is given by:

$$\omega_0 = \sqrt{\frac{k}{\mu}} = \omega_p(1 - i^2)^{1/4} = \sqrt{\frac{2\pi I_c}{\Phi_0 C_J}}(1 - i^2)^{1/4} \tag{4.51}$$

To find the dumping of the oscillation we can linearize the RCSJ equation around the equilibrium point ϕ_0, in absence of fluctuations, and we obtain the following differential equation:

$$\frac{1}{\omega_p^2}\ddot{\tilde{\phi}} + \frac{1}{\omega_c}\dot{\tilde{\phi}} + \cos(\phi_0)\tilde{\phi} = 0 \tag{4.52}$$

The solution of this equation is:

$$\tilde{\phi}(t) = C_1 e^{\lambda_1 t} + C_2 e^{\lambda_2 t} \tag{4.53}$$

$$\lambda_{1,2} = -\frac{1}{2\tau_N} \pm \sqrt{\frac{1}{4\tau_N^2} - \omega_0^2}, \qquad \tau_N = \frac{\omega_c}{\omega_p^2} = R_N C_J \tag{4.54}$$

So, for the initial hypothesis $\beta_c \gg 1$, we have $\omega_0 \gg 1/(4\tau_N^2)$ and the solution is a damped oscillation with frequency ω_0 and damping rate $\gamma = 1/(2\tau_N)$, or a relaxation time $\tau = 1/\gamma = 2\tau_N \gg \omega_0^-2$:

$$\tilde{\phi} = Ae^{-\gamma t}\cos(\omega_0 t + \theta_0) \tag{4.55}$$

This expression shows that the junction can support small-amplitude oscillations around a stable equilibrium point, with a frequency that depends on the bias current. The plasma frequency ω_p sets the scale for these oscillations, and the factor $(1 - i^2)^{1/4}$ indicates that the oscillation frequency decreases as the bias current approaches the critical current.

4.2.3 AC Josephson effect

Instead, consider now a Josephson junction biased with a constant current I that exceeds the critical current I_c. In this regime, the junction is in the resistive state, and following the RCSJ model, the total current can not be carried by the supercurrent alone, in addition the average value of the displacemente current I_D and the fluctuation current I_F are zero. So, some part of the current must be carried by the normal current I_N, and a finite voltage drop appears across the junction. In this case, the solution of the normalized RCSJ equation (4.39) is a running solution, where the phase ϕ increases monotonically in time, this corresponds into a current oscillation with frequency:

$$\omega = \dot{\phi}\frac{2\pi}{\Phi_0}\bar{V} \tag{4.56}$$

This effect is called the AC Josephson effect, the freqeuncy of the oscillation is proportional to the average voltage across the junction. This effect is symmetrical with respect to the sign of the current, substituting $\phi \to -\phi$ in the RCSJ equation (4.39) we obtain the same equation with a negative bias current $-i$.

Instead, if an AC current $I_{\mathrm{AC}} \sin(2\pi f_{\mathrm{AC}} t)$ is superimposed on the DC bias, the Josephson oscillation can phase-lock to the drive or to its harmonics. Whenever $\omega = n\, 2\pi f_{\mathrm{AC}}$ the average voltage is pinned to $\langle V \rangle_n = n\Phi_0 f_{\mathrm{AC}}$, producing constant-voltage plateaus in the I–V characteristic known as Shapiro steps [65]. Their width depends on I_{AC} through Bessel functions $J_n(2\pi I_{\mathrm{AC}} R_N/\Phi_0 f_{\mathrm{AC}})$ in the voltage-biased limit [66].

4.2.4 I-V

The I-V characteristic exhibits two distinct regions. For $|I| < I_c$, the junction remains in the superconducting state with zero voltage across it. In this regime, the phase ϕ is constant in time, and the supercurrent I_S carries the entire bias current. For $|I| > I_c$, the junction enters the resistive state, where a finite voltage develops and the current is carried by a combination of supercurrent and normal current through the shunt resistance.

The transition between these two regions occurs at the critical current I_c, which marks the maximum supercurrent that can flow through the junction without dissipation. In the resistive state, the voltage increases with bias current following the relation $V = R_n\sqrt{I^2 - I_c^2}$ for an ideal junction. The critical voltage (4.27) marks the onset of the resistive state.

Underdamped junctions ($\beta_c > 1$) exhibit hysteresis in the I-V characteristic, as shown in Figure 4.2.3 for a junction with $I_c = 59$ nA, $R_n = 5$ kΩ, $C = 8$ fF, yielding $\beta_c = 35.85$. When increasing the bias current (ascending branch), the junction remains in the zero-voltage superconducting state up to I_c, then abruptly switches to the resistive state at the critical voltage $V_c = 287.39$ μV. However, when decreasing the current (descending branch), the junction returns to the superconducting state only at a lower return current $I_r \approx 0.2I_c$. This hysteresis arises from the energy stored in the junction capacitance and the nonlinear dynamics of the phase evolution. The hysteresis gap $\Delta V = V_c$ increases with the Stewart-McCumber parameter β_c.

Underdamped junctions ($\beta_c > 1$) exhibit hysteresis in the I-V characteristic, as shown in Figure 1.2.3 for a junction with $I_c = 59$ nA, $R_n = 5$ kΩ, $C = 8$ fF, yielding $\beta_c = 35.85$. When increasing the bias current (ascending branch), the junction remains in the zero-voltage superconducting state up to I_c. In this plateau region ($V = 0$ for $I < I_c$), the phase ϕ evolves to a stable equilibrium value that accommodates the applied current through the Josephson relation $I = I_c \sin\phi$, while $\dot{\phi} = 0$ ensures zero voltage across the junction. At $I = I_c$, the static phase solution becomes unstable and the junction switches to the resistive state at the critical voltage $V_c = 287.39$ μV, where the phase begins to rotate in time ($\dot{\phi} \neq 0$), producing a finite time-averaged voltage. However, when decreasing the current (descending branch), the junction returns to the superconducting state only at a lower return current $I_r \approx 0.2I_c$. This hysteresis arises from the energy stored in the junction capacitance and the nonlinear dynamics of the phase evolution. The hysteresis gap $\Delta V = V_c$ increases with the Stewart-McCumber parameter β_c.

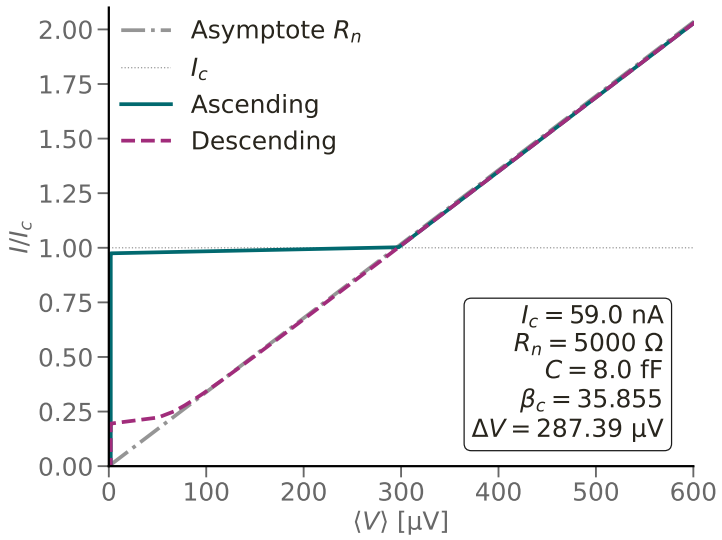


Figure 4.2.3: I-V hysteresis characteristic of a Josephson junction with $I_c = 59$ nA, $R_n = 5$ kΩ, and $C = 8$ fF. The superconducting state ($V = 0$) exists for $|I| < I_c$, while the resistive state ($V > V_c$) occurs for $|I| > I_c$. Hysteresis is observed in underdamped junctions, with return current $I_r < I_c$.

4.3 From Classical Junction Dynamics to the Transmon Qubit

The transmon qubit may be considered as an artificial atom formed by shunting a Josephson junction with a large external capacitance $C_S \gg C_J$. This design choice, introduced by Koch et al. [56], dramatically reduces the circuit's sensitivity to charge noise, the dominant decoherence mechanism in earlier Cooper-pair box qubits, while preserving sufficient anharmonicity to enable selective two-level quantum control. The key insight is to operate in the regime where the Josephson energy E_J greatly exceeds the charging energy E_C (typically $E_J/E_C \sim 50$-100), flattening the energy spectrum and exponentially suppressing charge dispersion [56]. In modern transmon devices, two Josephson junctions are used in a SQUID configuration, which allows for tunability of the effective Josephson energy E_J by applying an external magnetic flux. However, for the objective of this thesis we will consider a single junction transmon.

From the perspective of the RCSJ model developed in Section 4.2.1, the transmon operates in the underdamped regime ($\beta_c \gg 1$, or equivalently $\alpha \ll 1$) with zero applied bias current. Under these conditions, the phase ϕ remains localized near the minimum of a single cosine potential well, and the system's dynamics reduce to those of a weakly anharmonic quantum oscillator. The relevant quantum states $|0\rangle, |1\rangle, |2\rangle, \ldots$ correspond to bound eigenstates within this well, analogous to vibrational levels in a molecular potential. Crucially, microwave control pulses induce transitions between these discrete levels without driving the junction into the dissipative voltage state—a regime that would destroy quantum coherence through avalanche-like phase slips over the barrier.

In this section, we derive the quantum Hamiltonian of the transmon starting from the classical RCSJ framework. While the full quantum dynamics govern coherent qubit manipulation, our primary interest here is the qubit's role in dispersive readout. In that regime, projective measurement collapses the qubit into a definite eigenstate $|n\rangle$, which then acts as a state-dependent nonlinear impedance that shifts the resonance frequency of a coupled readout cavity. This state-dependent shift forms the basis for high-fidelity single-shot qubit measurements.

For simplicity, a single-junction transmon is considered, neglecting the fluctuating current I_F from the resistive channel. This approximation is justified in the high-Q limit where dissipation timescales ($T_1 \approx$ 10-100 μs) far exceed gate operation times ($\approx$ 10-100 ns). Following standard transmon literature, the potential is written as $U(\phi) = -E_J(\cos\phi + i\phi)$. This differs from the form used in Section 4.2.1 ($U(\phi) = E_J(1 - \cos\phi - i\phi)$) by an additive constant. Since only energy differences are observable, both conventions yield identical physical predictions. At zero bias current, this reduces to the standard Josephson potential $U(\phi) = -E_J \cos\phi$.

4.3.1 Classical Hamiltonian and Canonical Quantization

The classical dynamics of a Josephson junction shunted by capacitance C_S can be formulated in Hamiltonian terms using the charge Q and phase ϕ as canonically conjugate variables. The total energy comprises the electrostatic energy stored in the total capacitance $C_\Sigma = C_S + C_J$ and the Josephson potential energy (see equation 4.9):

$$H_{\text{classical}} = \frac{Q^2}{2C_\Sigma} - E_J \cos\phi \tag{4.57}$$

where $E_J = \Phi_0 I_c/(2\pi)$ is the Josephson energy, that can be rewritten as $E_J = \hbar I_c/(2e)$, because of Eq. (4.13). The first term represents the electrostatic (kinetic) energy, analogous to $p^2/(2m)$ in particle mechanics, while the second term is the Josephson potential energy. The charge Q accumulated on the capacitor and the superconducting phase difference ϕ satisfy the classical Poisson bracket

$$\{Q, \phi\}_{\text{Poisson}} = 1 \tag{4.58}$$

confirming their status as canonical conjugates. To see this explicitly, note that the capacitance relation $Q = C_\Sigma V$ combined with the second Josephson relation (Eq. 4.15) yields

$$Q = C_\Sigma \frac{\Phi_0}{2\pi} \frac{\mathrm{d}\phi}{\mathrm{d}t} = C_\Sigma \frac{\Phi_0}{2\pi} \dot{\phi} \tag{4.59}$$

which identifies Q as the canonical momentum conjugate to the generalized coordinate ϕ.

Canonical quantization proceeds by promoting Q and ϕ to Hermitian operators $\hat{Q}$ and $\hat{\phi}$ satisfying the canonical commutation relation, arleady introduced in Eq. (4.3):

$$[\hat{\phi}, \hat{Q}] = i\hbar \tag{4.60}$$

The quantum Hamiltonian is obtained by replacing classical variables with their operator counterparts:

$$\hat{H} = \frac{\hat{Q}^2}{2C_\Sigma} - E_J \cos\hat{\phi} \tag{4.61}$$

To facilitate solution of the eigenvalue problem, we express the charge operator in terms of the Cooper pair number operator $\hat{n}$, which counts the number of excess Cooper pairs on the junction: $\hat{Q} = 2e\hat{n}$. Substituting into the kinetic energy term yields

$$\frac{\hat{Q}^2}{2C_\Sigma} = \frac{(2e)^2\hat{n}^2}{2C_\Sigma} = \frac{2e^2}{C_\Sigma}\hat{n}^2 \tag{4.62}$$

Defining the charging energy as the electrostatic cost of adding one excess Cooper pair,

$$E_C \equiv \frac{e^2}{2C_\Sigma} \tag{4.63}$$

the kinetic term becomes $4E_C\hat{n}^2$, and the quantum Hamiltonian takes the canonical form

$$\hat{H} = 4E_C\hat{n}^2 - E_J \cos\hat{\phi} \tag{4.64}$$

This Hamiltonian describes a competition between two energy scales: the charging energy E_C, which penalizes charge fluctuations and favors localized charge eigenstates, and the Josephson energy E_J, which promotes phase coherence and favors delocalized superpositions. The dimensionless ratio E_J/E_C determines the operational regime. For $E_J/E_C \lesssim 1$ (charge qubit regime), eigenstates are nearly pure charge states $|n\rangle$, leading to strong sensitivity to electrostatic noise. For $E_J/E_C \gtrsim 20$ (transmon regime), eigenstates spread over many charge states, providing exponential suppression of charge noise[56] at the cost of reduced anharmonicity.

4.3.2 Representation in the Charge Basis

The eigenstates of the Cooper pair number operator $\hat{n}|n\rangle = n|n\rangle$ with $n \in \mathbb{Z}$ form a complete orthonormal basis satisfying $\langle n|n'\rangle = \delta_{nn'}$. In this basis, the charging energy term is diagonal, while the Josephson term couples adjacent charge states. To see this explicitly, we exploit the canonical commutation relation between phase and charge. From $[\hat{\phi}, \hat{Q}] = i\hbar$ and $\hat{Q} = 2e\hat{n}$, it follows that

$$[\hat{\phi}, \hat{n}] = \frac{i\hbar}{2e} = i \tag{4.65}$$

where in the last step we have adopted natural units $\hbar/2e = 1$ commonly used in the circuit QED literature[2]. This commutation relation implies that $e^{i\hat{\phi}}$ acts as a raising operator in the charge basis:

$$e^{i\hat{\phi}}|n\rangle = |n+1\rangle \tag{4.66}$$

which can be verified using the Baker-Campbell-Hausdorff formula[3]. Expressing the cosine as $\cos\hat{\phi} = (e^{i\hat{\phi}} + e^{-i\hat{\phi}})/2$, we obtain the matrix elements

$$\langle n|\cos\hat{\phi}|n'\rangle = \frac{1}{2}\left(\delta_{n,n'+1} + \delta_{n,n'-1}\right) \tag{4.67}$$

Thus the Josephson term connects only charge states differing by $\Delta n = \pm 1$, representing single-Cooper-pair tunneling events.

[2]This choice simplifies notation without loss of generality. Physical dimensions can be restored by replacing $\hat{\phi} \to (2e/\hbar)\hat{\phi}$ and $\hat{n} \to \hat{n}$ in final expressions.

[3]Expanding $e^{i\hat{\phi}}\hat{n}e^{-i\hat{\phi}} = \hat{n} + [\hat{n}, i\hat{\phi}] + \frac{1}{2!}[[\hat{n}, i\hat{\phi}], i\hat{\phi}] + \cdots = \hat{n} + 1$ shows that conjugation by $e^{i\hat{\phi}}$ shifts the eigenvalue by one unit.

The complete Hamiltonian matrix in the truncated charge basis $n \in [-n_{\max}, \ldots, n_{\max}]$ is

$$H_{nn'} = 4E_C n^2 \delta_{nn'} - \frac{E_J}{2}\left(\delta_{n,n'+1} + \delta_{n,n'-1}\right) \tag{4.68}$$

yielding a symmetric tridiagonal structure with diagonal elements $H_{nn} = 4E_C n^2$ (charging energy) and off-diagonal couplings $H_{n,n\pm1} = -E_J/2$ (Josephson tunneling). For example, with $n_{\max} = 2$ the matrix reads

$$H = \begin{pmatrix} 16E_C & -\frac{E_J}{2} & 0 & 0 & 0 \\ -\frac{E_J}{2} & 4E_C & -\frac{E_J}{2} & 0 & 0 \\ 0 & -\frac{E_J}{2} & 0 & -\frac{E_J}{2} & 0 \\ 0 & 0 & -\frac{E_J}{2} & 4E_C & -\frac{E_J}{2} \\ 0 & 0 & 0 & -\frac{E_J}{2} & 16E_C \end{pmatrix}. \tag{4.69}$$

The tridiagonal form enables efficient numerical diagonalization via specialized algorithms (e.g., LAPACK's `dsteqr`) with computational cost scaling as $\mathcal{O}(n_{\max}^2)$ rather than $\mathcal{O}(n_{\max}^3)$ for dense matrices. For typical transmon parameters ($E_J/E_C \sim 50$), convergence to spectroscopic precision ($\lesssim 10^{-4}$ relative error) requires $n_{\max} \sim$ 20-30.

4.3.3 Energy Spectrum and Anharmonicity

The transmon operates in the regime $E_J/E_C \gtrsim 20$, where eigenstates become highly delocalized in the charge basis but localized in phase near $\phi \approx 0$. This permits an analytical approximation by expanding the cosine potential to quartic order:

$$-E_J \cos\hat{\phi} \approx -E_J + \frac{E_J}{2}\hat{\phi}^2 - \frac{E_J}{24}\hat{\phi}^4 \tag{4.70}$$

Dropping the constant offset $-E_J$, the transmon Hamiltonian (4.64) becomes:

$$\hat{H}_{\text{trans}} \approx 4E_C\hat{n}^2 + \frac{E_J}{2}\hat{\phi}^2 - \frac{E_J}{24}\hat{\phi}^4 \tag{4.71}$$

We treat this as a harmonic oscillator with quartic perturbation:

$$\hat{H}_{\text{trans}} = \hat{H}_0 + \hat{H}_{\text{anh}} \tag{4.72}$$

where

$$\hat{H}_0 = 4E_C\hat{n}^2 + \frac{E_J}{2}\hat{\phi}^2 \qquad \hat{H}_{\text{anh}} = -\frac{E_J}{24}\hat{\phi}^4 \tag{4.73}$$

The unperturbed Hamiltonian $\hat{H}_0$ is a quantum harmonic oscillator with effective "spring constant" $k_{\text{eff}} = E_J$ and "mass" $m_{\text{eff}} = C_\Sigma$. To diagonalize $\hat{H}_0$, we introduce ladder operators via:

$$\hat{\phi} = \phi_{\text{zpf}} \left(\hat{a} + \hat{a}^\dagger \right) \tag{4.74}$$

$$\hat{n} = i n_{\text{zpf}} \left(\hat{a}^\dagger - \hat{a} \right) \tag{4.75}$$

where the zero-point fluctuations are defined by:

$$\phi_{\text{zpf}} = \left(\frac{2E_C}{E_J} \right)^{1/4} \qquad n_{\text{zpf}} = \left(\frac{E_J}{32E_C} \right)^{1/4} \tag{4.76}$$

These satisfy the commutation relation $[\hat{\phi}, \hat{n}] = i$ (equivalent to $[\hat{a}, \hat{a}^\dagger] = 1$). Substituting (4.74)-(4.75) into (4.73) and simplifying yields:

$$\hat{H}_0 = \hbar \omega_{\text{osc}} \left(\hat{a}^\dagger \hat{a} + \tfrac{1}{2} \right) \qquad \omega_{\text{osc}} = \sqrt{\frac{8E_J E_C}{\hbar^2}} \tag{4.77}$$

where the prefactor $\sqrt{8E_J E_C}$ is the geometric mean of charging and Josephson energies, characteristic of the LC-oscillator analogy ($\omega = 1/\sqrt{LC}$ with $C \approx C_\Sigma$, $L \approx \Phi_0^2/(4\pi^2 E_J)$). The eigenstates $|n\rangle$ of $\hat{H}_0$ satisfy $\hat{a}^\dagger \hat{a}|n\rangle = n|n\rangle$ with energies:

$$E_n^{(0)} = \hbar \omega_{\text{osc}} \left(n + \tfrac{1}{2} \right) \tag{4.78}$$

The quartic term $\hat{H}_{\text{anh}} = -\frac{E_J}{24} \hat{\phi}^4$ introduces anharmonicity. Using (4.74), $\hat{\phi}^4$ is expressed in ladder operators as:

$$\begin{aligned} \hat{\phi}^4 &= \phi_{\text{zpf}}^4 \left(\hat{a} + \hat{a}^\dagger \right)^4 \\ &= \phi_{\text{zpf}}^4 \Big[\hat{a}^4 + 4\hat{a}^3 \hat{a}^\dagger + 6\hat{a}^2 (\hat{a}^\dagger)^2 + 4\hat{a} (\hat{a}^\dagger)^3 + (\hat{a}^\dagger)^4 \\ &\quad + (\text{normal-ordered terms with } \hat{a}^\dagger \hat{a}) \Big] \end{aligned} \tag{4.79}$$

Using the commutator $[\hat{a}, \hat{a}^\dagger] = 1$ to normal-order products (e.g., $\hat{a}^2 (\hat{a}^\dagger)^2 = (\hat{a}^\dagger)^2 \hat{a}^2 + 2\hat{a}^\dagger \hat{a} + 1$), the diagonal part (terms proportional to $(\hat{a}^\dagger \hat{a})^k$) yields the first-order energy correction:

$$E_n^{(1)} = \langle n | \hat{H}_{\text{anh}} | n \rangle = -\frac{E_J}{24} \phi_{\text{zpf}}^4 \langle n | (\hat{a} + \hat{a}^\dagger)^4 | n \rangle \tag{4.80}$$

The only nonzero contributions from $(\hat{a}+\hat{a}^\dagger)^4$ acting on $|n\rangle$ come from terms that return $|n\rangle$. Evaluating the binomial expansion:

$$\begin{aligned}\langle n|(\hat{a}+\hat{a}^\dagger)^4|n\rangle &= \langle n|\hat{a}\hat{a}^\dagger\hat{a}^\dagger\hat{a}^\dagger + 4\hat{a}\hat{a}^\dagger\hat{a}\hat{a}^\dagger + \hat{a}^\dagger\hat{a}\hat{a}\hat{a}^\dagger + \cdots|n\rangle \\ &= 6(2n^2+2n+1)\end{aligned} \tag{4.81}$$

where we used $\hat{a}|n\rangle = \sqrt{n}|n-1\rangle$, $\hat{a}^\dagger|n\rangle = \sqrt{n+1}|n+1\rangle$, and normal-ordering relations. Substituting $\phi_{\text{zpf}}^4 = (2E_C/E_J)$ from (4.76):

$$E_n^{(1)} = -\frac{E_J}{24}\cdot\frac{2E_C}{E_J}\cdot 6(2n^2+2n+1) = -\frac{E_C}{2}(2n^2+2n+1) \tag{4.82}$$

The total energy to first order is:

$$E_n \approx E_n^{(0)} + E_n^{(1)} = \hbar\omega_{\text{osc}}\left(n+\tfrac{1}{2}\right) - \frac{E_C}{2}(2n^2+2n+1) \tag{4.83}$$

The $|0\rangle \to |1\rangle$ transition frequency is:

$$\begin{aligned}\omega_{01} &= \frac{E_1-E_0}{\hbar} = \omega_{\text{osc}} - \frac{E_C}{2\hbar}\left[(2\cdot 1^2+2\cdot 1+1)-(2\cdot 0^2+2\cdot 0+1)\right] \\ &= \omega_{\text{osc}} - \frac{E_C}{2\hbar}(5-1) = \omega_{\text{osc}} - \frac{2E_C}{\hbar}\end{aligned} \tag{4.84}$$

Expressing $\omega_{\text{osc}} = \sqrt{8E_JE_C}/\hbar$:

$$\omega_{01}/2\pi = \frac{1}{2\pi\hbar}\left(\sqrt{8E_JE_C} - 2E_C\right) \tag{4.85}$$

Similarly, the $|1\rangle \to |2\rangle$ transition frequency is:

$$\omega_{12} = \frac{E_2-E_1}{\hbar} = \omega_{\text{osc}} - \frac{E_C}{2\hbar}\left[(2\cdot 4+4+1)-(5)\right] = \omega_{\text{osc}} - \frac{4E_C}{\hbar} \tag{4.86}$$

The anharmonicity, defined as the detuning between consecutive transitions[4],

$$\alpha \equiv \omega_{12}-\omega_{01} = \left(\omega_{\text{osc}} - \frac{4E_C}{\hbar}\right) - \left(\omega_{\text{osc}} - \frac{2E_C}{\hbar}\right) = -\frac{2E_C}{\hbar} \tag{4.87}$$

is negative, indicating level compression. For typical parameters ($E_C/h \sim 200$ MHz, $f_{01} \sim 5$ GHz), the anharmonicity $|\alpha|/(2\pi) \sim 400$ MHz represents $\sim 8\%$ of the qubit frequency. This magnitude is crucial: large enough to enable selective addressing of the $|0\rangle \leftrightarrow |1\rangle$ transition with microwave pulses of bandwidth $\sim$ 20-50 MHz without exciting $|1\rangle \leftrightarrow |2\rangle$, yet small enough to maintain gate fidelities

[4]The discrepancy between $\alpha = -2E_C/\hbar$ (first-order perturbation) and the commonly cited $\alpha \approx -E_C/\hbar$ [56] arises from higher-order corrections in E_C/E_J. The latter includes second-order perturbation theory contributions from off-diagonal elements of $\hat{H}_{\text{anh}}$, which partially cancel the $2E_C$ term. For $E_J/E_C \gtrsim 50$ (typical transmons), the correction factor approaches unity, yielding $\alpha \to -E_C/\hbar$.

above 99.9% through calibrated pulse shaping that accounts for higher-level leakage.

|| The eigenvalue problem:

$$\hat{H}|\psi_i\rangle = E_i|\psi_i\rangle \tag{4.88}$$

is solved numerically by diagonalizing the Hamiltonian matrix in the truncated charge basis. The resulting discrete spectrum $\{E_0, E_1, E_2, \ldots\}$ with $E_0 < E_1 < E_2 < \cdots$ provides the complete energy level structure of the device. Each eigenstate can be expressed as a superposition over the charge basis:

$$|\psi_i\rangle = \sum_{n=-n_{\max}}^{n_{\max}} c_{i,n}|n\rangle \tag{4.89}$$

where the expansion coefficients $\{c_{i,n}\}$ form the eigenvectors of the Hamiltonian matrix. ||
Figure 4.3.1 illustrates the potential energy landscape and the first four eigenstates of a transmon with $E_J/E_C = 33.3$. The cosine potential $U(\phi) = -E_J \cos\phi$ is shown as a solid curve, with the horizontal dashed lines indicating the calculated energy eigenvalues E_0, E_1, E_2, E_3.

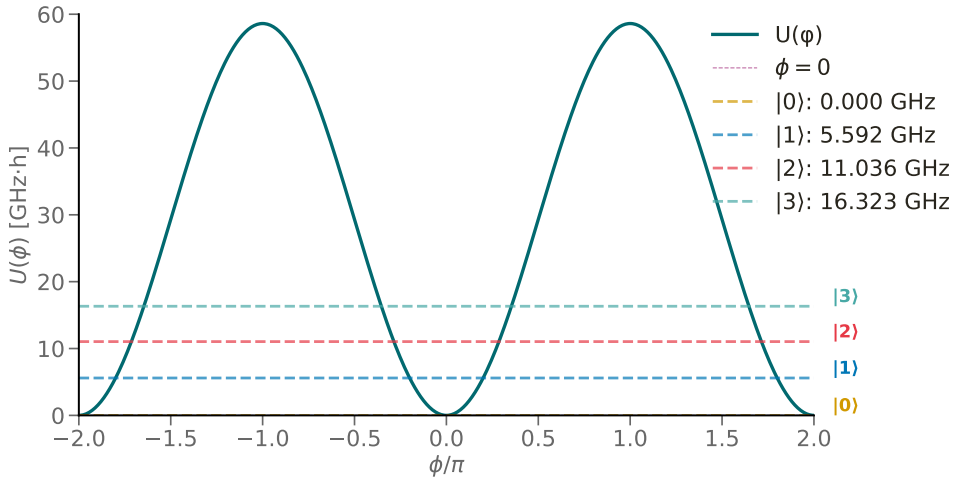


Figure 4.3.1: Energy spectrum of the transmon. First four energy levels E_i (dashed lines) compared to potential energy levels (solid lines).

4.3.4 Wavefunctions in the Phase Representation

While the charge basis facilitates numerical diagonalization, the phase representation provides physical insight. The transformation $\langle\phi|n\rangle = e^{in\phi}/\sqrt{2\pi}$ (discrete Fourier transform) projects eigenstates onto the phase continuum:

$$\psi_i(\phi) = \langle\phi|\psi_i\rangle = \frac{1}{\sqrt{2\pi}} \sum_{n=-n_{\max}}^{n_{\max}} c_{i,n} e^{in\phi} \tag{4.90}$$

where $c_{i,n}$ are the eigenvector components from diagonalization. In the transmon regime, wavefunctions localize near $\phi = 0$ with characteristic width

$$\sigma_\phi = \left(\frac{2E_C}{E_J}\right)^{1/4} \tag{4.91}$$

For $E_J/E_C \sim 50$, this gives $\sigma_\phi \sim 0.4$ rad ($\sim 23°$), justifying the harmonic approximation and ensuring negligible tunneling to adjacent wells ($\phi \pm 2\pi$). The ground state is approximately Gaussian, $\psi_0(\phi) \propto \exp(-\phi^2/2\sigma_\phi^2)$, while excited states develop n nodes with spatial extent $\sim \sqrt{n+1}\,\sigma_\phi$. Even for $n \lesssim 5$, wavefunctions remain confined to $|\phi| < \pi$, preventing phase slips during quantum operations—a critical requirement for gate fidelity.

Figure 4.3.2 displays probability densities $|\psi_i(\phi)|^2$ for the first four eigenstates superimposed on the Josephson potential $U(\phi) = -E_J \cos\phi$. The ground state forms a symmetric peak at $\phi = 0$, while excited states exhibit increasing nodal structure (one, two, and three nodes for $|\psi_1|^2$, $|\psi_2|^2$, $|\psi_3|^2$) yet remain well-localized within a single well. This confinement ensures quantum gates operate within a controlled Hilbert space truncation (typically 3-5 levels), as population transfer to remote levels or phase slips would constitute irreversible coherence loss.

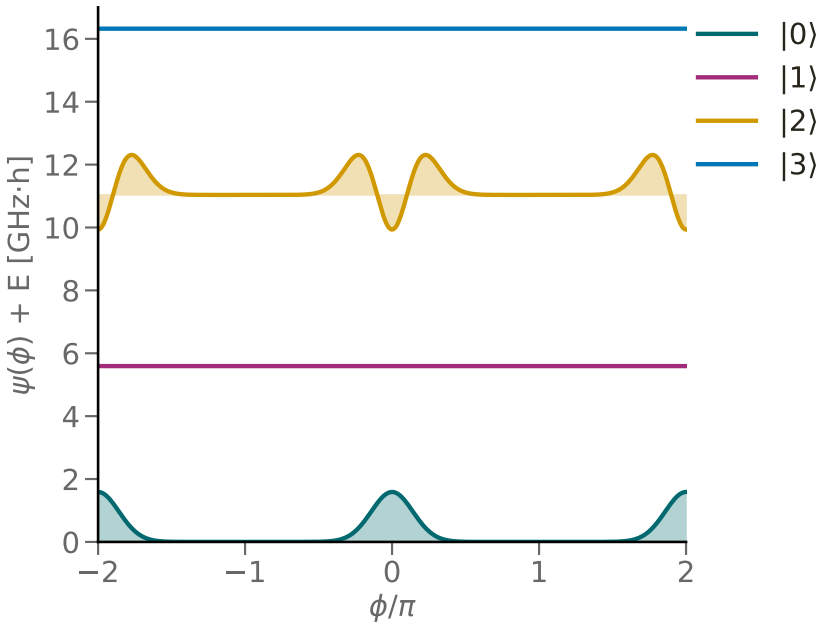


Figure 4.3.2: Eigenstates of the transmon in the phase representation for $E_J/E_C = 33.3$. Probability densities $|\psi_i(\phi)|^2$ for the four lowest eigenstates ($i = 0, 1, 2, 3$), vertically offset and colored according to their energy level. The ground state exhibits Gaussian-like localization with width $\sigma_\phi \approx 0.4$ rad, while excited states develop nodal structure reminiscent of harmonic oscillator wavefunctions. All states remain confined to $|\phi| < \pi$, confirming single-well dynamics. Parameters: $E_J/h = 29.3$ GHz, $E_C/h = 0.88$ GHz.

4.4 Effective Circuit Model for Dispersive Readout

The quantum Hamiltonian formalism developed in the preceding sections provides exact predictions for transmon eigenenergies and transition frequencies, which are essential for designing coherent quantum operations. However, in practical quantum computing architectures, the qubit must interface with classical measurement electronics, typically microwave transmission lines, amplifiers, and mixers—whose behavior is naturally described by circuit theory. This necessitates bridging quantum and classical descriptions in a manner that preserves the essential physics while enabling efficient simulation of large-scale readout networks.

The challenge lies in the fundamentally different nature of quantum and classical dynamics. During coherent gate operations, the transmon exists in superposition states $\alpha|0\rangle + \beta|1\rangle$ requiring full density matrix treatment to capture decoherence and entanglement. However, dispersive readout measurements, wherein a weak microwave probe tone at frequency f_r near but detuned from the qubit frequency f_{01} interrogates the system, operate in a regime where the qubit can be effectively treated as modifying the circuit parameters of coupled resonators without undergoing transitions[56]. In this dispersive limit, characterized by large detuning $\Delta = |f_r - f_{01}| \gg |\alpha|/(2\pi)$ and weak coupling, the quantum state manifests as a shift in the readout resonator's effective frequency: $f_r \to f_r + \chi_n$, where the dispersive shift χ_n depends on the qubit state $|n\rangle$. This frequency shift, typically $\chi \approx 1 - 100$ MHz for $f_r \approx 7$ GHz, is measured via homodyne detection of the reflected or transmitted probe signal.

Our approach, therefore, adopts a hybrid strategy tailored to dispersive readout simulation. We model the transmon junction as a classical nonlinear element (an extended RCSJ) whose effective parameters depend parametrically on the quantum state $n = 0, 1, 2, \ldots$ into which the qubit has been prepared or projected. This is justified because dispersive measurements are designed to extract state information with minimal back-action, effectively freezing the qubit in an eigenstate throughout the measurement duration ($\approx$ 100-1000 ns). The resulting circuit model reproduces the state-dependent frequency shifts and nonlinear response without explicitly solving the Schrödinger equation, enabling time-domain simulation of complete readout chains including impedance matching networks, parametric amplifiers, and signal processing components.

4.4.1 State-Dependent Junction Properties

The quantum state $|n\rangle$ of the transmon modifies the junction's circuit properties through expectation values of the phase operator. The Josephson current-phase relation in state $|n\rangle$ becomes:

$$\langle I_J \rangle_n = I_c \langle \sin \hat{\phi} \rangle_n, \tag{4.92}$$

where $\langle \cdots \rangle_n \equiv \langle n| \cdots |n\rangle$ denotes expectation in eigenstate $|n\rangle$. For small-amplitude perturbations around equilibrium ($\phi = 0$), the relevant quantity is the differential Josephson inductance:

$$L_{J,n} \equiv \left. \frac{\partial \Phi}{\partial I_J} \right|_n = \frac{\Phi_0}{2\pi I_c \langle \cos \hat{\phi} \rangle_n}. \tag{4.93}$$

Expanding the cosine expectation value for small phase fluctuations ($\langle \hat{\phi}^2 \rangle_n \ll 1$, valid in the transmon regime), we obtain:

$$\langle \cos \hat{\phi} \rangle_n = 1 - \frac{1}{2} \langle \hat{\phi}^2 \rangle_n + \mathcal{O}(\langle \hat{\phi}^4 \rangle_n), \tag{4.94}$$

yielding the state-dependent inductance:

$$L_{J,n} \approx \frac{L_J}{1 - \langle \hat{\phi}^2 \rangle_n / 2} \approx L_J \left(1 + \frac{\langle \hat{\phi}^2 \rangle_n}{2} \right), \tag{4.95}$$

where $L_J = \Phi_0/(2\pi I_c)$ is the bare Josephson inductance. Excited states possess larger phase variance—numerically, $\langle \hat{\phi}^2 \rangle_0 \sim \sigma_\phi^2$ for the ground state, while $\langle \hat{\phi}^2 \rangle_1 \approx 2\langle \hat{\phi}^2 \rangle_0$, resulting in increased inductance and correspondingly reduced resonance frequency when the junction is shunted by capacitance C_Σ.

More directly relevant to dispersive readout is the effective transition frequency accessible from state $|n\rangle$. When the qubit occupies state $|n\rangle$, weak perturbations couple predominantly to the $|n\rangle \leftrightarrow |n+1\rangle$ transition, characterized by frequency $f_{n,n+1} = (E_{n+1} - E_n)/h$. For the lowest two states, these are the qubit frequency f_{01} (from ground state) and the anharmonically shifted frequency $f_{12} = f_{01} + \alpha/(2\pi)$ (from first excited state), where $\alpha < 0$ is the anharmonicity. This state-dependent resonance condition is the microscopic origin of dispersive shifts in coupled resonators: a readout cavity with bare frequency f_r experiences an effective load impedance from the junction that depends on the detuning $\Delta_n = f_r - f_{n,n+1}$, shifting f_r by $\chi_n \propto g^2/\Delta_n$, where g is the qubit-cavity coupling rate.

4.4.2 Implementation via Effective Critical Current

To incorporate these quantum effects into circuit simulation, we parametrize the junction's critical current as a state-dependent quantity $I_{c,\text{eff}}(n)$ chosen to reproduce the correct transition frequencies. Treating the transmon as an LC oscillator, the resonance frequency is:

$$f_{\text{LC}} = \frac{1}{2\pi\sqrt{L_J C_\Sigma}} = \frac{1}{2\pi} \sqrt{\frac{2\pi I_c}{\Phi_0 C_\Sigma}}. \tag{4.96}$$

Demanding that f_{LC} match the quantum-mechanical transition frequency $f_{n,n+1}$ when the qubit is in state $|n\rangle$, we solve for the effective critical current:

$$I_{c,\mathrm{eff}}(n) = \frac{2\pi f_{n,n+1}^2 \Phi_0 C_\Sigma}{2\pi} = \frac{\Phi_0 C_\Sigma}{\pi} f_{n,n+1}^2. \tag{4.97}$$

Normalizing by the reference state $n = 0$ to express this as a scaling factor:

$$I_{c,\mathrm{eff}}(n) = I_{c,\mathrm{eff}}(0) \left(\frac{f_{n,n+1}}{f_{01}} \right)^2, \tag{4.98}$$

where $I_{c,\mathrm{eff}}(0)$ is calibrated to reproduce f_{01} from the quantum diagonalization. For instance, with $f_{01} = 5.0$ GHz and $\alpha/(2\pi) = -200$ MHz, state $|1\rangle$ yields $I_{c,\mathrm{eff}}(1) = I_{c,\mathrm{eff}}(0) \times (4.8/5.0)^2 \approx 0.922\, I_{c,\mathrm{eff}}(0)$, reducing the resonance frequency by $\sim 8\%$.

The modified current-phase relation becomes:

$$I_J(\phi; n) = I_{c,\mathrm{eff}}(n) \sin\phi, \tag{4.99}$$

which is implemented in Verilog-A[5] as a voltage-controlled current source. The complete implementation is detailed in Appendix A. The state parameter n is supplied as an external control signal, enabling classical circuit simulations with the qubit in a fixed eigenstate.

4.4.3 Limitations of the Effective Model

This effective circuit model accurately captures dispersive readout physics under several well-defined conditions. First, the probe amplitude must remain in the small-signal regime: $|eV_{\mathrm{probe}}/(hf_{01})| \ll 1$, ensuring $|\phi| \ll 1$ such that $\sin\phi \approx \phi$ and the junction behaves as a linear inductor modulated by state-dependent $I_{c,\mathrm{eff}}$. For typical readout powers (~ -100 to -90 dBm at the resonator, corresponding to $\bar{n} \sim$ 1-10 photons for $Q \sim 10^4$), the phase amplitude at the junction remains $|\phi| \sim 10^{-2}$-10^{-1} rad, well within the linear regime. Second, we assume the qubit occupies a definite eigenstate $|n\rangle$ throughout the measurement window. This is justified in the dispersive regime where the measurement is quantum non-demolition (QND): the detuning $\Delta \gg \kappa, \gamma$ (cavity linewidth, qubit damping rate) suppresses transitions, projecting the qubit into an energy eigenstate that remains stable during photon integration times ($\sim \mu$s).

Coherent superpositions $\alpha|0\rangle + \beta|1\rangle$ are not directly representable in this framework; instead, ensemble-averaged signals (corresponding to $|\alpha|^2$ and $|\beta|^2$ weighted responses) must be computed via repeated simulations.

[5]Verilog-A is a hardware description language for analog/mixed-signal circuits, enabling compact models to be integrated into SPICE-class simulators.

Within these bounds, the model successfully reproduces key experimental observables: the dispersive shift χ extracted from readout resonator spectroscopy, the state-dependent phase rotation in the IQ plane of homodyne signals, and the Kerr nonlinearity (self-Kerr coefficient K) arising from higher-order phase fluctuations. Importantly, it enables circuit co-design of readout chains—optimizing resonator coupling, impedance matching, and amplifier placement—without resorting to full master equation simulations that scale prohibitively for multi-qubit systems.

4.5 Validation and Application of the Effective Junction Model

The quantum-classical hybrid approach developed in Section 4.4 was implemented in Verilog-A and subjected to different simulation scenarios, progressing from fundamental Josephson relations to full transmon circuit response.

4.5.1 Design Rationale and Parameter Selection

The junction parameters were chosen to reproduce the characteristics of small-area Al/AlO_x/Al tunnel junctions employed in fixed-frequency transmon qubits [54], [56]. We selected a critical current $I_c = 59$ nA and normal-state resistance $R_n = 5$ kΩ, yielding a characteristic voltage $V_c = I_c R_n = 295$ μV. From the first Josephson relation, the corresponding Josephson inductance is:

$$L_J = \frac{\Phi_0}{2\pi I_c} = \frac{2.067 \times 10^{-15}\,\text{Wb}}{2\pi \times 59 \times 10^{-9}\,\text{A}} \approx 5.58\,\text{nH} \tag{4.100}$$

The junction capacitance was set to $C_J = 8$ fF, typical of junctions with critical current density $J_c \sim$ 1-10 A/cm^2 and area ~ 0.01 μm^2 [67]. This yields a bare plasma frequency:

$$f_p = \frac{1}{2\pi\sqrt{L_J C_J}} \approx 23.8\,\text{GHz} \tag{4.101}$$

and a Stewart-McCumber parameter [63], [64]:

$$\beta_c = \frac{2\pi I_c R_n^2 C_J}{\Phi_0} \approx 35.9 \tag{4.102}$$

Since $\beta_c \gg 1$, the junction operates in the underdamped regime: the phase dynamics is dominated by the restoring force of the Josephson potential and the inertia of the capacitance, with dissipation from R_n playing only a perturbative role. This results in hysteretic switching behavior in current-biased I-V characteristics [58], [68], a regime avoided in transmon operation through voltage or dispersive probing but essential for understanding the junction's intrinsic nonlinearity.

To realize a transmon qubit, the junction is shunted by a large external capacitance $C_s = 130\,\text{fF}$, giving a total capacitance $C_\Sigma = C_J + C_s = 138\,\text{fF}$. This reduces the charging energy from $E_C^{\text{bare}} = e^2/(2C_J) \sim 1.2\,\text{GHz}$ (unshunted Cooper-pair box) to:

$$E_C = \frac{e^2}{2C_\Sigma} = \frac{(1.602 \times 10^{-19})^2}{2 \times 138 \times 10^{-15}}\,\text{J} \approx h \times 140\,\text{MHz} \tag{4.103}$$

while the Josephson energy remains:

$$E_J = \frac{\Phi_0 I_c}{2\pi} \approx h \times 29.3\,\text{GHz} \tag{4.104}$$

The ratio $E_J/E_C \approx 209$ places the device firmly in the transmon regime ($E_J/E_C \gtrsim 50$ [56]), exponentially suppressing charge noise sensitivity while retaining sufficient anharmonicity for single-qubit addressability. The anharmonicity is $\alpha \approx -E_C \approx -140$ MHz. The linearized resonance frequency of the shunted junction is:

$$f_p^{(\text{T})} = \frac{1}{2\pi\sqrt{L_J C_\Sigma}} = \frac{\sqrt{8E_J E_C}}{h} \approx 5.736\,\text{GHz} \tag{4.105}$$

reduced by a factor $\sqrt{C_\Sigma/C_J} \approx 4.2$ from the bare junction plasma frequency. The quantum-mechanical eigenenergies, computed via numerical diagonalization of the Hamiltonian in Eq. (4.64) (Section 4.3), yield transition frequencies:

$$f_{01} = \frac{E_1 - E_0}{h} \approx 5.596\,\text{GHz}, \tag{4.106}$$

$$f_{12} = \frac{E_2 - E_1}{h} \approx 5.456\,\text{GHz}, \tag{4.107}$$

with anharmonicity $\alpha = 2\pi(f_{12} - f_{01}) \approx -2\pi \times 140$ MHz. These frequencies are slightly red-shifted from $f_p^{(\text{T})}$ due to quantum zero-point fluctuations and higher-order corrections beyond the harmonic approximation [69].

Physically, the shunt capacitance dominates the device footprint. While the Josephson junction occupies a submicron tunnel barrier area ($\lesssim 0.01\ \mu\text{m}^2$), C_s is realized by interdigitated or parallel-plate superconducting electrodes spanning several hundred micrometers, as shown in Figure 4.5.1. This micrograph depicts a representative fixed-frequency transmon: the large cross-shaped capacitor pads form C_s, while the Josephson junction (or SQUID in flux-tunable designs) resides in the narrow neck connecting them. The $\sim 16:1$ ratio C_s/C_J adopted here reflects typical fabrication trade-offs between qubit footprint (affecting cross-talk and resonator coupling) and charging energy requirements.

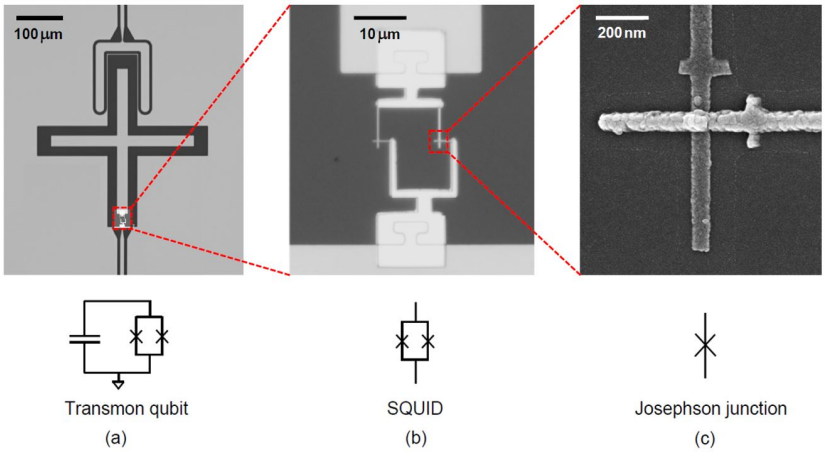


Figure 4.5.1: Optical and scanning electron micrographs of a flux-tunable transmon qubit. (a) The large cross-shaped electrodes form the shunt capacitance $C_s \sim 100$ fF. (b) Magnified view of the SQUID loop containing two Josephson junctions in parallel. (c) Individual junction showing the Al/AlO_x/Al trilayer structure (~ 100 nm scale). Adapted from [70].

4.5.2 DC Current-Phase Relation

Before testing dynamical behavior, we verified the fundamental Josephson current-phase relation in the static limit. Setting all time derivatives to zero in the RCSJ equation (4.39), the total current reduces to:

$$I(V, \phi) = I_c \sin\phi + \frac{V}{R_n}, \tag{4.108}$$

comprising the dissipationless supercurrent $I_c \sin\phi$ and the resistive quasiparticle current V/R_n. This was tested via DC operating-point simulations in Cadence Virtuoso, wherein the phase ϕ was externally fixed at discrete values while sweeping the applied voltage V. Figure 4.5.2 shows the resulting I-V curves.

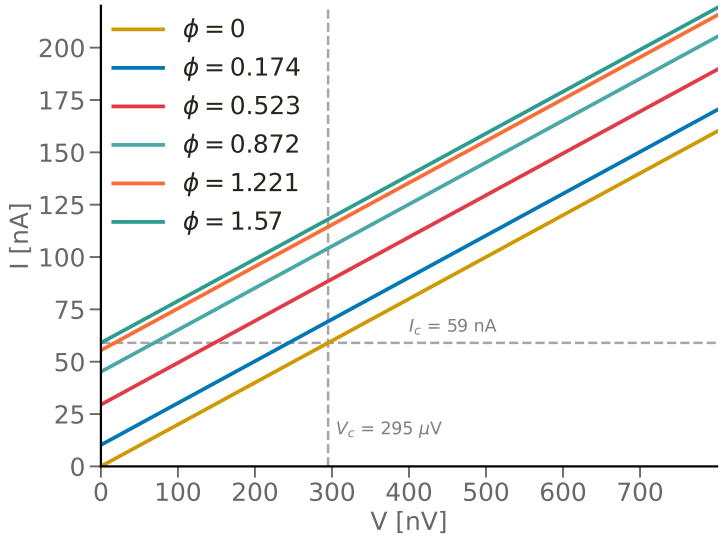


Figure 4.5.2: DC operating-point verification of the current-phase relation Eq. (4.108). Each curve corresponds to a fixed phase ϕ, yielding a straight line with slope $1/R_n$. The maximum supercurrent at $\phi = \pi/2$ confirms $I_c = 59$ nA.

All curves exhibit the predicted linear dependence on V with common slope $\mathrm{d}I/\mathrm{d}V = 1/R_n = 200$ μS, while the zero-voltage intercepts span $\pm I_c \sin\phi$. The curve at $\phi = \pi/2$ reaches the maximum supercurrent $I_c = 59$ nA, confirming correct implementation of the sinusoidal CPR. It is crucial to emphasize that each curve represents a locus of equilibrium states at constant ϕ, not a temporal trajectory. In a real current-biased junction, the phase evolves dynamically according to the second Josephson relation, producing hysteretic switching not visible in this static analysis. The characteristic voltage V_c marks the crossover where resistive dissipation V/R_n equals the maximum supercurrent, relevant for interpreting transient dynamics discussed next.

4.5.3 Voltage-Driven Josephson Oscillations

To verify the second Josephson relation (4.15), transient simulations were performed under constant voltage bias. This drives linear phase evolution $\phi(t) = \phi_0 + 2\pi V t/\Phi_0$, causing the supercurrent to oscillate at the Josephson frequency:

$$f_J = \frac{V}{\Phi_0} \approx 483.6\,\mathrm{GHz/mV}. \tag{4.109}$$

Figure 4.5.3 displays the time evolution of phase, supercurrent $I_J = I_c \sin\phi$, quasiparticle current $I_n = V/R_n$, and total current $I = I_J + I_n$ for three bias voltages spanning the range relevant to transmon operation (10-100 μV).

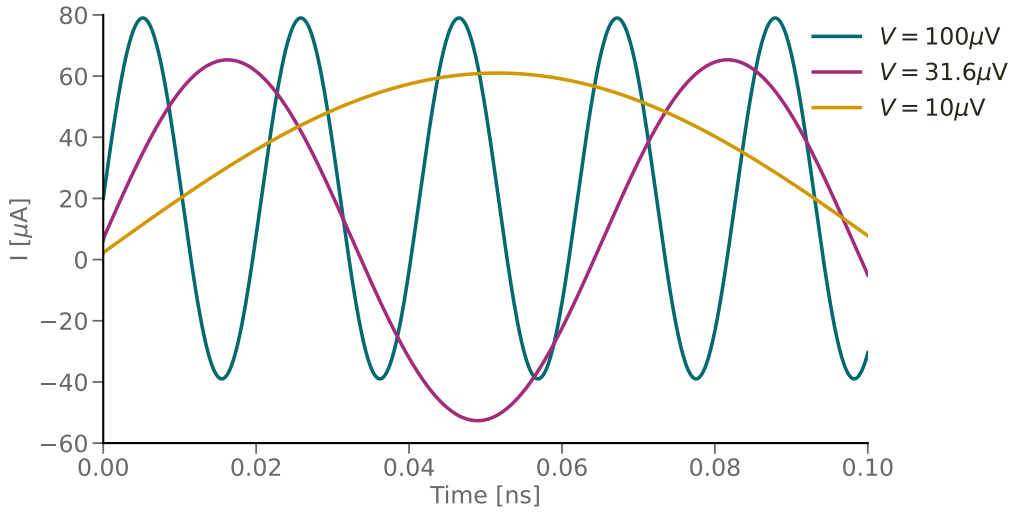


Figure 4.5.3: Transient response under constant voltage bias demonstrating the second Josephson relations: supercurrent oscillates sinusoidally at $f_J = V/\Phi_0$.

The total current waveform combines the high-frequency Josephson oscillation with the DC offset V/R_n, reproducing the behavior observed in Josephson voltage standards [71]. Table 4.1 compares the frequency predicted by Eq. (4.109) with the value extracted from the simulated waveforms. The agreement is better than 0.3% at all bias points, this confirms that the Verilog-A model reproduces

the fundamental voltage-to-frequency conversion of the Josephson effect, which is the same relation underlying the Josephson voltage standard [71].

Table 4.1: Comparison between the analytical Josephson frequency $f_J = V/\Phi_0$ and the frequency extracted from the transient simulations for different voltage biases.

Voltage bias V	Analytical f_J	Simulated f_J
100 μV	48.36 GHz	48.5 GHz
31.6 μV	15.28 GHz	15.31 GHz
10 μV	4.83 GHz	4.84 GHz

4.5.4 Shapiro Step Formation

As a stringent test of the model's nonlinear dynamics, we simulated the formation of Shapiro steps [65]. The junction was driven by a combined DC and AC current bias:

$$I(t) = I_{\mathrm{DC}} + I_{\mathrm{AC}} \sin(2\pi f_{\mathrm{AC}} t), \tag{4.110}$$

with $f_{\mathrm{AC}} = 20$ GHz (near the bare plasma frequency) and $I_{\mathrm{AC}} = 0.5 I_c$. When the internal Josephson oscillation phase-locks to the external drive frequency or its harmonics, the time-averaged voltage becomes quantized:

$$\langle V \rangle_n = n\, \Phi_0 f_{\mathrm{AC}}, \qquad n = 0, \pm 1, \pm 2, \ldots, \tag{4.111}$$

producing constant-voltage plateaus in the I-V characteristic. Figure 4.5.4 shows the simulated time-averaged voltage versus DC bias current.

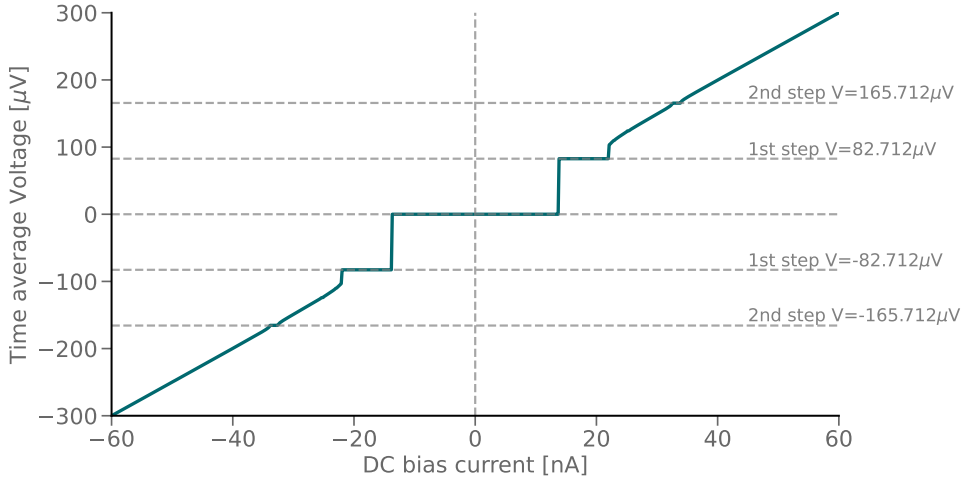


Figure 4.5.4: Simulated Shapiro step structure under AC drive at $f_{\mathrm{AC}} = 40$ GHz with amplitude $I_{\mathrm{AC}} = 0.5 I_c$. The constant-voltage plateaus occur at integer multiples of $\Phi_0 f_{\mathrm{AC}} \approx 82.71$ μV, confirming quantized phase-locking.

The plateaus appear at $\langle V \rangle = n \times 82.71\ \mu\text{V}$ for $n = 0, \pm 1, \pm 2$ precisely matching Eq. (4.111). The zero-voltage step ($n = 0$) corresponds to phase-locked supercurrent with no time-averaged dissipation. Higher-order steps become progressively narrower, with widths scaling as Bessel functions $J_n(I_{\text{AC}}/I_c)$ [66]. While Shapiro steps are not directly relevant to transmon readout (which operates in the small-signal dispersive regime), their successful reproduction demonstrates that the Verilog-A model correctly implements the full nonlinear RCSJ dynamics, including phase-locking under strong periodic driving—essential for validating parametric amplification and mixer models in future work.

4.5.5 State-Dependent Frequency Response

Having validated the classical RCSJ physics, we now demonstrate the quantum state-dependent behavior introduced via the effective critical current $I_{c,\text{eff}}(n)$ (Section 4.4.2). The transmon circuit, junction shunted by $C_s = 130$ fF, was analyzed in small-signal AC mode to extract its resonance frequency as a function of the quantum state parameter n.

According to the design calculations (Eqs. 4.106-4.107), the qubit should exhibit:

- State $|0\rangle$: resonance at $f_{01} = 5.596$ GHz (ground-to-first-excited transition),
- State $|1\rangle$: resonance at $f_{12} = 5.456$ GHz (first-to-second-excited transition),

corresponding to a frequency shift $\Delta f = \alpha/(2\pi) = -140$ MHz upon excitation from $|0\rangle$ to $|1\rangle$. In the circuit model, this shift is realized by adjusting $I_{c,\text{eff}}$ according to Eq. (4.98):

$$I_{c,\text{eff}}(n=1) = I_{c,\text{eff}}(n=0) \times \left(\frac{f_{12}}{f_{01}}\right)^2 \approx 0.951\, I_{c,\text{eff}}(n=0). \tag{4.112}$$

This 5% reduction in effective critical current decreases the Josephson inductance, thereby lowering the LC resonance frequency by the observed $\sim 2.5\%$.

Figure 4.5.5 shows the simulated S_{11} reflection coefficient magnitude for both states. The resonance dip shifts from 5.60 GHz ($n = 0$) to 5.44 GHz ($n = 1$), corresponding to an anharmonicity of approximately -160 MHz. This state-dependent shift is the circuit-level manifestation of anharmonicity and forms the basis for dispersive readout: when the transmon is coupled to a resonator with resonant frequency f_r, the resonator frequency shifts by $\chi \sim g^2/\Delta$, where Δ is the detuning and g is the coupling rate. Measuring this frequency shift (or equivalently, the phase of a reflected probe tone) reveals the qubit state without inducing transitions.

This validates the effective critical current approach (Eq. 4.98) for embedding discrete quantum energy levels into circuit simulation. The simulated anharmonicity $\alpha_{\text{sim}}/(2\pi) \approx -160$ MHz differs from the first-order estimate $-E_C/(2\pi) \approx -140$ MHz by about 15%. This discrepancy reflects higher-order perturbative corrections: the exact anharmonicity includes terms $\alpha \approx -E_C + \mathcal{O}(E_C^2/E_J)$ that are not entirely negligible at $E_J/E_C = 209$. For more accurate predictions, numerical diagonalization of the full transmon Hamiltonian should be employed.

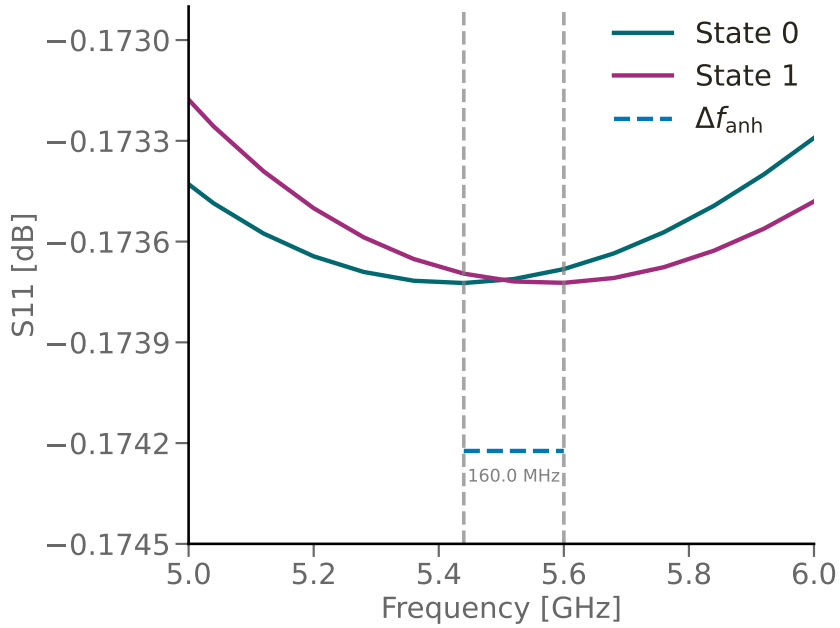


Figure 4.5.5: State-dependent frequency response of the transmon circuit model. S_{11} dB versus probe frequency for quantum state $|0\rangle$ and $|1\rangle$.

The successful reproduction of quantum anharmonicity via classical circuit parameters confirms that the hybrid model bridges quantum theory and circuit simulation, enabling co-design of readout resonators, impedance matching networks, and amplifier chains without resorting to computationally expensive equation solvers.

Chapter 5 Low Noise Amplifier

In radio communication systems, the signal received from the antenna is very weak, typically in the order of microvolts, and must be amplified while keeping at the minimum degradation of the signal-to-noise ratio (SNR). To achieve this, the first stage of amplification is a low-noise amplifier (LNA), that provides gain while adding minimal noise. It is positioned close as possible to the signal source in order to reduce the noise contribution from the transmission line. The importance of the LNA stems directly from the Friis formula for cascaded amplifiers, according to which the total noise of an amplifier chain is dominated by the first stage. The goal is thus an LNA with lowest noise and the highest gain possible.

The noise performance of an LNA is quantified by the **noise figure** (NF): the ratio of input to output signal-to-noise ratio expressed in decibels:

$$\mathrm{NF} = 10\log_{10}\left(\frac{\mathrm{SNR_{in}}}{\mathrm{SNR_{out}}}\right) = 10\log_{10}\left(1 + \frac{T_\mathrm{N}}{T_0}\right) \tag{5.1}$$

where $T_0 = 290$ K is the standard reference temperature and T_N is the amplifier's noise temperature defined as follows:

$$kT_\mathrm{N} = \frac{\int_0^\infty S_\mathrm{LNA}(f)df}{\int_0^\infty G_A(f)df} \tag{5.2}$$

where $S_\mathrm{LNA}(f)$ is the output available noise power spectral density added by the LNA, $G_A(f)$ is the available power gain of the amplifier, and k is the Boltzmann constant. Thus T_N represents the input referred noise temperature introduced by the amplifier.

Apart noise performance, the amplifier must provide avaible **power gain** high enough to ensure that noise from subsequent stages becomes negligible. Typical LNAs achieve gains of $20 - 40$ dB. However, excessive gain presents its own challenges: if too high, the amplifier may saturate or oscillate. Also important is the **bandwidth**, which must accommodate all working frequencies of interest.
Impedance matching to the standard $Z_0 = 50\,\Omega$ system minimizes reflections that would otherwise create standing waves, reduce effective gain, and potentially cause instabilities. The input match is particularly critical: poor matching not only degrades gain but also increases the effective noise temperature seen by the device. The reflection coefficients S_{11} (input) and S_{22} (output) are typically specified to be below -10 dB across the operating band.

Finally, **power consumption** is determined by the operating environment, in particular in cryogenic systems. Dilution refrigerators provide extremely limited cooling power at millikelvin temperatures, typically only 10 μW at 100 mK and 1 W at 4 K [72]. Minimizing power consumption is mandatory, in particular when we consider quantum processors where qubit numbers scale to hundreds or thousands of qubits, each requiring dedicated readout channels and the cumulative power consumption of

many parallel LNAs can exceed the refrigerator's cooling capacity. This motivates ultra-low-power designs, particularly, possible in advanced CMOS technologies where transistor efficiency improves with process scaling.

Semiconductor amplifiers based on CMOS or SiGe BiCMOS technologies offer compelling advantages: they integrate easily into standard fabrication processes, provide broadband operation spanning octaves of bandwidth, and achieve respectable noise temperatures of $T_{\mathrm{N}} \approx 4 - 10\,\mathrm{K}$ when operated at $4\,\mathrm{K}$. At the opposite extreme, superconducting amplifiers such as Josephson parametric amplifiers (JPAs) and traveling wave parametric amplifiers (TWPAs) push noise performance dramatically closer to the quantum limit, achieving $T_{\mathrm{N}} \approx 0.5 - 1\,\mathrm{K}$ [52] through parametric gain mechanisms in nonlinear Josephson junctions or kinetic inductance elements. However, this noise performance involve careful magnetic shielding, precise impedance engineering, delivery of pump tones at cryogenic temperatures. A third approach attempts to incorporate parametric gain elements typically varactor diodes providing voltage-dependent capacitance into conventional CMOS processes[73]. These parametric CMOS amplifiers aim to approach quantum limited noise without requiring superconducting materials, though current implementations achieve intermediate performance $T_{\mathrm{N}} \approx 1 - 10\ \mathrm{K}$ and remain an active area of research.

5.1 LNA Requirements

In Section 3.5, we derived the noise requirements for an LNA in a reflectometry readout system for quantum computing. By examining the state of the art of cryogenic LNAs, we can establish the typical specifications for such amplifiers. Beyond noise performance, the LNA must provide sufficient gain to suppress noise contributions from room-temperature electronics while maintaining adequate linearity. The bandwidth requirement must accommodate both the resonator carrier frequency and the information-bearing sidebands, typically on the order of 1 GHz for single-qubit experiments, expanding to $4{-}10$ GHz for systems employing frequency-division multiplexing to read out multiple qubits simultaneously. Table 5.1 summarizes the key performance metrics for an LNA in a quantum computing reflectometry readout chain.

Table 5.1: Typical requirements for an LNA in quantum computing reflectometry readout.

Parameter	**Specification**
Bandwidth	$1{-}10$ GHz
Gain	$20{-}40$ dB
Noise Figure	< 0.1 dB
Power Consumption	< 10 mW
IIP3	> -20 dBm

5.2 Cascoded based LNA

5.2.1 Circuit Topology and Design Methodology

The amplifier employs a modified Meyer topology with two cascode stages, as illustrated in Figure 5.2.1. Unlike conventional Meyer amplifiers that rely on global feedback between input and output, this design eliminates inter-stage feedback to reduce gain loss while maintaining wideband impedance matching through local shunt-shunt resistive feedback (R_F) at the input stage. The circuit comprises two cascode stages (Q1,Q2 and Q3,Q4) coupled by a source follower (M1), which provides inter-stage buffering and DC level shifting. The input matching network consists of a series inductor (L_B) and an emitter degeneration inductor (L_E), designed to achieve a target input impedance of $50\ \Omega$. The output stage is AC-coupled through a series capacitor (C_{out}) to the subsequent stage or measurementsystem.

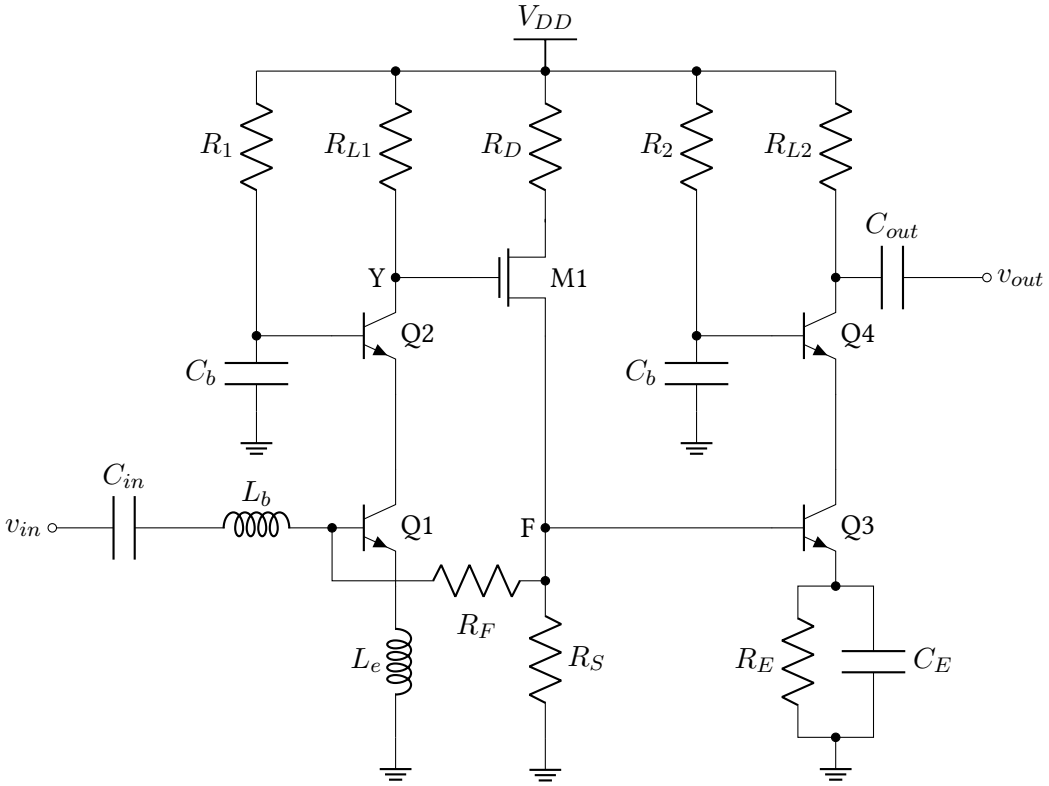


Figure 5.2.1: Schematic of the BiCMOS LNA architecture

5.2.2 DC Biasing and Operating Point

The circuit operates from a single supply voltage $V_{\mathrm{DD}} = 1.8$ V with resistive feedback to establish the quiescent operating points. The total power-consumption constraint imposes a quiescent supply current $I_{\mathrm{DD}} \approx 5.5$ mA.

Source-follower stage (M1). The source voltage of M1, denoted V_{F}, must exceed 0.95V to guarantee proper forward biasing of Q1 and Q3. A target value of $V_{\mathrm{F}} \approx 1$ V is therefore selected. The drain current of M1 can be written as

$$I_{D,\mathrm{M1}} = I_{B,Q1} + I_{B,Q3} + I_{R_{\mathrm{S}}} \tag{5.3}$$

where $I_{R_{\mathrm{S}}}$ denotes the current through the bias resistor R_S that sets the voltage at node F. By imposing $I_{D,\mathrm{M1}} \approx 1.6$ mA and noting that the base currents of Q1 and Q3 are negligible compared with I_{R_S}, the required resistance is

$$R_S = \frac{V_{\mathrm{F}}}{I_{D,\mathrm{M1}}} \approx \frac{1\ \mathrm{V}}{1.6\ \mathrm{mA}} \approx 625\ \Omega \tag{5.4}$$

The MOSFET M1 is sized with $W = 30$ μm and $L = 130$ nm, yielding a transconductance $g_m \approx 20$ mS and a threshold voltage $V_{\mathrm{th}} \approx 0.52$ V. The gate voltage of M1 can therefore be determined as

$$V_G = V_{\mathrm{F}} + V_{GS} = V_{\mathrm{F}} + \frac{I_D}{g_m} + V_{\mathrm{th}} \approx 1.6\ \mathrm{V} \tag{5.5}$$

First cascode stage (Q1–Q2). Transistor Q1 is biased at $V_{\mathrm{BE,Q1}} \approx 0.980$ V with a base current $I_{\mathrm{B,Q1}} \approx 1.7$ μA, corresponding to a collector current $I_{\mathrm{C,Q1}} \approx 2.8$ mA. Because Q2 is in a cascode configuration with Q1, it carries the same current, $I_{\mathrm{C,Q2}} \approx 2.8$ mA. The load resistor R_{L1} is therefore

$$R_{\mathrm{L1}} = \frac{V_{\mathrm{DD}} - V_{\mathrm{C,Q2}}}{I_{\mathrm{C,Q2}}} \approx 71\ \Omega \tag{5.6}$$

and the minimum value of the feedback resistor is set by the DC voltage drop between node F and the base of Q1:

$$R_{F,\mathrm{min}} = \frac{V_{\mathrm{F}} - V_{\mathrm{B,Q1}}}{I_{\mathrm{B,Q1}}} \approx 5.8\ \mathrm{k}\Omega \tag{5.7}$$

Second cascode stage (Q3–Q4). Transistor Q3 is biased at $V_{\mathrm{BE,Q3}} \approx 0.980$ V with a base current $I_{\mathrm{B,Q3}} \approx 1.0$ μA, yielding a collector current $I_{\mathrm{C,Q3}} \approx 1.7$ mA. Consequently, the emitter voltage of Q3 is $V_{E,Q3} = V_{\mathrm{F}} - V_{\mathrm{BE,Q3}} \approx 0.02$ V, from which the degeneration resistor is obtained as

$$R_{\mathrm{E}} = \frac{V_{\mathrm{E,Q3}}}{I_{\mathrm{C,Q3}}} \approx 12\ \Omega \tag{5.8}$$

5.2.3 Small-Signal Analysis

For the small-signal analysis, the amplifier is broken down into two sections: the first cascode stage together with the source follower, and the second cascode stage. Figure 5.2.2 shows the small-signal equivalent circuit in which the feedback loop is opened and the feedback resistor R_{F} appears as a shunt element at both the input and output ports, as prescribed by the shunt-shunt feedback analysis method [74]. The second cascode stage is represented at the source-follower output as an equivalent load resistance R'_{OUT}, corresponding to the input impedance of the second stage. Under the assumption that the bypass capacitances at the bases of Q2 and Q4 act as short circuits at the frequencies of interest, these bases are treated as AC ground. The analysis also accounts for the parasitic base-emitter capacitance $C_{\pi 1}$ of Q1 (omitted in the figure for clarity), which forms part of the input matching network together with the series base inductor L_{B} and the emitter degeneration inductor L_{E}.

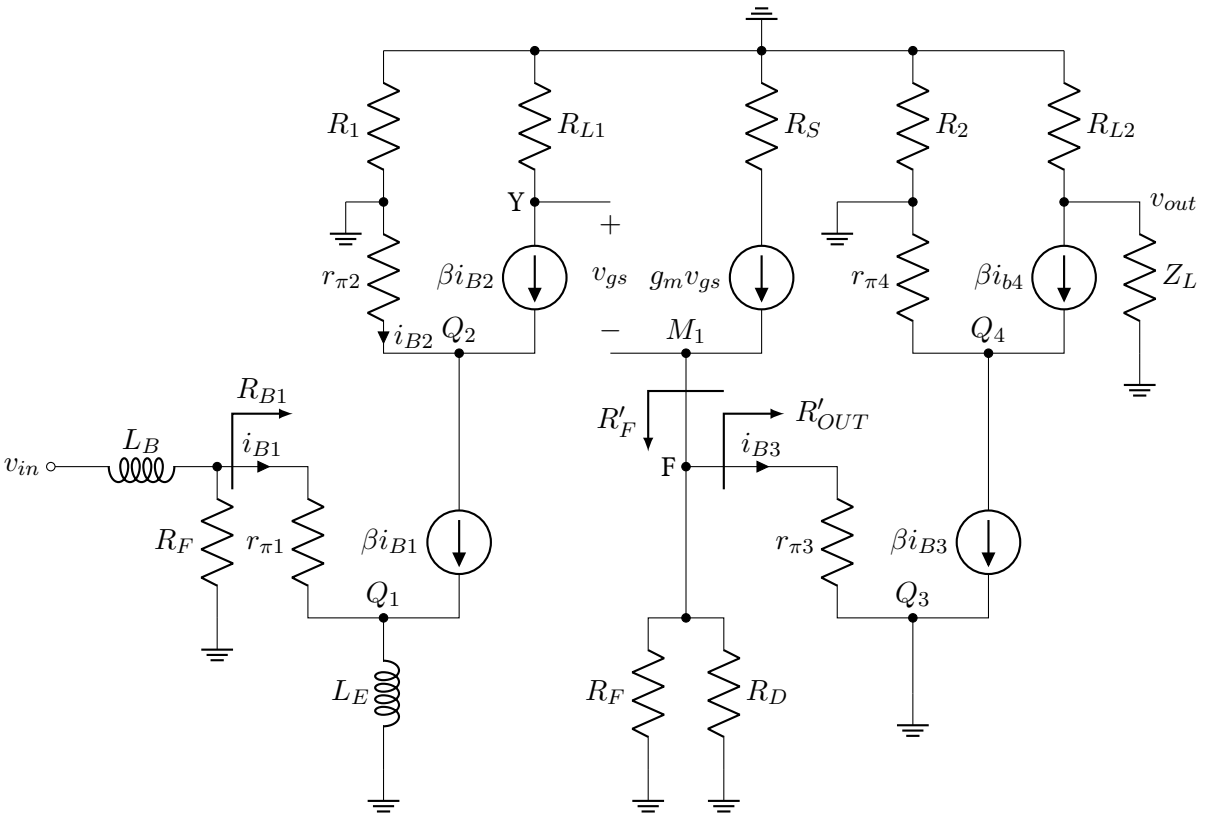


Figure 5.2.2: Small-signal equivalent circuit made open-loop condition. The feedback resistor R_F is duplicated into two equal resistors R_F because of the voltage-current feedback.

The voltage at node F, i.e. at the output of the source follower, is related to the voltage v_y at the output of the first cascode stage (collector of Q2) by the source-follower gain:

$$v_{\mathrm{F}} = \frac{g_m R'_{\mathrm{F}}}{1 + g_m R'_{\mathrm{F}}}\, v_y = k\, v_y \tag{5.9}$$

where $R'_{\mathrm{F}} = R_{\mathrm{F}} \parallel R_{\mathrm{D}} \parallel R'_{\mathrm{OUT}}$ is the total small-signal load impedance seen from the source terminal of M1. The cascode output voltage v_y can be expressed as

$$v_y = -\frac{\beta}{\beta+1}\,\beta\, R_{\mathrm{L1}}\, i_{\mathrm{B,Q1}} \approx -\beta\, R_{\mathrm{L1}}\, i_{\mathrm{B,Q1}} \tag{5.10}$$

Looking into the base of Q1, the input impedance Z_{B1} is given by

$$Z_{\mathrm{B1}} = r_{\pi 1} \parallel \frac{1}{j\omega C_{\pi 1}} + (\beta+1)\, j\omega L_{\mathrm{E}} = \frac{r_{\pi 1}}{1 + j\omega C_{\pi 1}\, r_{\pi 1}} + (\beta+1)\, j\omega L_{\mathrm{E}} \tag{5.11}$$

which corresponds also to the input impedance of the first cascode stage, in the open-loop configuration. The base current of Q1 can be related to the input current i_{IN} through the current-divider ratio:

$$i_{\mathrm{B,Q1}} = i_{\mathrm{IN}}\, \frac{R_{\mathrm{F}} \parallel Z_{\mathrm{B1}}}{Z_{\mathrm{B1}}} = i_{\mathrm{IN}}\, \frac{R_{\mathrm{F}}}{R_{\mathrm{F}} + Z_{\mathrm{B1}}} \tag{5.12}$$

The open-loop transimpedance gain of the first cascode stage with source follower is therefore

$$A_{\mathrm{OL}} = -\frac{v_{\mathrm{F}}}{i_{\mathrm{IN}}} = \frac{R_{\mathrm{F}}\, R_{\mathrm{L1}}\, \beta\, k}{R_{\mathrm{F}} + Z_{\mathrm{B1}}} \tag{5.13}$$

and the closed-loop transimpedance gain, with feedback factor $B = -1/R_{\mathrm{F}}$ for the shunt-shunt topology, is:

$$A_{\mathrm{CL}} = \frac{A_{\mathrm{OL}}}{1 + A_{\mathrm{OL}}\, B} = \frac{-R_{\mathrm{F}}\, R_{\mathrm{L1}}\, \beta\, k}{R_{\mathrm{F}} + Z_{\mathrm{B1}} + R_{\mathrm{L1}}\, \beta\, k} \tag{5.14}$$

The second stage is a cascode amplifier whose small-signal voltage gain is

$$A_2 = -g_{\mathrm{m,Q3}}\, (R_{\mathrm{L2}} \parallel Z_{\mathrm{L}}) \tag{5.15}$$

where $g_{\mathrm{m,Q3}}$ is the transconductance of Q3, R_{L2} is the load resistor, and Z_{L} is the external load impedance. The overall transimpedance gain of the complete amplifier is then

$$A_{\mathrm{IV}} = A_{\mathrm{CL}} \cdot A_2 = \frac{R_{\mathrm{F}}\, R_{\mathrm{L1}}\, \beta\, k\, g_{\mathrm{m,Q3}}\, (R_{\mathrm{L2}} \parallel Z_{\mathrm{L}})}{R_{\mathrm{F}} + Z_{\mathrm{B1}} + R_{\mathrm{L1}}\, \beta\, k} \tag{5.16}$$

The closed-loop input impedance of the amplifier is

$$Z_{\mathrm{in,CL}} = \frac{Z_{\mathrm{in,OL}}}{1 + A_{\mathrm{OL}}\, B} = \frac{R_{\mathrm{F}}\, Z_{\mathrm{B1}}}{R_{\mathrm{L1}}\, \beta\, k} \tag{5.17}$$

and the total input impedance, including the series base inductor, is

$$Z_{\mathrm{in}} = Z_{\mathrm{in,CL}} + j\omega L_{\mathrm{B}} = \frac{R_{\mathrm{F}}\, Z_{\mathrm{B1}}}{R_{\mathrm{L1}}\, \beta\, k} + j\omega L_{\mathrm{B}} \tag{5.18}$$

The overall voltage gain of the amplifier can be written as

$$A_v = \frac{v_{\text{out}}}{v_{\text{in}}} = \frac{A_{\text{IV}}}{Z_{\text{in}}} = \frac{R_{\text{L1}}\, R_{\text{L2}}\, R_{\text{F}}\, \beta\, g_{\text{m,Q3}}\, k}{(R_{\text{F}} + Z_{\text{B1}} + R_{\text{L1}}\, \beta\, k)\left(\dfrac{R_{\text{F}}\, Z_{\text{B1}}}{R_{\text{L1}}\, \beta\, k} + j\omega L_{\text{B}}\right)} \tag{5.19}$$

while the output impedance is

$$Z_{\text{out}} = R_{\text{L2}} \tag{5.20}$$

Finally, the overall current gain is

$$A_i = \frac{v_{\text{out}}}{i_{\text{in}}} = \frac{A_{\text{IV}}}{Z_{\text{out}}} = \frac{R_{\text{F}}\, R_{\text{L1}}\, \beta\, k\, g_{\text{m,Q3}}}{R_{\text{F}} + Z_{\text{B1}} + R_{\text{L1}}\, \beta\, k} \tag{5.21}$$

5.2.4 Noise Analysis

The dominant noise sources in the amplifier are the thermal noise of the resistors and the shot noise of the transistors. In this analysis, we focus exclusively on the transistor noise contributions, as the amplifier is designed to operate under cryogenic conditions where the thermal noise of the resistors is largely reduced. Following the approach in [75], each transistor is modelled by two noise current sources—one at the base and one at the collector—with spectral densities

$$S_{I_B} = 2q\, I_{\text{B}}\, \Delta f \qquad \text{and} \qquad S_{I_C} = 2q\, I_{\text{C}}\, \Delta f, \tag{5.22}$$

where q is the electron charge, I_{B} is the quiescent base current, and I_{C} is the quiescent collector current. In terms of mean-square noise currents these become

$$\overline{I_{\text{BN}}^2} = 2q\, I_{\text{B}}\, \Delta f \qquad \text{and} \qquad \overline{I_{\text{CN}}^2} = 2q\, I_{\text{C}}\, \Delta f. \tag{5.23}$$

This model is valid under the assumptions that the access resistances of the base, collector, and emitter terminals are negligible and that the noise sources are uncorrelated. The resulting noise equivalent circuit of a single BJT is shown in Figure 5.2.3.

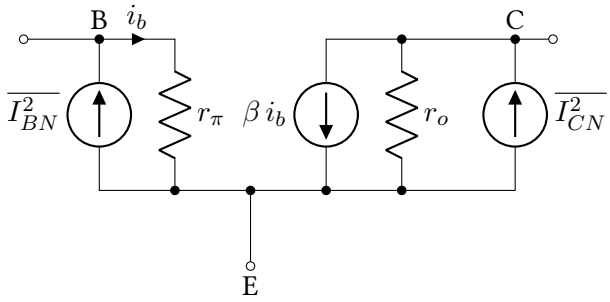


Figure 5.2.3: Noise model of a single BJT, represented by two noise current sources at the base and collector terminals.

Substituting this model into the small-signal equivalent circuit yields the noise circuit shown in Figure **??**, which includes the four noise current sources of the first cascode stage: I_{BN1}, I_{CN1}, I_{BN2}, and I_{CN2}. The noise contribution of the second cascode stage is neglected because it is suppressed by the gain of the first stage.

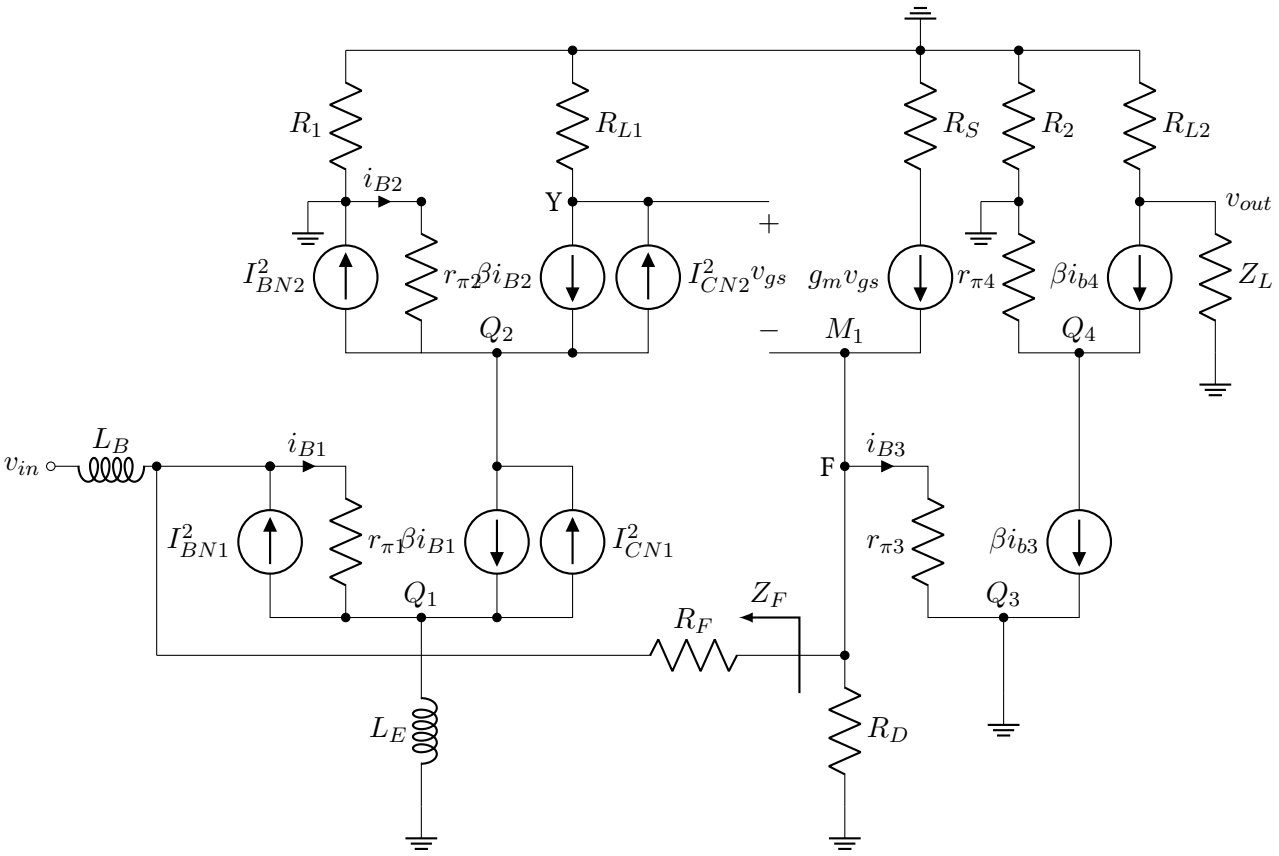


Figure 5.2.4: Small-signal equivalent circuit with the shot noise current sources I^2_{BN1}, I^2_{BN2}, I^2_{CN1}, and I^2_{CN2} added to the base and collector of Q1 and Q2.

Using this model, all noise sources can be referred to the amplifier input, allowing the entire LNA to be represented by an equivalent input-referred noise voltage source S_V and an equivalent input-referred noise current source S_I, as depicted in Figure 5.2.5.

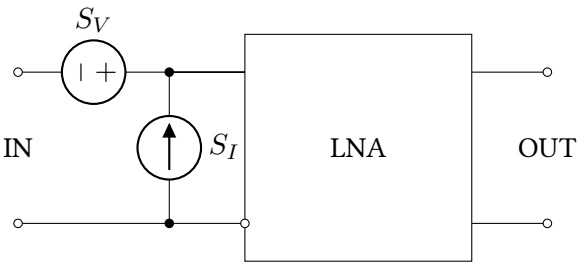


Figure 5.2.5: Equivalent input-referred noise model of the amplifier.

The total input-referred noise is calculated using the superposition principle: each noise source is propagated to the output and subsequently referred back tothe input.

Input-referred noise current

To obtain the input-referred noise current contributions, the input port is left open-circuited.

Source I_{BN1} (base of Q1). Tthe small inductance L_{E} presents negligible impedance at the frequencies of interest. Therefore, for small-signal analysis, the emitter is treated as AC ground, and this noise source does not contribute significantly to the output.[1] Because I_{BN1} is injected directly at the input, its contribution propagates to the output through the full current gain A_i:

$$i_{\mathrm{out,BN1}} = A_i \cdot I_{\mathrm{BN1}} \tag{5.24}$$

yielding the input-referred noise current

$$S'_I = \frac{\overline{i^2_{\mathrm{out,BN1}}}}{A_i^2} = 2q\, I_{\mathrm{B,Q1}}\, \Delta f \tag{5.25}$$

Source I_{CN1} (collector of Q1). For this source, we must trace the signal through the cascode and feedback path.[2] The voltage at the output of the first cascode stage is

$$v_y = (I_{\mathrm{CN1}} - \beta\, i_{\mathrm{b,Q1}})\, R_{\mathrm{L1}}\, \frac{\beta}{\beta+1} \approx (I_{\mathrm{CN1}} - \beta\, i_{\mathrm{b,Q1}})\, R_{\mathrm{L1}} \tag{5.26}$$

For compactness, we define the impedance looking into the feedback loop as

$$Z_{\mathrm{F}} = R_{\mathrm{F}} + \frac{r_{\pi,\mathrm{Q1}}}{1 + j\omega C_{\pi,\mathrm{Q1}}\, r_{\pi,\mathrm{Q1}}} + (\beta+1)\, j\omega L_{\mathrm{E}} \tag{5.27}$$

so that the base current of Q1 is $i_{\mathrm{b,Q1}} = v_{\mathrm{F}}/Z_{\mathrm{F}}$. The effective source-follower load impedance in this configuration is

$$R'_{\mathrm{F}} = R_{\mathrm{D}} \parallel r_{\pi,\mathrm{Q3}} \parallel Z_{\mathrm{F}} \tag{5.28}$$

and the corresponding source-follower gain factor is $k' = g_m R'_{\mathrm{F}}/(1 + g_m R'_{\mathrm{F}})$. So, the voltage at node F can be expressed as:

$$v_{\mathrm{F}} = v_y\, k' = \big(I_{\mathrm{CN1}} - \beta\, v_{\mathrm{F}}/Z_{\mathrm{F}}\big)\, R_{\mathrm{L1}}\, k' \quad \Rightarrow \quad v_{\mathrm{F}} = \frac{I_{\mathrm{CN1}}\, R_{\mathrm{L1}}\, k'}{1 + \beta\, R_{\mathrm{L1}}\, k'/Z_{\mathrm{F}}} \tag{5.29}$$

[1] The emitter inductor L_{E} is chosen small enough that $\omega L_{\mathrm{E}} \ll r_\pi/(\beta+1)$ over the bandwidth of interest.

[2] In the presence of $C_{\pi,\mathrm{Q1}}$, the effective current gain becomes frequency-dependent: $\beta_{\mathrm{eff}}(\omega) = g_m(r_{\pi,\mathrm{Q1}} \parallel 1/(j\omega C_{\pi,\mathrm{Q1}}))$. This modifies the loop gain and noise transfer functions at higher frequencies.

The output noise current is then

$$i_{\text{out,CN1}} = v_{\text{F}}\, g_{\text{m,Q3}} = \frac{I_{\text{CN1}}\, R_{\text{L1}}\, k'\, g_{\text{m,Q3}}}{1 + \beta\, R_{\text{L1}}\, k'/Z_{\text{F}}} \tag{5.30}$$

and the input-referred contribution is

$$S_{\text{ICN1}} = \frac{\overline{i^2_{\text{out,CN1}}}}{A_i^2} = 2q\, I_{\text{C,Q1}}\, \Delta f\, \frac{k'^2\, Z_{\text{F}}^2\, (R_{\text{L1}}\, \beta\, k + Z_{\text{F}})^2}{R_{\text{F}}^2\, \beta^2\, k^2\, (R_{\text{L1}}\, \beta\, k' + Z_{\text{F}})^2} \tag{5.31}$$

Source I_{BN2} (base of Q2). The cascode output voltage due to I_{BN2} is

$$v_y = -\frac{\beta}{\beta + 1}\, \beta\, R_{\text{L1}}\, i_{\text{b,Q2}} \approx -\beta\, R_{\text{L1}}\, i_{\text{b,Q2}} \tag{5.32}$$

from which the source-follower output and the feedback current follow as

$$v_{\text{F}} = v_y\, k' = -\beta\, i_{\text{b,Q2}}\, R_{\text{L1}}\, k' \qquad i_{\text{b,Q1}} = \frac{v_{\text{F}}}{Z_{\text{F}}} = -\frac{\beta\, i_{\text{b,Q2}}\, R_{\text{L1}}\, k'}{Z_{\text{F}}} \tag{5.33}$$

Applying KCL at the internal cascode node (emitter of Q2) yields

$$i_{\text{C,Q1}} = \beta\, i_{\text{b,Q1}} = -\frac{\beta^2\, i_{\text{b,Q2}}\, R_{\text{L1}}\, k'}{Z_{\text{F}}} = I_{\text{BN2}} - (\beta + 1)\, i_{\text{b,Q2}} \tag{5.34}$$

which can be solved for $i_{\text{b,Q2}}$:

$$i_{\text{b,Q2}} = \frac{I_{\text{BN2}}\, Z_{\text{F}}}{(\beta + 1)\, Z_{\text{F}} + \beta^2\, R_{\text{L1}}\, k'} \tag{5.35}$$

The resulting output noise current is

$$i_{\text{out,IBN2}} = v_{\text{F}}\, g_{\text{m,Q3}} = \frac{I_{\text{BN2}}\, Z_{\text{F}}\, \beta\, R_{\text{L1}}\, k'\, g_{\text{m,Q3}}}{(\beta + 1)\, Z_{\text{F}} + \beta^2\, R_{\text{L1}}\, k'} \tag{5.36}$$

and the input-referred noise current is

$$S_{\text{IBN2}} = \frac{\overline{i^2_{\text{out,IBN2}}}}{A_i^2} = 2q\, I_{\text{B,Q2}}\, \Delta f\, \frac{Z_{\text{F}}^2\, k'^2\, (R_{\text{L1}}\, \beta\, k + Z_{\text{F}})^2}{R_{\text{F}}^2\, k^2\, [(\beta + 1)\, Z_{\text{F}} + \beta^2\, R_{\text{L1}}\, k']^2} \tag{5.37}$$

Source I_{CN2} (collector of Q2). Proceeding analogously, the cascode output voltage is

$$v_y = (I_{\text{CN2}} - \beta\, i_{\text{b,Q2}})\, R_{\text{L1}} \tag{5.38}$$

from which

$$v_{\text{F}} = v_y\, k' = (I_{\text{CN2}} - \beta\, i_{\text{b,Q2}})\, R_{\text{L1}}\, k' \qquad i_{\text{b,Q1}} = \frac{v_{\text{F}}}{Z_{\text{F}}} \tag{5.39}$$

using KCL at the cascode node gives

$$i_{\mathrm{C,Q1}} = \beta\, i_{\mathrm{b,Q1}} = \frac{\beta\,(I_{\mathrm{CN2}} - \beta\, i_{\mathrm{b,Q2}})\, R_{\mathrm{L1}}\, k'}{Z_{\mathrm{F}}} = (\beta+1)\, i_{\mathrm{b,Q2}} - I_{\mathrm{CN2}} \tag{5.40}$$

which yields

$$i_{\mathrm{b,Q2}} = \frac{I_{\mathrm{CN2}}\,(Z_{\mathrm{F}} + R_{\mathrm{L1}}\,\beta\, k')}{(\beta+1)\, Z_{\mathrm{F}} + R_{\mathrm{L1}}\,\beta^2\, k'} \tag{5.41}$$

The output noise current becomes

$$\begin{aligned} i_{\mathrm{out,ICN2}} &= v_{\mathrm{F}}\, g_{\mathrm{m,Q3}} = I_{\mathrm{CN2}}\, R_{\mathrm{L1}}\, k'\, g_{\mathrm{m,Q3}} \left(1 - \frac{\beta\,(Z_{\mathrm{F}} + R_{\mathrm{L1}}\,\beta\, k')}{(\beta+1)\, Z_{\mathrm{F}} + R_{\mathrm{L1}}\,\beta^2\, k'}\right) \\ &= I_{\mathrm{CN2}}\, R_{\mathrm{L1}}\, k'\, g_{\mathrm{m,Q3}}\, \frac{\beta\, Z_{\mathrm{F}}}{(\beta+1)\, Z_{\mathrm{F}} + R_{\mathrm{L1}}\,\beta^2\, k'} \end{aligned} \tag{5.42}$$

and the input-referred contribution is

$$S_{\mathrm{ICN2}} = \frac{\overline{i^2_{\mathrm{out,ICN2}}}}{A_i^2} = 2q\, I_{\mathrm{C,Q2}}\, \Delta f\, \frac{k'^2\, Z_{\mathrm{F}}^2\, (Z_{\mathrm{F}} + R_{\mathrm{L1}}\,\beta\, k)^2}{R_{\mathrm{F}}^2\, k^2\, [(\beta+1)\, Z_{\mathrm{F}} + R_{\mathrm{L1}}\,\beta^2\, k']^2} \tag{5.43}$$

Input-referred noise voltage

To derive the input-referred noise voltage contributions, the input port is short-circuited to ground. The impedance looking into the feedback loop under this condition changes to

$$Z_{\mathrm{Fg}} = R_{\mathrm{F}} + \left(r_{\pi,\mathrm{Q1}} \parallel \frac{1}{j\omega C_{\pi,\mathrm{Q1}}} + (\beta+1)\, j\omega L_{\mathrm{E}}\right) \parallel j\omega L_{\mathrm{B}} \tag{5.44}$$

Source I_{BN1} (base of Q1). As previously noted, the small emitter inductance L_{E} provides negligible impedance at the operating frequencies, effectively placing the emitter at AC ground. Consequently, this noise source does not contribute significantly to the output noise voltage.[2] The noise generator I_{BN1} is loaded by the parallel combination of the inductor impedance $j\omega L_{\mathrm{B}}$ and the closed-loop input impedance $Z_{\mathrm{in,CL}}$. The resulting input current is

$$i_{\mathrm{in}} = I_{\mathrm{BN1}}\, \frac{j\omega L_{\mathrm{B}}}{Z_{\mathrm{in,CL}} + j\omega L_{\mathrm{B}}} \tag{5.45}$$

$$v_{\mathrm{out,IBN1}} = i_{\mathrm{in}}\, A_{\mathrm{IV}} \tag{5.46}$$

from which the input-referred noise voltage is

$$S_{\mathrm{VBN1}} = \frac{\overline{v^2_{\mathrm{out,IBN1}}}}{A_v^2} = 2q\, I_{\mathrm{B,Q1}}\, \Delta f\, \omega^2 L_{\mathrm{B}}^2 \tag{5.47}$$

Source I_{CN1} (collector of Q1). With the input shorted, the base current of Q1 is $i_{\mathrm{b,Q1}} = v_{\mathrm{F}}/Z_{\mathrm{Fg}}$, and the collector current is $i_{\mathrm{C,Q1}} = \beta\, i_{\mathrm{b,Q1}} - I_{\mathrm{CN1}}$. The cascode output voltage is

$$v_y = \frac{\beta}{\beta+1}\, i_{\mathrm{C,Q1}}\, R_{\mathrm{L1}} \approx R_{\mathrm{L1}}\,(\beta\, i_{\mathrm{b,Q1}} - I_{\mathrm{CN1}}) \tag{5.48}$$

Because $v_{\mathrm{F}} = v_y\, k'$, one can substitute and solve for v_{F}:

$$v_{\mathrm{F}} = R_{\mathrm{L1}}\, k'\,(\beta\, v_{\mathrm{F}}/Z_{\mathrm{Fg}} - I_{\mathrm{CN1}}) \quad \Rightarrow \quad v_{\mathrm{F}} = \frac{-I_{\mathrm{CN1}}\, R_{\mathrm{L1}}\, k'}{1 - \beta\, R_{\mathrm{L1}}\, k'/Z_{\mathrm{Fg}}} = \frac{I_{\mathrm{CN1}}\, R_{\mathrm{L1}}\, k'}{1 + R_{\mathrm{L1}}\, k'\, \beta/Z_{\mathrm{Fg}}} \tag{5.49}$$

The output noise voltage is therefore

$$v_{\mathrm{out,ICN1}} = v_{\mathrm{F}}\, g_{\mathrm{m,Q3}}\, R_{\mathrm{L2}} = \frac{I_{\mathrm{CN1}}\, R_{\mathrm{L1}}\, k'\, g_{\mathrm{m,Q3}}\, R_{\mathrm{L2}}}{1 + R_{\mathrm{L1}}\, k'\, \beta/Z_{\mathrm{Fg}}} \tag{5.50}$$

yielding the input-referred contribution

$$S_{\mathrm{VCN1}} = \frac{\overline{v_{\mathrm{out,ICN1}}^2}}{A_v^2} = 2q\, I_{\mathrm{C,Q1}}\, \Delta f\, \frac{k'^2\, Z_{\mathrm{Fg}}^2\, (R_{\mathrm{L1}}\,\beta\, k + Z_{\mathrm{F}})^2\, \left(\frac{R_{\mathrm{F}}\, Z_{\mathrm{B1}}}{R_{\mathrm{L1}}\,\beta\, k} + \omega L_{\mathrm{B}}\right)^2}{R_{\mathrm{F}}^2\, \beta^2\, k^2\, (R_{\mathrm{L1}}\,\beta\, k' + Z_{\mathrm{Fg}})^2} \tag{5.51}$$

Source I_{BN2} (base of Q2). The cascode output voltage and the propagated noise voltage are

$$v_y \approx -I_{\mathrm{BN2}}\, R_{\mathrm{L1}} \qquad v_{\mathrm{F}} = v_y\, k' = -I_{\mathrm{BN2}}\, R_{\mathrm{L1}}\, k' \tag{5.52}$$

$$v_{\mathrm{out,IBN2}} = v_{\mathrm{F}}\, g_{\mathrm{m,Q3}}\, R_{\mathrm{L2}} = -I_{\mathrm{BN2}}\, R_{\mathrm{L1}}\, k'\, g_{\mathrm{m,Q3}}\, R_{\mathrm{L2}} \tag{5.53}$$

The input-referred noise voltage is

$$S_{\mathrm{VBN2}} = \frac{\overline{v_{\mathrm{out,IBN2}}^2}}{A_v^2} = 2q\, I_{\mathrm{B,Q2}}\, \Delta f\, \frac{(R_{\mathrm{L1}}\,\beta\, k + Z_{\mathrm{F}})^2\, \left(\frac{R_{\mathrm{F}}\, Z_{\mathrm{B1}}}{R_{\mathrm{L1}}\,\beta\, k} + \omega L_{\mathrm{B}}\right)^2}{R_{\mathrm{F}}^2\, \beta^2\, k^2} \tag{5.54}$$

Source I_{CN2} (collector of Q2). From the cascode output,

$$v_y = -(\beta\, i_{\mathrm{b,Q2}} - I_{\mathrm{CN2}})\, R_{\mathrm{L1}} \qquad v_{\mathrm{F}} = v_y\, k' \qquad i_{\mathrm{b,Q1}} = \frac{v_{\mathrm{F}}}{Z_{\mathrm{Fg}}} \tag{5.55}$$

KCL at the cascode node gives

$$\beta\, i_{\mathrm{b,Q1}} = -\frac{\beta\,(\beta\, i_{\mathrm{b,Q2}} - I_{\mathrm{CN2}})\, R_{\mathrm{L1}}\, k'}{Z_{\mathrm{Fg}}} = (\beta+1)\, i_{\mathrm{b,Q2}} - I_{\mathrm{CN2}} \tag{5.56}$$

from which

$$i_{\mathrm{b,Q2}} = I_{\mathrm{CN2}}\, \frac{Z_{\mathrm{Fg}} + R_{\mathrm{L1}}\,\beta\, k'}{(\beta+1)\, Z_{\mathrm{Fg}} + R_{\mathrm{L1}}\,\beta^2\, k'} \tag{5.57}$$

The output noise voltage is

$$v_{\text{out,ICN2}} = v_{\text{F}}\, g_{\text{m,Q3}}\, R_{\text{L2}} = I_{\text{CN2}}\, R_{\text{L1}}\, R_{\text{L2}}\, g_{\text{m,Q3}}\, k' \left(1 - \frac{Z_{\text{Fg}} + R_{\text{L1}}\,\beta\, k'}{(\beta+1)\, Z_{\text{Fg}} + R_{\text{L1}}\,\beta^2\, k'}\right) \tag{5.58}$$

and the input-referred noise voltage is

$$S_{\text{VCN2}} = \frac{\overline{v^2_{\text{out,ICN2}}}}{A_v^2} = 2q\, I_{\text{C,Q2}}\, \Delta f\, \frac{k'^2\, (Z_{\text{F}} + R_{\text{L1}}\,\beta\, k)^2 \left(\frac{R_{\text{F}}\, Z_{\text{B1}}}{R_{\text{L1}}\,\beta\, k} + \omega L_{\text{B}}\right)^2}{R_{\text{F}}^2\, k^2\, \beta^2} \left(1 - \frac{Z_{\text{Fg}} + R_{\text{L1}}\,\beta\, k'}{(\beta+1)\, Z_{\text{Fg}} + R_{\text{L1}}\,\beta^2\, k'}\right)^2 \tag{5.59}$$

Total input-referred noise and noise figure

The total input-referred noise current and voltage spectral densities are obtained by summing the individual contributions:

$$S_{I,\text{tot}} = S_{\text{IBN1}} + S_{\text{ICN1}} + S_{\text{IBN2}} + S_{\text{ICN2}} \tag{5.60}$$

$$S_{V,\text{tot}} = S_{\text{VBN1}} + S_{\text{VCN1}} + S_{\text{VBN2}} + S_{\text{VCN2}} \tag{5.61}$$

The noise figure of the amplifier is then

$$NF = 1 + \frac{S_{V,\text{tot}}}{4kT\, R_s\, \Delta f} + \frac{S_{I,\text{tot}} \cdot R_s}{4kT\, \Delta f}. \tag{5.62}$$

5.2.5 Component Selection and Input Matching Design

The LNA was implemented in the IHP SG13G2 process, a 130 nm SiGe BiCMOS technology. To minimise noise, it is essential to keep the collector current density as low as practicable. Accordingly, the input transistor Q1 was designed with an emitter area $A_E = 48 \times 0.9 \times 0.07\ \mu\text{m}^2$ and biased at $I_C = 2.8$ mA, yielding a current density $J_C \approx 0.9\ \text{mA}/\mu\text{m}^2$. The cascode device Q2 employs a reduced emitter area $A_E = 36 \times 0.9 \times 0.07\ \mu\text{m}^2$ so as to minimise the base-collector capacitance, which directly loads the intermediate cascode node and limits the high-frequency gain. The NMOS source follower M1 was sized with $W = 30\ \mu$m and $L = 130$ nm.

The second cascode stage was designed with smaller-area transistors operating at a higher current density in order to maximise transconductance. Transistor Q3 has an emitter area of $A_E = 14 \times 0.9 \times 0.07\ \mu\text{m}^2$ and Q4 an emitter area of $A_E = 10 \times 0.9 \times 0.07\ \mu\text{m}^2$.

The input matching network was designed using the analytical expression for Z_{in} derived in Eq. (5.18). At the centre frequency $f_0 = 6.5$ GHz, the matching condition $Z_{\text{in}} = 50\ \Omega$ (real) imposes two simultaneous constraints: reactive cancellation, requiring the imaginary part to vanish, which determines L_B as a function of L_E and the transistor parasitics, and resistive matching, requiring the real part to equal $50\ \Omega$, which is primarily controlled by the feedback network through R_F and the inductive

degeneration via L_E. In order to properly simulate the amplifier, the series resistance of the inductors was included in the design, which was estimated around $0.15\ \Omega$ [76].

Initial component values were computed by substituting the small-signal parameters extracted from the SG13G2 HBT model at the chosen bias point into Eq. (5.18).

These initial estimates were subsequently refined through S-parameter simulations in Cadence Virtuoso, which account for the series resistance of the inductors, the complete transistor models (including base resistance and higher-order parasitics), and layout-induced coupling effects. Table 5.2 compares the analytically computed values with the simulation-optimised values.

Table 5.2: Comparison between analytically computed and simulation-optimised component values.

Component	**Analytical**	**Final (optimised)**	**Deviation**
L_B	700 pH	701 pH	$+0.1$ %
L_E	40 pH	38 pH	-5.0 %
R_{L1}	71 Ω	74 Ω	$+4.2$ %
R_{L2}	–	50 Ω	–
R_F	≥ 5.8 kΩ (DC min.)	2.3 kΩ	see text
C_c	–	3.3 pF	–

The load resistor R_{L1} was increased slightly from 71 Ω to 74 Ω to compensate for parasitic losses and to optimise the gain flatness across the band.

The most significant departure from the hand-calculated values concerns the feedback resistor R_F. The DC analysis of Section 5.2.2 yields a minimum value of $R_{F,\text{min}} \approx 5.8$ kΩ; however, the AC design requires a substantially lower value (2.3 kΩ) to provide sufficiently strong feedback for wideband input matching and gain stability. This reduction in R_F is justified by the fact that the potential at node F is aproximately $0.985\,\text{V}$, smaller than the previously assumed of $1V$, but higher enough to keep the cascode transistors in the active region.

5.2.6 Simulation and Performance Evaluation

The final LNA design achieves a simulated voltage gain of $A_v \approx 35$ dB with an input return loss $S_{11} \leq -11$ dB over the 1–12 GHz frequency range, as shown in Figure 5.2.6. The reverse isolation S_{12} is not plotted because it remains below -60 dB across the entire band.

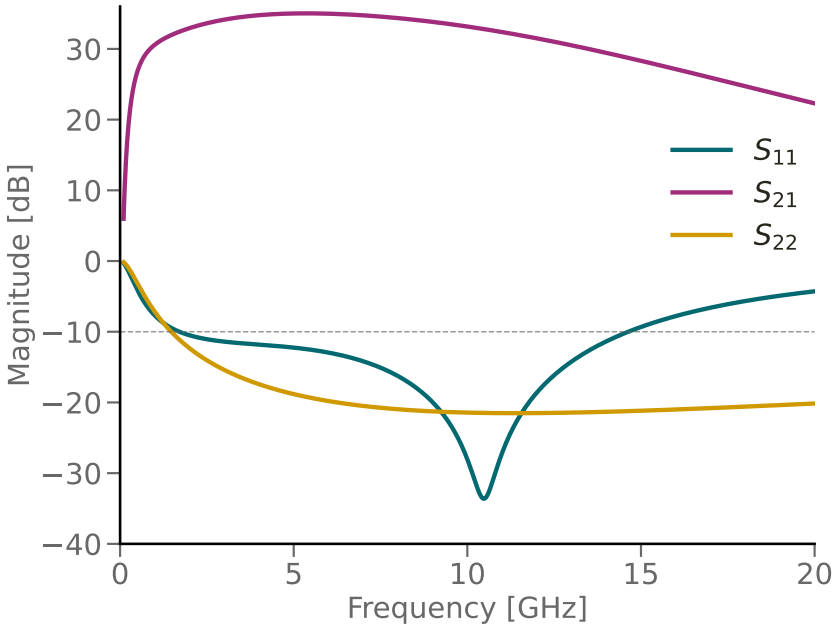
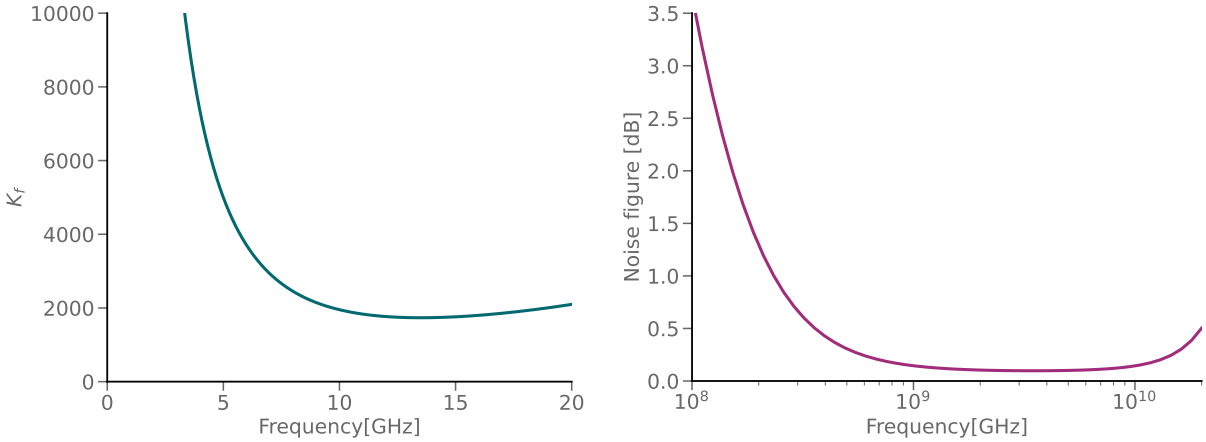


Figure 5.2.6: S-parameters of the cascode LNA.

Given the feedback topology, it is essential to verify unconditional stability. The Rollett stability factor is defined as

$$K = \frac{1 - |S_{11}|^2 - |S_{22}|^2 + |\Delta|^2}{2\,|S_{12}|\,|S_{21}|}, \tag{5.63}$$

where $\Delta = S_{11}\,S_{22} - S_{12}\,S_{21}$. The amplifier is unconditionally stable when $K > 1$ and $|\Delta| < 1$. Figure 5.2.7a confirms that both conditions are satisfied over the entire frequency range, with a minimum value of $K_{\min} \approx 1.7 \times 10^3$ at $f = 13.5$ GHz, indicating robust stability margins.



(a) (b)

Figure 5.2.7: (a)Rollett stability factor (K) of the cascode LNA. (b) Noise figure of the cascode LNA.

The simulated noise figure, shown in Figure 5.2.7b, remains below $NF \leq 0.5$ dB over the frequency range of interest, reaching a minimum of $NF_{\text{min}} \approx 0.09$ dB at $f = 3.3$ GHz, which corresponds to a noise temperature of approximately $T_n \approx 6$ K.

The simulated quiescent current is $I_{DD} \approx 5$ mA, corresponding to a DC power consumption of $P_{DC} \approx 9$ mW at $V_{DD} = 1.8$ V. This is justified by the fact that the feedback resistor R_F dictates also the DC biasing of Q1, so that, chosing a lower value of R_F to improve the input matching, the DC biasing of Q1 is also reduced, leading to a lower quiescent current.

Lasly, in figure 5.2.8 the simulated third-order input intercept point (IIP3) is shown, which is a measure of the linearity of the amplifier. The extracted value is $IIP3 \approx -28$ dBm at $f = 6.5$ GHz, indicating that the amplifier can handle moderate input power levels without significant distortion.

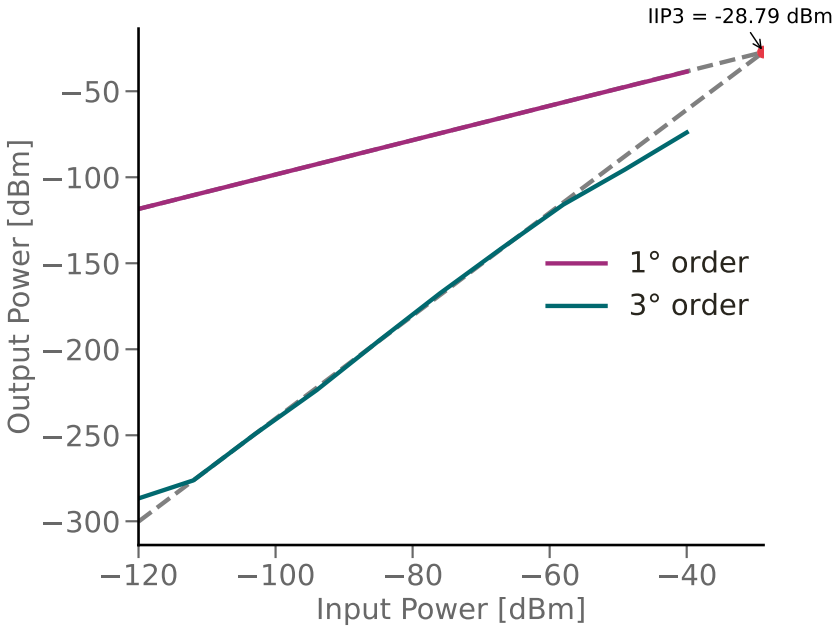


Figure 5.2.8: Simulated third-order input intercept point (IIP3) of the cascode LNA.

A comparison between the key analytical predictions and the simulated performance metrics is summarized in Table 5.3.

Table 5.3: Comparison between analytical predictions and simulated results at $f_C = 6.5$ GHz.

Parameter	**Analytical**	**Simulated**	**Unit**
Voltage gain $\lvert A_v \rvert$	36.73	34.89	dB
Input matching Z_{in}	$79.03 - 14.66j$	$73.66 - 11.4j$	Ω
Noise figure NF	0.11	0.10	dB
DC power consumption P_{DC}	10.98	9	mW

5.3 Common emitter based LNA

5.3.1 Circuit Topology and Design Methodology

The LNA consists of three stages with three BJTs in common emitter configuration, each individually biased. The input matching network is implemented through a degenerated inductor L_E at the emitter of the first transistor Q1, which resonates with the base-emitter capacitance of Q1 and a series inductor L_B at the base of Q1. Then the input matching network is completed with a LC parallel resonator at the input.

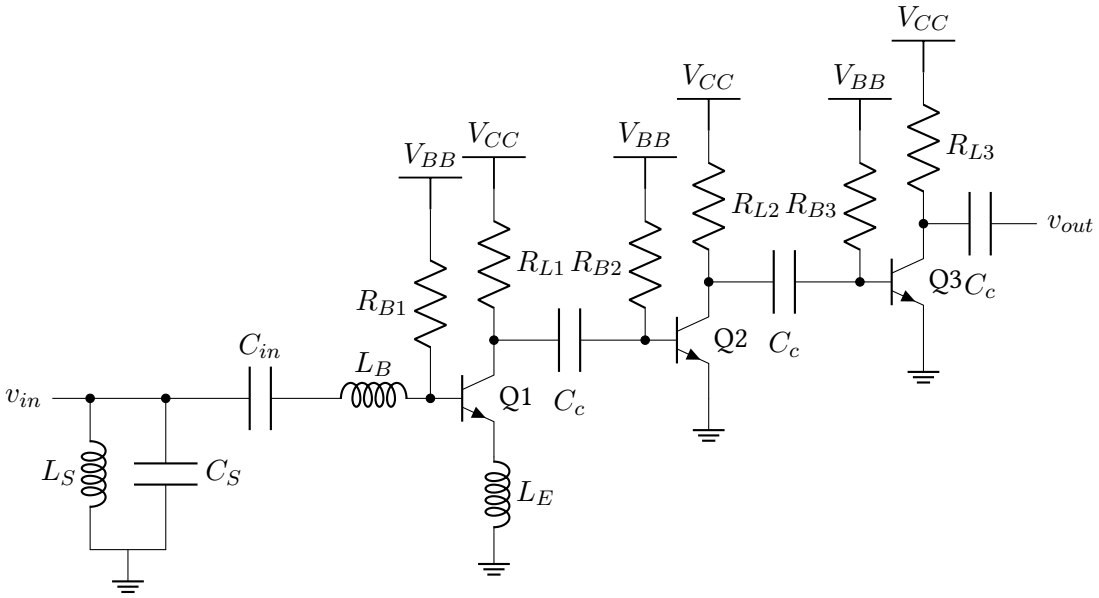


Figure 5.3.1: Schematic of the BJT-based LNA architecture

5.3.2 DC Biasing and Operating Point

The amplifier employs independent bias networks for each stage to ensure proper quiescent operating points across all transistors. Each BJT base is connected to a bias voltage V_{BB} through a bias resistor R_B, establishing the DC base current while maintaining AC isolation.

For transistor Q1, the DC base voltage is determined by the resistive divider formed between V_{BB} and ground through R_{B1}:

$$V_{\mathrm{B1}} = V_{\mathrm{BB}} - I_{\mathrm{B1}}\, R_{\mathrm{B1}} \tag{5.64}$$

The emitter voltage, accounting for the DC resistance of the emitter inductor L_{E} (typically negligible for practical inductors), is:

$$V_{\mathrm{E1}} = V_{\mathrm{B1}} - V_{\mathrm{BE1}} \tag{5.65}$$

where $V_{\mathrm{BE1}} \approx 0.98$ V.

The collector voltage is established by the voltage drop across the collector load resistor R_{L1}:

$$V_{\mathrm{C1}} = V_{\mathrm{CC}} - I_{\mathrm{C1}}\, R_{\mathrm{L1}} \tag{5.66}$$

For proper forward-active operation, the collector-base junction must be reverse-biased:

$$V_{\mathrm{CB1}} = V_{\mathrm{C1}} - V_{\mathrm{B1}} > 0 \tag{5.67}$$

Equivalently, the collector-emitter voltage must satisfy:

$$V_{\mathrm{CE1}} = V_{\mathrm{C1}} - V_{\mathrm{E1}} = V_{\mathrm{CC}} - I_{\mathrm{C1}}\, R_{\mathrm{L1}} - V_{\mathrm{BE1}} > V_{\mathrm{CE,sat}} \tag{5.68}$$

where $V_{\mathrm{CE,sat}} \approx 0.2$ V for SiGe HBTs.

To maintain low power consumption, a collector supply voltage of $V_{\mathrm{CC}} = 1.3$ V and a base supply voltage of $V_{\mathrm{BB}} = 1$ V are chosen. To achieve a favorable trade-off between gain and noise figure, the first stage is biased with $V_{\mathrm{BE1}} = 0.98$ V, which results in a collector current density of $J_{\mathrm{C1}} = 1$ mA/μm^2 and a base current density of $J_{\mathrm{B1}} = 0.5$ μA/μm^2. The collector current is set to $I_{\mathrm{C1}} = 3$ mA and the base current is $I_{\mathrm{B1}} = 1.34$ μA.

The biasing resistor R_{B1} can be calculated as:

$$R_{\mathrm{B1}} = \frac{V_{\mathrm{BB}} - V_{\mathrm{BE1}}}{I_{\mathrm{B1}}} = \frac{1 - 0.98}{1.34 \times 10^{-6}} \approx 14.9\ \mathrm{k\Omega} \tag{5.69}$$

and the collector load resistor R_{L1} is:

$$R_{\mathrm{L1}} = \frac{V_{\mathrm{CC}} - V_{\mathrm{CE1}}}{I_{\mathrm{C1}}} = \frac{1.3 - 1.1}{3 \times 10^{-3}} \approx 66.7\ \Omega \tag{5.70}$$

The subsequent stages Q2 and Q3 follow similar biasing principles, both with a grounded emitter configuration. The base-emitter voltage for each transistor is approximately $V_{\mathrm{BE}} \approx 0.98$ V, and the collector current density is set to $J_{\mathrm{C2}} = J_{\mathrm{C3}} = 1.8$ mA/μm^2. The collector currents are set to $I_{\mathrm{C2}} = I_{\mathrm{C3}} = 2.4$ mA, which results in base currents of $I_{\mathrm{B2}} = I_{\mathrm{B3}} = 1$ μA. The biasing resistors R_{B2} and R_{B3} are calculated as:

$$R_{\mathrm{B2}} = R_{\mathrm{B3}} = \frac{V_{\mathrm{BB}} - V_{\mathrm{BE}}}{I_{\mathrm{B2}}} = \frac{1 - 0.98}{1 \times 10^{-6}} \approx 20\ \mathrm{k\Omega} \tag{5.71}$$

and the collector load resistors R_{L2} and R_{L3} are:

$$R_{\mathrm{L2}} = R_{\mathrm{L3}} = \frac{V_{\mathrm{CC}} - V_{\mathrm{CE}}}{I_{\mathrm{C2}}} = \frac{1.3 - 1.2}{2.4 \times 10^{-3}} \approx 41.7\ \Omega \tag{5.72}$$

5.3.3 Small-Signal Analysis

The input impedance at the base of Q1, considering the base-emitter capacitance $C_{\pi 1}$ and the emitter degeneration inductor L_{E}, is given by:

$$Z_{\mathrm{in,Q1}} = r_{\pi 1} \parallel \left(\frac{1}{j\omega C_{\pi 1}} + j\omega L_{\mathrm{E}} \right) = \frac{r_{\pi 1} \left(\frac{1}{j\omega C_{\pi 1}} + j\omega L_{\mathrm{E}} \right)}{r_{\pi 1} + \frac{1}{j\omega C_{\pi 1}} + j\omega L_{\mathrm{E}}} \tag{5.73}$$

Considering the input matching network, the total input impedance is:

$$Z_{\mathrm{in}} = \left[(Z_{\mathrm{in,Q1}} \parallel R_{\mathrm{B1}}) + j\omega L_{\mathrm{B}} + \frac{1}{j\omega C_{\mathrm{in}}} \right] \parallel \frac{1}{j\omega C_{\mathrm{sh}}} \parallel j\omega L_{\mathrm{S}} \tag{5.74}$$

The current signal at the base of Q1 is:

$$i_{\mathrm{b1}} = \frac{v_{\mathrm{in}}}{(Z_{\mathrm{in,Q1}} \parallel R_{\mathrm{B1}}) + j\omega L_{\mathrm{B}} + \frac{1}{j\omega C_{\mathrm{in}}}} \tag{5.75}$$

and the voltage at the collector of Q1 is:

$$v_{\mathrm{c1}} = -\beta i_{\mathrm{b1}} Z_{\mathrm{c1}} \tag{5.76}$$

where Z_{c1} is the impedance looking from the collector of Q1 into the next stage, which includes the collector load resistor R_{L1} and the input impedance of the second stage $r_{\pi,\mathrm{Q2}}$:

$$Z_{\mathrm{c1}} = R_{\mathrm{L1}} \parallel r_{\pi,\mathrm{Q2}} \parallel R_{\mathrm{B2}} \tag{5.77}$$

Therefore, the small-signal voltage gain of the first stage is:

$$A_{\mathrm{v1}} = \frac{v_{\mathrm{c1}}}{v_{\mathrm{in}}} = -\beta \frac{Z_{\mathrm{c1}}}{(Z_{\mathrm{in,Q1}} \parallel R_{\mathrm{B1}}) + j\omega L_{\mathrm{B}} + \frac{1}{j\omega C_{\mathrm{in}}}} \tag{5.78}$$

For the second stage (common-emitter with grounded emitter):

$$A_{\mathrm{v2}} = \frac{-\beta Z_{\mathrm{c2}}}{r_{\pi,\mathrm{Q2}}} = -g_{\mathrm{m2}} Z_{\mathrm{c2}}, \tag{5.79}$$

where $Z_{\mathrm{c2}} = R_{\mathrm{L2}} \parallel r_{\pi,\mathrm{Q3}}$ is the impedance looking from the collector of Q2 into the next stage. Similarly, for the third stage:

$$A_{\mathrm{v3}} = -g_{\mathrm{m3}} Z_{\mathrm{c3}} = -g_{\mathrm{m3}} \left(R_{\mathrm{L3}} \parallel Z_{\mathrm{L}} \right) \tag{5.80}$$

where Z_{L} is the load impedance (typically $50\ \Omega$) transformed by the output coupling capacitor.

The total voltage gain of the three-stage amplifier is the product of individual stage gains:

$$A_{\mathrm{v}} = A_{\mathrm{v1}} A_{\mathrm{v2}} A_{\mathrm{v3}} = -\beta g_{\mathrm{m2}} g_{\mathrm{m3}} \frac{Z_{\mathrm{c1}} Z_{\mathrm{c2}} Z_{\mathrm{c3}}}{(Z_{\mathrm{in,Q1}} \parallel R_{\mathrm{B1}}) + j\omega L_{\mathrm{B}} + \frac{1}{j\omega C_{\mathrm{in}}}} \tag{5.81}$$

The overall current gain is:

$$A_{\mathrm{i}} = \frac{i_{\mathrm{out}}}{i_{\mathrm{in}}} = \frac{v_{\mathrm{out}}}{Z_{\mathrm{L}}} \frac{1}{i_{\mathrm{in}}} = \frac{A_{\mathrm{v}}}{Z_{\mathrm{L}}} Z_{\mathrm{in}} \tag{5.82}$$

and the overall transimpedance gain is:

$$A_{\mathrm{IV}} = \frac{v_{\mathrm{out}}}{i_{\mathrm{in}}} = A_{\mathrm{v}} Z_{\mathrm{in}} = -\beta g_{\mathrm{m2}} g_{\mathrm{m3}} \frac{Z_{\mathrm{c1}} Z_{\mathrm{c2}} Z_{\mathrm{c3}} Z_{\mathrm{in}}}{(Z_{\mathrm{in,Q1}} \parallel R_{\mathrm{B1}}) + j\omega L_{\mathrm{B}} + \frac{1}{j\omega C_{\mathrm{in}}}} \tag{5.83}$$

5.3.4 Noise Analysis

For the noise analysis, the dominant noise sources are the base current shot noise and the collector shot noise of each transistor, as well as the thermal noise from the resistors. In this analysis, we focus only on transistor noise, neglecting the contribution of the resistors, because the LNA operates in a cryogenic environment, where thermal noise is negligible. In particular, we evaluate the first stage, which is the most critical for the overall noise figure of the amplifier. As in the previous architecture, we model the noise contribution with two equivalent noise sources: one at the base and one at the collector of each transistor.

Input-Referred Noise Current

To calculate the input-referred noise current, we consider the open input configuration. The impedance looking into the input matching network is $Z = j\omega L_{\mathrm{B}} + \frac{1}{j\omega C_{\mathrm{in}}} + j\omega L_{\mathrm{E}} \parallel \frac{1}{j\omega C_{\mathrm{sh}}}$.

Base Noise Contribution (I_{BN1}) The base current noise source I_{BN1} at the base of Q1 produces a base current signal:

$$i_{\mathrm{b,Q1}} = I_{\mathrm{BN1}} \frac{Z \parallel R_{\mathrm{B1}} \parallel Z_{\mathrm{in,Q1}}}{Z_{\mathrm{in,Q1}}} \tag{5.84}$$

Note that in this calculation, the shunt inductor L_{E} to ground has been neglected in the parallel impedance calculation. The output noise voltage is:

$$v_{\mathrm{out,BN1}} = i_{\mathrm{b,Q1}} \beta Z_{\mathrm{c1}} A_{\mathrm{v2}} A_{\mathrm{v3}} \tag{5.85}$$

The contribution to the input-referred noise current spectral density is:

$$S_{\mathrm{IBN1}} = \frac{v_{\mathrm{n,out,BN1}}^2}{A_{\mathrm{IV}}^2} = 2qI_{\mathrm{B1}}\Delta f \frac{(Z \parallel R_{\mathrm{B1}} \parallel Z_{\mathrm{in,Q1}})^2 \left[(Z_{\mathrm{in,Q1}} \parallel R_{\mathrm{B1}}) + j\omega L_{\mathrm{B}} + \frac{1}{j\omega C_{\mathrm{in}}}\right]^2}{Z_{\mathrm{in,Q1}}^2 Z_{\mathrm{in}}^2} \tag{5.86}$$

Collector Noise Contribution (I_{CN1}) The collector current noise source I_{CN1} at the collector of Q1 produces an output noise voltage:

$$v_{\text{out,CN1}} = I_{\text{CN1}} \cdot Z_{\text{c1}} \cdot A_{\text{v2}} \cdot A_{\text{v3}} \tag{5.87}$$

The contribution to the input-referred noise current spectral density is:

$$S_{\text{ICN1}} = \frac{v_{\text{n,out,CN1}}^2}{A_{\text{IV}}^2} = 2qI_{\text{C1}}\Delta f \frac{\left[(Z_{\text{in,Q1}} \parallel R_{\text{B1}}) + j\omega L_{\text{B}} + \frac{1}{j\omega C_{\text{in}}}\right]^2}{\beta^2 Z_{\text{in}}^2} \tag{5.88}$$

Total Input-Referred Noise Current The total input-referred noise current spectral density is:

$$S_{I_{\text{in}}} = S_{\text{IBN1}} + S_{\text{ICN1}} = 2q\Delta f \frac{\left[(Z_{\text{in,Q1}} \parallel R_{\text{B1}}) + j\omega L_{\text{B}} + \frac{1}{j\omega C_{\text{in}}}\right]^2}{Z_{\text{in}}^2} \left(\frac{I_{\text{B1}} \left(Z \parallel R_{\text{B1}} \parallel Z_{\text{in,Q1}}\right)^2}{Z_{\text{in,Q1}}^2} + \frac{I_{\text{C1}}}{\beta^2} \right) \tag{5.89}$$

Input-Referred Noise Voltage

To calculate the input-referred noise voltage, we consider the short input configuration, where the input is shorted to ground. The impedance looking into the input matching network becomes $Z' = j\omega L_{\text{B}} + \frac{1}{j\omega C_{\text{in}}}$.

Base Noise Contribution (I_{BN1}) The base current noise source I_{BN1} at the base of Q1 produces a base current signal:

$$i_{\text{b,Q1}} = I_{\text{BN1}} \frac{Z' \parallel R_{\text{B1}} \parallel Z_{\text{in,Q1}}}{Z_{\text{in,Q1}}} \tag{5.90}$$

Again, the shunt inductor L_{S} to ground has been neglected. The output noise voltage is:

$$v_{\text{out,BN1}} = i_{\text{b,Q1}} \beta Z_{\text{c1}} A_{\text{v2}} A_{\text{v3}} \tag{5.91}$$

The contribution to the input-referred noise voltage spectral density is:

$$S_{\text{VBN1}} = \frac{v_{\text{out,BN1}}^2}{A_{\text{v}}^2} = 2qI_{\text{B1}}\Delta f \frac{\left(Z' \parallel R_{\text{B1}} \parallel Z_{\text{in,Q1}}\right)^2 \left[(Z_{\text{in,Q1}} \parallel R_{\text{B1}}) + j\omega L_{\text{B}} + \frac{1}{j\omega C_{\text{in}}}\right]^2}{Z_{\text{in,Q1}}^2} \tag{5.92}$$

Collector Noise Contribution (I_{CN1}) The collector current noise source I_{CN1} at the collector of Q1 produces an output noise voltage:

$$v_{\text{out,CN1}} = I_{\text{CN1}} \cdot Z_{\text{c1}} \cdot A_{\text{v2}} \cdot A_{\text{v3}} \tag{5.93}$$

The contribution to the input-referred noise voltage spectral density is:

$$S_{\text{VCN1}} = \frac{v_{\text{out,CN1}}^2}{A_{\text{v}}^2} = 2qI_{\text{C1}}\Delta f \frac{\left[(Z_{\text{in,Q1}} \parallel R_{\text{B1}}) + j\omega L_{\text{B}} + \frac{1}{j\omega C_{\text{in}}}\right]^2}{\beta^2} \tag{5.94}$$

Total Input-Referred Noise Voltage The total input-referred noise voltage spectral density is:

$$S_{V_{\text{in}}} = S_{\text{VBN1}} + S_{\text{VCN1}} = 2q\Delta f \left[(Z_{\text{in,Q1}} \parallel R_{\text{B1}}) + j\omega L_{\text{B}} + \frac{1}{j\omega C_{\text{in}}}\right]^2 \left(\frac{I_{\text{B1}} \left(Z' \parallel R_{\text{B1}} \parallel Z_{\text{in,Q1}}\right)^2}{Z_{\text{in,Q1}}^2} + \frac{I_{\text{C1}}}{\beta^2}\right) \tag{5.95}$$

Noise Figure

The noise figure of the amplifier can be calculated as:

$$\text{NF} = 1 + \frac{S_{I_{\text{in}}} Z_{\text{S}}}{4kT\Delta f} + \frac{S_{V_{\text{in}}}}{4kTZ_{\text{S}}\Delta f} \tag{5.96}$$

where Z_{S} is the source impedance, k is the Boltzmann constant, T is the absolute temperature, and Δf is the bandwidth. In this analysis, we are neglecting the cross-correlation between the two noise sources, which is a reasonable assumption for SiGe HBTs.

5.3.5 Component Selection and Input Matching Design

Transistor Sizing and Bias Point Selection

The transistor sizes are selected to achieve the target collector current densities while optimizing the noise performance. The first stage transistor Q_1 is the most critical for the overall noise figure and requires careful sizing. A larger emitter area reduces the parasitic base resistance r_b, which is a dominant noise contributor in SiGe HBTs, but at the cost of increased parasitic capacitances (C_π, C_μ) that limit the bandwidth.

The selected layout for Q_1 employs $N_E = 58$ emitter fingers with unit dimensions $L_{\text{E}} = 0.9$ μm and $W_{\text{E}} = 0.07$ μm, yielding a total emitter area of $A_{\text{E1}} = 58 \times 0.9 \times 0.07 \approx 3.65$ μm^2. At a collector current of $I_{\text{C1}} = 3$ mA, the resulting current density is $J_{\text{C1}} = I_{\text{C1}}/A_{\text{E1}} \approx 0.82$ mA/μm^2, which falls within the optimal range for minimum noise figure in the selected SiGe technology.

The second and third stage transistors Q_2 and Q_3 employ $N_E = 14$ emitter fingers of the same unit dimensions, resulting in a smaller emitter area $A_{\text{E2}} = A_{\text{E3}} \approx 0.88$ μm^2. Smaller devices are sufficient for the subsequent stages since their noise contribution is suppressed by the gain of the preceding stages, and the reduced parasitic capacitances help maintain the amplifier bandwidth. At a collector current of $I_{\text{C2}} = I_{\text{C3}} = 2$ mA, the current density is $J_{\text{C2}} = J_{\text{C3}} \approx 2.3$ mA/μm^2.

Input Matching Network Design

The emitter degeneration inductor L_E introduces a real component in the input impedance of Q_1 without contributing thermal noise. For a common-emitter stage with inductive degeneration, the real part of the input impedance at the resonant frequency is approximately given by [77]:

$$R_{\text{eq}}(\omega_C) \approx \frac{g_{\text{m1}} L_E}{C_{\pi 1}} = \omega_T L_E \tag{5.97}$$

where $\omega_T = 2\pi f_T$ is the transit angular frequency of the transistor. A degeneration inductance of $L_E = 25$ pH is selected, yielding an equivalent input resistance of $R_{\text{eq}}(\omega_C) \approx 33\ \Omega$ at the design center frequency $f_C = 6.5$ GHz. Following the analysis in [77], this value satisfies the condition $26\ \Omega < R_{\text{eq}} < 96\ \Omega$ required for wideband return loss better than -10 dB using the LC-ladder matching technique. It is worth noting that R_{eq} need not be exactly $50\ \Omega$; in fact, values slightly below R_0 can be exploited to trade input matching margin for improved noise matching.

The input matching network is synthesized following the LC-ladder approach described in [77]. The network comprises a parallel L_S–C_S resonator at the input port, a series coupling capacitor C_{in}, and a series base inductor L_B. Unlike the cascode topology analyzed in [77], the common-emitter first stage exhibits a more pronounced Miller effect due to the base-collector capacitance C_μ, which modifies the effective input impedance. Nevertheless, the LC-ladder matching strategy remains applicable, as the design targets resistive matching at the center frequency and relies on the dual-resonance structure to extend the bandwidth.

The series combination of L_B and C_{in} is designed to resonate near the center frequency, thereby canceling the net series reactance and presenting a predominantly real impedance to the source:

$$f_{\text{res,series}} = \frac{1}{2\pi\sqrt{L_B \cdot C_{\text{in}}}} \approx f_C = 6.5\ \text{GHz} \tag{5.98}$$

At this frequency, the input impedance is dominated by R_{eq}, resulting in a reflection coefficient of:

$$\text{S}_{11}(f_C) = -20\log_{10}\left|\frac{R_{\text{eq}} - R_0}{R_{\text{eq}} + R_0}\right| = -20\log_{10}\left|\frac{33 - 50}{33 + 50}\right| \approx 13.8\ \text{dB} \tag{5.99}$$

which provides adequate margin with respect to the $S_{11} \leq -10$ dB specification.

The parallel L_S–C_S tank introduces a second resonance that extends the matching bandwidth by providing controlled impedance transformation at frequencies away from f_C. According to the LC-ladder theory [77], the approximate S_{11} bandwidth is:

$$\omega_H - \omega_L \approx \frac{\sqrt{R_1 R_{\text{eq}} - R_{\text{eq}}^2}}{L_B} \tag{5.100}$$

where $R_1 = R_{\text{IN}}(\omega_L) = R_{\text{IN}}(\omega_H)$ is the real part of the input impedance at the band edges. Setting $R_1 \cdot R_{\text{eq}} = R_0^2$, which ensures equal return loss at the center frequency and at the band edges, yields $R_1 = R_0^2/R_{\text{eq}} = 2500/33 \approx 75.8\ \Omega$. Substituting into (5.100) with $L_B = 400$ pH:

$$f_H - f_L \approx \frac{1}{2\pi} \cdot \frac{\sqrt{75.8 \times 33 - 33^2}}{400 \times 10^{-12}} \approx 15 \text{ GHz} \tag{5.101}$$

indicating that the LC-ladder structure can, in principle, support a very wide matching bandwidth centered around $f_C = 6.5$ GHz.

The analytically derived starting values are subsequently refined through iterative circuit simulation, accounting for the frequency-dependent transistor parasitics, interconnect losses, and the trade-off between power matching and noise matching. In particular, to properly simulate the noise performance of the amplifier, the series resistance of the inductors was included in the design, which was estimated around $0.15\ \Omega$ [76]. The final component values obtained after simulation are summarized in Table 5.4.

Table 5.4: Input matching network component values.

Component	**Symbol**	**Value**
Emitter degeneration inductor	L_E	25 pH
Base series inductor	L_B	400 pH
Series coupling capacitor	C_{in}	1.3 pF
Shunt inductor	L_S	900 pH
Shunt capacitor	C_S	280 fF

Load Resistor Selection

The collector load resistors determine both the DC operating point and the AC gain-bandwidth product of each stage. The first stage employs a reduced load resistance of $R_{\text{L1}} = 20\ \Omega$ compared to the initial analytical estimate. This value is chosen to extend the bandwidth of the first stage, as the -3 dB bandwidth of each common-emitter stage is approximately $f_{-3\text{dB}} \approx 1/(2\pi R_L C_{\text{out}})$, where C_{out} is the total parasitic capacitance at the collector node. The resulting collector-emitter voltage is:

$$V_{\text{CE1}} = V_{\text{CC}} - I_{\text{C1}} R_{\text{L1}} = 1.3 - 3 \times 10^{-3} \times 20 = 1.24 \text{ V} \tag{5.102}$$

which provides ample headroom above $V_{\text{CE,sat}} \approx 0.2$ V. The second and third stages employ $R_{\text{L2}} = R_{\text{L3}} = 50\ \Omega$, yielding:

$$V_{\text{CE2}} = V_{\text{CE3}} = V_{\text{CC}} - I_{\text{C2}} R_{\text{L2}} = 1.3 - 2 \times 10^{-3} \times 50 = 1.2 \text{ V} \tag{5.103}$$

The base bias resistors are finalized at $R_{B1} = R_{B2} = R_{B3} = 14$ kΩ after simulation, providing the required base currents while ensuring sufficient AC isolation from the bias supply. A summary of the final circuit parameters is provided in Table 5.5.

Table 5.5: Summary of final circuit component values.

Parameter	Stage 1	Stage 2	Stage 3
Transistor size ($N_E \times L_E \times W_E$)	$58 \times 0.9 \times 0.07$ μm	$14 \times 0.9 \times 0.07$ μm	$14 \times 0.9 \times 0.07$ μm
Collector current I_C	3 mA	2 mA	2 mA
Collector load R_L	20 Ω	50 Ω	50 Ω
Bias resistor R_B	14 kΩ	14 kΩ	14 kΩ
V_{CE}	1.24 V	1.2 V	1.2 V

5.3.6 Simulation and Performance Evaluation

The performance of the three-stage common-emitter LNA is evaluated through circuit-level simulation and compared with the analytical predictions derived in the preceding sections.

The simulated S-parameters of the LNA are shown in Fig. 5.3.2. The forward voltage gain S_{21} reaches a peak value of approximately $A_{v,max} \approx 55$ dB at $f = 3.93$ GHz, with less than 17 dB of gain variation over the frequency range of 4.95 GHz to 17.15 GHz. The input reflection coefficient satisfies $S_{11} \leq -10$ dB over the band from 4.95 GHz to 17.15 GHz, confirming the effectiveness of the LC-ladder matching network designed in Section 5.3.5. The reverse isolation S_{12} remains below -60 dB across the entire band (not shown for clarity).

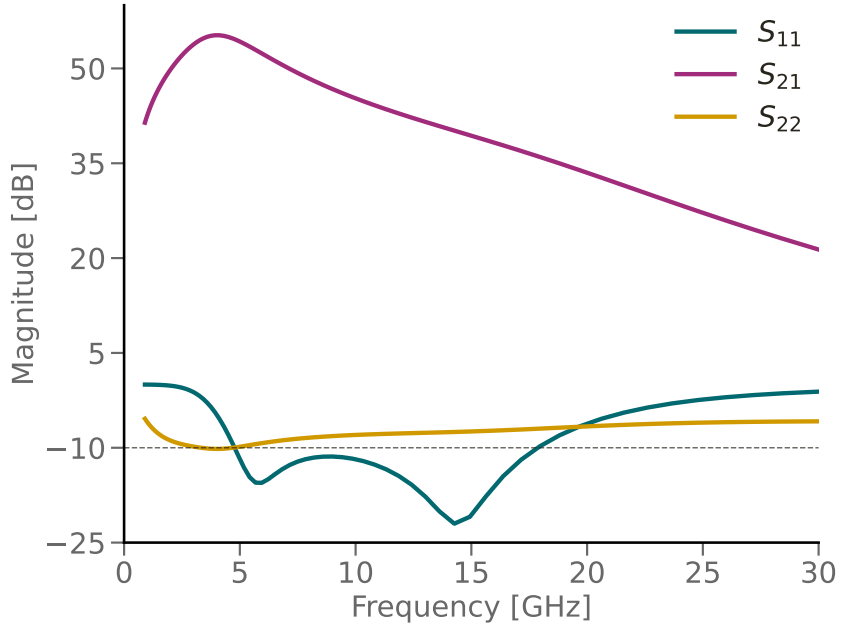


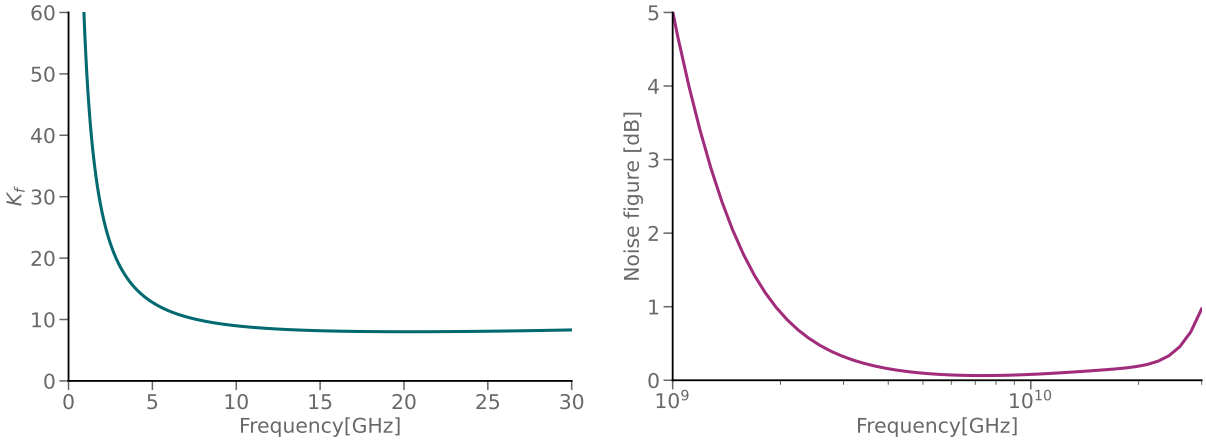
Figure 5.3.2: Simulated S-parameters of the three-stage common-emitter LNA.

These results can be compared with the analytical voltage gain expression derived in Eq. (5.81). At the center frequency $f_C = 6.5$ GHz, the analytical model predicts $|A_v(f_C)| \approx 51$ dB, which is in reasonable agreement with the simulated value of 51.19 dB.

The stability of the amplifier is a critical concern for a multi-stage topology without the isolation benefits of a cascode structure. The Rollett stability factor (K-factor), defined as:

$$K = \frac{1 - |S_{11}|^2 - |S_{22}|^2 + |\Delta|^2}{2|S_{12}||S_{21}|} \tag{5.104}$$

where $\Delta = S_{11}S_{22} - S_{12}S_{21}$, is used to assess unconditional stability. The amplifier is unconditionally stable when $K > 1$ and $|\Delta| < 1$ simultaneously. The simulated K-factor is reported in Fig. 5.3.3a, where it can be observed that $K > 1$ over the entire frequency range of interest. The auxiliary condition $|\Delta| < 1$ is also verified over the full band.



(a) (b)

Figure 5.3.3: (a)Rollett stability factor (K) of the three-stage LNA. (b) Noise figure of the three-stage LNA.

The simulated noise figure is shown in Fig. 5.3.3b. Over the frequency range of interest, the noise figure remains below NF ≤ 0.15 dB, with a minimum value of $\text{NF}_{\text{min}} \approx 63$ mdB at $f = 7.37$ GHz. This corresponds to an equivalent noise temperature of approximately $T_n \approx 4.2$ K at the reference temperature of $T_{\text{ref}} = 290$ K, calculated using the relation:

$$T_n = T_{\text{ref}} \left(10^{\text{NF}/10} - 1\right) \approx 290 \times \left(10^{0.063/10} - 1\right) \approx 4.2 \text{ K} \tag{5.105}$$

The analytical noise model developed in Section 5.2.4 predicts a noise figure of $\text{NF}_{\text{analytical}} \approx 57$ mdB at $f_C = 6.5$ GHz, which can be compared with the simulated value to assess the validity of the simplifications adopted in the analysis, notably the neglect of resistor thermal noise and the base resistance noise contribution.

A comparison between the key analytical predictions and the simulated performance metrics is summarized in Table 5.6. The analytical DC power consumption is calculated as:

$$P_{\mathrm{DC}} = V_{\mathrm{CC}}(I_{\mathrm{C1}} + I_{\mathrm{C2}} + I_{\mathrm{C3}}) = 1.3 \times (3 + 2 + 2) \times 10^{-3} = 9.1 \text{ mW} \tag{5.106}$$

Table 5.6: Comparison between analytical predictions and simulated results at $f_C = 6.5$ GHz.

Parameter	**Analytical**	**Simulated**	**Unit**
Voltage gain $\lvert A_v \rvert$	51	51.19	dB
Input matching S_{11}	≤ -13.8	< -14.18	dB
Noise figure NF	0.057	0.050	dB
DC power consumption P_{DC}	9.1	9.72	mW

The simulated results confirm the validity of the design approach based on the LC-ladder matching methodology [77]. The discrepancies between analytical and simulated values are attributed to the simplified transistor models used in the hand analysis, the neglect of parasitic interconnect elements, and the frequency dependence of the transistor parameters.

5.4 LNA State of the Art

The modern landscape of cryogenic low-noise amplifiers spans multiple technology platforms, each offering distinct trade-offs between noise performance, bandwidth, power consumption, and system complexity. Semiconductor amplifiers based on CMOS or SiGe BiCMOS achieve noise temperatures of $T_{\mathrm{N}} \sim 4$-10 K when operated at 4 K, offering ease of integration, broad bandwidth spanning octaves, and moderate power consumption. These values, while excellent compared to room-temperature amplifiers $T_{\mathrm{N}} \sim 300$ K, remain an order of magnitude above the standard quantum limit, which at 7 GHz corresponds to $T_{\mathrm{N}}^{\mathrm{SQL}} = hf/(2k_{\mathrm{B}}) \approx 0.34$ K. Superconducting amplifiers such as Josephson parametric amplifiers (JPAs) and traveling-wave parametric amplifiers (TWPAs) achieve $T_{\mathrm{N}} \sim 0.5$–1 K, approaching within a factor of 2-3 of the quantum limit through parametric gain in nonlinear Josephson junctions. However, this exceptional performance requires magnetic shielding, precise impedance engineering, cryogenic pump tone delivery, and typically exhibits limited bandwidth and reduced dynamic range.

Figure 5.4.1 compares gain versus power consumption across technologies. CMOS amplifiers cluster in a low-power regime 4-120 mW, while providing gains of 20-40 dB gain, while SiGe BiCMOS designs occupy a higher-power, higher-gain region 8-100 mW and gains of 30-35 dB. The two designs from this work achieve 36.4 dB (cascode) and 51.2 dB (common-emitter) with 9.1-9.7 mW consumption, placing them among the most power-efficient high-gain implementations.The superior high-frequency performance of SiGe heterojunction bipolar transistors (HBTs), characterized by f_{T} values exceeding 300 GHz even at cryogenic temperatures, makes them particularly attractive for ultra-wideband designs for operation above 10 GHz where CMOS performance degrades. Parametric amplifiers (PAs), whether CMOS-integrated or discrete superconducting devices, present minimal DC power consumption (a few milliwatts for CMOS-based designs, essentially zero for superconducting JPAs), but this metric is somewhat misleading since their operation depends critically on pump tone delivery, which itself consumes power at the cryogenic stage and adds system complexity.

Figure 5.4.2 reveals the noise performance as a function of operating frequency. CMOS and SiGe semiconductor amplifiers cluster in the $T_{\mathrm{N}} \sim 4$-20 K range across the 1-10 GHz band. Superconducting amplifiers (JPAs) demonstrate $T_{\mathrm{N}} \sim 0.5$–0.6 K. Parametric CMOS amplifiers (PAs), which embed varactor-based parametric gain stages into conventional semiconductor processes, occupy an intermediate regime with $T_{\mathrm{N}} \sim 13$–78 K depending on pump optimization and operating point. These devices represent an active research frontier: they aim to approach quantum-limited noise without requiring superconducting materials, though current implementations have not yet matched the performance of optimized conventional CMOS LNAs. The two designs from this work achieve $T_{\mathrm{N}} \sim 4.2$–4.9 K in the 6–7 GHz range, competitive with the best reported SiGe implementations.

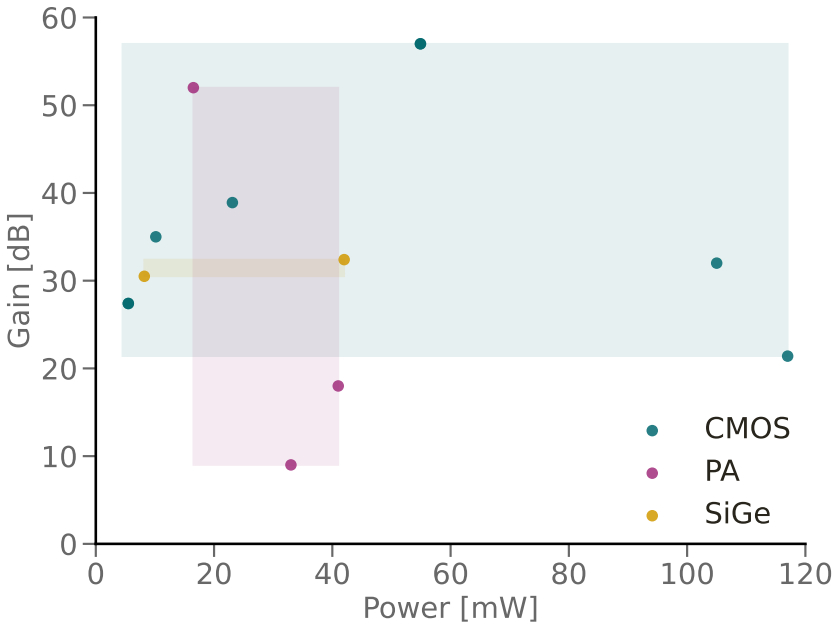


Figure 5.4.1: Power consumption versus gain for cryogenic LNAs across different technology platforms: Semiconductor (CMOS, SiGe BiCMOS), Parametric CMOS (PA), and Superconducting (JPA). JPAs operate at millikelvin temperatures with negligible DC power but require pump tones. Data compiled from Table 5.7.

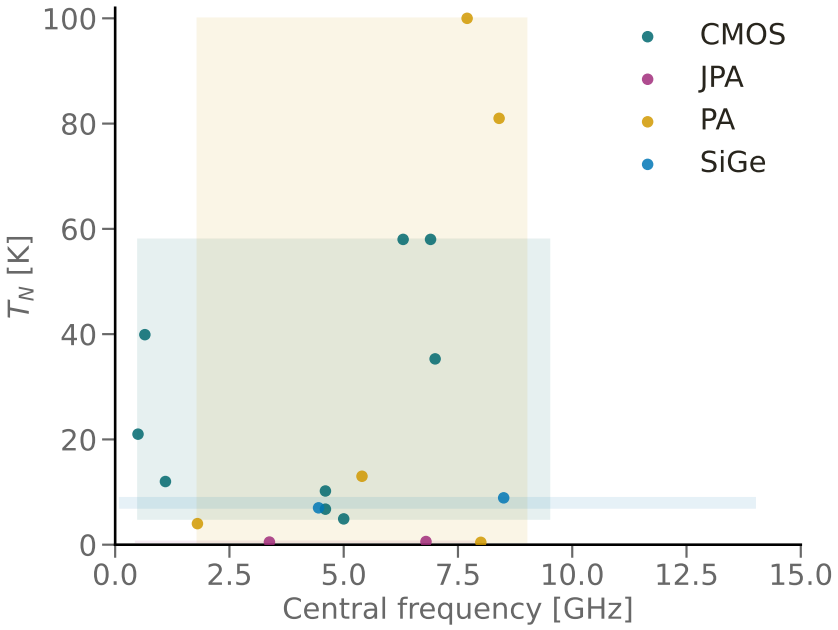


Figure 5.4.2: Noise temperature T_N versus center frequency for cryogenic LNAs. Semiconductor amplifiers (CMOS, SiGe BiCMOS) operate at physical temperatures $T_e = 4$–8 K. Superconducting JPAs operate at millikelvin temperatures ($T_e = 20$–80 mK). The designs from this work (BiCMOS, HBT) achieve $T_N \sim 4.2$–4.9 K, competitive with the best SiGe implementations. Data compiled from Table 5.7.

Table 5.7 provides detailed performance metrics for representative cryogenic LNAs spanning the available technologies. The data reveal several architectural trade-offs. CMOS implementations in mature nodes (160-nm, 65-nm) achieve respectable noise performance ($T_{\mathrm{N}} \sim 6$–10 K) with moderate power consumption (23–55 mW), while advanced nodes (22-nm FDSOI, 28-nm) push toward lower power (4–10 mW) at comparable or slightly improved noise, though sometimes with reduced gain or narrower bandwidth. SiGe BiCMOS amplifiers demonstrate their strength in wideband operation: the Peng et al. [78] design covering 0.1–8.8 GHz achieves $T_{\mathrm{N}} = 7$ K with 30.5 dB gain using only 8.2 mW. These octave-spanning or decade-bandwidth designs are invaluable for frequency-multiplexed readout of large qubit arrays, where resonators are distributed across several GHz to avoid crosstalk.

Reference	**Type**	T_{N} [K]	**Gain** [dB]	**Frequency** [GHz]	T_{e} [K]	**Power** [mW]
Patra et al. [79]	CMOS	6.75	57	3.9–5.3	4.0	54.9
Das et al. [80]	CMOS	10.2	38.9	3.9–5.3	7.0	23.1
Sheldon et al. [81]	CMOS	12	32	0.7–1.5	12.0	105
Gao et al. [82]	CMOS	58	27.4	4.3–9.5	6.0	5.5
Das et al. [83]	CMOS	4.9	35	4.0–6.0	8.0	4.5–15.8
Tao et al. [84]	CMOS	39.9	21.4	0.5–0.8	4.0	117
Gao et al. [85]	CMOS	58	27.4	4.7–7.9	6.0	5.5
Aja et al. [86]	SiGe	8.9	32.4	3.0–14.0	7.2	42
Peng et al. [78]	SiGe	7	30.5	0.1–8.8	3.6	8.2
Caglar et al. [87]	CMOS	35.3	—	6.0–8.0	4.2	4.2
Lee et al. [88]	PA	169	26	10	300.0	—
Mehrpoo et al. [73]	PA	100	9	6.8–8.6	8.5	33
Patra et al. [79]	CMOS	21	57	0.5	4.5	54.9
Baek et al. [89]	PA	13	17	5.3–5.5	0.08	—
Macklin et al. [90]	JPA	0.6	24	5.6–8.0	0.03	—
Ranzani et al. [91]	JPA	0.5	17	0.45–6.3	0.02	—
Lee et al. [92]	PA	0.45	18	7.0–9.0	—	41
Gray et al. [93]	PA	—	26	0.15–1.15	258.0	—
Geng et al. [94]	PA	78	52	—	4.2	16.5
Sadler et al. [95]	PA	81	15	8.4	80.0	—
Nagai et al. [96]	PA	4	20	1.8	15.0	—
This Work (Cascode)	BiCMOS	4.9	36.4	4.95–17.15	4.0	9.7
This Work (CE)	SiGe	4.2	51.2	4.95–17.15	4.0	9.1

Table 5.7: Performance comparison of selected cryogenic LNAs for quantum applications. T_{N} denotes the amplifier noise temperature referred to the input. T_{e} is the physical (environmental) temperature at which the measurements were performed. Type classifications: CMOS and SiGe are conventional semiconductor amplifiers; JPA are superconducting Josephson parametric amplifiers based on superconducting junctions; PA are CMOS-based parametric amplifiers using varactor-pumped gain stages. Where only noise figure (NF) was reported in the literature, T_{N} is inferred using $T_{\mathrm{N}} = T_0(10^{\mathrm{NF}/10} - 1)$ with $T_0 = 290$ K. Bandwidth indicates 3-dB rolloff points or full operating range for wideband designs.

Superconducting amplifiers occupy a different regime entirely: JPA implementations by Macklin et al. [90] and Ranzani et al. [91] achieve $T_{\mathrm{N}} \sim 0.5$–0.6 K with gains of 17–24 dB over bandwidths ranging from hundreds of MHz to several GHz, but operating at millikelvin temperatures (20–30 mK) and requiring negligible DC power since their Josephson junctions are dissipationless. The true cost appears in system complexity: each JPA requires a dedicated pump tone generated by a cryogenic or room-temperature microwave source, precise impedance matching through on-chip transformers or $\lambda/4$ sections, magnetic shielding to prevent flux trapping in superconducting loops, and careful thermal anchoring. Parametric CMOS amplifiers, such as the Baek et al. [89] example achieving $T_{\mathrm{N}} = 13$ K with 17 dB gain over 5.3–5.5 GHz at 80 mK, attempt to bridge the gap by providing parametric gain in a semiconductor platform, though their noise performance currently falls short of both conventional CMOS LNAs and superconducting devices.

The critical question of whether a high-performance SiGe LNA can replace the traditional JPA+LNA cascade hinges on a system-level analysis of noise budgets and readout fidelity. In a typical two-stage configuration, a JPA with $T_{\mathrm{N},1} \sim 0.6$ K and gain $G_1 = 20$ dB is followed by a semiconductor LNA with $T_{\mathrm{N},2} \sim 5$ K. According to the Friis formula, the total system noise temperature is $T_{\mathrm{N}}^{\mathrm{tot}} = T_{\mathrm{N},1} + T_{\mathrm{N},2}/G_1 \approx 0.6 + 5/100 = 0.65$ K, dominated almost entirely by the JPA. A single-stage SiGe LNA with $T_{\mathrm{N}} \sim 4$ K would increase system noise by a factor of approximately 6, translating to a $\sqrt{6} \approx 2.4\times$ increase in voltage noise $\sigma(V_m)$. For a marginally resolved signal where the signal-to-noise ratio (SNR) in the JPA+LNA system is 20 (corresponding to readout fidelity $\mathcal{F} \approx 95\%$), the single-LNA system would see SNR degraded to approximately 8, reducing fidelity to perhaps 85–90% depending on the specific signal distribution and decision threshold.

However, this simplistic comparison omits several critical factors. First, JPAs exhibit limited dynamic range: input powers above approximately -100 dBm cause gain compression, distorting the signal and degrading measurement fidelity. In frequency-multiplexed readout where multiple resonators are interrogated simultaneously, the combined power can easily exceed this threshold, necessitating careful power partitioning or time-domain sequencing that complicates experimental protocols. Second, JPAs require pump tones at frequencies carefully tuned to avoid spurious mixing products and maintain phase stability, adding complexity to the cryogenic microwave environment. A wideband SiGe LNA operating across 4–8 GHz or wider can simultaneously amplify dozens of resonators without compression, tolerates magnetic fields, and requires no pump infrastructure. For quantum computing architectures targeting hundreds of qubits with readout fidelities of 95–99%—sufficient for many near-term algorithms and potentially compatible with certain quantum error correction schemes if other noise sources are adequately suppressed—the simplicity of a single-LNA architecture may outweigh the noise penalty. Conversely, applications demanding the highest possible fidelity, such as surface code quantum error correction where $\mathcal{F} > 99.9\%$ is required, benefit decisively from JPA-based readout despite the added complexity.

The choice of LNA technology ultimately depends on a multi-dimensional trade-off space encompassing noise performance, bandwidth, power consumption, scalability, and system complexity. For single-qubit or few-qubit exploratory experiments where simplicity and rapid iteration are paramount, CMOS LNAs in mature nodes (65-nm, 130-nm) provide adequate performance ($T_{\mathrm{N}} \sim 5$–10 K, 30–40 dB gain, 1–2 GHz bandwidth) with minimal power dissipation and straightforward integration, achieving readout fidelities of 90–95% that suffice for gate calibration and basic quantum algorithm demonstrations. Large-scale quantum processors with tens to hundreds of qubits employing frequency-division multiplexing favor wideband SiGe BiCMOS designs covering 4–8 GHz or broader, enabling simultaneous readout of many resonators without reconfiguration. The higher per-channel power consumption (20–50 mW) is acceptable because it amortizes across many qubits, and the superior noise performance ($T_{\mathrm{N}} \sim 4$–7 K) compared to CMOS relaxes constraints on signal power and integration time.

Applications demanding the highest fidelity—such as surface code quantum error correction with $\mathcal{F} > 99.9\%$, demonstration of quantum advantage in fault-tolerant algorithms, or single-shot readout of exotic spin states with weak coupling—justify the complexity of superconducting amplifiers. The $\sim 6\times$ reduction in system noise temperature compared to semiconductor LNAs translates directly to improved measurement SNR, enabling shorter integration times that reduce susceptibility to qubit dephasing, or allowing readout of weaker signals from detuned or parasitic resonator modes. However, deploying JPAs at scale remains challenging: a 100-qubit processor would require 100 independent JPAs, each with dedicated pump circuitry, magnetic shielding, and cryogenic wiring, substantially complicating the experimental setup. Emerging parametric CMOS amplifiers, if their noise performance can be improved to $T_{\mathrm{N}} \sim 2$–3 K through refined designs and optimized pump strategies, might eventually occupy a valuable middle ground: quantum-limited-class noise without superconductivity.

An emerging question in quantum computing system architecture is whether advanced semiconductor technologies, particularly SiGe BiCMOS amplifiers, can obviate the traditional two-stage configuration of a JPA followed by a semiconductor LNA. Eliminating the JPA would dramatically simplify cryogenic wiring, reduce magnetic field sensitivity, and avoid the narrow-bandwidth constraints of parametric amplifiers, albeit at the cost of a modest increase in system noise temperature. For many quantum computing applications where readout fidelities of 95–99% suffice, this trade-off may be advantageous, especially as qubit counts scale and the complexity of deploying dozens of JPAs becomes prohibitive.

Chapter 6 CMOS Circulator

6.1 The Ideal Three-Port Circulator

A circulator is a three-port microwave network characterised by a cyclic, non-reciprocal routing of electromagnetic energy. In its ideal form the device transmits a signal entering any port entirely to the next port in the circulation sequence while presenting perfect isolation to the remaining port. Denoting the three ports by indices 1, 2, 3 and choosing the circulation sense $1 \to 2 \to 3 \to 1$, the scattering matrix reads

$$\mathbf{S}_{\text{circ}} = \begin{bmatrix} 0 & 0 & 1 \\ 1 & 0 & 0 \\ 0 & 1 & 0 \end{bmatrix} \tag{6.1}$$

This matrix is *unitary* ($\mathbf{S}^{\dagger}\mathbf{S} = \mathbf{I}$), confirming that the ideal circulator is lossless, yet it is manifestly *not symmetric* ($\mathbf{S} \neq \mathbf{S}^{T}$), implying non-reciprocity. By the Lorentz reciprocity theorem, any linear, time-invariant medium with symmetric constitutive tensors yields a symmetric scattering matrix; therefore, realising Equation (6.1) necessarily requires either a magnetically biased medium (as in conventional ferrite circulators) or a *time-variant* network that breaks the underlying symmetry of the wave equation.

6.1.1 Phase-Interference Interpretation

The cyclic routing described by Equation (6.1) can be understood in terms of constructive and destructive wave interference inside a closed signal loop. Consider the circulator as a looped network with two parallel signal paths connecting two generic ports of the loop, labelled path A and path B, with respective insertion phase shifts θ_A and θ_B. If a unit-amplitude signal is injected at the input, the superposition at the output is

$$V_{\text{out}} = \frac{1}{2}\left(e^{-j\theta_A} + e^{-j\theta_B}\right) = e^{-j\frac{\theta_A+\theta_B}{2}} \cos\!\left(\frac{\theta_A - \theta_B}{2}\right) \tag{6.2}$$

while a signal travelling in the reverse direction through the same two paths, but acquiring phase shifts θ'_A and θ'_B, produces

$$V_{\text{out}}^{\text{rev}} = \frac{1}{2}\left(e^{-j\theta'_A} + e^{-j\theta'_B}\right) = e^{-j\frac{\theta'_A+\theta'_B}{2}} \cos\!\left(\frac{\theta'_A - \theta'_B}{2}\right) \tag{6.3}$$

Lossless forward transmission requires $|V_{\text{out}}| = 1$, hence

$$\theta_A - \theta_B = 2k\pi, \qquad k \in \mathbb{Z} \quad \text{(constructive interference)} \tag{6.4}$$

while perfect reverse isolation requires $|V_{\text{out}}^{\text{rev}}| = 0$, hence

$$\theta'_A - \theta'_B = (2k+1)\pi, \qquad k \in \mathbb{Z} \quad \text{(destructive interference)} \tag{6.5}$$

If both paths were reciprocal, i.e. $\theta'_A = \theta_A$ and $\theta'_B = \theta_B$, Equations (6.4) and (6.5) could never be satisfied simultaneously. Non-reciprocity therefore demands that at least one of the two paths contributes a direction-dependent phase.

6.1.2 Staggered-Commutation Architecture

A possible approach to realise the required non-reciprocal phase response is to employ a *staggered-commutation* scheme. This architecture decomposes the signal loop into three branches [50]: two *reciprocal* branches, each providing a fixed phase shift α independent of signal direction, and one *non-reciprocal* branch that produces phase shift β in the forward direction and γ in the reverse direction. The overall phase accumulated along the two paths of the loop for forward and reverse propagation is:

$$\theta_{\text{fwd}} = 2\alpha + \beta \qquad \theta_{\text{rev}} = 2\alpha - \gamma \tag{6.6}$$

Imposing the constructive/destructive conditions of Equations (6.4)-(6.5) on the overall loop phase, and assuming $\gamma = 0^\circ$, yields the minimal solution

$$\alpha = 90^\circ, \qquad \beta = 180^\circ \tag{6.7}$$

which gives $\theta_{\text{fwd}} = 360^\circ$ (constructive) and $\theta_{\text{rev}} = 180^\circ$ (destructive). Equivalently, the non-reciprocal branch must realise a $180^\circ/0^\circ$ gyrator function when viewed from opposing signal directions, and each reciprocal branch must contribute a fixed 90° delay. This condition can be schematically represented in the block diagram of Figure 6.1.1.

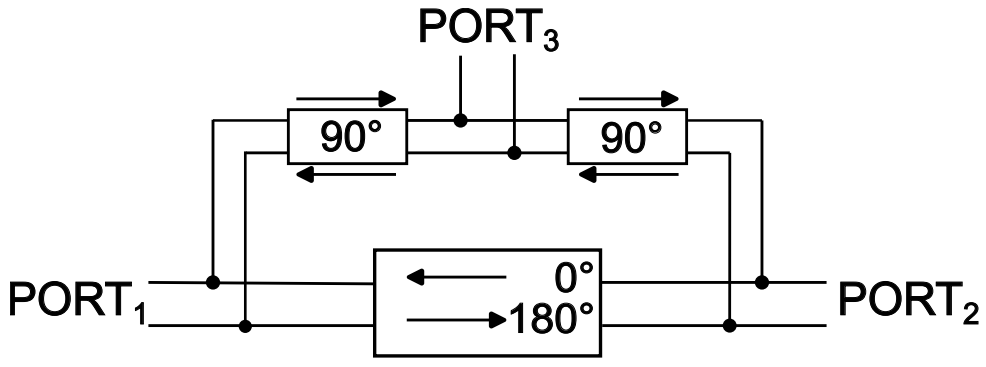


Figure 6.1.1: Block diagram of the staggered-commutation circulator. Two reciprocal 90° branches and one non-reciprocal $180^\circ/0^\circ$ branch form a closed loop. Constructive interference (360°) enables forward transmission; destructive interference (180°) provides reverse isolation.

6.1.3 Target Specifications

In the context of superconducting and spin-qubit readout, conventional ferrite circulators [97] deliver excellent RF performance with sub-decibel insertion loss, zero power consumption, and cryogenic compatibility. However, their physical dimensions ($35 \times 45\,\mathrm{mm}^2$) are incompatible with the scalability demands of multi-qubit processors. An integrated CMOS replacement must operate in the 5-$8\,\mathrm{GHz}$ readout band while satisfying stringent constraints on power dissipation imposed by the limited cooling capacity of dilution refrigerators. At the base-temperature stage ($T \approx 20\,\mathrm{mK}$) the available cooling power is of the order of $10\ \mu\mathrm{W}$, far below any active-circuit budget; at the $4\,\mathrm{K}$ stage, however, budgets of several milliwatts are feasible.

A further requirement arises from frequency-multiplexed readout, in which many qubits share a single RF line: if each qubit occupies a $10\,\mathrm{MHz}$ channel with $10\,\mathrm{MHz}$ guard spacing, 100 qubits demand $2\,\mathrm{GHz}$ of contiguous circulator bandwidth. Table 6.1 summarises the target specifications alongside those of a representative commercial ferrite device.

Parameter	**Ferrite circ.** [97]	**CMOS target**
Working temperature	0.02 – 4 K	0.02 – 300 K
Centre frequency	6 GHz	6.5 GHz
Bandwidth	4 GHz	2 GHz
Insertion loss	0.4 dB	< 1 dB
Isolation	18 dB	≥ 18 dB
Noise temperature	7 K	< 1 K
Area	$35 \times 45\,\mathrm{mm}^2$	$< 5 \times 5\,\mathrm{mm}^2$
Power consumption	0 W	< 2 mW

Table 6.1: Requirements for an integrated cryogenic circulator compared with a commercial ferrite device.

6.2 Non-Reciprocal Branch: From Gyrators to All-Pass Filters

6.2.1 Gyrator Principle via Staggered Mixing

The non-reciprocal branch can be realised without magnetic materials by interposing a linear, reciprocal filter between two modulation stages whose local-oscillator (LO) phases differ by a controlled offset [51]. In its most robust form the modulator is implemented as a pair of balanced I/Q mixers, leading to a *double-branch* topology, as shown in Figure 6.2.1.

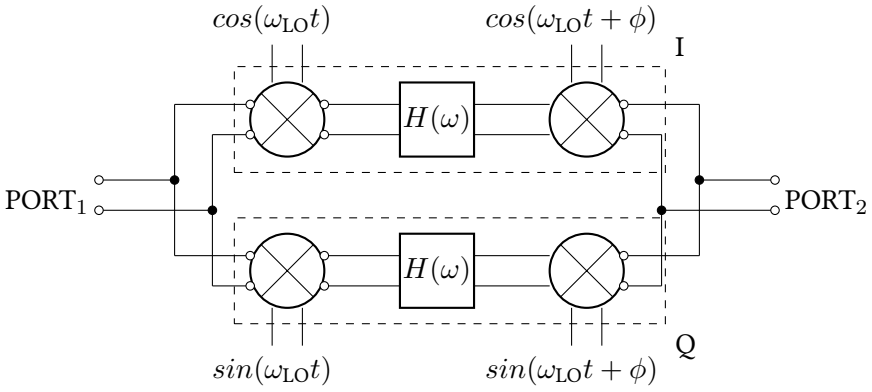


Figure 6.2.1: Schematic of the gyrator-based non-reciprocal branch. The input signal at PORT$_1$ is split into two quadrature paths, each comprising a passive mixer and a second-order bridged-T all-pass filter. The output mixers recombine the two paths at PORT$_2$. The phase shift ϕ of the output LO signals is set to $-\pi/2$ to achieve non-reciprocity.

Consider two parallel paths (labelled I and Q), each consisting of an input mixer, an internal filter $H(\omega)$, and an output mixer. The input mixers of path I and path Q are driven by $\cos(\omega_{\mathrm{LO}}t)$ and $\sin(\omega_{\mathrm{LO}}t)$, respectively, while the output mixers are driven by $\cos(\omega_{\mathrm{LO}}t+\phi)$ and $\sin(\omega_{\mathrm{LO}}t+\phi)$, with ϕ a design parameter.

A monochromatic input signal $x(t)=\cos(\omega_{\mathrm{in}}t)$ entering through the input mixers is frequency-translated to two intermediate components at

$$\omega_L=\omega_{\mathrm{in}}-\omega_{\mathrm{LO}} \qquad \omega_H=\omega_{\mathrm{in}}+\omega_{\mathrm{LO}} \tag{6.8}$$

In the I path, the baseband spectrum after the first mixer is

$$X_I(\omega)=\tfrac{1}{2}\big[\delta(\omega-\omega_L)+\delta(\omega-\omega_H)\big] \tag{6.9}$$

while in the Q path the 90°-shifted LO yields

$$X_Q(\omega)=\tfrac{1}{2}\big[-j\,\delta(\omega-\omega_L)+j\,\delta(\omega-\omega_H)\big] \tag{6.10}$$

Each component then traverses the internal filter, acquiring phase shifts

$$\phi_1 \triangleq \angle H(\omega_L) \qquad \phi_2 \triangleq \angle H(\omega_H) \tag{6.11}$$

Ideally, the filter $H(\omega)$ is lossless, exhibiting unit magnitude $|H(\omega)| = 1$ across the operating band while providing the necessary phase response.

Upon up-conversion through the output mixers (driven with additional phase offset ϕ), the signals recombine at ω_{in}. A detailed bookkeeping of the phasors in each path shows that the components at $\omega_{\text{in}} \pm 2\omega_{\text{LO}}$ generated in the I and Q paths carry opposite signs and therefore cancel, while the four components at ω_{in} add constructively provided

$$\phi_1 - \phi_2 = 2\phi \tag{6.12}$$

When this condition is met, in absence of any loss the output signal has unit amplitude and a phase offset $\phi - \phi_1$. So the forward transmission coefficient is therefore

$$S_{21} = e^{-j(\phi-\phi_1)} \tag{6.13}$$

Analogous analysis for a signal entering from the opposite port yields a reverse transmission coefficient

$$S_{12} = e^{-j(-\phi-\phi_1)} \tag{6.14}$$

This double-branch mixing scheme implements non-reciprocal transmission: the forward and reverse insertion phases differ by 2ϕ.

6.2.2 Signal-Flow Analysis in the Phase–Frequency Domain

Figure 6.2.2 traces the evolution of a unit-amplitude tone at ω_{in} through the double-branch non-reciprocal section, tracking both amplitude and phase at every node in the frequency domain.

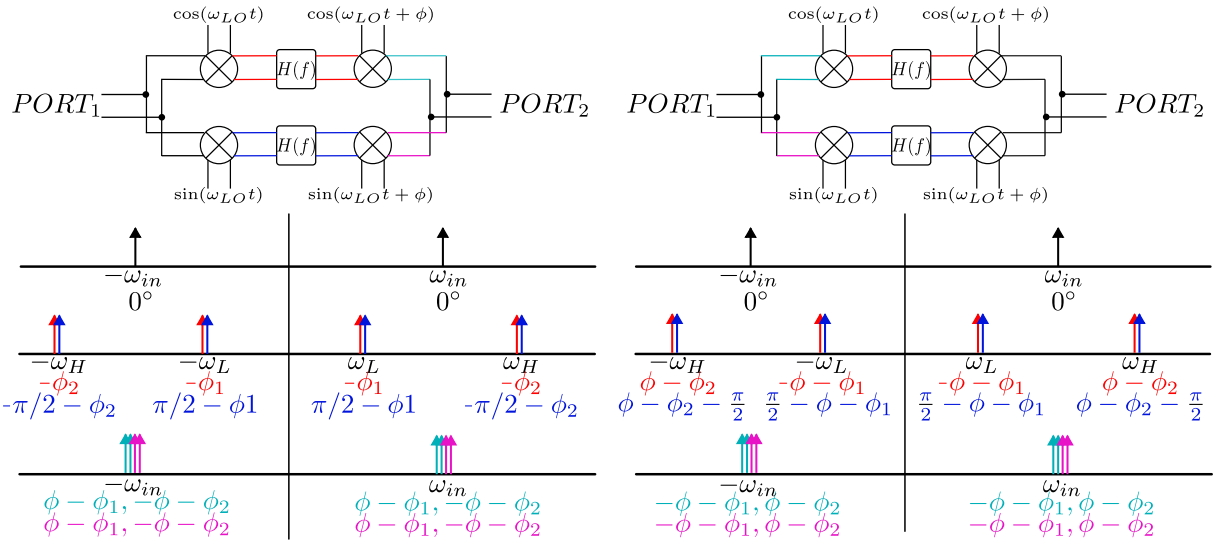


Figure 6.2.2: Phase-frequency domain signal-flow diagram for (left) forward and (right) reverse propagation through the non-reciprocal branch. Spectral lines are annotated with complex amplitude $A\angle\theta$. At each mixing stage the input tone splits into two sidebands; the internal filter rotates their phases by ϕ_1 and ϕ_2; the output mixing stage recombines the four resulting components at ω_{in}. The image products at $\omega_{\text{in}} \pm 2\omega_{\text{LO}}$ cancel pairwise between the I and Q paths.

Forward propagation (Figure 6.2.2a). A unit tone $1\angle 0°$ at ω_{in} enters PORT$_1$. In the I path, the input mixer (driven by $\cos\omega_{\text{LO}}t$) produces two equal-amplitude components

$$\tfrac{1}{2}\angle 0° \text{ at } \omega_L \qquad \tfrac{1}{2}\angle 0° \text{ at } \omega_H \tag{6.15}$$

after the internal filter, each sideband is rotated by the corresponding filter phase ϕ_1 or ϕ_2 without amplitude change:

$$\tfrac{1}{2}\angle -\phi_1 \text{ at } \omega_L \qquad \tfrac{1}{2}\angle -\phi_2 \text{ at } \omega_H \tag{6.16}$$

In the Q path (driven by $\sin\omega_{\text{LO}}t = \cos(\omega_{\text{LO}}t - \pi/2)$), the sidebands acquire additional phases from the 90°-shifted LO:

$$\tfrac{1}{2}\angle +\pi/2 \text{ at } \omega_L \qquad \tfrac{1}{2}\angle -\pi/2 \text{ at } \omega_H \tag{6.17}$$

After traversing the all-pass filter, each sideband is rotated by the corresponding filter phase ϕ_1 or ϕ_2 without amplitude change.

$$\tfrac{1}{2}\angle +\pi/2-\phi_1 \text{ at } \omega_L \qquad \tfrac{1}{2}\angle -\pi/2-\phi_2 \text{ at } \omega_H \tag{6.18}$$

The output mixers (driven with LO phase offset ϕ) up-convert each sideband back to ω_{in}, generating four phasors that, under condition (6.12), sum coherently to a single tone at ω_{in} with amplitude 1 composed of the four phasors:

$$\tfrac{1}{2}\angle\phi - \phi_1 \text{ from } I \text{ path}, \omega_L \qquad \tfrac{1}{2}\angle{-\phi} - \phi_2 \text{ from } I \text{ path}, \omega_H \tag{6.19}$$

$$\tfrac{1}{2}\angle\phi - \phi_1 \text{ from } Q \text{ path}, \omega_L \qquad \tfrac{1}{2}\angle{-\phi} - \phi_2 \text{ from } Q \text{ path}, \omega_H \tag{6.20}$$

In order for the four phasors to add constructively, the internal filter must satisfy $\phi_1 - \phi_2 = 2\phi$, yielding a forward insertion phase of $\phi - \phi_1$.
To summarise, the forward propagation through the non-reciprocal branch produces a single tone at ω_{in} with amplitude 1 and phase $\phi - \phi_1$.

Reverse propagation (Figure 6.2.2b). A unit tone at ω_{in} enters PORT_2. The output mixers now act as down-converters and the input mixers as up-converters; crucially, the LO phases are encountered in the *opposite* order. So at the output of the first mixing stage on the I path, the two sidebands are:

$$\tfrac{1}{2}\angle{-\phi} \text{ at } \omega_L \qquad \tfrac{1}{2}\angle{+\phi} \text{ at } \omega_H \tag{6.21}$$

After the internal filter, each sideband is rotated by the corresponding filter phase ϕ_1 or ϕ_2 without amplitude change:

$$\tfrac{1}{2}\angle{-\phi} - \phi_1 \text{ at } \omega_L \qquad \tfrac{1}{2}\angle{+\phi} - \phi_2 \text{ at } \omega_H \tag{6.22}$$

In the Q path, the 90°-shifted LO produces sidebands with additional phases:

$$\tfrac{1}{2}\angle{-\phi + \pi/2} \text{ at } \omega_L \qquad \tfrac{1}{2}\angle{+\phi - \pi/2} \text{ at } \omega_H \tag{6.23}$$

After traversing the all-pass filter, each sideband is rotated by the corresponding filter phase ϕ_1 or ϕ_2 without amplitude change.

$$\tfrac{1}{2}\angle{-\phi + \pi/2 - \phi_1} \text{ at } \omega_L \qquad \tfrac{1}{2}\angle{+\phi - \pi/2 - \phi_2} \text{ at } \omega_H \tag{6.24}$$

The second mixing stage up-converts each sideband back to ω_{in}, generating four phasors that, under condition (6.12), sum coherently to a single tone at ω_{in} with amplitude 1 composed of the four phasors:

$$\tfrac{1}{2}\angle{-\phi} - \phi_1 \text{ from } I \text{ path}, \omega_L \qquad \tfrac{1}{2}\angle{+\phi} - \phi_2 \text{ from } I \text{ path}, \omega_H \tag{6.25}$$

$$\tfrac{1}{2}\angle{-\phi} - \phi_1 \text{ from } Q \text{ path}, \omega_L \qquad \tfrac{1}{2}\angle{+\phi} - \phi_2 \text{ from } Q \text{ path}, \omega_H \tag{6.26}$$

This reversal changes the sign of the accumulated LO-phase contribution, so the four recombined phasors yield a tone with phase $-\phi - \phi_1$.

Net non-reciprocal phase. The difference between forward and reverse insertion phases is

$$\Delta\Phi = (\phi - \phi_1) - (-\phi - \phi_1) = 2\phi \tag{6.27}$$

With $\phi = -\pi/2$ one obtains $\Delta\Phi = -\pi$, i.e. the desired 180° non-reciprocal phase shift required by the staggered-commutation scheme.

Energy conservation in the mixing process

Denote by P_{in} the available power at ω_{in}. After the first mixing stage the power is equally split between ω_L and ω_H in each of the two paths, giving a total intermediate-frequency power

$$P_{\text{IF}} = 2 \times 2 \times \frac{P_{\text{in}}}{4} = P_{\text{in}} \tag{6.28}$$

where the first factor of 2 accounts for the two (I/Q) paths and the second for the two sidebands per path, each carrying one quarter of the input power (ideal balanced mixer with conversion loss $1/2$ per sideband). The internal all-pass filter is, by construction, lossless ($|H(\omega)| = 1$), so P_{IF} is fully preserved. At the output mixer stage, the image components at $\omega_{\text{in}} \pm 2\omega_{\text{LO}}$ cancel (verified algebraically above), and the four surviving components at ω_{in} must therefore carry the entire power P_{in}, confirming lossless, unitary transmission. Any deviation from perfect image cancellation caused, for example, by I/Q amplitude or phase imbalance, re-distributes a fraction of P_{in} to the image frequencies, directly degrading the insertion loss of the branch.

6.2.3 Design Equations and Clock-Phase Selection

Combining Equations (6.13)–(6.14) with the staggered-commutation requirement of Equation (6.7), the non-reciprocal branch must provide a forward phase of $+180^\circ$ and a reverse phase of 0° (or vice versa, depending on the chosen circulation sense). Setting $\phi - \phi_1 = +\pi$ and $-\phi - \phi_1 = 0$ yields:

$$\begin{cases} \phi = -\dfrac{\pi}{2}, \\ \phi_1 - \phi_2 = 2\phi = -\pi, \\ \phi_1 = +\dfrac{\pi}{2} \qquad \phi_2 = -\dfrac{\pi}{2} \end{cases} \tag{6.29}$$

These three equations fully constrain the design:

1. The first equation fixes the LO phase offset to -90°, i.e. a differential I/Q clock scheme, which simultaneously suppresses sensitivity to duty-cycle mismatch.
2. The second equation requires the internal filter to impose a phase difference of 180° between the two intermediate frequencies ω_L and ω_H.
3. The third equation sets the absolute phase at ω_L to 90°, which, combined with the second, implies $\phi_2 = -90^\circ$ (equivalently 270°).

6.3 All-Pass Filter Design

6.3.1 Clock Frequency and Modulation Index

The power dissipated in the mixer switches scales with the product $C_{\text{sw}}\,\omega_{\text{LO}}\,V_{\text{LO}}^2$, where C_{sw} is the total parasitic capacitance of the switches. To remain within the 2 mW power budget (Table 6.1), the clock frequency must be substantially lower than ω_{in}. Defining the *modulation index*

$$m \triangleq \frac{\omega_{\text{in}}}{\omega_{\text{LO}}} \tag{6.30}$$

one seeks the largest feasible m. With a centre frequency $f_{\text{in}} = 6.5\,\text{GHz}$, choosing $m = 5$ gives $f_m = 1.3\,\text{GHz}$, a value at which CMOS clock drivers can operate efficiently.

6.3.2 Limitations of Artificial Transmission Lines

In earlier circulator implementations [51], [98], the internal filter was realised as a lumped-element artificial transmission line (ATL) designed to approximate a quarter-wavelength delay at ω_{LO}. Each ATL section provides a unit delay

$$t_d = \sqrt{L_s C_s} = \frac{1}{\omega_{\text{in}}} \tag{6.31}$$

where L_s and C_s are the section inductance and capacitance, and the upper bound on usable bandwidth is set by the Bragg frequency $\omega_B = 2/\sqrt{L_s C_s}$. The number of sections required to obtain the total delay $T_d = T_{\text{LO}}/4$, with $T_{\text{LO}} = 2\pi/\omega_{\text{LO}}$, is

$$n = \frac{T_d}{t_d} = \frac{\pi}{2}\,m \tag{6.32}$$

For $m = 5$ this yields $n \approx 8$ sections, and the total series inductance is

$$L_t^{(\text{ATL})} = n\,L_s = \frac{\pi}{2}\,m\,\frac{Z_0}{\omega_{\text{in}}} = 7.85\,\frac{Z_0}{\omega_{\text{in}}} \tag{6.33}$$

with $Z_0 = 50\ \Omega$. Besides occupying large silicon area, each additional inductor contributes finite-Q loss; the aggregate insertion loss grows roughly as n/Q_L, making this approach impractical for $m \geq 5$.Moreover, the phase response of an n-section ATL is

$$\theta_{\text{ATL}}(\omega) = -\,n \cdot 2\arcsin\!\left(\frac{\omega}{\omega_B}\right) \tag{6.34}$$

becomes increasingly non-linear as ω approaches the Bragg frequency, limiting the bandwidth over which the 180° phase-difference condition of Equation (6.29) is maintained.

6.3.3 Second-Order Bridged-T All-Pass Filter

A fundamentally different strategy is to replace the multi-section ATL with a *single* second-order all-pass filter that achieves the required 180° phase excursion between ω_L and ω_H through a steep, highly dispersive phase characteristic rather than through accumulated delay. The general transfer function of a second-order all-pass filter is:

$$H(s) = \frac{s^2 - \dfrac{\omega_0}{Q}\, s + \omega_0^2}{s^2 + \dfrac{\omega_0}{Q}\, s + \omega_0^2}. \tag{6.35}$$

and the corresponding phase response is

$$\angle H(\omega) = -\,2\arctan\left[\frac{\omega_0 \omega}{Q(\omega_0^2 - \omega^2)}\right] \tag{6.36}$$

which spans a total excursion of 360° as ω sweeps from 0 to ∞, passing through -180° at the centre frequency ω_0. Differentiating Equation (6.36) with respect to ω yields the group delay

$$\tau(\omega) = \frac{2Q\,\omega_0\left(\omega_0^2 + \omega^2\right)}{Q^2\left(\omega_0^2 - \omega^2\right)^2 + \omega_0^2\omega^2} \tag{6.37}$$

which peaks in the vicinity of ω_0, where it equals $\tau(\omega_0) = 4Q/\omega_0$; a higher Q produces a steeper phase transition, concentrating the 360° excursion within a narrower band centred on ω_0.

A second-order all-pass function can be realised with several topologies; among these, the bridged-T LC network is particularly attractive for integrated implementation because it minimises the number of lossy inductors. Moreover, the bridged-T topology can be implemented in differential form, which is compatible with the differential I/Q modulation scheme of the non-reciprocal branch. The single-ended bridged-T LC network, shown in Figure 6.3.1a, consists of two series capacitors C_1 forming the arms of the T, a bridging inductor L_1 connected across them, and a shunt branch formed by the series connection of L_2 and C_2. For convenience, the components are represented by their impedances,

$$Z_a = \frac{1}{sC_1} \qquad Z_b = sL_1 \qquad Z_c = \tfrac{1}{sC_2} + sL_2 \tag{6.38}$$

The component values are derived by requiring that the overall transfer function match the all-pass characteristic of Equation (6.35). The analysis is greatly simplified by Bartlett's bisection theorem, which states that any symmetric two-port network is equivalent to a symmetric lattice whose series and diagonal arms are, respectively, the short-circuit and open-circuit impedances of the bisected half-network. The bridged-T is bisected along its vertical symmetry plane: Z_b, which crosses the plane, is split into two series halves of impedance $Z_b/2$, whereas Z_c, which lies on the plane, is split into two parallel elements of impedance $2Z_c$. The resulting half-network is shown in Figure 6.3.1b.

With the terminals lying on the symmetry plane left open or short-circuited together, the half-network impedances are

$$Z_{oc} = Z_a + \frac{Z_b}{2} \qquad Z_{sc} = \frac{Z_b}{2} \parallel 2Z_c \tag{6.39}$$

respectively. As shown in Figure 6.3.1c, the equivalent lattice has Z_{sc} in the series arms and Z_{oc} in the diagonal arms. Substituting Equation (6.38),

$$Z_{oc} = \frac{2L_2 s^2 + \left(\dfrac{1}{C_1} + \dfrac{2}{C_2}\right)}{s}, \qquad Z_{sc} = \frac{sL_1}{2 + s^2 L_1 C_1} \tag{6.40}$$

The first design condition is a constant, purely resistive input impedance at all frequencies, $Z_{in} = Z_0$. For a symmetric lattice the image impedance is $Z_{in} = \sqrt{Z_{oc} Z_{sc}}$, so that, using

$$Z_{oc} Z_{sc} = \frac{L_1 \left[2L_2 s^2 + \left(\dfrac{1}{C_1} + \dfrac{2}{C_2}\right)\right]}{2 + s^2 L_1 C_1} = Z_0^2 = 1\ \Omega^2 \tag{6.41}$$

Since this identity must hold for every s, the coefficients of equal powers of s in the numerator and denominator must be equal, which yields

$$2L_1 L_2 = L_1 C_1 \ \Rightarrow\ C_1 = 2L_2, \tag{6.42}$$

$$L_1 \left(\frac{1}{C_1} + \frac{2}{C_2}\right) = 2 \ \Rightarrow\ \frac{1}{C_1} + \frac{2}{C_2} = \frac{2}{L_1}. \tag{6.43}$$

The second condition is that the transfer function assumes the form of Equation (6.35). For a constant-resistance lattice terminated in $Z_0 = 1\ \Omega$, the transfer function is

$$H(s) = \frac{1 - Z_{sc}}{1 + Z_{sc}} = \frac{2 + s^2 L_1 C_1 - L_1 \left[2L_2 s^2 + \left(\frac{1}{C_1} + \frac{2}{C_2}\right)\right]}{2 + s^2 L_1 C_1 + L_1 \left[2L_2 s^2 + \left(\frac{1}{C_1} + \frac{2}{C_2}\right)\right]} = \frac{s^2 - \frac{1}{C_1} s + \frac{2}{L_1 C_1}}{s^2 + \frac{1}{C_1} s + \frac{2}{L_1 C_1}} \tag{6.44}$$

This is already an all-pass function, since the numerator is the mirror image of the denominator, $N(s) = D(-s)$. Comparing with Equation (6.35) gives

$$\frac{1}{C_1} = \frac{\omega_0}{Q} \ \Rightarrow\ C_1 = \frac{Q}{\omega_0} \tag{6.45}$$

$$\frac{2}{L_1 C_1} = \omega_0^2 \ \Rightarrow\ L_1 = \frac{2}{\omega_0^2 C_1} = \frac{2}{\omega_0 Q} \tag{6.46}$$

The remaining values follow from Equations (6.42) and (6.43):

$$L_2 = \frac{C_1}{2} = \frac{Q}{2\omega_0} \tag{6.47}$$

$$C_2 = \frac{2L_1C_1}{2C_1 - L_1} = \frac{\dfrac{4}{\omega_0^2}}{\dfrac{2}{\omega_0}\left(Q - \dfrac{1}{Q}\right)} = \frac{2Q}{\omega_0\,(Q^2-1)} \tag{6.48}$$

Note that a physically realisable (positive) C_2 requires $Q > 1$. Finally, the values are denormalised to the characteristic impedance Z_0 by multiplying the inductances by Z_0 and dividing the capacitances by Z_0:

$$L_1 = \frac{2Z_0}{\omega_0 Q}, \qquad L_2 = \frac{Q\,Z_0}{2\omega_0}, \qquad C_1 = \frac{Q}{\omega_0 Z_0}, \qquad C_2 = \frac{2Q}{\omega_0(Q^2-1)\,Z_0} \tag{6.49}$$

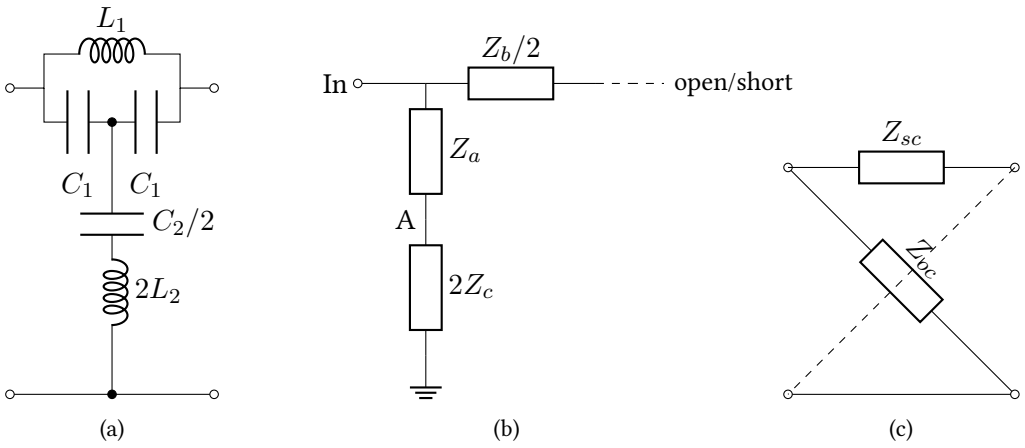
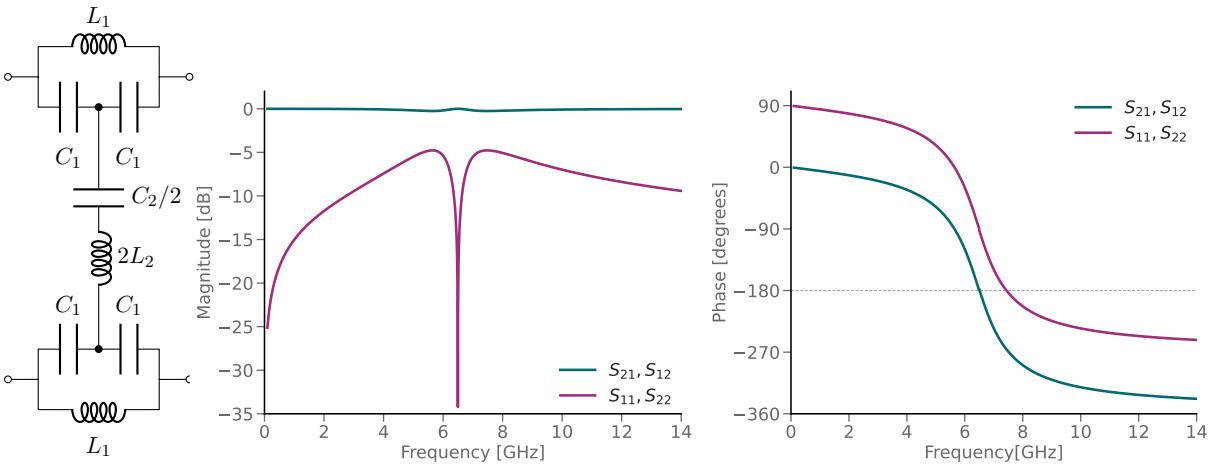


Figure 6.3.1: Second-order bridged-T LC all-pass filter: (a) single-ended circuit schematic, (b) half-network obtained by Bartlett's bisection, and (c) equivalent lattice network.

The differential form of the bridged-T all-pass filter is obtained by duplicating the single-ended circuit and connecting the two copies in a differential configuration, as shown in Figure 6.3.2a. The shunt branches of the two copies meet at a virtual ground, which acts as the differential-mode return path. The two shunt branches are therefore connected in series between the two centre nodes, so that the two C_2 capacitors merge into a single capacitor $C_2/2$ and the two L_2 inductors merge into a single inductor $2L_2$, reducing the total component count.



(a) (b) (c)

Figure 6.3.2: Differential second-order bridged-T LC all-pass filter: (a) circuit schematic, (b) simulated S-parameters, and (c) phase response.

6.3.4 Determination of the Quality Factor

The second design equation in (6.29) requires $\phi_1 - \phi_2 = -\pi$ which, since phases are defined modulo 2π, is equivalent to $\phi_1 - \phi_2 = \pi$. Setting $\omega_0 = \omega_{\text{in}}$ so that the filter centre coincides with the circulator centre frequency, the two intermediate frequencies are $\omega_L = \omega_0 - \omega_{\text{LO}}$ and $\omega_H = \omega_0 + \omega_{\text{LO}}$. Evaluating Equation (6.36) at these frequencies, and selecting the branch of the arctangent that keeps the phase continuous through $-\pi$ at ω_0, one obtains

$$\phi_1 \triangleq \angle H(\omega_0 - \omega_{\text{LO}}) = -2\arctan\left(\frac{1}{Q}\,\frac{\omega_0}{\omega_{\text{LO}}}\,\frac{\omega_0 - \omega_{\text{LO}}}{2\omega_0 - \omega_{\text{LO}}}\right) \tag{6.50}$$

$$\phi_2 \triangleq \angle H(\omega_0 + \omega_{\text{LO}}) = -2\arctan\left(\frac{1}{Q}\,\frac{\omega_0}{\omega_{\text{LO}}}\,\frac{\omega_0 + \omega_{\text{LO}}}{2\omega_0 + \omega_{\text{LO}}}\right) + \pi \tag{6.51}$$

In the regime $\omega_0 \gg \omega_{\text{LO}}$ (valid for $m = 5$), the fractions $(\omega_0 \pm \omega_{\text{LO}})/(2\omega_0 \pm \omega_{\text{LO}})$ both tend to $1/2$, and one obtains

$$\phi_2 - \phi_1 \;\approx\; 4\arctan\left(\frac{\omega_0}{2Q\,\omega_{\text{LO}}}\right) \tag{6.52}$$

Imposing $\phi_2 - \phi_1 = \pi$ yields

$$Q = \frac{1}{2}\,\frac{\omega_0}{\omega_{\text{LO}}} = \frac{m}{2} \tag{6.53}$$

For $m = 5$, $\omega_0 = 2\pi \times 6.5\,\text{GHz}$, and $\omega_{\text{LO}} = 2\pi \times 1.3\,\text{GHz}$, the required quality factor is $Q = 2.5$. Substituting this value into the exact expressions (6.50) and (6.51) gives $\phi_1 - \phi_2 \approx 181.8^\circ$, which confirms the validity of the approximation. Such a low pole quality factor is a favourable feature: the filter response is only mildly sensitive to the finite quality factor of on-chip spiral inductors, so that the design remains robust against component losses.

6.3.5 Dimensioning of the All-Pass Filter Components

With $\omega_0 = 2\pi \times 6.5\,\text{GHz}$, $Q = 2.5$, and $Z_0 = 50\ \Omega$, Equations (6.49) give the following single-ended component values:

$$\begin{aligned} L_1 &= \frac{2 \times 50}{2\pi \times 6.5{\times}10^9 \times 2.5} = 0.98\ \text{nH} \\ L_2 &= \frac{2.5 \times 50}{2 \times 2\pi \times 6.5{\times}10^9} = 1.53\ \text{nH} \\ C_1 &= \frac{2.5}{2\pi \times 6.5{\times}10^9 \times 50} = 1.22\ \text{pF} \\ C_2 &= \frac{2 \times 2.5}{2\pi \times 6.5{\times}10^9 \times (2.5^2 - 1) \times 50} = 0.57\ \text{pF} \end{aligned} \tag{6.54}$$

In the differential implementation of Figure 6.3.2a, the shunt branch is realised with $C_2/2 = 0.23\,\text{pF}$ and $2L_2 = 3.06\,\text{nH}$. The simulated S-parameters and phase response of the differential filter are reported in Figures 6.3.2b and 6.3.2c, respectively. The input matching confirms the constant-resistance behaviour of the network over the whole band, while the transmission phase crosses $-180°$ at $f_0 = 6.5\,\text{GHz}$ and exhibits a $180°$ difference between $f_L = 5.2\,\text{GHz}$ and $f_H = 7.8\,\text{GHz}$, as required by Eq (6.29).

The total series inductance per I or Q path is

$$L_t^{(\text{AP})} = L_1 + L_2 = \frac{Z_0}{\omega_{\text{in}}}\left(\frac{2}{Q} + \frac{Q}{2}\right) = \frac{Z_0}{\omega_{\text{in}}}\left(\frac{4\omega_{\text{LO}}}{\omega_{\text{in}}} + \frac{\omega_{\text{in}}}{4\omega_{\text{LO}}}\right) = 2.05\,\frac{Z_0}{\omega_{\text{in}}} \tag{6.55}$$

which is $3.8\times$ smaller than the ATL value of Equation (6.33), even before accounting for the factor-of-two duplication required by the I/Q double-branch topology. The reduction in total inductance translates directly into smaller die area and lower series-resistance loss.

6.3.6 First-Order Lattice All-Pass Filter (Reciprocal Branches)

Each reciprocal branch must provide a fixed $90°$ phase shift at ω_0. A first-order lattice all-pass filter, shown in Figure 6.3.3a, achieves this with a single inductor and capacitor per path. Its transfer function is in the form of:

$$H(s) = \frac{\omega_0 - s}{\omega_0 + s} \tag{6.56}$$

with $|H(j\omega)| = 1$ and phase

$$\angle H(\omega) = -2\arctan\left(\frac{\omega}{\omega_0}\right) \tag{6.57}$$

In this case the network is already in lattice form, so Bartlett's theorem is not required: the series arms have impedance $Z_a = sL_3$ and the diagonal arms $Z_b = 1/(sC_3)$, which play the roles of Z_{sc} and Z_{oc}, respectively. The constant-resistance condition $Z_{in} = \sqrt{Z_a Z_b} = Z_0$ becomes

$$Z_a Z_b = sL_3 \cdot \frac{1}{sC_3} = \frac{L_3}{C_3} = Z_0^2 \ \Rightarrow\ L_3 = Z_0^2\, C_3 \tag{6.58}$$

which is inherently frequency-independent and therefore yields a single constraint, leaving one free parameter, as expected for a first-order network. The transfer function of the constant-resistance lattice terminated in Z_0 is

$$H(s) = \frac{Z_0 - Z_a}{Z_0 + Z_a} = \frac{Z_0 - sL_3}{Z_0 + sL_3} = \frac{\frac{1}{C_3} - sL_3}{\frac{1}{C_3} + sL_3} = \frac{\omega_0 - s}{\omega_0 + s} \tag{6.59}$$

which is already an all-pass function. Comparing with Equation (6.56),

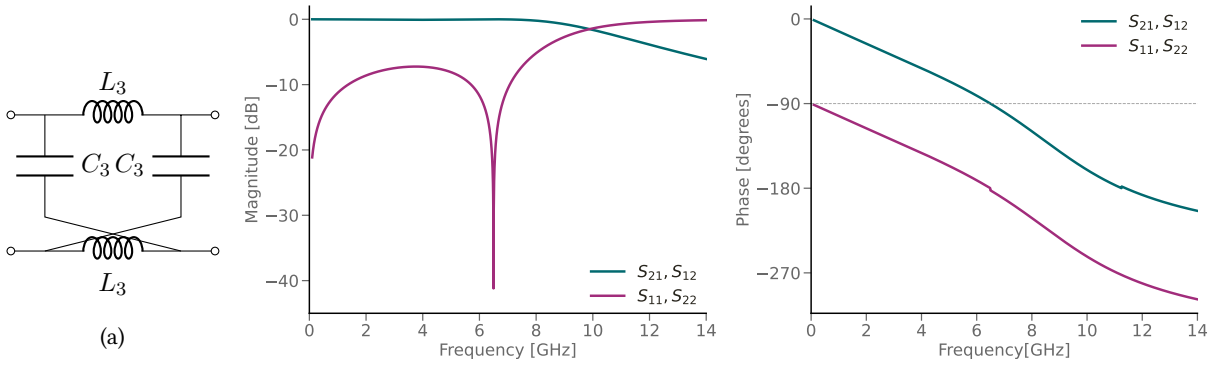
$$\omega_0 = \frac{Z_0}{L_3} \;\Rightarrow\; L_3 = \frac{Z_0}{\omega_0} \tag{6.60}$$

$$C_3 = \frac{L_3}{Z_0^2} \;\Rightarrow\; C_3 = \frac{1}{\omega_0 Z_0} \tag{6.61}$$

It is worth noting that the only design parameter is ω_0, the frequency at which the phase shift equals $-90°$. The group delay of the first-order all-pass filter is

$$\tau(\omega) = \frac{2\omega_0}{\omega_0^2 + \omega^2} \qquad \tau(0) = \frac{2}{\omega_0} = \frac{2L_3}{Z_0} \qquad \tau(\omega_0) = \frac{1}{\omega_0} = \frac{L_3}{Z_0} \tag{6.62}$$

Setting $\omega_0 = \omega_{\text{in}}$ therefore provides the required $-90°$ phase shift at the centre frequency, satisfying the reciprocal-branch requirement of Equation (6.7).



(a) (b) (c)

Figure 6.3.3: First-order lattice LC all-pass filter: (a) circuit schematic, (b) simulated S-parameters, and (c) phase response.

The component values for the first-order all-pass filter are therefore:

$$L_3 = \frac{50}{2\pi \times 6.5 \times 10^9} = 1.22 \text{ nH} \qquad C_3 = \frac{1}{2\pi \times 6.5 \times 10^9 \times 50} = 0.49 \text{ pF} \tag{6.63}$$

The corresponding simulated S-parameters and phase response are shown in Figures 6.3.3b and 6.3.3c, respectively: the network is matched over the whole band, and the transmission phase equals $-90°$ at $f_0 = 6.5\,\text{GHz}$, following the smooth $-2\arctan(\omega/\omega_0)$ characteristic predicted by Equation (6.57).

6.4 Bandwidth Analysis

The circulator bandwidth is ultimately limited by the frequency range over which the total circulation phase ϕ_{tot} remains close to zero. Following Section 6.1.2, define

$$\phi_{\text{tot}}(\omega_{\text{in}}) \triangleq \big[\phi_2(\omega_{\text{in}}) - \phi_1(\omega_{\text{in}})\big] - 2\,\phi_3(\omega_{\text{in}}), \tag{6.64}$$

where ϕ_1, ϕ_2 are evaluated at $\omega_L = \omega_{\text{in}} - \omega_{\text{LO}}$ and $\omega_H = \omega_{\text{in}} + \omega_{\text{LO}}$ via Equation (6.36), and ϕ_3 is the first-order all-pass phase evaluated at ω_{in} via Equation (6.57).

At the design centre, $\phi_{\text{tot}}(\omega_0) = \pi - 2 \times \pi/2 = 0$ by construction. As ω_{in} departs from ω_0, the three phase terms deviate from their nominal values. The key advantage of the all-pass architecture is that the deviation of $\phi_2 - \phi_1$ is *non-monotonic*: it shows a plateau around ω_0 (zero first derivative), whereas ϕ_3 deviates monotonically. Because the two deviations partially cancel, the net ϕ_{tot} remains small over a wider band than in the ATL case, where all phase deviations are monotonic and additive.

To quantify this, one can Taylor-expand ϕ_{tot} around ω_0. Using Equations (6.36) and (6.57) and setting $\Delta\omega = \omega_{\text{in}} - \omega_0$:

$$\phi_{\text{tot}}(\omega_0 + \Delta\omega) \approx \underbrace{\phi_{\text{tot}}(\omega_0)}_{=0} + \underbrace{\phi'_{\text{tot}}(\omega_0)}_{=0}\,\Delta\omega + \frac{1}{2}\,\phi''_{\text{tot}}(\omega_0)\,(\Delta\omega)^2 + \mathcal{O}(\Delta\omega^3). \tag{6.65}$$

The vanishing of the first-order term is a consequence of the plateau in $\phi_2 - \phi_1$; the circulator bandwidth is therefore determined by the second-order coefficient and by the maximum tolerable phase error ϵ:

$$|\Delta\omega|_{\max} \approx \sqrt{\frac{2\epsilon}{|\phi''_{\text{tot}}(\omega_0)|}}. \tag{6.66}$$

Simulation and measurement both confirm that, for $\epsilon = 20^\circ$, the all-pass architecture sustains a fractional bandwidth of approximately 28%, compared with 18% for a six-section ATL with equivalent modulation index.

6.5 CMOS Circulator Implementation

Figure 6.5.1 presents the complete schematic of the proposed circulator. The architecture directly maps the theoretical framework developed above: two reciprocal branches (first-order lattice filters) and one non-reciprocal branch (two parallel second-order bridged-T all-pass filters with I/Q passive mixers).

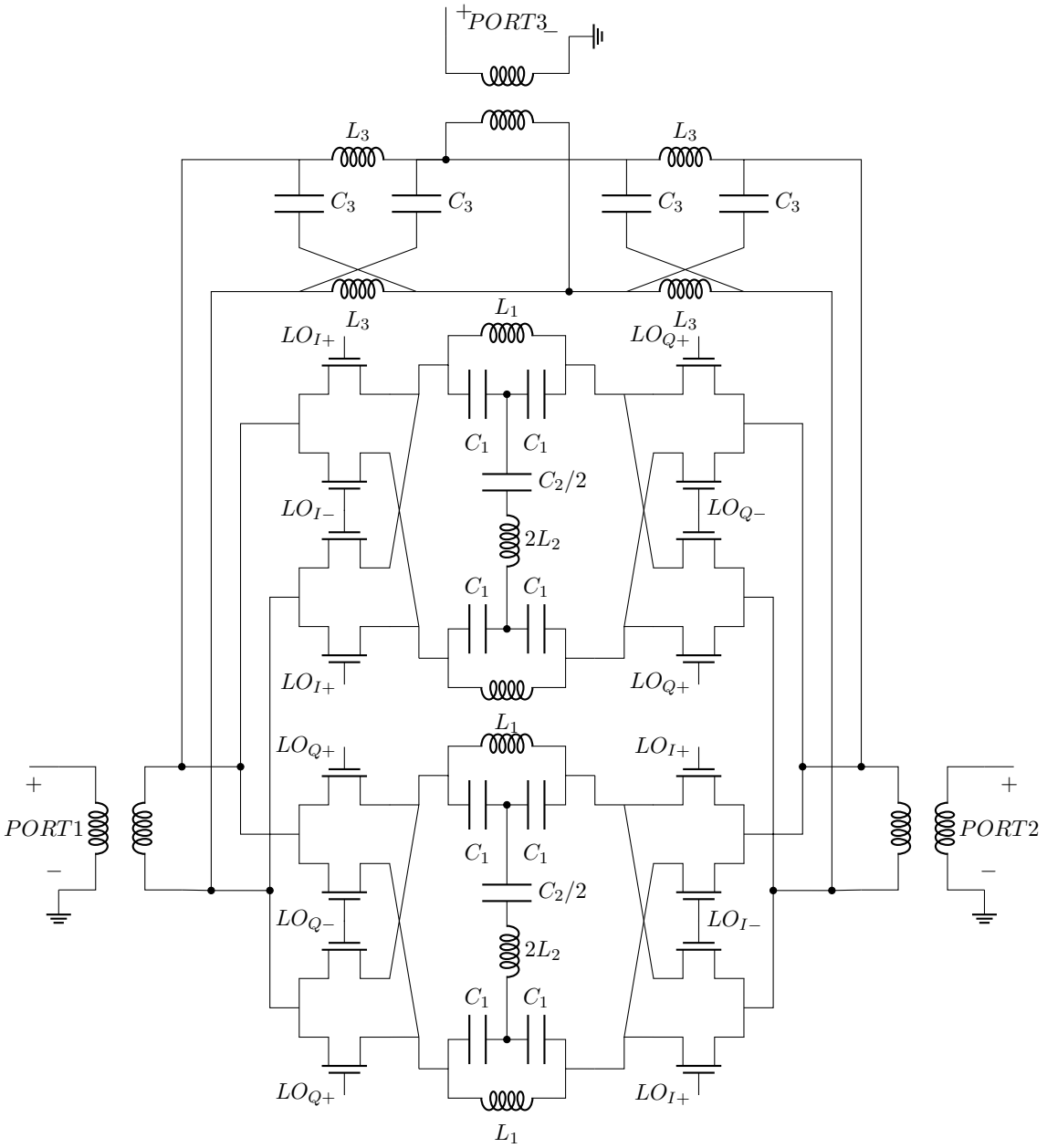


Figure 6.5.1: Complete schematic of the CMOS circulator. The three ports are interfaced through on-chip transformer baluns. The non-reciprocal branch contains two parallel I/Q paths, each comprising a passive nMOS mixer pair and a second-order bridged-T all-pass filter. The two reciprocal branches are first-order lattice all-pass filters.

6.5.1 Mixer Design

The passive mixers are realised as differential nMOS-only switches in the same technology, SG13G2 130 nm BiCMOS usded to design the LNA. The switch on-resistance R_{ON} and parasitic capacitance C_p are the two critical parameters: R_{ON} contributes directly to insertion loss by appearing in series with the signal path, while C_p introduces unwanted reciprocal and non-reciprocal phase shifts that perturb the designed all-pass filter response.

To choose the transistor size, the following trade-off must be considered: increasing the width W reduces R_{ON} but increases C_p, whereas reducing W has the opposite effect. Through several iterations of circuit simulation for different transistor sizes, we obtained the s-parameters reported in Table 6.2 at the operating frequency of 6.5 GHz for various transistor widths with a channel length of $L = 130$ nm. We observe that the insertion loss (S_{21}, S_{32}, S_{13}) improves, while the isolation (S_{23}, S_{31}, S_{12}) degrades with increasing width. A width of $W = 70$ μm is chosen as a good compromise between insertion loss and occupied area.

Width (μm)	30	50	70	100
S11 (dB)	-13.99	-14.48	-15.22	-15.14
S12 (dB)	-22.65	-32.19	-42.57	-32.76
S13 (dB)	-2.55	-1.94	-1.63	-1.44
S21 (dB)	-5.04	-3.89	-3.31	-3.06
S22 (dB)	-13.98	-14.47	-15.22	-14.51
S23 (dB)	-10.13	-12.72	-15.61	-18.21
S31 (dB)	-10.13	-12.73	-15.62	-17.68
S32 (dB)	-2.55	-1.94	-1.63	-1.50
S33 (dB)	-28.33	-25.93	-23.69	-22.30

Table 6.2: S-parameters of the mixer for different transistor widths with channel length $L = 130$ nm at $f = 6.5$ GHz.

6.6 Clock Generation Circuit

6.6.1 Architecture

The mixers require four differential clock phases at the LO frequency of 1.3 GHz. To generate them, an on-chip clock generation circuit has been implemented, as illustrated in Figure 6.6.1. The circuit is driven by an external sinusoidal reference at twice the LO frequency (2.6 GHz), which is processed by a chain of stages.

An active balun, built around a common-gate/common-source transistor pair, converts the single-ended input into a differential signal of sufficient amplitude. A cascade of self-biased inverting stages then progressively amplifies and clips the waveform, turning the sinusoid into a square wave with fast rising and falling edges. A latch-based divide-by-2 stage generates the four clock phases at 1.3 GHz. Finally, phase-alignment circuits and output buffers compensate for the propagation-delay differences between the four paths and provide the drive strength needed to switch the mixer transistors.

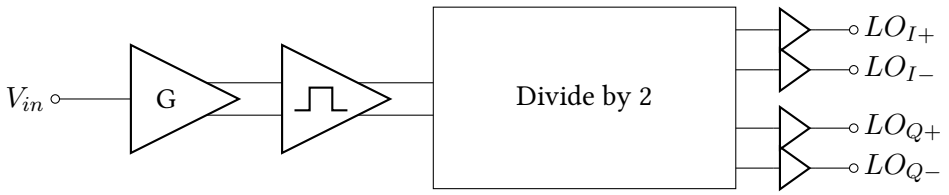


Figure 6.6.1: Block diagram of the on-chip clock generation circuit: the single-ended 2.6 GHz input is amplified, squared, divided by two and buffered to generate four differential 1.3 GHz clock signals with 90° phase separation.

6.6.2 Active Balun

The first stage of the chain converts the single-ended input into a differential signal with sufficient amplitude to drive the following squaring stages. Figure 6.6.2 shows the schematic of the active balun. Transistors M_1 and M_2 form a common-gate/common-source pair that produces two anti-phase replicas of the input; these are AC-coupled to a differential pair (M_3, M_4) with tail current source M_5, which provides additional gain and improves both the common-mode rejection and the balance of the two outputs.

The reference signal is generated at room temperature and delivered to the cryogenic stage through a coaxial cable. Assuming an amplitude of 0.1 mV at the chip input (about -70 dBm in $50\,\Omega$), the active balun must provide a voltage gain of at least 9 dB to ensure that the following squaring stages are driven into saturation. In addition, the circuit must maintain good amplitude and phase balance between the two outputs over the operating band around 2.6 GHz, with a target phase error below 5° and an amplitude mismatch below 0.5 dB.

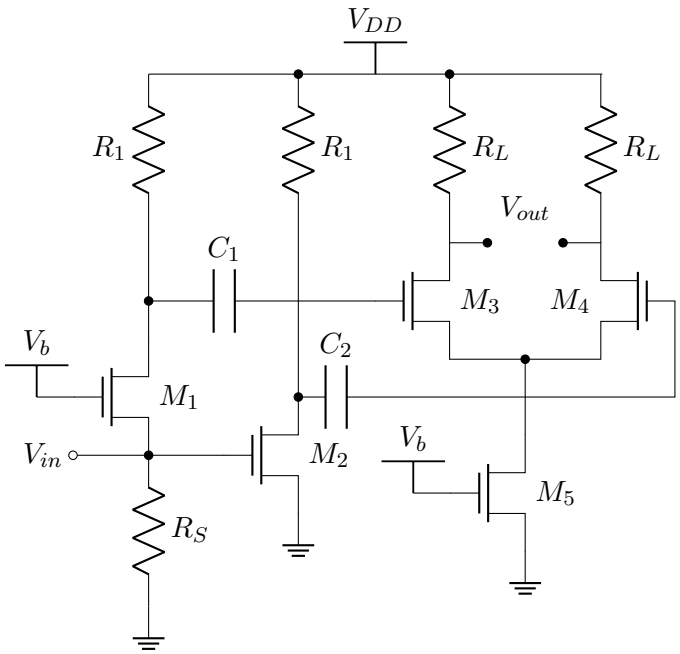


Figure 6.6.2: Schematic of the active balun: common-gate amplifier (M_1), common-source amplifier (M_2) and differential pair (M_3, M_4) with tail current source (M_5).

DC Operating Point

The supply voltage is $V_{\text{DD}} = 1.8\,\text{V}$ and the bias voltage is $V_b = \frac{7}{9}V_{\text{DD}} \approx 1.4\,\text{V}$. The gate-source voltage of M_1 is

$$V_{\text{GS1}} = V_b - V_{\text{S1}} = V_b - I_{\text{D1}}R_S \tag{6.67}$$

where V_{S1} is the source voltage of M_1 and I_{D1} its drain current. The drain voltage is

$$V_{\text{D1}} = V_{\text{DD}} - I_{\text{D1}}R_1 \tag{6.68}$$

To keep M_1 in saturation, the drain-source voltage must satisfy

$$V_{\text{DS1}} = V_{\text{D1}} - V_{\text{S1}} = V_{\text{DD}} - I_{\text{D1}}(R_1 + R_S) > V_{\text{GS1}} - V_{\text{TH}} \tag{6.69}$$

The gate of the common-source transistor M_2 is connected to the source of M_1, hence

$$V_{\text{GS2}} = V_{\text{S1}} = I_{\text{D1}}R_S \tag{6.70}$$

A key design choice is to size M_1 and M_2 so that, under nominal conditions, they operate with equal gate-source voltages and carry equal drain currents, which yields balanced signal swings at the two drains.

Setting $V_{\mathrm{GS1}} = V_{\mathrm{GS2}}$ and $I_{\mathrm{D1}} = I_{\mathrm{D2}} = I_D$ in Equations (6.67) and (6.70) gives

$$V_b - I_D R_S = I_D R_S \quad \Rightarrow \quad I_D = \frac{V_b}{2R_S} \tag{6.71}$$

With $V_b = 1.4\,\mathrm{V}$ and $R_S = 5\,\mathrm{k\Omega}$, the bias current is $I_D = 140\,\mu\mathrm{A}$, which offers a good trade-off between transconductance and power consumption. The drain resistor R_1 is chosen to maximise the voltage gain while preserving adequate headroom. With $R_1 = 1\,\mathrm{k\Omega}$,

$$V_{\mathrm{D1}} = V_{\mathrm{D2}} = V_{\mathrm{DD}} - I_D R_1 = 1.8 - (140 \times 10^{-6})(1000) = 1.66\,\mathrm{V} \tag{6.72}$$

Since $V_{\mathrm{S1}} = I_D R_S = 0.7\,\mathrm{V}$, the drain-source voltages are $V_{\mathrm{DS1}} = 0.96\,\mathrm{V}$ and $V_{\mathrm{DS2}} = 1.66\,\mathrm{V}$. Both exceed the overdrive voltage $V_{\mathrm{OV}} = V_{\mathrm{GS}} - V_{\mathrm{TH}} \approx 0.1\,\mathrm{V}$ expected for a threshold voltage $V_{\mathrm{TH}} \approx 0.6\,\mathrm{V}$ at $4\,\mathrm{K}$, so both devices remain in saturation.

The differential pair is biased by the tail current source M_5, whose gate is connected to V_b and whose source is grounded, so that

$$I_{\mathrm{tail}} = I_{\mathrm{D3}} + I_{\mathrm{D4}} = 2I_{\mathrm{branch}} \tag{6.73}$$

with $I_{\mathrm{branch}} \approx 170\,\mu\mathrm{A}$ per branch. The load resistors are set to $R_L = 4\,\mathrm{k\Omega}$, which provides sufficient output swing while keeping M_3 and M_4 in saturation.

Small-Signal Analysis

The input signal v_{in} is applied simultaneously to the source of M_1, which therefore operates as a common-gate stage, and to the gate of M_2, which operates as a common-source stage. The input impedance is set by the common-gate device:

$$Z_{\mathrm{in}} \approx \frac{1}{g_{m1}} \parallel R_S \approx \frac{1}{g_{m1}} \tag{6.74}$$

where g_{m1} is the transconductance of M_1. With $g_{m1} \approx 1\,\mathrm{mS}$, $Z_{\mathrm{in}} \approx 100\,\Omega$.

The small-signal drain voltages of the two devices are

$$v_{d1} = +g_{m1} R_1\, v_{\mathrm{in}}, \tag{6.75}$$

$$v_{d2} = -g_{m2} R_1\, v_{\mathrm{in}}, \tag{6.76}$$

so that, for matched transistors ($g_{m1} = g_{m2} = g_m$), the first stage delivers two outputs of equal amplitude and opposite phase, with a single-ended gain

$$A_{v1} = g_m R_1 \tag{6.77}$$

With $g_m = 1\,\text{mS}$ and $R_1 = 1\,\text{k}\Omega$, $A_{v1} = 1$: the first stage acts essentially as a unity-gain single-ended-to-differential converter, and the voltage gain is provided by the differential pair. The coupling capacitors C_1 and C_2 block the DC component while passing the $2.6\,\text{GHz}$ signal with negligible attenuation.

For a balanced differential pair with matched devices ($g_{m3} = g_{m4}$) and load resistors R_L, the differential gain is $A_{v,\text{diff}} = g_{m3} R_L$, and the differential output voltage is

$$v_{\text{out,diff}} = v_{\text{out}+} - v_{\text{out}-} = A_{v,\text{diff}}\,(v_{d1} - v_{d2}) = 2\,g_{m3} R_L \cdot g_m R_1\, v_{\text{in}} \tag{6.78}$$

The total voltage gain of the active balun is therefore

$$A_{v,\text{total}} = \frac{v_{\text{out,diff}}}{v_{\text{in}}} = 2\,g_m R_1 \cdot g_{m3} R_L \tag{6.79}$$

With $g_{m3} = 2\,\text{mS}$ and $R_L = 4\,\text{k}\Omega$ this yields $A_{v,\text{total}} = 2 \cdot 1 \cdot 8 = 16$ (24 dB), which comfortably exceeds the $9\,\text{dB}$ requirement and leaves margin for process variations and temperature-dependent changes of the transconductances.

The amplitude and phase balance of the outputs is determined by the matching of M_3/M_4 and of the load resistors, and by the symmetry of the layout; a common-centroid arrangement of the differential pair and matched resistor arrays are therefore adopted. The bandwidth is limited by the poles at the drain nodes, $\omega_{p1} \approx 1/[R_1(C_{\text{db1}} + C_{\text{gd1}} + C_{\text{gs3}})]$ and $\omega_{p2} \approx 1/[R_L(C_{\text{db3}} + C_{\text{load}})]$; owing to the larger load resistance, the output pole is the critical one at $2.6\,\text{GHz}$

Implementation Details

The active balun is implemented with M_1 and M_2 sized at $W/L = 1\,\mu\text{m}/0.13\,\mu\text{m}$, and M_3 and M_4 at $W/L = 10\,\mu\text{m}/0.14\,\mu\text{m}$. The tail current source M_5 is sized at $W/L = 10\,\mu\text{m}/0.18\,\mu\text{m}$. The resistors are $R_S = 5\,\text{k}\Omega$, $R_1 = 1\,\text{k}\Omega$ and $R_L = 4\,\text{k}\Omega$. The coupling capacitance is $C_1 = C_2 = 6\,\text{pF}$, which provides negligible attenuation at the operating frequency.

6.6.3 Squaring Stage

The squaring stage converts the sinusoidal output of the active balun into a square wave. It consists of a CMOS inverter with a feedback resistor R_F connected between output and input, as shown in Figure 6.6.3.

The input signal V_{in} is applied to the gates of both P_1 and N_1, and the output V_{out} is taken at their common drain node. When the input rises above the switching threshold of the inverter, N_1 conducts more strongly than P_1 and pulls the output low; when the input falls below the threshold, P_1 prevails and pulls the output high.

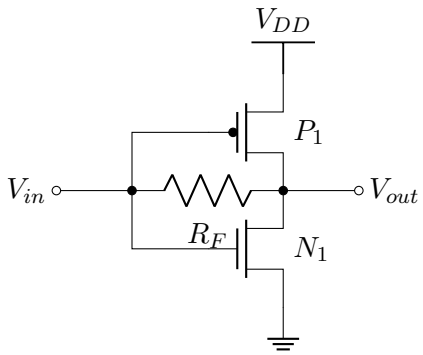


Figure 6.6.3: Squaring stage: a CMOS inverter (P_1, N_1) with feedback resistor R_F, which self-biases the stage at its switching threshold.

Ignoring R_F, the circuit is a standard inverter, whose switching threshold V_M is set by the transistor sizes and threshold voltages. The transfer characteristic is the usual S-shaped curve, with a sharp transition as the input crosses V_M. At this point both transistors are in saturation ($V_{\mathrm{DS}} > V_{\mathrm{GS}} - V_{\mathrm{TH},N}$ for the NMOS and $V_{\mathrm{SD}} > V_{\mathrm{SG}} - |V_{\mathrm{TH},P}|$ for the PMOS), and their currents are

$$I_{\mathrm{D},N} = \frac{1}{2} k_n \frac{W_n}{L_n} (V_{\mathrm{GS},N} - V_{\mathrm{TH},N})^2 \tag{6.80}$$

$$I_{\mathrm{D},P} = \frac{1}{2} k_p \frac{W_p}{L_p} (V_{\mathrm{SG},P} - |V_{\mathrm{TH},P}|)^2 \tag{6.81}$$

With no load at the output the two currents must be equal, so the switching threshold is obtained from

$$\frac{1}{2} k_n \frac{W_n}{L_n} (V_M - V_{\mathrm{TH},N})^2 = \frac{1}{2} k_p \frac{W_p}{L_p} (V_{\mathrm{DD}} - V_M - |V_{\mathrm{TH},P}|)^2 \tag{6.82}$$

which gives

$$V_M = \frac{V_{\mathrm{DD}} - |V_{\mathrm{TH},P}| + r\, V_{\mathrm{TH},N}}{1 + r}, \qquad r = \sqrt{\frac{k_n W_n L_p}{k_p W_p L_n}} \tag{6.83}$$

The transistors are sized so that $V_M = V_{\mathrm{DD}}/2$, which maximises the symmetric input range and yields a 50% duty cycle at the output.

The feedback resistor R_F closes a DC negative-feedback loop around the inverter: in the absence of an input signal, the only consistent operating point is $V_{\mathrm{in}} = V_{\mathrm{out}} = V_M$, so that the stage is self-biased at its own switching threshold. Since the input is AC-coupled, the incoming sinusoid is centred on V_M and every zero crossing produces an output transition, while the high gain of the inverter around V_M sharpens the edges. R_F is chosen large compared to the source impedance so that it does not load the signal path, and the resulting high-pass corner with the coupling capacitor lies well below $2.6\,\mathrm{GHz}$. Cascading several such stages progressively increases the amplitude and clips the waveform into a square wave.

Implementation Details

After iterative simulation and optimization, a suitable ratio between PMOS and NMOS transistor sizes was found to compensate for the lower hole mobility in the PMOS device, ensuring balanced pull-up and pull-down currents and placing the inverter switching threshold at half the supply voltage ($V_M = 0.9\,\mathrm{V} \approx V_{\mathrm{DD}}/2$):

$$\frac{(W/L)_{\mathrm{PMOS}}}{(W/L)_{\mathrm{NMOS}}} = \frac{385/130}{150/130} \approx 2.57 \tag{6.84}$$

To provide sufficient current to drive the following stages, the transistors are scaled by a factor of 10, resulting in $W_{\mathrm{PMOS}} = 3.85\,\mu\mathrm{m}$, $L_{\mathrm{PMOS}} = 130\,\mathrm{nm}$, $W_{\mathrm{NMOS}} = 1.5\,\mu\mathrm{m}$, and $L_{\mathrm{NMOS}} = 130\,\mathrm{nm}$. The feedback resistor is set to $R_F = 200\,\mathrm{k\Omega}$, which is large enough to avoid loading the input signal and to set the high-pass corner frequency below $2.6\,\mathrm{GHz}$.

6.6.4 Frequency Divider

The frequency divider generates the four quadrature clock phases ($0°$, $90°$, $180°$ and $270°$) at $1.3\,\mathrm{GHz}$ from the $2.6\,\mathrm{GHz}$ square-wave clock.

The divider is implemented with four differential D-latches arranged as two master-slave pairs, as illustrated in Figure 6.6.4. Within each pair, the master latch is transparent when CLK is high and holds its state when CLK is low, while the slave latch has the opposite behaviour, obtained by swapping the clock connections. Latches L_1 and L_2 form the first master-slave pair; latches L_3 and L_4 form the second one, with identical clock phasing, and operate in parallel with the first pair.

The outputs of the two pairs are cross-coupled: the non-inverted output Q of L_2 drives the inverted input $\overline{D}$ of L_3, while $\overline{Q}$ of L_2 drives the non-inverted input D of L_3; symmetrically, the outputs of L_4 are cross-coupled back to the inputs of L_1. This inversion in the feedback path makes the circuit operate as a divide-by-2 counter with complementary outputs.

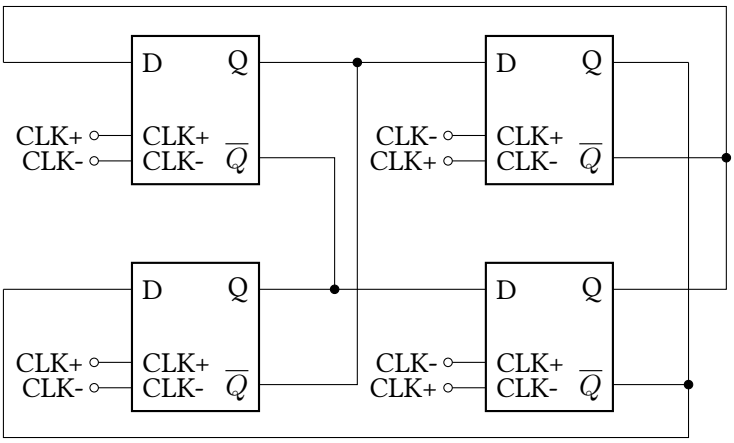


Figure 6.6.4: Latch-based quadrature frequency divider.

The differential architecture offers several advantages for high-frequency cryogenic operation:

1. **Common-mode noise rejection:** differential signalling inherently rejects common-mode noise and supply fluctuations, which is particularly important at cryogenic temperatures, where the circuit may be exposed to electromagnetic interference from nearby quantum devices.
2. **Reduced clock-skew sensitivity:** by using both phases of the differential clock, the circuit achieves better timing symmetry and reduced sensitivity to clock-distribution delays.
3. **Inherent quadrature generation:** the two cross-coupled master-slave pairs naturally produce four outputs with nominal 90° spacing: Q and $\overline{Q}$ of the first pair provide the 0° and 180° phases, those of the second pair the 90° and 270° phases.

The divider operates at the full input frequency of $2.6\,\mathrm{GHz}$ and delivers two differential output pairs at $1.3\,\mathrm{GHz}$, which correspond to the in-phase ($LO_{I\pm}$) and quadrature ($LO_{Q\pm}$) clocks of Figure 6.6.1. These outputs feed the phase-alignment circuits and output buffers described in Section 6.6.5.

Latch Implementation

Each D-latch is implemented with a differential topology optimised for high-speed operation at cryogenic temperature. Figure 6.6.5 shows one half of the latch, which consists of a clocked CMOS inverter (M_1-M_4) followed by a static inverter (M_5-M_6); two such half-cells, cross-coupled as in the logic diagram of Figure 6.6.6, form the complete differential latch.

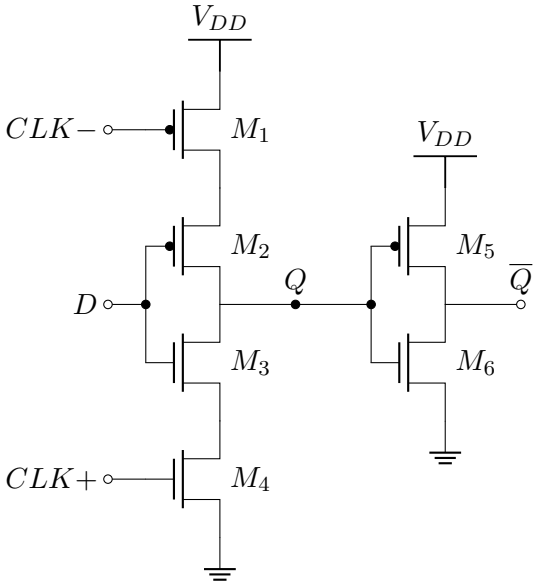


Figure 6.6.5: Half-cell of the differential D-latch: clocked inverter (M_1-M_4) followed by a static inverter (M_5-M_6).

During the transparent phase (CLK+ high, CLK− low), the PMOS M_1 and the NMOS M_4 are both on, and M_2-M_3 behave as a standard inverter driven by the input D: node Q is thus set to the complement of D, and the static inverter M_5-M_6 regenerates $\overline{Q}$. During the hold phase (CLK+ low), M_1 and M_4 are off and the clocked inverter is in a high-impedance state, isolating Q from the input; the sampled state is retained by the loop formed by the two cross-coupled half-cells, which acts as a bistable memory element.

Logical Operation and State Evolution

To understand the frequency-division mechanism, it is instructive to examine the logical representation of the divider shown in Figure 6.6.6. Each latch is represented by a clock-controlled NOT gate followed by a plain NOT gate; the cross-connection between the two parallel paths turns each pair of plain gates into a bistable storage element. The complementary clock signals CLK and $\overline{\text{CLK}}$ alternately enable the first stage (nodes A, $\overline{A}$) and the second stage (nodes B, $\overline{B}$), creating a sequential state machine.

Consider an initial state with CLK at logic high and $B = 1$. The circuit evolves as follows.

Initial state (CLK $= 1$). The first stage is transparent: its clock-controlled gates propagate the feedback from the second stage. Since $B = 1$, the first stage settles to $A = 0$, $\overline{A} = 1$. The second stage is in hold, because $\overline{\text{CLK}} = 0$ disables its clock-controlled gates, and retains $B = 1$, $\overline{B} = 0$.

First transition (CLK: $1 \rightarrow 0$). The roles reverse: the first stage holds ($A = 0$, $\overline{A} = 1$) while the second becomes transparent and samples $\overline{A} = 1$, which sets $B = 1$, $\overline{B} = 0$. In this particular transition B was already high, so the second stage does not change state; this is a consequence of the chosen initial condition.

Second transition (CLK: $0 \rightarrow 1$). The first stage becomes transparent again and samples $\overline{B} = 0$, so that $A = 1$, $\overline{A} = 0$. The second stage holds ($B = 1$, $\overline{B} = 0$).

Third transition (CLK: $1 \rightarrow 0$). The second stage samples $\overline{A} = 0$, so that $B = 0$, $\overline{B} = 1$. The first stage holds ($A = 1$, $\overline{A} = 0$).

Fourth transition (CLK: $0 \rightarrow 1$). The first stage samples $\overline{B} = 1$, returning to $A = 0$, $\overline{A} = 1$, which completes one full cycle of the outputs.

Each complete cycle of the outputs A and B thus requires two full cycles of the input clock: the nodes toggle at half the input frequency, implementing the divide-by-2 function.

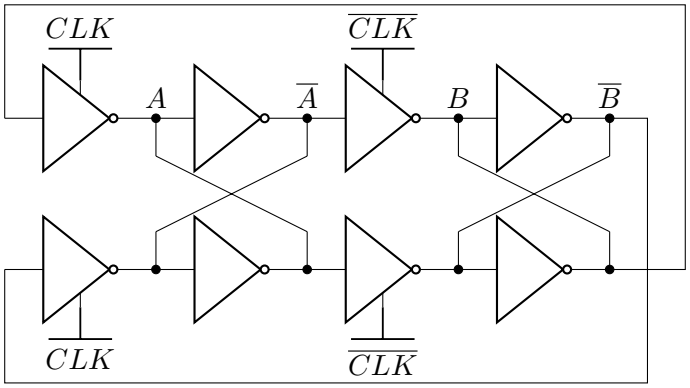


Figure 6.6.6: Logic representation of the frequency divider.

Figure 6.6.7 shows the timing diagram of the divider over several clock cycles. An important feature of this topology is that the two stages operate with a $90°$ phase offset at the divided frequency:

- the first stage (A, $\overline{A}$) changes state on every rising edge of CLK;
- the second stage (B, $\overline{B}$) changes state on every falling edge of CLK;
- rising and falling edges of CLK are separated by half an input period;
- the two stages are offset by $180°$ of the input clock, which corresponds to $90°$ at the output frequency.

This inherent quadrature relationship is precisely what is required for the mixer clocks: the four outputs A, $\overline{A}$, B, $\overline{B}$ provide the $0°$, $180°$, $90°$ and $270°$ phases, i.e. LO_{I+}, LO_{I-}, LO_{Q+} and LO_{Q-}.

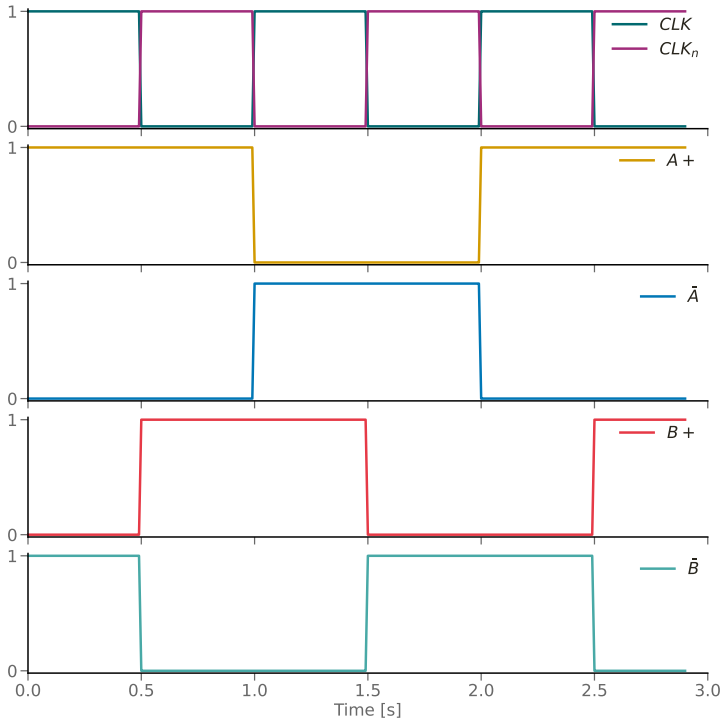


Figure 6.6.7: Timing diagram of the frequency divider, showing the $90°$ offset between the two stages at the divided frequency.

Implementation Details

Following the same considerations on PMOS-to-NMOS sizing to compensate for the mobility difference and achieve a switching threshold of $V_M = 0.9\,\mathrm{V}$, the transistors are scaled by a factor of 4 from the minimum size, resulting in $W_{\mathrm{PMOS}} = 1.54\,\mu\mathrm{m}$, $L_{\mathrm{PMOS}} = 130\,\mathrm{nm}$, $W_{\mathrm{NMOS}} = 0.6\,\mu\mathrm{m}$, and $L_{\mathrm{NMOS}} = 130\,\mathrm{nm}$.

6.6.5 Phase Alignment and Output Buffers

The phase aligner circuit is implemented using a cascade of inverters, as shown in Figure 6.6.8. This topology generates complementary outputs with controlled phase shifts to compensate for timing mismatches in the signal paths. The circuit ensures that the quadrature signals maintain the required 90° phase relationship at the mixer inputs, which is critical for proper I/Q demodulation.

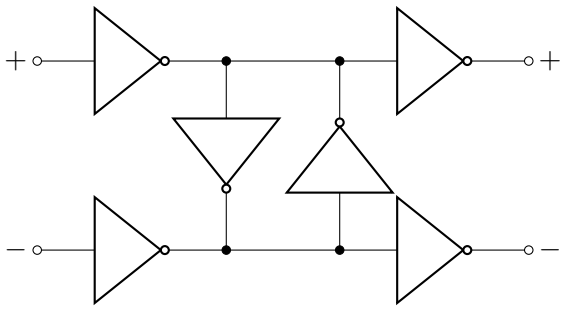


Figure 6.6.8: Logic diagram of the differential phase-alignment circuit.

The couple signal of the differential inputs ($+$ and $-$) is fed into the first inverter stage, which generates an intermediate signal at the first internal nodes. The two middle nodes are connected together by a cross-coupled inverter pair, which ensures that the outputs are complementary and maintains the differential nature of the signals. The final stage consists of two inverters that drive the output buffers, providing sufficient drive strength to the mixer inputs while preserving the phase alignment.

The key principle behind this topology is that each inverter introduces a fixed propagation delay t_p, which at 2.6 GHz (period $T \approx 385\,\mathrm{ps}$) translates into a phase shift. The cross-coupled stage in the middle acts as a differential regenerator: by forcing the two signal paths to interact through the cross-connection, any accumulated timing skew between the positive and negative branches is equalized. This ensures that both outputs experience identical total delay and maintain precise complementarity, which is essential for preserving the 90° phase relationship between the in-phase (I) and quadrature (Q) local oscillator signals fed to the mixers. Importantly, this phase aligner is a *passive* (non-adaptive) circuit: the phase correction is determined at design time by transistor sizing, layout symmetry, and routing geometry, and remains fixed during operation.

Implementation Details

Following the same considerations on PMOS-to-NMOS sizing to compensate for the mobility difference and achieve a switching threshold of $V_M = 0.9\,\mathrm{V}$, the transistors are scaled by a factor of 50 from the minimum size. This larger scaling is necessary because the phase aligner must drive the substantial capacitive load of the mixer inputs. The resulting transistor sizes are $W_{\mathrm{PMOS}} = 19.5\,\mu\mathrm{m}$, $L_{\mathrm{PMOS}} = 130\,\mathrm{nm}$, $W_{\mathrm{NMOS}} = 7.5\,\mu\mathrm{m}$, and $L_{\mathrm{NMOS}} = 130\,\mathrm{nm}$.

To reduce the occupied area, a tapered buffer topology can be considered, in which the inverter widths increase gradually along the signal path. This approach allows only the final stage to have maximum width for driving the load, while earlier stages remain smaller, reducing the overall circuit area and power consumption.

6.7 Results

This section reports the simulation results of the proposed receiver front-end blocks: the CMOS circulator and the LO generation chain, composed of the active balun, the squaring stage, the frequency divider, and the phase aligner. All simulations are performed in the SG13G2 130 nm BiCMOS technology at the operating frequency of 6.5 GHz. The circulator is characterised in terms of S-parameters, noise, and large-signal linearity, together with the response of the all-pass networks that implement the non-reciprocal phase shift. The LO chain is characterised block by block, from the static and dynamic behaviour of the elementary CMOS inverter up to the complete time-domain waveforms delivered to the mixer.

6.7.1 Circulator

S-parameters. Figure 6.7.1 shows the simulated magnitude of the S-parameters of the circulator for the final design point (70 μm). At 6.5 GHz the transmission along the circulation direction exhibits an insertion loss of 3.31 dB from port 1 to port 2 (S_{21}), 1.63 dB from port 2 to port 3 (S_{32}), and 1.63 dB from port 3 to port 1 (S_{13}). In the reverse direction, the isolation is 42.57 dB between port 2 and port 1 (S_{12}), 15.61 dB between port 3 and port 2 (S_{23}), and 15.62 dB between port 1 and port 3 (S_{31}), the latter being the transmitter-to-receiver leakage path that ultimately sets the self-interference level at the receiver input. All three ports are well matched, with return losses of 15.22 dB at ports 1 and 2 (S_{11}, S_{22}) and 23.69 dB at port 3 (S_{33}). The insertion loss remains within these values over a 28% fractional bandwidth centred at 6.5 GHz. The corresponding phase response is reported in Figure 6.7.2.

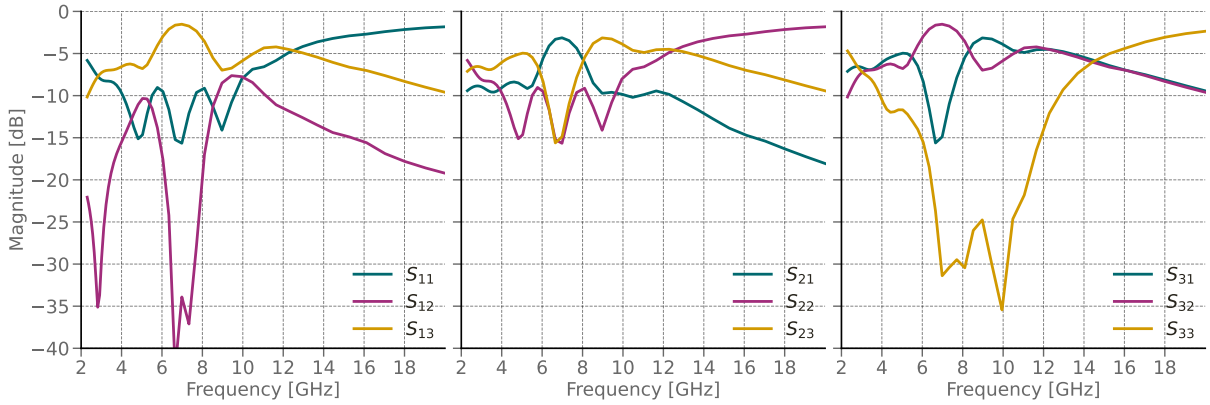


Figure 6.7.1: Simulated S-parameter magnitude of the proposed CMOS circulator. At 6.5 GHz the insertion loss is 3.31 dB (S_{21}) and 1.63 dB (S_{32}, S_{13}), while the isolation is 42.57 dB (S_{12}), 15.61 dB (S_{23}), and 15.62 dB (S_{31}).

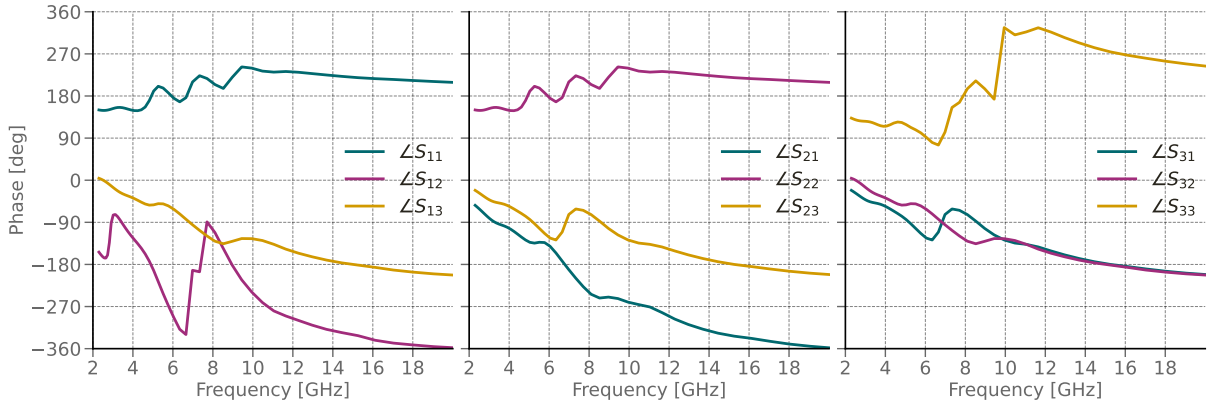
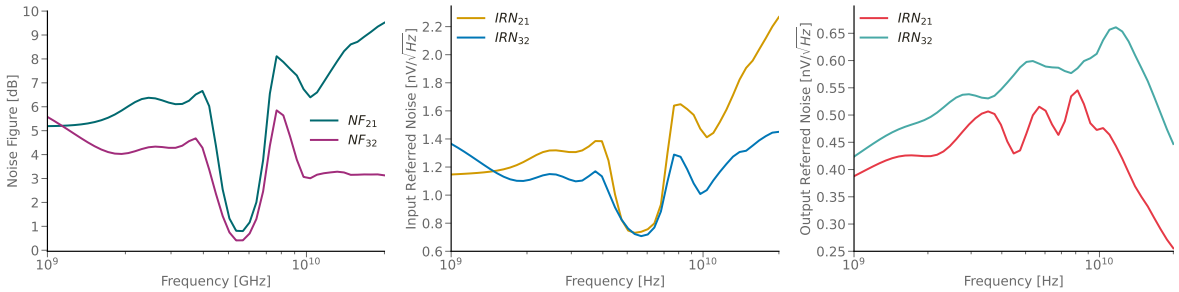


Figure 6.7.2: Simulated S-parameter phase of the proposed CMOS circulator.

Noise. Figure 6.7.3a reports the simulated noise figure of the circulator along the receive path as a function of frequency; at 6.5 GHz the noise figure is 2.01 dB, for the path from port 1 to port 2, and 1.31 dB for the path from port 2 to port 3.The input-referred and output-referred noise voltage spectral densities are shown in Figures 6.7.3b and 6.7.3c,at the operating frequency, respectively, and amount to $0.8\,\mathrm{nV}/\sqrt{\mathrm{Hz}}$ and $0.48\,\mathrm{nV}/\sqrt{\mathrm{Hz}}$ for the path from port 1 to port 2, and $0.77\,\mathrm{nV}/\sqrt{\mathrm{Hz}}$ and $0.59\,\mathrm{nV}/\sqrt{\mathrm{Hz}}$ for the path from port 2 to port 3.



(a) (b) (c)

Figure 6.7.3: Simulated noise performance of the circulator: (a) noise figure along the receive path, (b) input-referred noise voltage spectral density, and (c) output-referred noise voltage spectral density.

Linearity. The large-signal behaviour of the circulator is assessed through two-tone and single-tone power sweeps. Figure 6.7.4a shows the fundamental and third-order intermodulation output powers along the port 1 to port 2 path as a function of the input power. The extrapolation of the two curves, whose fitted slopes are 1.00 and 3.21, yields an input-referred third-order intercept point $\mathrm{IIP}_3 = 22.11\,\mathrm{dBm}$. The same analysis along the port 2 to port 3 path, reported in Figure 6.7.4b, gives $\mathrm{IIP}_3 = 22.11\,\mathrm{dBm}$, with fitted slopes of 1.00 and 3.25. The slight deviation of the third-order slope from the ideal value of 3 indicates a minor contribution of higher-order terms in the swept power range.

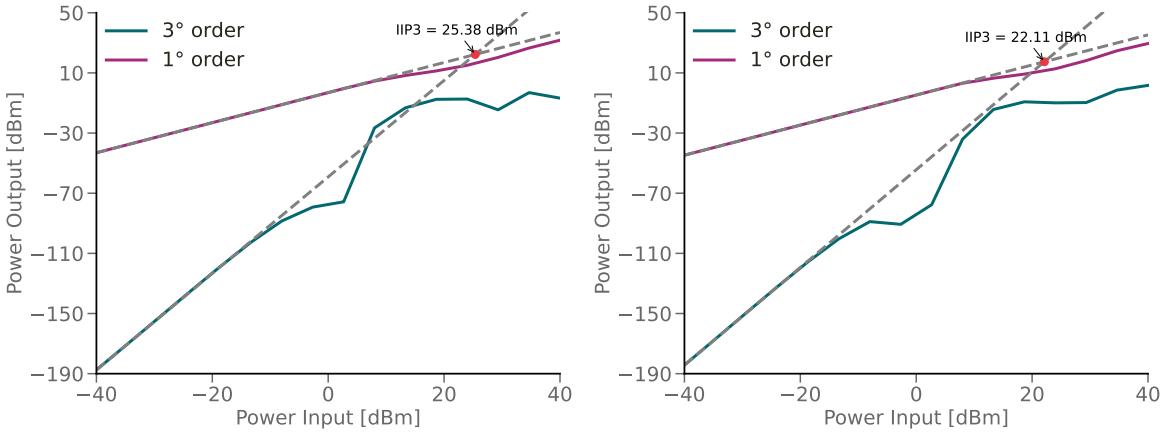


Figure 6.7.4: Simulated two-tone tests of the circulator: (a) port 1 to port 2 path, yielding $\mathrm{IIP}_3 = 25.38$ dBm, and (b) port 2 to port 3 path, yielding $\mathrm{IIP}_3 = 22.11$ dBm.

The gain compression is reported in Figure 6.7.5. Along the port 1 to port 2 path, the small-signal gain of -3.11 dB, in agreement with the value of S_{21}, is compressed by 1 dB at an input power of 10.17 dBm, corresponding to an output-referred $P_{21\mathrm{dB}}$ of 6.06 dBm. The transmitter-to-receiver leakage path (S_{31}) deviates by 1 dB from its small-signal value at an input power of 10.24 dBm, so that the isolation is preserved up to essentially the same power level as the transmission path. Figure 6.7.6 shows the output spectrum of the circulator under single-tone excitation at 6.5 GHz, where the spurious components generated by the switching operation are all below -240 dBm with respect to the fundamental tone.

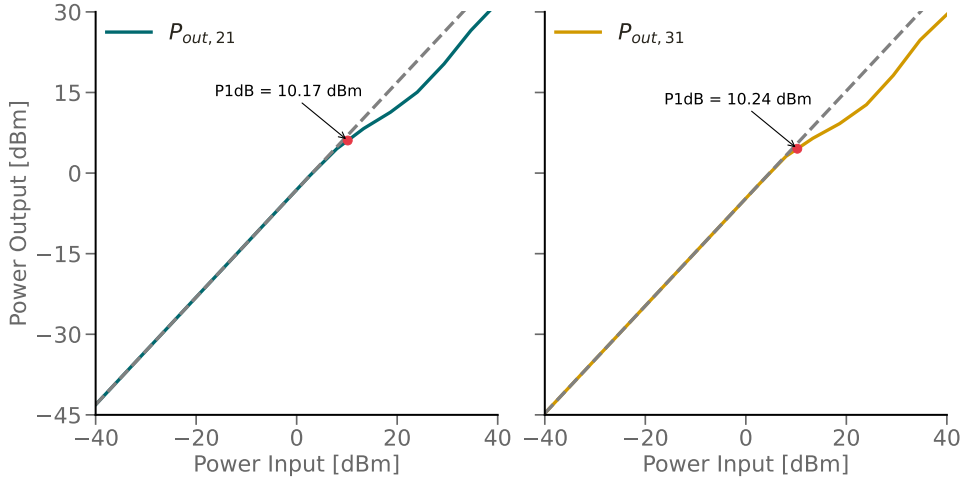


Figure 6.7.5: Gain compression of the circulator along the port 1 to port 2 path (left) and the port 2 to port 3 path (right). The input-referred $P_{21\mathrm{dB}}$ is 10.17 dBm, corresponding to an output-referred $P_{1\mathrm{dB}}$ of 6.06 dBm. The transmitter-to-receiver leakage path (P_{31}) deviates by 1 dB from its small-signal value at an input power of 10.24 dBm, so that the isolation is preserved up to essentially the same power level as the transmission path.

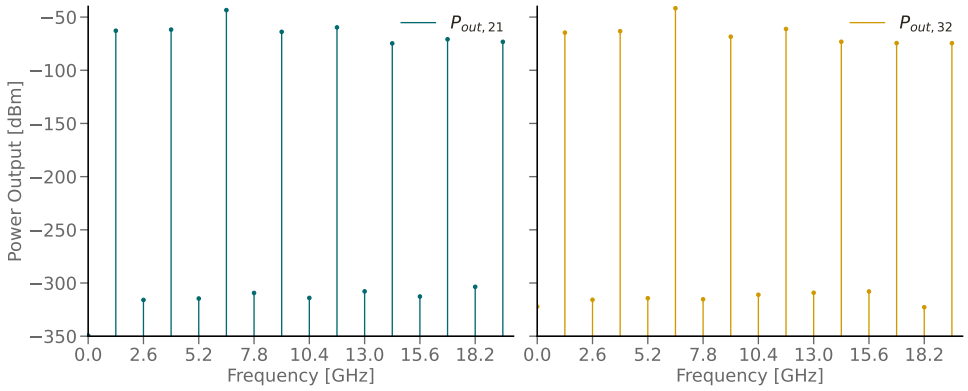


Figure 6.7.6: Simulated output spectrum of the circulator under single-tone excitation at 6.5 GHz, showing the spurious components generated by the switching operation. Left: port 1 to port 2 path; right: port 2 to port 3 path.

All-pass networks. The non-reciprocal behaviour relies on the phase shifts introduced by the all-pass networks in the two branches. Figures 6.7.7 and 6.7.8 show the simulated magnitude and phase response of the reciprocal and non-reciprocal branches, respectively. The two first-order lattice all-pass filters provide a total phase shift of $-90°$ at 6.5 GHz, while the two parallel second-order bridged-T all-pass filters provide a total phase shift of $180°$ at the same frequency. The resulting non-reciprocal phase shift is therefore $90°$, as required for circulation.

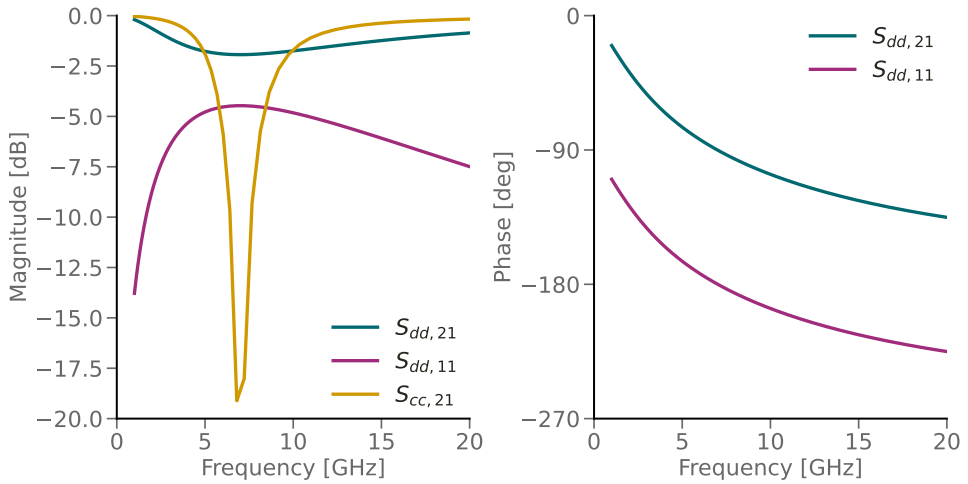


Figure 6.7.7: Simulated magnitude and phase response of the reciprocal branches of the circulator. The two first-order lattice all-pass filters provide a total phase shift of $-90°$ at the centre frequency of 6.5 GHz.

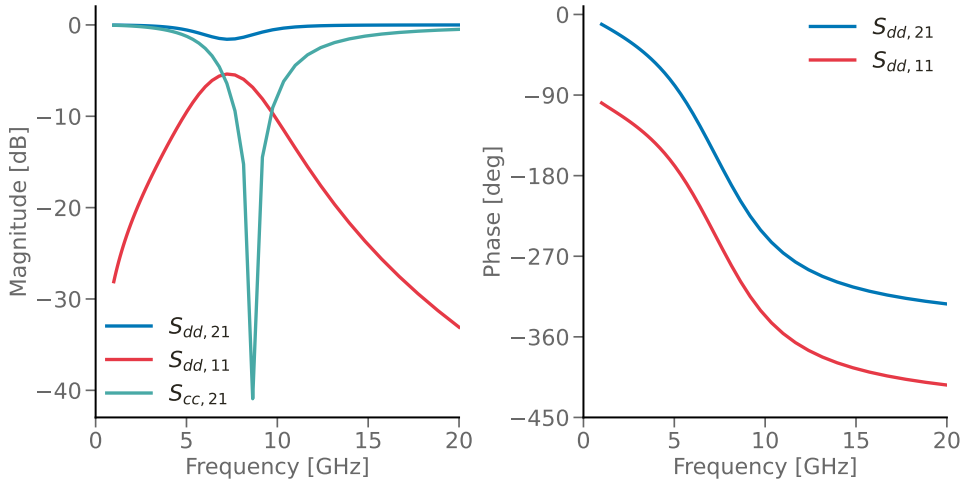
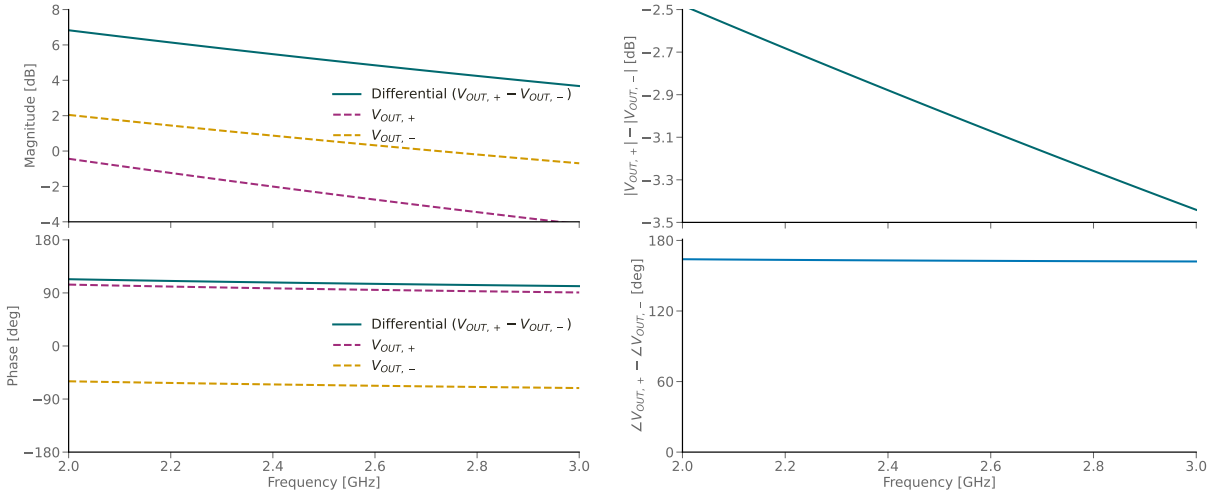


Figure 6.7.8: Simulated magnitude and phase response of the non-reciprocal branch of the circulator. The two parallel second-order bridged-T all-pass filters provide a total phase shift of 180° at the centre frequency of 6.5 GHz.

6.7.2 LO Generation Chain

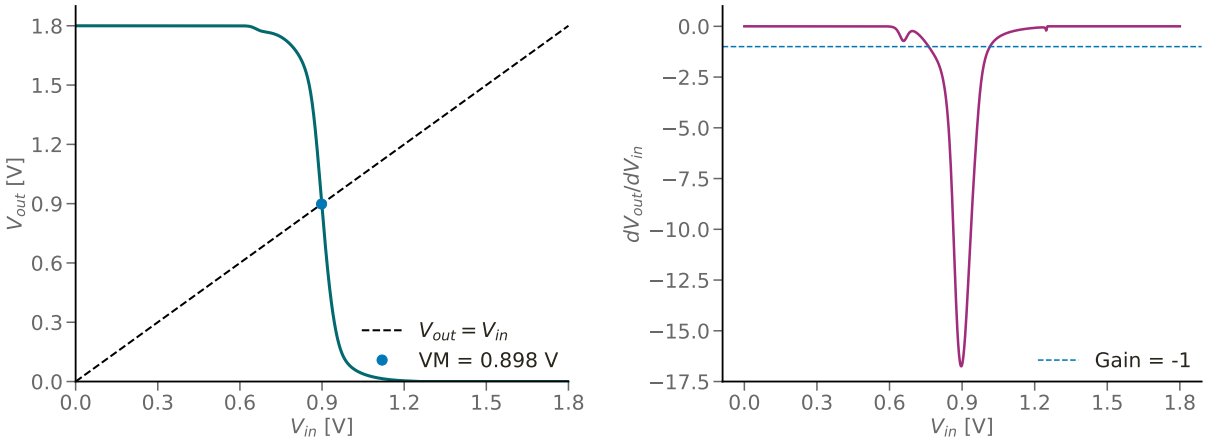
Active balun. Figure 6.7.9a shows the time-domain output waveforms of the active balun when driven by a single-ended tone at 2.6 GHz. The two outputs V_{out1} and V_{out2} are in anti-phase with a differential amplitude of 0.9 mV, corresponding to a single-ended to differential gain of 5 dB. The balance of the two outputs is quantified in Figure 6.7.9b, which reports the amplitude and phase imbalance as a function of frequency: at 2.6 GHz the amplitude imbalance is -3.07 dB and the phase imbalance is 162°. These residual errors are subsequently absorbed by the squaring stage, which regenerates a full-swing digital clock regardless of small amplitude differences between the two phases.



(a) (b)

Figure 6.7.9: (a) Simulated output magnitudes and phase of the active balun driven by a single-ended tone with amplitude of -70 dBm; (b) simulated amplitude and phase imbalance of the active balun outputs as a function of frequency.

CMOS inverter. The CMOS inverter is the elementary cell of the squaring stage, of the latches composing the frequency divider, and of the phase aligner; its static and dynamic characterisation is therefore reported first. Figure 6.7.10a shows the voltage transfer characteristic obtained from a DC sweep of the input voltage, while Figure 6.7.10b shows the corresponding small-signal voltage gain. The PMOS-to-NMOS sizing ratio of 2.57 places the switching threshold at $V_M = 0.898\,\mathrm{V} \approx V_{DD}/2$, as required for a symmetric and balanced squaring of the differential input. The output levels are $V_{OL} = 0\,\mathrm{V}$ and $V_{OH} = 1.8\,\mathrm{V}$, and the maximum gain in the transition region is $-16.75\,\mathrm{V/V}$. The unity-gain points define the input logic levels $V_{IL} = 0.763\,\mathrm{V}$ and $V_{IH} = 1.013\,\mathrm{V}$, which correspond to noise margins $NM_L = 0.763\,\mathrm{V}$ and $NM_H = 0.787\,\mathrm{V}$. The nearly identical noise margins confirm the symmetry of the characteristic around $V_{DD}/2$.



(a) (b)

Figure 6.7.10: Simulated static behaviour of the CMOS inverter: (a) voltage transfer characteristic, showing the switching threshold $V_M = 0.898\,\mathrm{V}$ and the input logic levels $V_{IL} = 0.763\,\mathrm{V}$ and $V_{IH} = 1.013\,\mathrm{V}$; (b) small-signal voltage gain as a function of the input voltage, with maximum gain of $-16.75\,\mathrm{V/V}$ at $V_{in} = V_M$.

The dynamic behaviour is characterised in Figure 6.7.11, which shows a detail of the output transitions in response to an ideal input step. The propagation delays, measured at 50% of the swing, are $t_{pLH} = 3.76\,\mathrm{ps}$ for the low-to-high transition and $t_{pHL} = 5.19\,\mathrm{ps}$ for the high-to-low transition, resulting in an average propagation delay $t_p = 4.47\,\mathrm{ps}$. The slightly longer high-to-low delay reflects the larger gate capacitance associated with the wider PMOS device, which loads the output node during the discharge phase.

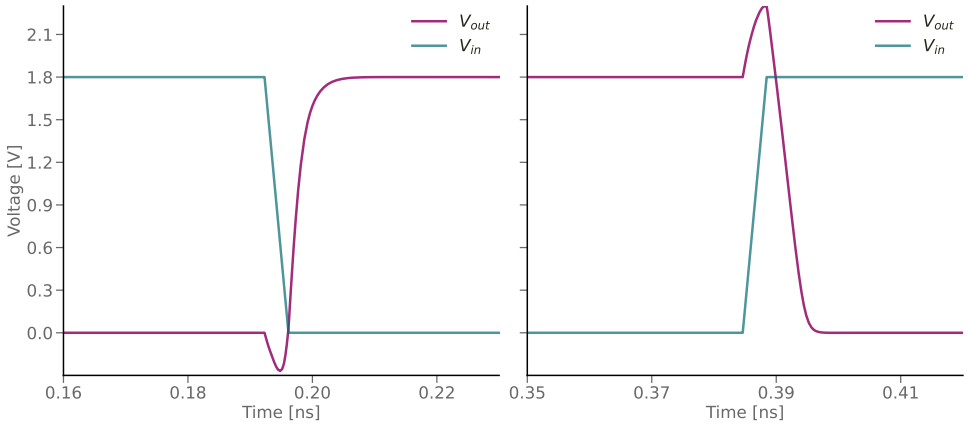


Figure 6.7.11: Detail of the simulated output transitions of the CMOS inverter. The propagation delays are $t_{pLH} = 3.76\,\text{ps}$ and $t_{pHL} = 5.19\,\text{ps}$.

Squaring stage. Figure 6.7.12 shows the transient response of the squaring stage driven by the differential sinusoidal output of the balun. The stage converts the input into a full-swing differential square wave CLK with rise and fall times equal to that of the CMOS inverter.

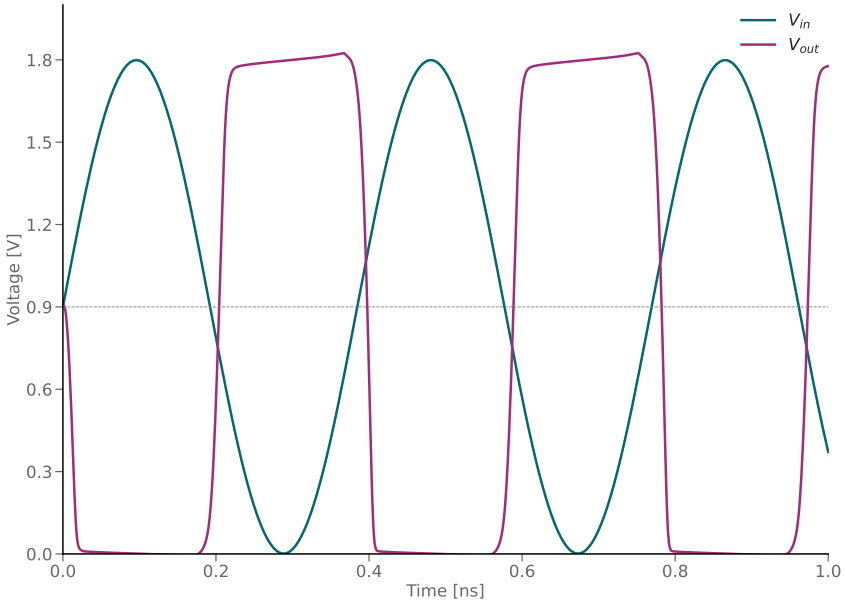


Figure 6.7.12: Simulated transient waveforms of the squaring stage: differential sinusoidal input from the balun and full-swing differential square-wave output CLK.

D latch. The frequency divider is built from two D latches connected in a master-slave configuration with the output fed back to the input in inverted form. The behaviour of the single latch is verified in a dedicated test bench with a differential clock CLK_{diff} and a data input D that changes state while the latch is opaque.

Figure 6.7.13 shows the complete waveforms of the differential clock, of the input D, and of the output over a 1 ns window. The clock crosses zero at 0.194, 0.387, 0.579, 0.771, and 0.964 ns, while the input D switches at 0.196, 0.581, and 0.965 ns, i.e. approximately 2 ps after each falling edge of the clock, when the latch has just entered the opaque phase. As expected, these input transitions are not propagated to the output, which holds its previous value until the next rising edge of the clock makes the latch transparent again. The output then switches at 0.401 ns and at 0.782 ns, following the clock rising edges at 0.387 ns and 0.771 ns.

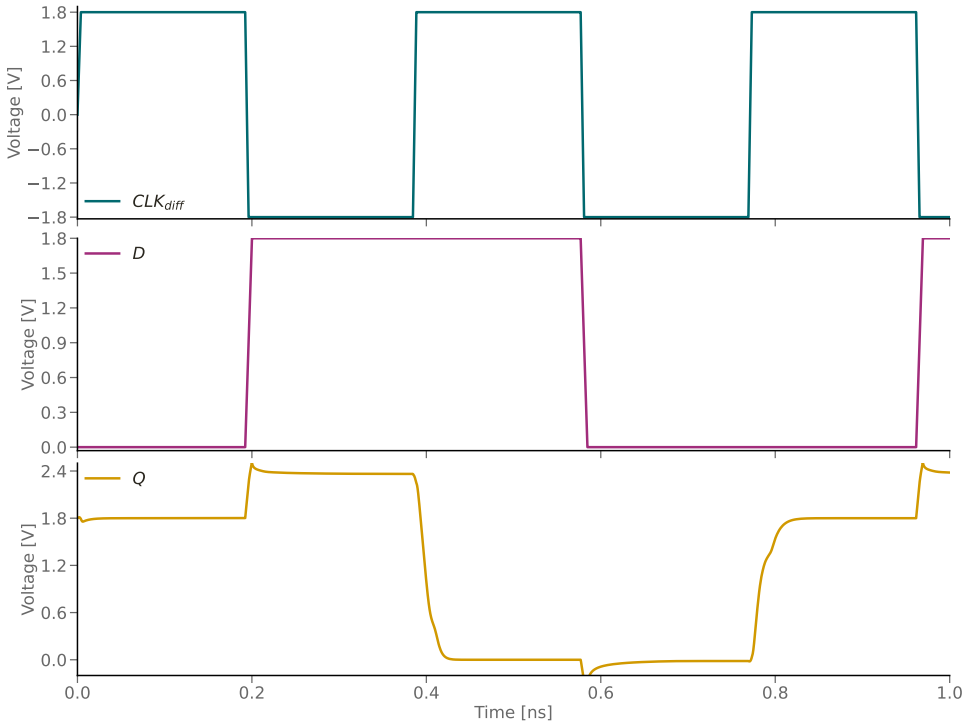


Figure 6.7.13: Simulated waveforms of the D latch: differential clock CLK_{diff}, data input D, and output. The dotted vertical lines mark the clock zero crossings.

Figure 6.7.14 shows a detail of the two output transitions, in the windows 0.3–0.4 ns and 0.7–0.9 ns, together with the differential clock and the shaded interval in which the latch is transparent. The clock-to-output delay, measured from the zero crossing of CLK_{diff} to the 50% crossing of the output, is 14.3 ps for the high-to-low transition and 10.8 ps for the low-to-high transition. The output swing extends slightly beyond the supply rails, with an overshoot up to 2.51 V and an undershoot down to -0.31 V, as a consequence of the very fast edges combined with the capacitive coupling at the output node; the excursion is confined to the transition instants and does not affect the logic levels in steady state.

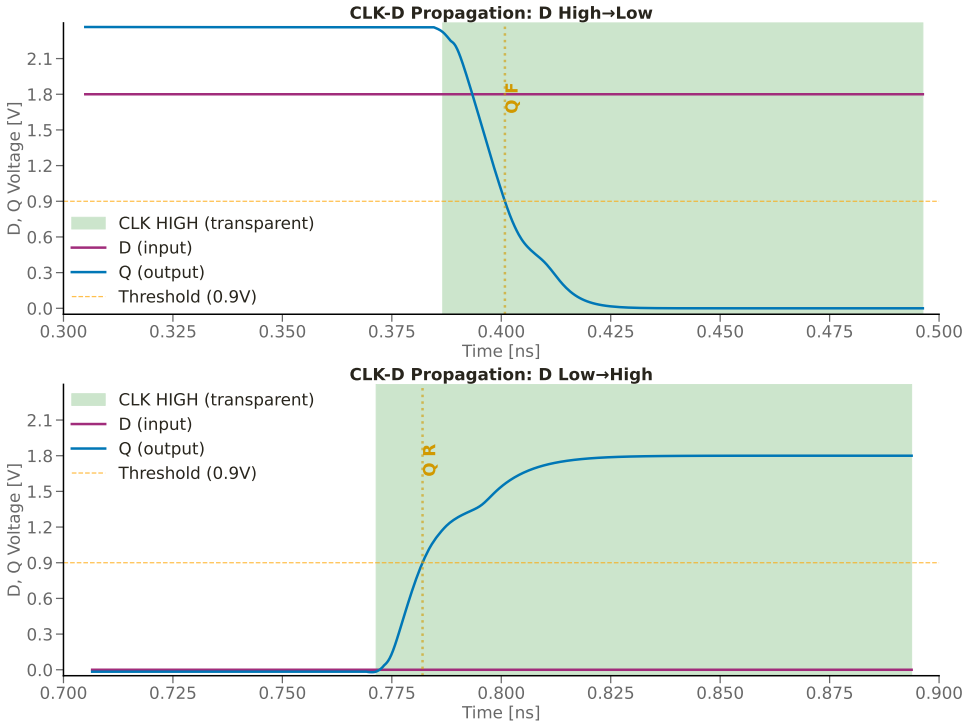


Figure 6.7.14: Detail of the D latch output transitions following the clock rising edges. The shaded regions indicate the intervals in which $CLK_{diff} > 0$ and the latch is transparent. The clock-to-output delay is $14.3\,\text{ps}$ for the high-to-low transition and $10.8\,\text{ps}$ for the low-to-high transition.

Frequency divider and phase aligner. Figure 6.7.15 shows the time-domain waveforms along the complete LO generation chain. Starting from the single-ended input tone V_{in} at $6.5\,\text{GHz}$, the active balun produces the differential signal $V_{diff} = V_{out1} - V_{out2}$, which is squared to obtain the differential clock CLK. The frequency divider then halves the clock frequency and generates the four signals A^+, A^-, B^+, B^- at $3.25\,\text{GHz}$. Finally, the phase aligner produces the quadrature LO signals LO_I^+, LO_I^-, LO_Q^+, LO_Q^- that drive the mixer switches.

The propagation delays of the frequency divider are $t_{pHL} = 19\,\text{ps}$ for the high-to-low transition and $t_{pLH} = 25\,\text{ps}$ for the low-to-high transition, consistently with the cascade of two latch stages characterised above.

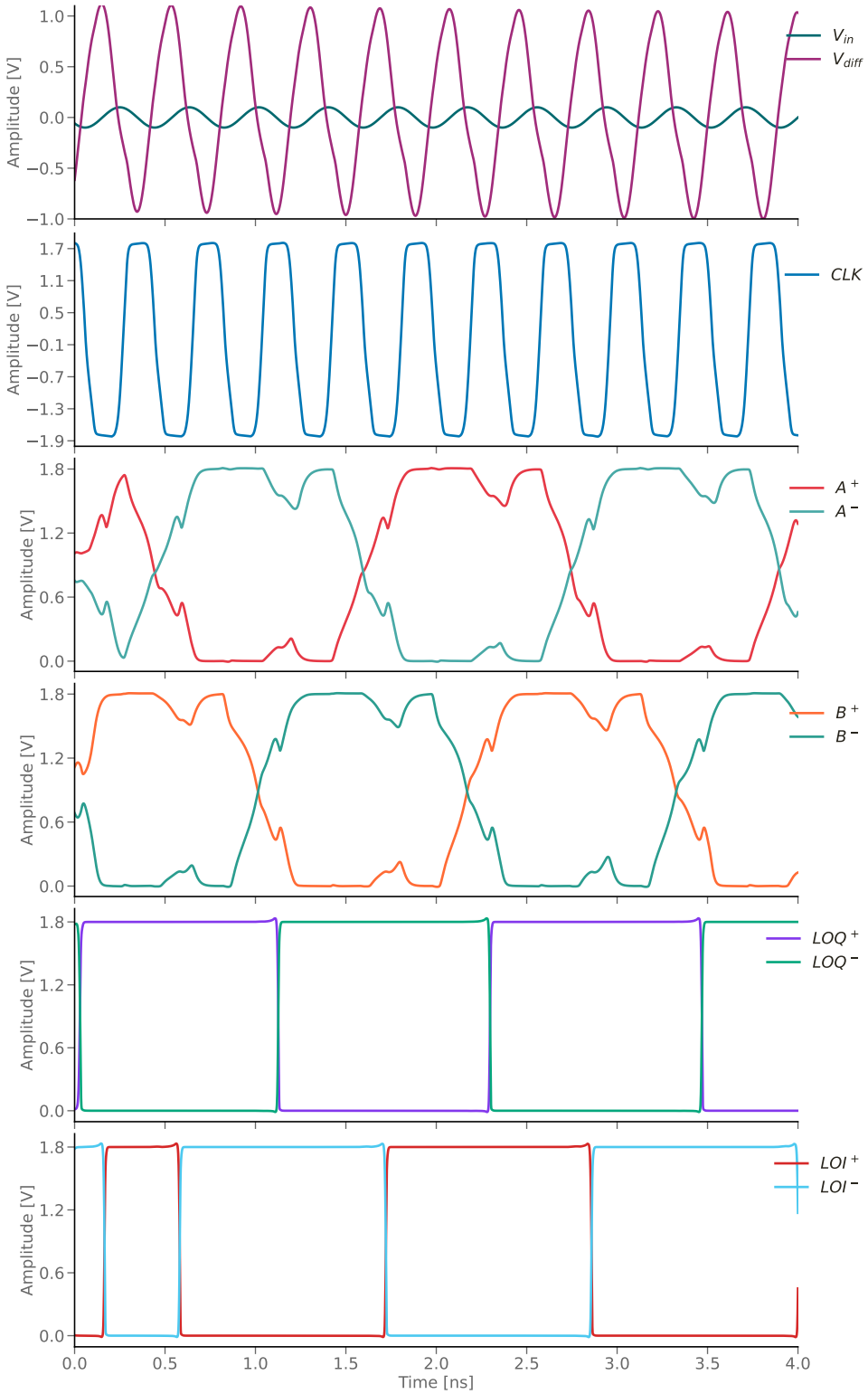


Figure 6.7.15: Simulated waveforms of the LO generation chain: input tone V_{in}, differential balun output V_{diff}, squared clock CLK, frequency divider outputs ($A^{\pm}$, $B^{\pm}$), and phase-aligned quadrature LO signals ($LO_I^{\pm}$, $LO_Q^{\pm}$).

6.7.3 Summary

Table 6.3 summarises the main simulated performance figures of the front-end blocks.

Table 6.3: Summary of the simulated performance at 6.5 GHz.

Block	**Parameter**	**Value**
Circulator	Insertion loss (S_{21} / S_{32} / S_{13})	3.31 / 1.63 / 1.63 dB
	Isolation (S_{12} / S_{23} / S_{31})	42.6 / 15.6 / 15.6 dB
	Return loss (S_{11} / S_{22} / S_{33})	15.2 / 15.2 / 23.7 dB
	Fractional bandwidth	28%
	Noise figure$_{21}$	2.01 dB
	Noise figure$_{21}$	1.31 dB
	IIP_3 (1→2 / 2→3)	25.4 / 22.1 dBm
	Input P_{1dB} (1→2)	10.2 dBm
Active balun	Gain / phase imbalance	-3.07 dB / 162°
CMOS inverter	V_M	0.898 V
	NM_L / NM_H	0.763 / 0.787 V
	t_{pLH} / t_{pHL}	3.76 / 5.19 ps
D latch	Clock-to-output delay (H→L / L→H)	14.3 / 10.8 ps
Frequency divider	t_{pHL} / t_{pLH}	19 / 25 ps
LO chain	Total power consumption	26.76 mW

Chapter 7 System-Level Simulations and Performance

7.1 Complete Readout Chain Integration

The preceding chapters have introduced the individual building blocks of the cryogenic reflectometry receiver: the CMOS circulator that separates the incident probe tone from the reflected signal, the two low-noise amplifier topologies proposed for the first gain stage. Each block has so far been characterised alone, against a nominal $50\,\Omega$ source and load. This chapter closes the loop by connecting them to the device that the receiver is ultimately meant to observe, namely a transmon qubit dispersively coupled to a readout resonator, and by evaluating the resulting end-to-end performance.

The measurement principle is the one established in Chapter 3. A continuous probe tone at $f_p = 6.5\,\mathrm{GHz}$ is delivered through the circulator to the resonator; the reflected wave carries, in its amplitude and phase, the information on the instantaneous resonance frequency and therefore on the qubit state, according to the reflection coefficient of Eq. (3.20). The circulator routes the reflected wave to the LNA, whose noise figure sets the sensitivity of the whole chain, and the amplified signal is then down-converted to baseband by the mixer, where the in-phase and quadrature components I and Q are extracted. The dispersive interaction discussed in Section 3.2 is what makes this measurement possible: the small state-dependent reactance of the qubit, which would be undetectable in a direct broadband reflection measurement, is transduced by the resonator into a shift of a narrow Lorentzian line, and hence into a macroscopic displacement of the reflected phasor in the complex plane [35], [41].

Of the elements that compose this chain, the readout resonator is the only one that has not yet been sized and simulated. The analytical description of Section 3.2 is general; in this chapter it is specialised to the frequency of $6.5\,\mathrm{GHz}$ and to the transmon whose Josephson junction was modelled in Chapter 4. Section 7.2 therefore presents the design of the resonator, from the first-order analytical sizing to the circuit refined by simulation, and its stand-alone characterisation. The following sections then assemble the complete chain, and quantify signal integrity, signal-to-noise ratio, readout contrast and measurement time for the two LNA variants, before comparing the result with the state of the art.

7.2 Readout Resonator Design

7.2.1 Specifications and Design Constraints

The resonator must satisfy a set of requirements that follow directly from the analysis of Section 3.2. Its resonance frequency must coincide with the probe frequency, $f_r = 6.5\,\mathrm{GHz}$, which is also the centre frequency for which the circulator, the LNAs and the LO chain have been designed. It must be detuned from the qubit transition by a quantity $\Delta = \omega_r - \omega_q$ large compared with the coupling g, so that the dispersive approximation holds and the measurement is quantum non-demolition to a good approximation; at the same time, since the dispersive shift scales as g^2/Δ, Eq. (3.28), the detuning cannot be made arbitrarily large without destroying the readout contrast. Its linewidth κ_{tot} must be dominated by the external coupling, $\kappa_{\mathrm{ext}} \gg \kappa_{\mathrm{int}}$, so that the reflected signal is efficiently extracted towards the circulator and the response does not depend critically on the poorly controlled internal losses; the linewidth also sets the ring-up time $\sim 1/\kappa_{\mathrm{tot}}$ of the resonator, which bounds from below the measurement time. Finally, the Purcell decay of Eq. (3.29) must remain small enough not to limit the qubit lifetime.

The transmon considered here is the one characterised in Chapter 4. Its junction has a critical current $I_c = 59\,\mathrm{nA}$ and a normal-state resistance $R_n = 5\,\mathrm{k\Omega}$; the intrinsic junction capacitance $C_{JJ} = 8\,\mathrm{fF}$ is shunted by an external capacitance $C_{sh} = 130\,\mathrm{fF}$, giving a total qubit capacitance $C_q = 138\,\mathrm{fF}$. The resulting energy ratio $E_J/E_C = 208.8$ places the device deep in the transmon regime [40], with a fundamental transition $f_{01} = 5.596\,\mathrm{GHz}$, a first excited transition $f_{12} = 5.456\,\mathrm{GHz}$ and hence an anharmonicity $\alpha/2\pi = -140.4\,\mathrm{MHz}$. With the probe frequency fixed at $6.5\,\mathrm{GHz}$, the qubit-resonator detuning is $\Delta/2\pi = f_r - f_{01} = 904\,\mathrm{MHz}$, in the range commonly adopted for dispersive readout [99].

7.2.2 Analytical Sizing

The resonator is implemented as the lumped parallel LC tank of Fig. 3.2.2, capacitively coupled to the $Z_0 = 50\,\Omega$ feedline through C_c and to the qubit through C_g. The first design choice is the characteristic impedance of the tank, $Z_r = \sqrt{L_r/C_r}$, which fixes the ratio between inductance and capacitance for a given resonance frequency. Setting $Z_r = Z_0$ gives

$$L_r = \frac{Z_0}{\omega_r} = 1.224\,\mathrm{nH} \qquad C_r = \frac{1}{\omega_r Z_0} = 489.7\,\mathrm{fF} \tag{7.1}$$

so that the tank presents, at resonance, an impedance level comparable to that of the line; this mirrors the behaviour of the distributed coplanar-waveguide resonators normally used in circuit QED, whose lumped equivalent has Z_r of the order of Z_0 [100], and keeps the coupling capacitor in the range of a few femtofarads. The internal losses are described by a parallel resistance $R = Q_{\mathrm{int}} Z_r$; assuming $Q_{\mathrm{int}} = 10^4$, a conservative figure for a lumped superconducting resonator [38], one obtains $R = 500\,\mathrm{k\Omega}$ and an internal decay rate $\kappa_{\mathrm{int}}/2\pi = f_r/Q_{\mathrm{int}} = 0.65\,\mathrm{MHz}$.

With $Z_r = Z_0$ the external quality factor of Eq. (3.10) takes a particularly transparent form. Since $C_r = 1/(\omega_r Z_0)$, the product $Z_0 \omega_r$ equals $1/C_r$ and

$$Q_{\mathrm{ext}} = \frac{C_r}{Z_0 \omega_r C_c^2} = \left(\frac{C_r}{C_c}\right)^2 \qquad \kappa_{\mathrm{ext}} = \omega_r \left(\frac{C_c}{C_r}\right)^2 \tag{7.2}$$

The external linewidth therefore grows quadratically with the coupling capacitance, and the overcoupled condition $\kappa_{\mathrm{ext}} \gg \kappa_{\mathrm{int}}$ requires $C_c/C_r \gg Q_{\mathrm{int}}^{-1/2} = 10^{-2}$. Choosing $C_c = 18\,\mathrm{fF}$ gives $Q_{\mathrm{ext}} = 740$ and $\kappa_{\mathrm{ext}}/2\pi = 0.65\,\mathrm{MHz}$, so that the loaded quality factor is $Q_L = 689$ and the total linewidth $\kappa_{\mathrm{tot}}/2\pi = 9.432\,\mathrm{MHz}$. The ratio $\kappa_{\mathrm{ext}}/\kappa_{\mathrm{int}} \approx 13.5$ places the resonator well into the overcoupled regime: at resonance the reflection coefficient is $\Gamma(\omega_r) = (\kappa_{\mathrm{int}} - \kappa_{\mathrm{ext}})/(\kappa_{\mathrm{int}} + \kappa_{\mathrm{ext}}) \approx -0.81$, i.e. most of the incident power is reflected with a phase inversion, and the phase of Γ sweeps the full 360° across the resonance.

The coupling to the qubit is governed by C_g. From Eq. (3.27) with $C_g = 8\,\mathrm{fF}$, gives $g/2\pi = 86.11\,\mathrm{MHz}$ and $\Delta/g = 10.5$, comfortably inside the dispersive regime.

Because the transmon is a weakly anharmonic oscillator rather than a two-level system, the resonator pull cannot be described by the single shift g^2/Δ of Eq. (3.28). When the qubit is in $|0\rangle$ the resonator exchanges virtual photons with the $0 \leftrightarrow 1$ transition and is displaced by $\chi_0 = g^2/(\omega_{01} - \omega_r)$; when the qubit is in $|1\rangle$ the relevant transition is $1 \leftrightarrow 2$ and the displacement becomes $\chi_1 = g^2/(\omega_{12} - \omega_r)$. The state-dependent separation of the two dressed resonances is then

$$\chi = \chi_0 - \chi_1 = \frac{g^2\,\alpha}{\Delta\,(\Delta - \alpha)}, \tag{7.3}$$

which coincides with the transmon dispersive shift derived by Koch *et al.* [40] and is smaller than the two-level estimate g^2/Δ by the factor $\alpha/(\Delta - \alpha) \approx 0.13$. Numerically, $\chi_0/2\pi = -8.202\,\mathrm{MHz}$, $\chi_1/2\pi = -7.099\,\mathrm{MHz}$ and $|\chi|/2\pi = 1.102\,\mathrm{MHz}$. This first sizing therefore yields $|\chi|/\kappa_{\mathrm{tot}} \approx 0.019$, far from the optimum $\chi \sim \kappa_{\mathrm{tot}}/2$ identified in Section 3.2: the two dressed resonances are largely unresolved and the separation of the reflected phasors is a small fraction of the available circle.

Probing at $f_p = f_r$, the reflected phasors for the two qubit states are $\Gamma_0 = 0.075 - 1.609\,i$ and $\Gamma_1 = 0.140 - 1.717\,i$, separated by $|\Gamma_0 - \Gamma_1| = 0.126$. A figure of merit that weights the IQ contrast and the depth of the resonance against the linewidth peaks at $C_c \approx 7.5\,\mathrm{fF}$; the larger value of $15\,\mathrm{fF}$ was nevertheless retained for the first design because a linewidth of several megahertz is needed to keep the measurement time compatible with the qubit coherence and to tolerate fabrication-induced frequency offsets. The Purcell rate of Eq. (3.29) evaluates, for this first design, to $\kappa_{\mathrm{Purcell}}/2\pi = \kappa_{\mathrm{ext}} g^2/(2\pi\Delta^2) \approx 21\,\mathrm{kHz}$, corresponding to a Purcell-limited lifetime of about $7.6\,\mu\mathrm{s}$, which is acceptable for a first design but confirms the relevance of the trade-off discussed in Section 3.2.

7.2.3 Circuit Implementation and Simulation

The analytical values of Section 7.2.2 were used as the starting point for the circuit-level implementation in Cadence, whose test bench is sketched in Fig. 7.2.1. The feedline is represented by a $50\,\Omega$ port, the tank by the parallel connection of L_r, C_r and the transmon model in parallel with $C_q = 130\,\mathrm{fF}$, according to the small-signal model of Chapter 4. The response is obtained from an S-parameter analysis of the single port over a window of a few hundred megahertz around $6.5\,\mathrm{GHz}$, and the resonance frequency. The loaded, internal and external quality factors are extracted by fitting the simulated $\Gamma(\omega)$ to the Lorentzian form of Eq. (3.20) [101], [102]. In this fit, κ_{tot} is identified with the full width at half maximum of the absorbed power $1-|\Gamma|^2$, while the ratio $\kappa_{\mathrm{ext}}/\kappa_{\mathrm{tot}}$ follows from the value of Γ at resonance, $\kappa_{\mathrm{ext}}/\kappa_{\mathrm{tot}} = [1-\Gamma(\omega_r)]/2$, the overcoupled branch being selected by the 360° phase excursion.

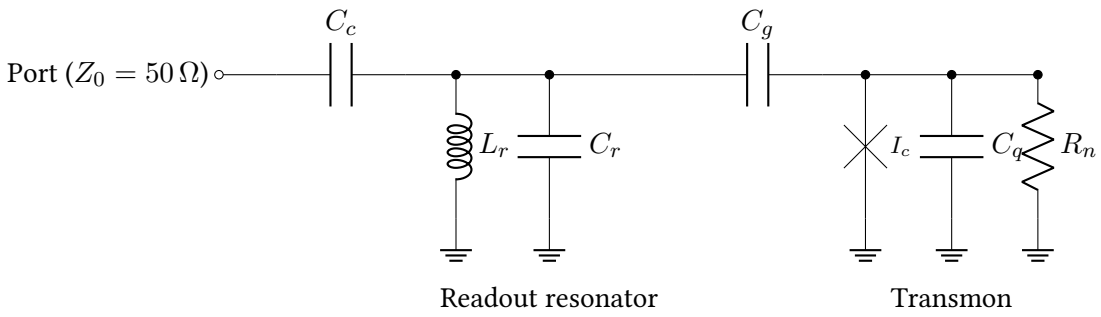


Figure 7.2.1: Single-port test bench used for the circuit-level simulation of the readout resonator loaded by the transmon. The junction is represented, for the small-signal analysis, by its linearised Josephson inductance in parallel with the total qubit capacitance $C_q = C_{JJ} + C_{sh}$ and the normal-state resistance R_n.

Both the feedline branch and the qubit branch appear, from the tank node, as additional shunt reactances: the reactance of C_c at $6.5\,\mathrm{GHz}$, about $1.4\,\mathrm{k\Omega}$, is much larger than Z_0, so that the feedline branch behaves essentially as a capacitance C_c to ground, while the qubit branch adds the series combination of C_g with the effective admittance of the transmon.

The design was consequently refined in three steps. The tank capacitance was reduced from $489.7\,\mathrm{fF}$ to $C_r = 472\,\mathrm{fF}$, i.e. by about $18\,\mathrm{fF}$, to compensate the loading and re-centre the resonance at $6.5\,\mathrm{GHz}$, the inductance being kept at $L_r = 1.224\,\mathrm{nH}$; the bare tank alone would resonate at $6.62\,\mathrm{GHz}$, and the difference is exactly the pulling introduced by the coupling branches. The gate capacitance was raised from 8 to $C_g = 15\,\mathrm{fF}$ in order to recover readout contrast: according to Eq. (3.27) the coupling becomes $g/2\pi \approx 161.5\,\mathrm{MHz}$ and, from Eq. (7.3), the state-dependent separation grows by the factor $(15/8)^2 \approx 3.5$ to $|\chi|/2\pi \approx 3.875\,\mathrm{MHz}$. The detuning ratio decreases to $\Delta/g \approx 5.6$, values that still satisfy the dispersive condition with a margin but that constrain the probe power. The Purcell rate increases correspondingly to $\kappa_{\mathrm{Purcell}}/2\pi \approx 0.11\,\mathrm{MHz}$, i.e. a Purcell-limited T_1 of about $1.4\,\mu\mathrm{s}$; this figure highlights that, for a final implementation, a Purcell filter of the kind discussed in Section 3.2 [44] would be required, and it is taken here as a known limitation of the unfiltered architecture.

Table 7.1 summarises the component values of the first-order model and of the refined design.

Table 7.1: Component values of the readout resonator: first-order analytical sizing and design refined by circuit simulation. The derived quantities in the lower part of the table are computed with Eqs. (3.10), (3.27) and (7.3).

Parameter	Analytical model	Refined design
Tank inductance L_r	1.224 nH	1.224 nH
Tank capacitance C_r	489.7 fF	472 fF
Internal loss resistance R	500 kΩ	500 kΩ
Coupling capacitance C_c	15 fF	18 fF
Gate capacitance C_g	8 fF	15 fF
Qubit capacitance $C_q = C_{JJ} + C_{sh}$	138 fF	138 fF
Q_{int} (assumed)	10^4	10^4
Q_{ext}	1066	≈ 710
$\kappa_{\text{ext}}/2\pi$	6.10 MHz	≈ 8.72 MHz
$\kappa_{\text{tot}}/2\pi$	6.75 MHz	≈ 9.43 MHz
$g/2\pi$	53.1 MHz	≈ 161.5 MHz
Δ/g	17	≈ 5.6
$\lvert\chi\rvert/2\pi$	0.42 MHz	≈ 3.875 MHz
$\lvert\chi\rvert/\kappa_{\text{tot}}$	0.06	≈ 0.05

7.2.4 Simulation Results

Figure 7.2.2 and 7.2.3 present both the magnitude (dB) and phase of reflection coefficient S_{11} of the resonator in two configurations: the bare resonator only, and the resonator with the line coupling capacitance C_c, respectively.

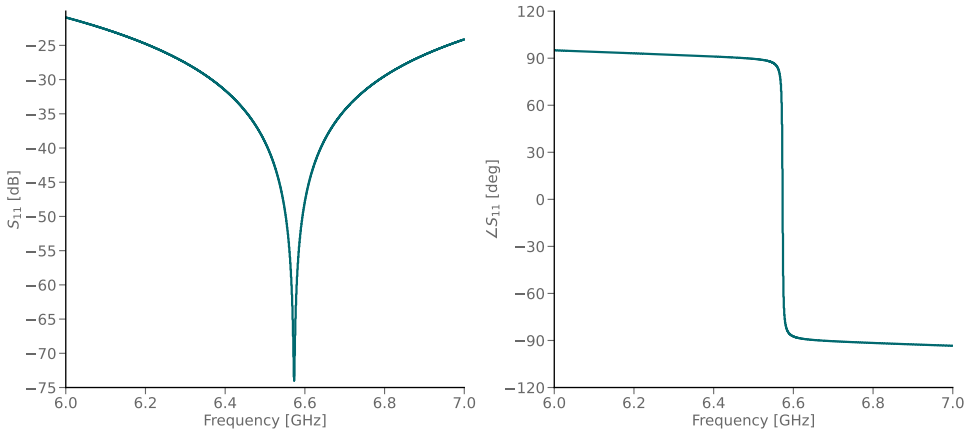


Figure 7.2.2: Reflection coefficient S_{11} of the bare resonator: magnitude (left) and phase (right) response. The resonance is centred at $f_0 = 6.58$ GHz.

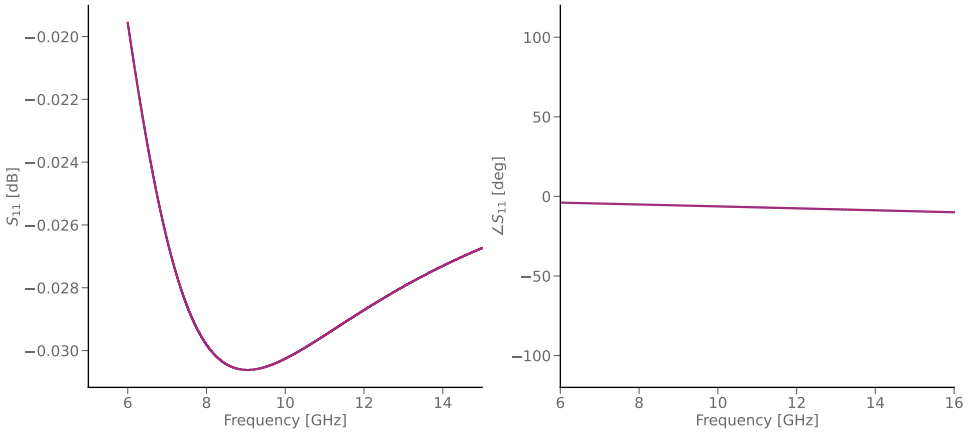


Figure 7.2.3: Reflection coefficient S_{11} of the resonator with capacitive coupling: magnitude (left) and phase (right) response.

The stand-alone characterisation of the resonator, loaded by the transmon in its ground and excited state, is reported in Figs. 7.2.4. The two resonances are centred at $f_0 = 6.386\,\text{GHz}$ and $f_1 = 6.383\,\text{GHz}$, and the reflection dips reaches $|\Gamma(\omega_0)| = -14.62\,\text{dB}$ and $|\Gamma(\omega_1)| = -10.75\,\text{dB}$, to be compared with the value of $-1.2\,\text{dB}$ ($|\Gamma| \approx 0.87$) predicted by the analytical expression for the overcoupled tank. The corresponding phase response, exhibits the full $360°$ excursion characteristic of the overcoupled regime, with the steepest slope, $\mathrm{d}\phi/\mathrm{d}f_0 = 46.55\,°/\text{MHz}$ and $\mathrm{d}\phi/\mathrm{d}f_1 = 37.45\,°/\text{MHz}$, at resonance; it is this slope that converts the dispersive shift into the phase displacement detected by the IQ demodulator.

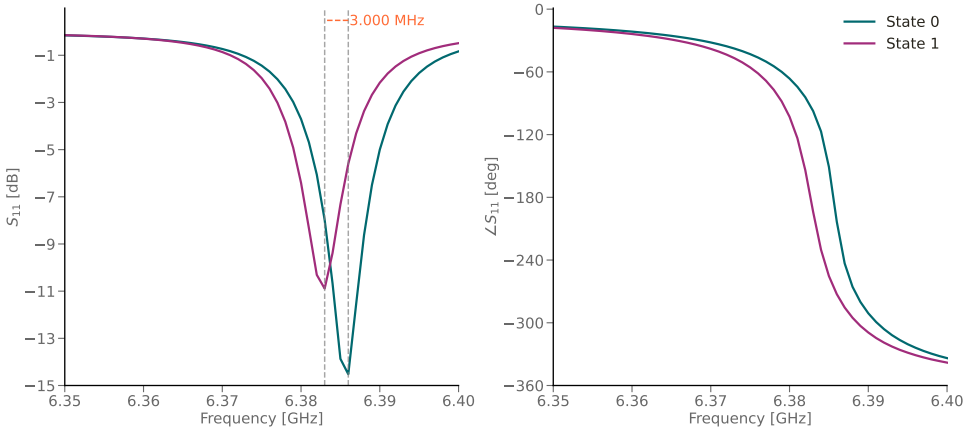


Figure 7.2.4: Simulated magnitude of the reflection coefficient of the readout resonator loaded by the transmon in the ground state. The resonance is centred at $f_0 = XX$ GHz with a full width at half maximum of the absorbed power of XX MHz.

7.3 Simulation Results

The complete reflectometry chain comprises the readout resonator and the transmon, the CMOS active circulator presented in Chapter 6, one LNA stage and the IQ demodulator. For the purpose of this study, and as justified in previouse chapters, becaus of the transmon is ”static”, so it can’t change state from $|0\rangle$ to $|1\rangle$ during the measurement, the qubit as an infinite lifetime, and the measurement is performed in a single-shot manner, the readout chanin dosn’t need of a Purcell filter, and in addition it’s possible to use a simple ideal sinusoidal tone as the probe signal, without the need of a pulse shaping. The readout chain is simulated in two configuraion with the two LNA topologies studied in Chapter 5. The last stage of the chain is the IQ demodulator, which down-converts the reflected signal to baseband and produces the in-phase (I) and quadrature (Q) components, usess two stock mixers from the Cadence library, and a low-pass filter to remove the high-frequency components. The demodulator is driven by a local oscillator (LO) at the probe frequency $f_p = 6.5\,\text{GHz}$, which is assumed to be perfectly phase-locked to the probe tone. The LO amplitude is set to $-20\,\text{dBm}$, and the mixers are biased in their linear region.

Figure 7.3.1 and Figure 7.3.2 shows the time-domain I and Q signals for both qubit states ($|0\rangle$ and $|1\rangle$), using the two LNA configurations. The state-dependent separation of the IQ trajectories is clearly observable, with the cascode-based LNA providing superior noise performance.

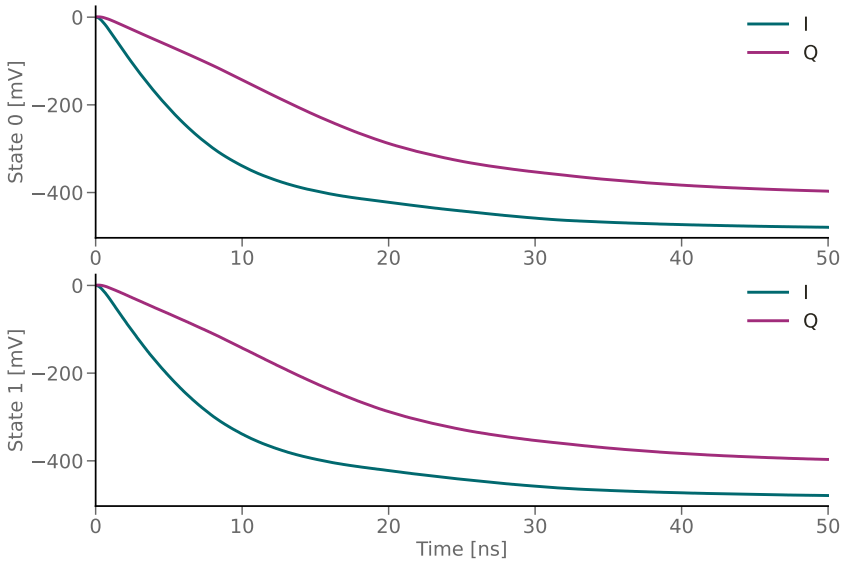


Figure 7.3.1: Time-domain I and Q demodulator output for qubit states $|0\rangle$ (blue) and $|1\rangle$ (red). (a,b) Cascode-based LNA. (c,d) Common-emitter-based LNA. Integration time: 40 ns.

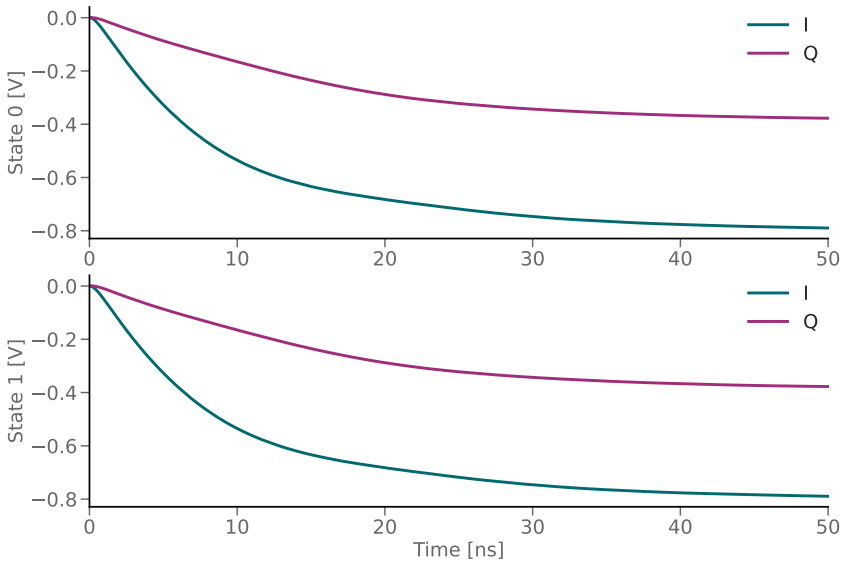
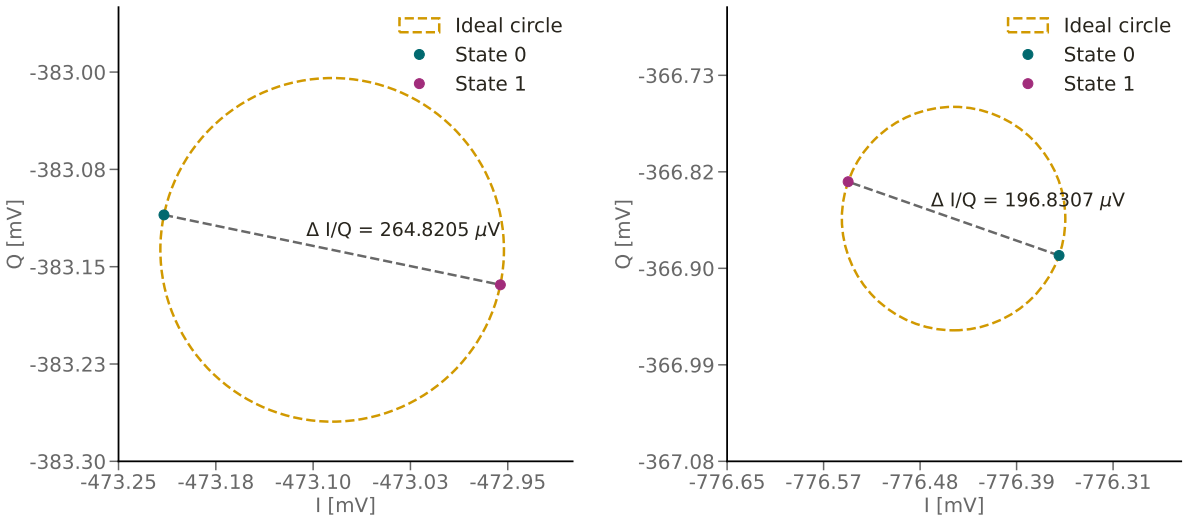


Figure 7.3.2: Time-domain I and Q demodulator output for qubit states $|0\rangle$ (blue) and $|1\rangle$ (red). (a,b) Cascode-based LNA. (c,d) Common-emitter-based LNA. Integration time: 40 ns.

To quantify the state discrimination capability, we performed single-shot measurements sampling the I/Q signals at 40 ns, and plotted the resulting IQ points on the complex plane. Figures 7.3.3a and Figure 7.3.3b illustrate the distributions of the two qubit states for both LNA configurations. The Euclidean distance between the cluster centroids provides a direct measure of the signal separation d_{sep}, while the cluster spread quantifies the measurement noise. The state separation can be quantified as:

$$d_{\text{sep}} = \sqrt{(I_1 - I_0)^2 + (Q_1 - Q_0)^2}, \tag{7.4}$$

where (I_0, Q_0) and (I_1, Q_1) are the mean values of the IQ distributions for states $|0\rangle$ and $|1\rangle$.



(a) (b)

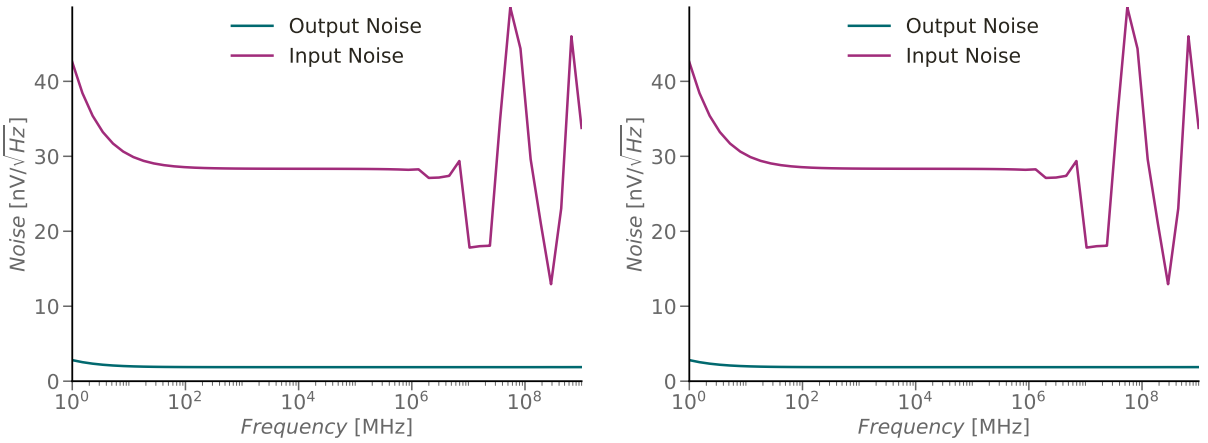
Figure 7.3.3: Single-shot IQ measurements on the complex plane with 40 ns integration time. Each point represents a single measurement. (a) Cascode-based LNA: state separation $d_{\text{sep}} = 264.82\ \mu$V. (b) Common-emitter-based LNA: state separation $d_{\text{sep}} = 196.83\ \mu$V.

The cascode-based LNA exhibits a significantly larger state separation, indicating a stronger signal response to the qubit state, thanks also to its good linearity and input matching, merit of the feedback configuration of the first cascode stage.

7.3.1 Noise Analysis

The noise performance of the readout chain is critical for achieving high-fidelity qubit measurements. We performed detailed noise simulations to characterize both the input-referred noise and the output noise of the complete readout chain. The simulations were carried out by measuring the noise spectral density at the output of the entire chain and then referring it back to the input. Since the signal path from input to I/Q outputs is symmetrical, the noise density was measured on only one side; this assumption was verified by comparing the results with the noise density measured on the other side of the chain. Furthermore, since the noise originates from the readout hardware itself rather than from the qubit-state-dependent dispersive signal, it is independent of the qubit state, allowing a single noise characterization to be applied consistently across all measurement outcomes.

Figures 7.3.4 presents the simulated noise spectral density at the input and output of the LNA for both configurations. The input-referred noise density determines the fundamental sensitivity limit of the measurement, while the output noise includes contributions from all stages of the amplification chain.



(a) (b)

Figure 7.3.4: Simulated noise spectral density. (a) Cascode-based LNA configuration. (b) Common-emitter-based LNA configuration.

Consider the output noise at baseband, the noise standard deviation σ_j for each qubit state can be calculated from the measured noise spectral density, integrated over the effective bandwidth of the demodulator. In this case, the effective bandwidth is determined by the outup low-pass filter of the IQ demodulator, which is set to $B = 100\,\text{MHz}$. For the cascode-based LNA, the integrated noise standard deviations are $\sigma_{cc} = 19.3\,\mu\text{V}$ while for the common-emitter-based LNA, they are $\sigma_{ce} = 18.7\,\mu\text{V}$. To quantify the readout performance in terms of measurement fidelity, from equation (3.89) which leads to a fidelity of $F = 99.99999\%$ for the cascode-based LNA and $F = 99.99997\%$ for the common-emitter-based LNA.

Chapter 8 Conclusions and Future Work

8.1 Summary of the Work

This thesis has addressed the design and simulation of a complete cryogenic readout chain for a superconducting transmon qubit, based on dispersive reflectometry and implemented in the IHP SG13G2 130 nm SiGe BiCMOS technology, one of the few commercial platforms whose process design kit includes device models validated at 4 K. The work was motivated by the need to demonstrate that a readout system can achieve discrete yet promising results without resorting to the complex and expensive circuit that currently dominates superconducting qubit readout: Josephson parametric amplifiers (JPAs), which require dedicated pump tones and careful tuning, and bulky passive circulators, which occupy significant space and impose strict magnetic shielding requirements. By implementing a compact, CMOS-based analogue front-end directly at the 4 K stage of the dilution refrigerator, this approach sidesteps these bottlenecks and paves the way to integration and the scalability needed for fault-tolerant quantum processors with hundreds or thousands of qubits. Relocating the readout electronics closer to the qubits also reduces the number of coaxial lines entering the cryostat, relieves the thermal budget at the coldest stages, and enables the channel density required by large-scale architectures. Achieving this goal required that the classical electronics be co-designed and co-simulated with the quantum device, and this system-level perspective, bridging quantum and classical domains, has been the guiding principle of the entire work.

The chain was assembled from blocks that are individually the subject of active research and, in several cases, still experimental in nature: a cryogenic SiGe low-noise amplifier intended to operate without a preceding Josephson parametric amplifier, an active CMOS circulator based on staggered commutation and all-pass filters intended to replace the bulky ferrite component, a fully integrated local-oscillator generation chain, a lumped readout resonator and, most notably, a compact Verilog-A model of the transmon that embeds its quantum eigenstates into a standard circuit simulator. Integrating such a heterogeneous set of blocks into a single simulation environment, and demonstrating that the resulting system discriminates the qubit states, is the principal outcome of this thesis.

8.2 Main Results

The work has produced quantitative results at every level of the design hierarchy, which are briefly recalled here.

Device level. Simulations with the $4\,\mathrm{K}$ model cards (Chapter 2) confirmed the favourable behaviour of the SiGe HBT upon cooling: the peak current gain rises from about 820 to about 2700, the Gummel slope steepens from 40 to $9.6\,\mathrm{mV/dec}$, the turn-on voltage shifts from 0.80 to $0.87\,\mathrm{V}$, and the ideality factor increases to about 20, consistent with the transition from diffusive to tunnelling-dominated transport reported in the literature. Self-heating and Early effect are essentially suppressed, which justified the simplified small-signal models adopted for the amplifier design. For the NMOS devices, the expected threshold-voltage shift of 100–$200\,\mathrm{mV}$, the steeper subthreshold slope and the mobility enhancement were verified and taken into account in the sizing of the digital LO chain.

System requirements. The analytical treatment of reflectometry and dispersive coupling (Chapter 3) translated the target single-shot fidelity into circuit specifications. For a $99\,\%$ fidelity, a contrast factor $C = 0.2$, an input power of $-100\,\mathrm{dBm}$ and a $1\,\mathrm{MHz}$ detection bandwidth, the required system noise temperature is about $27\,\mathrm{K}$, corresponding to an LNA noise figure of roughly $0.4\,\mathrm{dB}$. This figure, although demanding, is within reach of SiGe technology at $4\,\mathrm{K}$ and set the design target for Chapter 5.

Qubit model. A Verilog-A implementation of the RCSJ model (Chapter 4) was validated against the fundamental Josephson phenomenology: the DC current–phase relation, the AC Josephson frequency (reproduced to better than $0.3\,\%$), the hysteretic I–V characteristic of the underdamped junction ($\beta_c \approx 36$) and the formation of Shapiro steps at integer multiples of $\Phi_0 f_{AC}$. The model was then extended with a state-dependent effective critical current, derived by matching the classical LC resonance to the quantum transition frequencies f_{01} and f_{12} obtained from numerical diagonalisation of the transmon Hamiltonian. The resulting circuit element reproduces the anharmonicity of the device ($-160\,\mathrm{MHz}$ simulated versus $-140\,\mathrm{MHz}$ from first-order perturbation theory) and allows the qubit, frozen in the $|0\rangle$ or $|1\rangle$ eigenstate, to be placed directly in a SPICE-class netlist.

Low-noise amplifiers. Two topologies were designed, analysed and simulated(Chapter 5). The two-stage cascode amplifier with local shunt-shunt feedback achieves a gain of about $35\,\mathrm{dB}$, $S_{11} \leq -11\,\mathrm{dB}$ over 1–$12\,\mathrm{GHz}$, a minimum noise figure of $0.09\,\mathrm{dB}$ ($T_N \approx 6\,\mathrm{K}$) and unconditional stability, at a power consumption of $9\,\mathrm{mW}$. The three-stage common-emitter amplifier with LC-ladder input matching achieves about $51\,\mathrm{dB}$ of gain, $S_{11} \leq -10\,\mathrm{dB}$ from 4.95 to $17.15\,\mathrm{GHz}$ and a minimum noise figure of $63\,\mathrm{mdB}$ ($T_N \approx 4.2\,\mathrm{K}$) at $9.1\,\mathrm{mW}$. Both designs meet the noise requirement derived in Chapter 3 with margin, and the comparison with the state of the art places them among the most power-efficient high-gain cryogenic implementations reported, with noise temperatures competitive with the best SiGe results. The agreement between hand analysis and simulation (within $2\,\mathrm{dB}$ in gain and a few hundredths of a decibel in noise figure) confirms the validity of the small-signal and shot-noise models adopted.

Active circulator and LO chain. The CMOS circulator (Chapter 6) was designed from first principles, from the phase-interference interpretation of non-reciprocity to the synthesis of the second-order bridged-T and first-order lattice all-pass filters that replace the artificial transmission lines of earlier implementations, reducing the total inductance by a factor of 3.8 and yielding a fractional bandwidth of $28\,\%$. At $6.5\,\mathrm{GHz}$ the simulated device exhibits insertion losses of 3.31, 1.63 and $1.63\,\mathrm{dB}$ along the circulation direction, isolations of 42.6, 15.6 and $15.6\,\mathrm{dB}$, return losses better than $15\,\mathrm{dB}$ on all ports, a noise figure of 1.31–$2.01\,\mathrm{dB}$, an input $P_{1\mathrm{dB}}$ above $10\,\mathrm{dBm}$ and an IIP3 above $22\,\mathrm{dBm}$, figures that are largely adequate for the sub-nanowatt signal levels of qubit readout. The complete LO generation chain (active balun, self-biased squaring inverters, latch-based quadrature divider and phase aligner) was designed and simulated down to the transistor level, providing the four $1.3\,\mathrm{GHz}$ clock phases from a single $2.6\,\mathrm{GHz}$ reference delivered from room temperature, thereby saving three coaxial lines per circulator.

System level. The readout resonator was sized analytically and refined by simulation to resonate at $6.5\,\mathrm{GHz}$ in the overcoupled regime ($\kappa_{\mathrm{tot}}/2\pi \approx 9.4\,\mathrm{MHz}$, $\kappa_{\mathrm{ext}}/\kappa_{\mathrm{int}} \approx 13$), with a coupling $g/2\pi \approx 160\,\mathrm{MHz}$ and a dispersive shift $|\chi|/2\pi \approx 3.9\,\mathrm{MHz}$ to the transmon of Chapter 4. The full chain (resonator, transmon, circulator, LNA and IQ demodulator) was then simulated in the time domain (Chapter 7). With a $40\,\mathrm{ns}$ capture time, the two qubit states produce well-separated points on the IQ plane, with centroid separations of $265\,\mu\mathrm{V}$ (cascode LNA) and $197\,\mu\mathrm{V}$ (common-emitter LNA) against integrated output noise standard deviations of about $19\,\mu\mathrm{V}$ in a $100\,\mathrm{MHz}$ demodulation bandwidth. Under the assumptions of the model, this corresponds to a Gaussian state-assignment error far below 10^{-6}, i.e. the noise of the electronics is not the factor that would limit the readout fidelity.

Taken together, these results show that a fully integrated BiCMOS readout front-end, without ferrite components and without a Josephson parametric amplifier, is able in simulation to resolve the state of a transmon in a single shot within a few tens of nanoseconds, while dissipating a few tens of milliwatts at the $4\,\mathrm{K}$ stage. Given the number of experimental blocks that had to be brought together, and the fact that several of them (the circulator, the LO chain, the qubit model) have no direct precedent in this technology, this is regarded as a notable outcome.

8.3 Limitations and Expected Discrepancies with Measurements

The results presented here are simulation results, and it is appropriate to state explicitly the assumptions on which they rest and the degradation that is to be expected when moving to silicon.

First, all circuits were simulated at the schematic level. Layout parasitics, interconnect losses, substrate coupling and the finite quality factor of the on-chip spiral inductors and transformer baluns were only partially accounted for (through an estimated series resistance of the inductors). Post-layout extraction is expected to reduce the LNA gain and increase its noise figure, and to degrade the insertion loss and, above all, the isolation of the circulator, which relies on the precise cancellation of the I/Q image products and is therefore sensitive to amplitude and phase imbalance in the mixers, in the all-pass filters and in the LO phases.

Second, while the HBT models are validated at $4\,\mathrm{K}$, some cryogenic phenomena remain difficult to capture in compact models: the saturation of the noise improvement attributed to shot noise, self-heating in a vacuum environment with poor thermal conduction, the kink effect and the increased mismatch of MOS devices, and the possible deviation of passive components. The measured noise temperature of the LNAs is therefore expected to be somewhat higher than the 4–$6\,\mathrm{K}$ obtained here, in line with the spread observed in the literature between simulated and measured cryogenic LNAs.

Third, several system-level idealisations were adopted. The qubit is static and does not decay during the measurement, the probe is a continuous ideal tone, the demodulator LO is perfectly phase-locked and noiseless, the mixers are behavioural, and the readout resonator has no Purcell filter, so that the Purcell-limited lifetime of about $1.4\,\mu\mathrm{s}$ for the refined design would be unacceptable in a real experiment. The fidelities quoted in Chapter 7 must therefore be read as an upper bound set by the electronics alone, not as a prediction of the experimentally achievable fidelity, which will be dominated by qubit relaxation during the measurement, by measurement-induced dephasing and by residual LO leakage.

8.4 Future Directions

This work paves the way for several research directions, which may be grouped according to the level of the design hierarchy they concern.

Physical implementation and experimental validation. The natural next step is the layout of the individual blocks, their post-layout verification (layaut vs schematic and parassitics extraction) and a tape-out in the SG13G2 process, followed by characterisation at $4\,\mathrm{K}$ in a cryostat. Measurements of the LNA noise temperature by the Y-factor or cold-attenuator method, of the circulator S-parameters and of the LO chain phase error would provide the first experimental validation of the design methodology and of the cryogenic models on which it rests. The comparison between simulated and measured

data would, in turn, allow the models and the design margins to be calibrated for subsequent iterations.

Robustness analysis. Corner, Monte Carlo and mismatch analyses at cryogenic temperature should be carried out on the complete chain, with particular attention to the blocks whose function depends on matching: the I/Q balance of the circulator mixers, the quadrature accuracy of the frequency divider, the symmetry of the phase aligner and the balance of the active balun. Where the sensitivity proves excessive, the fixed phase alignment could be replaced by an adaptive scheme (a delay-locked loop or a digitally trimmed delay line) and the balun imbalance corrected by redesign.

Circulator and LO chain. The circulator can be improved by refining the mixer sizing and clock overlap, by adding a second modulation harmonic or a higher modulation index to reduce the LO power, and by adopting tapered output buffers to reduce the area and power of the phase aligner. A quantitative power budget of the LO chain and an analysis of LO leakage towards the resonator, which could dephase the qubit, are also required. In the longer term, the integration of a low-power cryogenic PLL would remove the need for the external $2.6\,\mathrm{GHz}$ reference altogether.

Readout resonator and filtering. The addition of a Purcell filter between the resonator and the circulator, and its co-design with the circulator input impedance, would remove the lifetime limitation identified in Chapter 7. The design space of C_c, C_g and Δ should be explored systematically to approach the optimum $\chi \approx \kappa_{\mathrm{tot}}/2$, and the effect of the probe power on the dispersive approximation (critical photon number) should be quantified for the refined design.

Qubit modelling. The hybrid quantum-classical model developed in Chapter 4 is perhaps the most promising direction of this work. Its immediate extension is the inclusion of dynamics: energy relaxation T_1 and dephasing T_2 as stochastic transitions of the state variable, the higher levels $|2\rangle, |3\rangle$ with their transition frequencies, and the flux-tunable SQUID variant. A further step is the coupling of the circuit simulator to a Lindblad master equation or to a quantum-trajectory solver, so that measurement-induced dephasing, quantum non-demolition violations and the back-action of the probe on the qubit could be studied in the same environment as the electronics. Such a tool would enable true co-simulation of the quantum and classical parts of the system, which is precisely the requirement identified in the Introduction as one of the three conditions for scalable cryogenic electronics. The same framework could be extended to other qubit platforms, notably spin qubits read out by gate reflectometry, whose state-dependent capacitance fits naturally in the model.

Pulsed and multiplexed readout. The continuous-wave probe should be replaced by the shaped (raised-cosine) pulses of Section 3.6, with the associated matched-filter integration in the digital domain, and the optimal integration time determined against a decaying qubit. Frequency-division multiplexing of several resonators on a single line, which is the ultimate motivation for the $28\,\%$ bandwidth

of the circulator and the multi-octave bandwidth of the LNAs, should be demonstrated in simulation, including the intermodulation between channels and the resulting linearity requirements.

Towards a complete cryogenic transceiver. Finally, the receive chain designed here could be complemented by the remaining functions of a cryogenic qubit interface: an integrated IQ demodulator with cryogenic mixers and baseband amplifiers, a low-power analogue-to-digital converter and the digital thresholding logic, on the receive side; a pulse generator and up-converter for qubit control, on the transmit side. The choice between a single SiGe LNA and a JPA-plus-LNA cascade, discussed in Chapter 5, could also be revisited by integrating a parametric CMOS or a cryogenic varactor-based pre-amplification stage.

8.5 Closing Remarks

The central message of this thesis is that the readout of a superconducting qubit can—and must—be treated as a unified microwave circuit-design challenge, one in which the quantum device itself takes its rightful place alongside transistors and passives in the circuit simulator. By bridging two worlds that have traditionally lived apart—the cryogenic physics of the Josephson junction at $4\,\mathrm{K}$ and the analogue design discipline of RF receiver chains—this work has demonstrated that it is possible to simulate, predict, and optimize the discrimination of quantum states using the same tools, the same intuition, and the same engineering rigor applied to any conventional communication system.

Starting from first principles—the device physics of MOSFETs deep in the subthreshold regime, the nonlinear dynamics of the transmon, the noise mechanisms that set the ultimate sensitivity—and proceeding methodically through the design of every block in the chain, the thesis has shown that a compact, integrable, ferrite-free BiCMOS readout front-end is not merely a theoretical curiosity, but a realistic and scalable option for the cryogenic interfaces of future fault-tolerant quantum processors. The performance obtained, while awaiting experimental confirmation and inevitably subject to the nonidealities of fabrication, layout parasitics, and real-world operating conditions, already suggests that the path toward hundreds or thousands of qubit channels need not pass through the fragile, bulky, and power-hungry infrastructure of Josephson parametric amplifiers and passive circulators.

More fundamentally, this work establishes that the co-simulation approach introduced here—treating the quantum and classical subsystems as parts of a single, continuous signal chain—offers a practical and intellectually coherent bridge between two domains that have for too long been separated by disciplinary boundaries and by the limitations of available simulation tools. It is this synthesis, this refusal to treat the qubit as a black box or the cryogenic amplifier as an afterthought, that has made possible the results presented in these pages, and that points the way toward the system-level co-design paradigm that large-scale quantum computing will ultimately demand.

Appendix A Verilog-A Code for Josephson Junction

This appendix provides a detailed technical explanation of the Verilog-A implementation of the Josephson junction model discussed in Section 4.2.1. The code implements a state-dependent RCSJ model that modifies the effective critical current based on the quantum eigenstate occupied by the qubit.

A.0.1 Module Structure and Interface

The Verilog-A module `jj_rcsj_quantum` defines a three-terminal device:

- `p`, `n`: Inout terminals representing the positive and negative nodes of the junction, respectively. These are the primary electrical connections through which current flows.
- `state_ctrl`: Input terminal that receives a control voltage encoding the quantum state of the qubit. This signal is generated by external control logic or measurement feedback circuits. It is also possible to substitute this with a internal parameter for static state testing.

All three terminals are declared with the `electrical` discipline, indicating they represent voltage-current relationships governed by Kirchhoff's laws. The module does not expose internal phase nodes to the circuit netlist, maintaining encapsulation of the Josephson phase dynamics.
The module accepts the following parameters that characterize the physical junction and its quantum properties:

Physical Junction Parameters

- `Ic`: Critical current of the junction in amperes. This parameter must be positive and represents the maximum supercurrent the junction can sustain at zero voltage.
- `Rn`: Normal-state resistance in ohms. This represents the quasiparticle tunneling resistance when the junction voltage exceeds the superconducting gap.
- `C`: Junction capacitance in farads. This is the intrinsic capacitance C_{JJ} arising from the tunnel barrier geometry. The external shunt capacitance C_{sh} must be added as a separate lumped element in the circuit netlist.
- `phi_init`: Initial phase across the junction in radians. This sets the phase boundary condition at $t = 0$ and can be used to model flux-biased states or specific initialization protocols.

Quantum Spectroscopic Parameters

- `f_01`: Transition frequency between ground state $|0\rangle$ and first excited state $|1\rangle$ in hertz. This frequency is determined from numerical diagonalization of the transmon Hamiltonian with the given circuit parameters.

- `f_12`: Transition frequency between first excited state $|1\rangle$ and second excited state $|2\rangle$ in hertz. The difference $f_{12} - f_{01}$ yields the anharmonicity.
- `alpha_anh`: Anharmonicity in hertz. This parameter is provided for reference and documentation purposes but is not directly used in the current implementation, as f_{12} already encodes the anharmonic shift.

Operating Mode Parameter

- `quantum_mode`: Binary flag controlling the model behavior. Range: [0:1].
  - Value 0: Classical RCSJ model with constant I_c, independent of quantum state.
  - Value 1: Quantum dispersive model with state-dependent effective critical current.

  This parameter enables direct comparison between classical and quantum-aware simulations within the same testbench.

A.0.2 Internal Variables

The analog block utilizes the following real-valued variables to track the junction's dynamical state:

- `phi`: Josephson phase in radians, computed by integrating the voltage according to 4.15.
- `Phi0`: Magnetic flux quantum $\Phi_0 = h/(2e)$ in webers, calculated from fundamental constants.
- `f_eff`: Effective transition frequency in hertz, selected based on the current quantum state.
- `L_eff`: Effective Josephson inductance in henrys, computed from the flux quantum and critical current.
- `state`: Decoded quantum state index (0 or 1) derived from the control voltage `state_ctrl`.
- `Ic_eff`: State-dependent effective critical current in amperes.
- `f_classical`: Reference frequency for normalization, set equal to f_{01}.

A.0.3 Verilog-A Source Code

The complete Verilog-A module implementation is provided below:

```
`include "constants.vams"
`include "disciplines.vams"

module jj_rcsj_quantum (p, n, state_ctrl);
    inout p, n;
    input state_ctrl;
    electrical p, n, state_ctrl;

    // Device parameters
    parameter real Ic = 59e-9 from (0:inf);
    parameter real Rn = 5000.0 from (0:inf);
    parameter real C = 8e-15 from (0:inf);
    parameter real phi_init = 0.0;
```

```
14
15      parameter real f_01 = 5.5923e9;   // Freq |0|1 [Hz]
16      parameter real f_12 = 5.4433e9;   // Freq |1|2 [Hz]
17      parameter real alpha_anh = -149.1e6; // Anharmonicity [Hz]
18
19      // Flag to switch between classical RCSJ and quantum dispersive model
20      // 0 = RCSJ classico, 1 = quantum dispersive
21      parameter real quantum_mode = 1 from [0:1];
22
23      real phi;          // Phase across the junction
24      real Phi0;         // Quantized flux
25      real f_eff;        // Effective frequency of the qubit
26      real L_eff;        // Effective inductance
27      real state;        // Quantum state (0 or 1)
28      real Ic_eff;
29      real f_classical;
30
31      analog begin
32          Phi0 = `P_H / (2.0 * `P_Q);  // 2.0678e-15 Wb
33          state = (V(state_ctrl) > 0.5) ? 1.0 : 0.0;
34
35          // Dispersive shift model
36          if (quantum_mode > 0.5) begin
37
38              f_eff = (state > 0.5) ? f_12 : f_01;
39
40              // Effective inductance of the junction
41              L_eff = Phi0 / (2.0 * `M_PI * Ic);
42
43              // Linearized model around =0 for small oscillations
44              // V = L_eff * dI/dt
45
46              // Phase from voltage
47              phi = idt(2.0 * `M_PI * V(p,n) / Phi0, phi_init);
48
49              f_classical = f_01; // Usa f_01 come riferimento
50              Ic_eff = Ic * pow(f_eff/f_classical, 2.0);
51
52              // Superconducting current
53              I(p,n) <+ Ic_eff * sin(phi);
54
55              // Resistive and capacitive currents
56              I(p,n) <+ V(p,n) / Rn;
57              I(p,n) <+ C * ddt(V(p,n));
58
59          end else begin
60              // Classical RCSJ model
```

```
            phi = idt(2.0 * `M_PI * V(p,n) / Phi0, phi_init);

            I(p,n) <+ Ic * sin(phi);
            I(p,n) <+ V(p,n) / Rn;
            I(p,n) <+ C * ddt(V(p,n));
        end
    end
endmodule
```

Listing A.1: Verilog-A implementation of the quantum-aware Josephson junction model.

A.0.4 Analog Block: Operational Logic

The core computational logic resides within the `analog begin ... end` block, which executes at every simulation timestep to update the junction's electrical state. Understanding the execution flow requires recognizing that Verilog-A describes *relationships* rather than sequential algorithms—the simulator's equation solver iteratively enforces consistency across all declared contributions.

The block begins by computing fundamental physical constants. The magnetic flux quantum $\Phi_0 = h/(2e)$ is calculated from Planck's constant and elementary charge using the predefined constants `` `P_H `` and `` `P_Q `` from the `constants.vams` library.

Quantum state information enters through the `state_ctrl` terminal. A simple threshold comparison decodes the binary quantum state: voltages below threshold map to ground state $|0\rangle$, while voltages above threshold indicate the first excited state $|1\rangle$. This digital encoding scheme aligns with standard logic-level conventions and can be driven directly by voltage-controlled sources representing measurement outcomes. The decoded state value determines which transition frequency governs the junction's response.

The subsequent logic branches based on the `quantum_mode` parameter, permit to chose whitch behaviors to use, classical or quantum-aware within the same model structure. When quantum corrections are enabled (`quantum_mode > 0.5`), the model implements state-dependent frequency matching through effective parameter modulation. This permit a easly use of this model in simulations without the need of substituting the model.

In quantum mode, a ternary operator selects the appropriate transition frequency: f_{01} for ground state excitations probing the $|0\rangle \leftrightarrow |1\rangle$ transition, or f_{12} for excited state perturbations coupling to $|1\rangle \leftrightarrow |2\rangle$.

The temporal evolution of the Josephson phase follows from integrating the AC Josephson relation (4.15). The `idt()` function accumulates the integral:

$$phi(t) = \phi_{\text{init}} + \int_0^t (2\pi/\Phi_0) V(\tau)\, d\tau \tag{A.1}$$

where the junction voltage `V(p,n)` drives phase advancement. The initial condition `phi_init` allows modeling of flux-biased states or continuation from previous simulation segments.

The quantum state dependence manifests through the effective critical current calculation. Setting

$f_{\text{classical}} = f_{01}$ as the normalization reference, the code computes $I_{c,\text{eff}} = I_c(f_{\text{eff}}/f_{01})^2$ using the `pow()` function for floating-point exponentiation. This relation, derived from equating the transmon's quantum plasma frequency to the classical RCSJ resonance condition, ensures that $I_{c,\text{eff}} = I_c$ in the ground state while reducing it by approximately 5% when the qubit occupies $|1\rangle$, consistent with the $140\ MHz$ anharmonic shift encoded in the frequency parameters.

THe output current contributions are then defined by the standard RCSJ equations, as sum of three parallel branches: supercurrent, resistive, and capacitive. The supercurrent branch contributes $I_{c,\text{eff}} \sin(\phi)$, where the state-modulated critical current directly affects the effective inductance and plasma frequency. The resistive branch adds quasiparticle tunneling current V/R_n, providing dissipation with resistance assumed independent of quantum state—a valid approximation for weak measurement tones that do not populate continuum states above the superconducting gap. Finally, the capacitive branch contributes displacement current $C\,dV/dt$ through the `ddt()` time-derivative operator, accounting for the junction's geometric capacitance C_{JJ}.

The contribution operator `<+` sums these currents at the `(p,n)` branch, and its idempotent, commutative properties allow multiple assignments without order dependence.

When quantum corrections are disabled (`quantum_mode` ≤ 0.5), the model simplifies to the standard RCSJ formulation. The same phase integration and current contributions apply, but I_c replaces $I_{c,\text{eff}}$ throughout, eliminating state dependence. The `state_ctrl` input is effectively ignored, and the junction behaves as a purely classical nonlinear element, to simulate parametric mixing circuits where quantum coherence is irrelevant.

Bibliography

[1] A. Montanaro, "Quantum algorithms: An overview," *npj Quantum Information*, vol. 2, p. 15 023, 2016.

[2] F. Sebastiano, "Fundamentals of cryo-cmos circuits and systems for quantum computing: Challenges and prospects in interfacing future quantum computers," *IEEE Solid-State Circuits Magazine*, vol. 17, no. 3, pp. 61–71, 2025.

[3] F. Battistel et al., "Real-time decoding for fault-tolerant quantum computing: Progress, challenges and outlook," *Nano Futures*, vol. 7, no. 3, p. 032 003, 2023.

[4] J. C. Bardin, D. Sank, O. Naaman, and E. Jeffrey, "Quantum computing: An introduction for microwave engineers," *IEEE Microwave Magazine*, vol. 21, no. 8, pp. 24–44, 2020.

[5] H. Zu, W. Dai, and A. De Waele, "Development of dilution refrigerators—a review," *Cryogenics*, vol. 121, p. 103 390, 2022.

[6] R. C. Kwende, D. Rosenstock, C. Wang, and J. C. Bardin, "Design and characterization of a 6-mW cryogenic SiGe IC for superconducting qubit readout," *IEEE Transactions on Microwave Theory and Techniques*, vol. 73, no. 1, pp. 234–244, 2025.

[7] Z. Zou, S. Raman, and J. C. Bardin, "A 1.6-mW cryogenic SiGe LNA IC for quantum readout applications achieving 2.6-K average noise temperature from 3 to 6 GHz," *IEEE Microwave and Wireless Technology Letters*, vol. 34, no. 6, pp. 753–756, 2024.

[8] E. Charbon et al., "Cryo-cmos for quantum computing," pp. 13.5.1–13.5.4, 2016.

[9] J. C. Bardin, D. Sank, O. Naaman, and E. Jeffrey, "Quantum computing: An introduction for microwave engineers," *IEEE Microwave Magazine*, vol. 21, no. 8, pp. 24–44, 2020.

[10] J. D. Cressler, "The sige hbt at cryogenic temperatures: Invited pager," in *2023 IEEE BiCMOS and Compound Semiconductor Integrated Circuits and Technology Symposium (BCICTS)*, IEEE, 2023, pp. 274–279.

[11] A. Beckers, F. Jazaeri, A. Grill, S. Narasimhamoorthy, B. Parvais, and C. Enz, "Physical model of low-temperature to cryogenic threshold voltage in mosfets," *IEEE Journal of the Electron Devices Society*, vol. 8, pp. 780–788, 2020.

[12] H.-C. Han, F. Jazaeri, A. D'Amico, A. Baschirotto, E. Charbon, and C. Enz, "Cryogenic characterization of 16 nm finfet technology for quantum computing," in *ESSCIRC 2021 - IEEE 47th European Solid State Circuits Conference (ESSCIRC)*, 2021, pp. 71–74.

[13] Z. Li, C. Luo, T. Lu, J. Xu, W. Kong, and G. Guo, "Cryogenic characerization and modeling of standard cmos down to liquid helium temperature for quantum computing," *arXiv preprint arXiv:1811.11497*, 2018.

[14] H. Rücker, J. Korn, and J. Schmidt, "Operation of sige hbts at cryogenic temperatures," in *2017 IEEE Bipolar/BiCMOS Circuits and Technology Meeting (BCTM)*, IEEE, 2017, pp. 17–20.

[15] Y. Varshni, "Temperature dependence of the energy gap in semiconductors," *Physica*, vol. 34, no. 1, pp. 149–154, 1967, issn: 0031-8914.

[16] J. Benserhir, Y. Zou, H.-C. Han, Y. Peng, and E. Charbon, "Broadband noise characterization of sige hbts down to 4k," *IEEE Journal of the Electron Devices Society*, 2025.

[17] J. C. Bardin, D. Sank, O. Naaman, and E. Jeffrey, "Quantum computing: An introduction for microwave engineers," *IEEE Microwave Magazine*, vol. 21, no. 8, pp. 24–44, 2020.

[18] A. A. Cherepanov, I. L. Novikov, and V. Y. Vasiliev, "An evaluation of sige hbt operation at cryogenic temperatures," in *2019 20th International Conference of Young Specialists on Micro/Nanotechnologies and Electron Devices (EDM)*, IEEE, 2019, pp. 23–27.

[19] A. J. Joseph, J. D. Cressler, D. M. Richey, R. C. Jaeger, and D. L. Harame, "Neutral base recombination and its influence on the temperature dependence of early voltage and current gain-early voltage product in uhv/cvd sige heterojunction bipolar transistors," *IEEE Transactions on Electron Devices*, vol. 44, no. 3, pp. 404–413, 1997.

[20] P. S. Chakraborty et al., "A 0.8 thz f_{max} sige hbt operating at 4.3 k," *IEEE Electron Device Letters*, vol. 35, no. 2, pp. 151–153, 2014.

[21] M. Schröter and X. Jin, "A physics-based analytical formulation for the tunneling current through the base of bipolar transistors operating at cryogenic temperatures," *IEEE Transactions on Electron Devices*, vol. 70, no. 1, pp. 247–253, 2022.

[22] J. Yuan et al., "An investigation of negative differential resistance and novel collector–current kink effects in sige hbts operating at cryogenic temperatures," *IEEE Transactions on Electron Devices*, vol. 54, no. 3, pp. 504–516, 2007.

[23] L. Song, H. Homulle, E. Charbon, and F. Sebastiano, "Characterization of bipolar transistors for cryogenic temperature sensors in standard cmos," in *2016 IEEE SENSORS*, IEEE, 2016, pp. 1–3.

[24] H. Ying et al., "Compact modeling of sige hbts for design of cryogenic control and readout circuits for quantum computing," in *2020 IEEE BiCMOS and Compound Semiconductor Integrated Circuits and Technology Symposium (BCICTS)*, IEEE, 2020, pp. 1–4.

[25] F. Liu, Z. Deng, and Y. Liu, "Cryogenic bandgap reference circuit with compact model parameter extraction of mosfets and bjts for hpge detectors," *IEEE Transactions on Nuclear Science*, vol. 67, no. 10, pp. 2209–2216, 2020.

[26] S. Bonen et al., "Cryogenic characterization of the high frequency and noise performance of sige hbts from dc to 70 ghz and down to 2 k," *IEEE Microwave and Wireless Components Letters*, vol. 32, no. 6, pp. 696–699, 2022.

[27] D. Prele et al., "Standard sige technologies operating at 4 k for front-end readout of squid arrays," in *2006 8th International Conference on Solid-State and Integrated Circuit Technology Proceedings*, 2006, pp. 191–193.

[28] L. Najafizadeh et al., "Sub-1-k operation of sige transistors and circuits," *IEEE Electron Device Letters*, vol. 30, no. 5, pp. 508–510, 2009.

[29] S. Weinreb, J. C. Bardin, and H. Mani, "Design of cryogenic sige low-noise amplifiers," *IEEE transactions on microwave theory and techniques*, vol. 55, no. 11, pp. 2306–2312, 2007.

[30] E. Crabbe, G. Patton, J. Stork, J. Comfort, B. Meyerson, and J.-C. Sun, "Low temperature operation of si and sige bipolar transistors," in *International Technical Digest on Electron Devices*, IEEE, 1990, pp. 17–20.

[31] J. D. Cressler, "Silicon-germanium as an enabling technology for extreme environment electronics," *IEEE Transactions on Device and Materials Reliability*, vol. 10, no. 4, pp. 437–448, 2010.

[32] A. Wallraff et al., "Strong coupling of a single photon to a superconducting qubit using circuit quantum electrodynamics," *Nature*, vol. 431, no. 7005, pp. 162–167, 2004.

[33] R. Ludwig, *RF Circuit Design: Theory & Applications, 2/e*. Pearson Education India, 2009.

[34] J. Li and P. Burke, "Measurement of the combined quantum and electrochemical capacitance of a carbon nanotube," *Nature Communications*, vol. 10, Aug. 2019.

[35] A. Blais, A. L. Grimsmo, S. M. Girvin, and A. Wallraff, "Circuit quantum electrodynamics," *Reviews of Modern Physics*, vol. 93, no. 2, May 2021, issn: 1539-0756.

[36] D. J. Ibberson, L. A. Ibberson, G. Smithson, J. A. Haigh, S. Barraud, and M. F. Gonzalez-Zalba, "Low-temperature tunable radio-frequency resonator for sensitive dispersive readout of nanoelectronic devices," *Applied Physics Letters*, vol. 114, no. 12, 2019, issn: 1077-3118.

[37] F. Vigneau et al., "Probing quantum devices with radio-frequency reflectometry," *Applied Physics Reviews*, vol. 10, no. 2, p. 021 305, Feb. 2023, issn: 1931-9401.

[38] D. Pozar, *Microwave Engineering*. Wiley, 2011, isbn: 9780470631553.

[39] O. Kamigaito, "Circuit-model formulas for external-q factor of resonant cavities with capacitive and inductive coupling," *arXiv preprint arXiv:2005.05843*, 2020.

[40] J. Koch et al., "Charge-insensitive qubit design derived from the cooper pair box," *Physical Review A*, vol. 76, no. 4, Oct. 2007, issn: 1094-1622.

[41] A. Blais, R.-S. Huang, A. Wallraff, S. M. Girvin, and R. J. Schoelkopf, "Cavity quantum electrodynamics for superconducting electrical circuits: An architecture for quantum computation," *Physical Review A*, vol. 69, no. 6, 2004, issn: 1094-1622.

[42] R. Hanai, A. McDonald, and A. Clerk, "Intrinsic mechanisms for drive-dependent purcell decay in superconducting quantum circuits," *Phys. Rev. Res.*, vol. 3, p. 043 228, 4 Dec. 2021.

[43] A. A. Houck et al., "Controlling the spontaneous emission of a superconducting transmon qubit," *Physical Review Letters*, vol. 101, no. 8, Aug. 2008, issn: 1079-7114.

[44] E. A. Sete, J. M. Martinis, and A. N. Korotkov, "Quantum theory of a bandpass purcell filter for qubit readout," *Physical Review A*, vol. 92, no. 1, 2015, issn: 1094-1622.

[45] M. Boissonneault, J. M. Gambetta, and A. Blais, "Improved superconducting qubit readout by qubit-induced nonlinearities," *Phys. Rev. Lett.*, vol. 105, p. 100 504, 10 Sep. 2010.

[46] J. Gambetta, W. A. Braff, A. Wallraff, S. M. Girvin, and R. J. Schoelkopf, "Protocols for optimal readout of qubits using a continuous quantum nondemolition measurement," *Physical Review A*, vol. 76, no. 1, 2007, issn: 1094-1622.

[47] A. A. Clerk, M. H. Devoret, S. M. Girvin, F. Marquardt, and R. J. Schoelkopf, "Introduction to quantum noise, measurement, and amplification," *Reviews of Modern Physics*, vol. 82, no. 2, pp. 1155–1208, Apr. 2010, issn: 1539-0756.

[48] E. Paladino, Y. M. Galperin, G. Falci, and B. L. Altshuler, "1/f noise: Implications for solid-state quantum information," *Reviews of Modern Physics*, vol. 86, no. 2, pp. 361–418, Apr. 2014, issn: 1539-0756.

[49] T. Walter et al., "Rapid high-fidelity single-shot dispersive readout of superconducting qubits," *Physical Review Applied*, vol. 7, no. 5, p. 054 020, 2017.

[50] N. Reiskarimian and H. Krishnaswamy, "Magnetic-free non-reciprocity based on staggered commutation," *Nature communications*, vol. 7, no. 1, p. 11 217, 2016.

[51] T. Dinc, A. Nagulu, and H. Krishnaswamy, "A millimeter-wave non-magnetic passive soi cmos circulator based on spatio-temporal conductivity modulation," *IEEE Journal of Solid-State Circuits*, vol. 52, no. 12, pp. 3276–3292, 2017.

[52] Z. Hao, J. Cochran, Y.-C. Chang, H. M. Cole, and S. Shankar, "Wireless josephson parametric amplifier above 20 ghz," *Applied Physics Letters*, vol. 128, no. 1, Jan. 2026, issn: 1077-3118.

[53] D. P. DiVincenzo, "The physical implementation of quantum computation," *Fortschritte der Physik: Progress of Physics*, vol. 48, no. 9-11, pp. 771–783, 2000.

[54] P. Krantz, M. Kjaergaard, F. Yan, T. P. Orlando, S. Gustavsson, and W. D. Oliver, "A quantum engineer's guide to superconducting qubits," *Applied Physics Reviews*, vol. 6, no. 2, p. 021 318, 2019.

[55] M. Kjaergaard et al., "Superconducting qubits: Current state of play," *Annual Review of Condensed Matter Physics*, vol. 11, pp. 369–395, 2020.

[56] J. Koch et al., "Charge-insensitive qubit design derived from the Cooper pair box," *Physical Review A*, vol. 76, no. 4, p. 042 319, 2007.

[57] J. Bardeen, L. N. Cooper, and J. R. Schrieffer, "Theory of superconductivity," *Physical Review*, vol. 108, no. 5, pp. 1175–1204, 1957.

[58] M. Tinkham, *Introduction to Superconductivity*, 2nd ed. Mineola, NY: Dover Publications, 2004.

[59] B. S. Deaver and W. M. Fairbank, "Experimental evidence for quantized flux in superconducting cylinders," *Physical Review Letters*, vol. 7, no. 2, pp. 43–46, 1961.

[60] R. Doll and M. Näbauer, "Experimental proof of magnetic flux quantization in a superconducting ring," *Physical Review Letters*, vol. 7, no. 2, pp. 51–52, 1961.

[61] B. D. Josephson, "Possible new effects in superconductive tunnelling," *Physics Letters*, vol. 1, no. 7, pp. 251–253, 1962.

[62] V. Ambegaokar and A. Baratoff, "Tunneling between superconductors," *Physical Review B*, vol. 134, no. 4A, A935–A941, 1963.

[63] W. C. Stewart, "Current-voltage characteristics of Josephson junctions," *Applied Physics Letters*, vol. 12, no. 8, pp. 277–280, 1968.

[64] D. E. McCumber, "Effect of ac impedance on dc voltage-current characteristics of superconductor weak-link junctions," *Journal of Applied Physics*, vol. 39, no. 7, pp. 3113–3118, 1968.

[65] S. Shapiro, "Josephson currents in superconducting tunneling: The effect of microwaves and other observations," *Physical Review Letters*, vol. 11, no. 2, pp. 80–82, 1963.

[66] K. K. Likharev, *Dynamics of Josephson Junctions and Circuits*. New York: Gordon and Breach, 1986.

[67] R. Barends et al., "Coherent Josephson qubit suitable for scalable quantum integrated circuits," *Physical Review Letters*, vol. 111, no. 8, p. 080 502, 2013.

[68] A. Barone and G. Paternò, *Physics and Applications of the Josephson Effect*. New York: John Wiley & Sons, 1982.

[69] J. A. Schreier et al., "Suppressing charge noise decoherence in superconducting charge qubits," *Physical Review B*, vol. 77, no. 18, p. 180 502, 2008.

[70] T. E. Roth, R. Ma, and W. C. Chew, "An introduction to the transmon qubit for electromagnetic engineers," *arXiv preprint arXiv:2106.11352*, 2021.

[71] R. L. Kautz, "Noise, chaos, and the Josephson voltage standard," *Reports on Progress in Physics*, vol. 59, no. 8, pp. 935–992, 1996.

[72] H. Zu, W. Dai, and A. de Waele, "Development of dilution refrigerators—a review," *Cryogenics*, vol. 121, p. 103 390, 2022, issn: 0011-2275.

[73] M. Mehrpoo, F. Sebastiano, E. Charbon, and M. Babaie, "A cryogenic cmos parametric amplifier," *IEEE Solid-State Circuits Letters*, vol. 3, pp. 5–8, 2020.

[74] B. Razavi and R. Behzad, *RF microelectronics*. Prentice hall New York, 2012, vol. 2.

[75] P. D. Petrova, "Noise modeling and analysis of a bjt common–emitter stage," *Electronic Components, Systems and Technologies*, p. 495,

[76] Q. Berlingard et al., "Rf performances at cryogenic temperature of inductors integrated in a fdsoi technology," *Solid-State Electronics*, vol. 194, p. 108 285, 2022.

[77] Z. Chen, H. Gao, and P. G. Baltus, "A design approach for sige low-noise amplifiers using wideband input matching," pp. 1–4, 2018.

[78] Y. Peng, J. Benserhir, M. Castaneda, A. Fognini, C. Bruschini, and E. Charbon, "A 0.32× 0.12 mm 2 cryogenic bicmos 0.1–8.8 ghz low noise amplifier achieving 4 k noise temperature for snwd readout," *IEEE Transactions on Microwave Theory and Techniques*, vol. 72, no. 4, pp. 2179–2192, 2024.

[79] B. Patra et al., "Cryo-cmos circuits and systems for quantum computing applications," *IEEE Journal of Solid-State Circuits*, vol. 53, no. 1, pp. 309–321, 2017.

[80] S. Das, S. Raman, and J. C. Bardin, "Design and implementation of a 3.9-to-5.3 ghz 65 nm cryo-cmos lna with an average noise temperature of 10.2 k," in *2022 IEEE/MTT-S International Microwave Symposium-IMS 2022*, IEEE, 2022, pp. 719–722.

[81] A. Sheldon and L. Belostotski, "Cryo-cmos low-noise amplifier for the square kilometre array," in *2018 18th International Symposium on Antenna Technology and Applied Electromagnetics (ANTEM)*, IEEE, 2018, pp. 1–2.

[82] Z. Gao et al., "A 5.5-7.9 ghz double quadrature cryo-cmos receiver featuring a wideband noise matching lna for quantum applications," in *2025 IEEE International Symposium on Circuits and Systems (ISCAS)*, IEEE, 2025, pp. 1–5.

[83] S. Das, S. Raman, and J. C. Bardin, "A 4-to-6-ghz cryogenic cmos lna with 4.4-k average noise temperature in 22-nm fdsoi," *IEEE Microwave and Wireless Technology Letters*, vol. 34, no. 4, pp. 411–414, 2024.

[84] Z. Tao, L. Yang, W. He, and H. Chen, "A 0.5-0.8 ghz cryogenic lna with 0.7 db nf in 180nm cmos," in *2024 IEEE MTT-S International Wireless Symposium (IWS)*, IEEE, 2024, pp. 1–3.

[85] Z. Gao et al., "A cryo-tolerant> 40-db irr, 4.7–7.9-ghz double quadrature cryo-cmos receiver with a broadband lna for scalable quantum applications," *IEEE Transactions on Very Large Scale Integration (VLSI) Systems*, 2025.

[86] B. Aja, E. Villa, L. de la Fuente, and E. Artal, "Cryogenic performance of a 3–14 ghz bipolar sige low-noise amplifier," *Cryogenics*, vol. 99, pp. 18–24, 2019.

[87] A. Caglar, S. Van Winckel, S. Brebels, P. Wambacq, and J. Craninckx, "A 4.2 mw 4k 6-8ghz cmos lna for superconducting qubit readout," in *2021 IEEE Asian Solid-State Circuits Conference (A-SSCC)*, IEEE, 2021, pp. 1–3.

[88] W. Lee and E. Afshari, "Low-noise parametric resonant amplifier," *IEEE Transactions on Circuits and Systems I: Regular Papers*, vol. 58, no. 3, pp. 479–492, 2010.

[89] G. Baek et al., "13-kt noise cryo-cmos parametric amplifier at 80 mk for quantum computers," in *2022 IEEE Symposium on VLSI Technology and Circuits (VLSI Technology and Circuits)*, IEEE, 2022, pp. 236–237.

[90] C. Macklin et al., "A near–quantum-limited josephson traveling-wave parametric amplifier," *Science*, vol. 350, no. 6258, pp. 307–310, 2015.

[91] L. Ranzani, G. Ribeill, B. Hassick, and K. C. Fong, "Wideband josephson parametric amplifier with integrated transmission line transformer," in *2022 IEEE International Conference on Quantum Computing and Engineering (QCE)*, IEEE, 2022, pp. 314–319.

[92] W. Lee and E. Afshari, "An 8ghz, 0.45 db nf cmos lna employing noise squeezing," in *2011 IEEE Radio Frequency Integrated Circuits Symposium*, IEEE, 2011, pp. 1–4.

[93] B. Gray, F. Ramirez, B. Melville, A. Suarez, and J. S. Kenney, "A broadband double-balanced phase-coherent degenerate parametric amplifier," *IEEE microwave and wireless components letters*, vol. 21, no. 11, pp. 607–609, 2011.

[94] Y. Geng, H. Lin, B. Wang, and C. Wang, "Cryo-cmos dual-qubit homodyne reflectometer array with degenerate parametric amplification," *IEEE Journal of Solid-State Circuits*, vol. 59, no. 10, pp. 3290–3306, 2024.

[95] J. Sadler and W. Wells, "Cryogenically cooled x-band parametric amplifier," *Proceedings of the IEEE*, vol. 52, no. 3, pp. 305–305, 1964.

[96] T. Nagai, J. Murakami, T. Tarui, S. Yoshida, and H. Yonemitsu, "Low noise receiver with helium cooled parametric amplifier," *Proceedings of the IEEE*, vol. 54, no. 6, pp. 882–883, 1966.

[97] G. Viola and D. P. DiVincenzo, "Hall effect gyrators and circulators," *Phys. Rev. X*, vol. 4, p. 021 019, 2 May 2014.

[98] A. Nagulu and H. Krishnaswamy, "Non-magnetic cmos switched-transmission-line circulators with high power handling and antenna balancing: Theory and implementation," *IEEE Journal of Solid-State Circuits*, vol. 54, no. 5, pp. 1288–1303, 2019.

[99] P. Krantz, M. Kjaergaard, F. Yan, T. P. Orlando, S. Gustavsson, and W. D. Oliver, "A quantum engineer's guide to superconducting qubits," *Applied Physics Reviews*, vol. 6, no. 2, p. 021 318, 2019.

[100] M. Göppl et al., "Coplanar waveguide resonators for circuit quantum electrodynamics," *Journal of Applied Physics*, vol. 104, no. 11, p. 113 904, 2008.

[101] S. Probst, F. B. Song, P. A. Bushev, A. V. Ustinov, and M. Weides, "Efficient and robust analysis of complex scattering data under noise in microwave resonators," *Review of Scientific Instruments*, vol. 86, no. 2, p. 024 706, 2015.

[102] M. S. Khalil, M. J. A. Stoutimore, F. C. Wellstood, and K. D. Osborn, "An analysis method for asymmetric resonator transmission applied to superconducting devices," *Journal of Applied Physics*, vol. 111, no. 5, p. 054 510, 2012.